Noble Metallic Multi-layer and Tin Oxide Based Alternative Transparent Conducting Electrodes for Optoelectronic Devices

A thesis

submitted in partial fulfillment of the requirements

for the award of the degree of

Doctor of Philosophy

in

Physics

submitted by

REDDIVARI MUNIRAMAIAH

(Roll. No. 701966)

Under the Supervision of

Prof. D. Paul Joseph

Department of Physics

National Institute of Technology Warangal

Hanamkonda, Telangana, India - 506004

(November, 2023)

Department of Physics
National Institute of Technology Warangal,
Hanamkonda, Telangana, India - 506004.

Declaration by the Candidate

I hereby declare that the work presented in the thesis entitled **"Noble Metallic Multi-layer and Tin Oxide Based Alternative Transparent Conducting Electrodes for Optoelectronic Devices"** in partial fulfillment of the requirements for the award of the Degree of **Doctor of Philosophy** submitted to the Department of Physics, National Institute of Technology Warangal is an authentic record of my own reasearch work carried out during the period from December 2019 to November 2023 under the supervision of **Prof. D. Paul Joseph**, Associate Professor, Department of Physics, National Institute of Technology Warangal.

The subject matter presented in this thesis has not been submitted for the award of any other degree at any other Institute/University.

Place: Warangal
Date: 06/11/2023

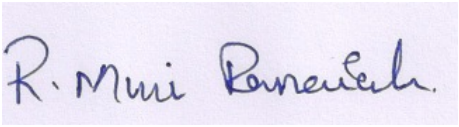

Reddivari Muniramaiah
Roll No: 701966

Department of Physics
National Institute of Technology Warangal,
Hanamkonda, Telangana, India-506004.

Certificate

This is to certify that the work presented in this thesis entitled **"Noble Metallic Multi-layer and Tin Oxide Based Alternative Transparent Conducting Electrodes for Optoelectronic Devices"** is a bonafide work carried out by **Mr. Reddivari Muniramaiah**, **Roll No: 701966** under my supervision and was not submitted elsewhere for the award of any other degree.

.

Place: Warangal
Date: 06/11/2023

Prof. D. Paul Joseph
Associate Professor
Department of Physics
NIT Warangal.

Dedicated to my family

ACKNOWLEDGMENTS

It is a great pleasure for me to express my respect and deep sense of gratitude to my Ph.D. supervisor Dr. D. Paul Joseph, Associate Professor, Department of Physics, National Institute of Technology, Warangal, for his guidance, enthusiastic involvement and persistent encouragement during the planning and execution of this research work. I also gratefully acknowledge his painstaking efforts in thoroughly tuning and improving the manuscripts and the thesis.

I am highly obliged to Prof. Bidyadhar Subudhi, Director, National Institute of Technology, Warangal and Prof. T. Venkatappa Rao, Head, Department of Physics for providing the facilities, help and encouragement for carrying out the research work. I also express my sincere thanks to the former Director, Prof. N. V. Ramana Rao, NIT Warangal and Heads of Department of Physics, for their valuable support rendered. I express my sincere thanks to the Ministry of Education, Govt. of India, for the financial support in the form of institute fellowship.

I sincerely thank the members of the Doctoral scrutiny committee (DSC) Prof. K. Thangaraju, Dr. V. Jayalakshmi, Department of Physics, NIT-Warangal, and Prof. Vishnu Shanker, Department of Chemistry, NIT-Warangal, for their valuable suggestions at every stage of my research work.

I am very much thankful to Prof. D. Haranath, and Dr. R. Rakesh Kumar for providing facilities for making the ACEL and PENG devices, respectively. I am thankful to Dr. M. Kovendhan, Department of Physics and Nanotechnology, SRM Institute of Science and Technology, Kattankulathur, Tamilnadu and Dr. V. Ganapathy, ARCI, Hyderabad, India for their help in several experimental measurements. I sincerely thank Dr. Murali Banavoth, Associate Professor, School of Chemistry, University of Hyderabad, for permitting me to carry out solar cell device fabrication and characterization in his laboratory.I am extremely thankful to Prof. Davide Mariotti and Dr. Dilli Babu Padmanaban, School of Engineering, Ulster University, UK, for their valuable help for measuring the surface work function of my samples by Kelvin probe method. I also thank Dr. M. Manivel Raja, Advanced Magnetics Group, Defence Metallurgical Research Laboratory (DMRL), Hyderabad for his help in depositing metallic thin films, and Dr. Gangalakurthi Lakshminarayana, RCI, DRDO, Hyderabad for his help in conducting optical profiler measurements.

I am thankful to senior faculty members of the department, Prof. L. Ramgopal Reddy, Prof. R. L. N. Sai Prasad, Prof. K. Venugopal Reddy, Prof. D. Dinakar and Prof. Sobha for their encouragement and support.

I take this opportunity to express my gratitude to Prof. P. Abdul Azeem, Prof. P. Syam Prasad, Prof. Sourabh Roy, Dr. Kusum Kumari, Dr. V. Jayalakshmi, Dr. K. Udaykumar, Dr. Vijay Kumar, Dr. Surya K. Ghosh, Dr. Hitesh Borkar, Dr. Aalu Boda, Department of Physics, NIT-Warangal for their valuable advice, encouragement and moral support during the course of my research.

I extend my sincere thanks to CRIF, NIT-Warangal for providing XRD and SEM-EDX characterization facilities for my samples.

With all happiness I acknowledge the cheerful assistance rendered by all my senior research colleagues Dr. R. Ramarajan, Dr. N. Purushotham Reddy, Dr. Benjamin Hudson Baby, and my juniors Mr. Gouranga Maharana, and Ms. Yuvashree Jayavelu for their encouragement thoughout the period of my research work.

I thank my dear friends Mr. K. Naveenkumar, Mr. S. Babu Rao, Mr. K. A. K. Durga Prasad, Ms. P. Supraja, Ms. M. Rakshita, Ms. T. Lavanya, Mrs. S. P. Ramadevi, Ms. Anjali Babu, and other co-research scholars for their munificent support. I would also like to express my deep and sincere thanks to all others whose names are not mentioned here, who have helped me either directly or indirectly in my research work.

I am obliged to my parents Mr. R. Munikrishna Reddy and Mrs. R. Gurramma for their moral support, love, encouragement and blessings to complete this task. I specially thank my brother Mr. R. Gopal, sister Mrs. M. Jayanthi and sister-in-law Mrs. R. Priya for thier patience, love and encouragement.

I am also thankful to the anonymous reviewers of my research publications for their comments and suggestions which were very helpful in shaping my research work.

I would also like to extend my special thanks to all the staff members, Department of Physics, NIT-Warangal for their timely help and cooperation extended throughout the course.

Finally, I am indebted and grateful to God the Almighty for helping me in this endeavor and throughout my life.

Reddivari Muniramaiah

Preface

In recent years, transparent conducting electrode (TCE) materials have attracted considerable attention for potential applications in optoelectronic devices due to their unique electrical and optical properties. More importantly, drastically increasing display device's usage cause more demand for indium tin oxide (ITO) and fluorine doped tin oxide (FTO) electrodes. The scarcity of indium and optimization difficulty of FTO lead to intense exploration of alternative materials. Therefore, the development of highly efficient and cost-effective TCEs are today's demand.

There are several alternative materials that are extensively explored for TCE application such as, metal nanowires, carbon nanotubes, graphene, multi-oxide systems, and conducting organic polymer materials. However, the problem is, even though the metallic nanowires show good electrical properties, it possesses a low figure of merit values due to low optical property, and stability compared to metal oxide based TCE materials. The carbon based TCE materials show low electrical transport properties, and organic TCE materials are expensive and less stable than metal oxide system. More interestingly, the binary metal oxide optimization is easier than ternary metal oxide system in controlling the phase formation. These aspects inspired to explore alternative materials for existing ITOs and FTOs. For the flexible electrodes, ultrathin noble metallic multi layers were deposited on the PET substrate using sputtering technique in multi-layer and tri-layer architectures.

For unpliable electrodes, the binary TCO material by doping with various elements using the cost-effective spray deposition technique. The AO_2 binary rutile structure offers high flexibility to incorporate dopants at the 'A' site yielding doped rutile structure. In AO_2 rutile structure, altering the stoichiometry or doping with different donor elements of a different valence state help in tuning the optical and electrical properties appreciably. Among the AO_2 systems, SnO_2 is one of the best host material for effective transparent conducting electrodes. This research work mainly focuses to explore SnO_2 by doping with various elements. The systems explored are F-doped SnO_2 (FTO), Nb and F co-doped SnO_2 (NFTO), and Nb and Sb co-doped SnO_2 (NATO). Finally, various optimized TCE films were tested as TCE in dye sensitized solar cell (DSSC), Piezoelectric nanogenerators (PENG) and alternating current electroluminescent (ACEL) devices.

The research work presented in this thesis is organized into seven chapters, which are briefly described as follows:

i) **Chapter 1** This chapter provides a general introduction to the TCE materials. An extensive literature review on the previously reported TCEs and its classification based on the non-oxide and oxide-based materials, elucidating their basic properties and performance. A detailed review of literature on different deposition methods of metallic and metal oxide electrodes are concisely presented. Fundamentals of various applications of the thin film TCEs in devices like DSSC, PENG and ACEL devices are also discussed briefly. The strategy for identifying the alternative TCE materials for supplementing the existing ITO and FTOs are outlined. This chapter is concluded with the motivation, objectives, and scope of the proposed thesis work.

ii) **Chapter 2** This chapter begins with introduction to thin films, thin-film growth methods, and thin-film formation modes. Deposition of metal electrodes on flexible PET substrate using sputtering technique and metal oxide electrodes onto the glass substrate using chemical spray pyrolysis technique are elaborated. This chapter further gives brief overview of various analytical instruments and its fundamental principles of operation, along with specifications of the actual instrument used to characterize the prepared samples. This chapter is concluded with fabrication procedure of DSSC, PENG and ACEL optoelectronic devices and related measurement details are also elaborated.

iii) **Chapter 3** This chapter deals with the structural, morphological, optical, and electrical properties of the sputter deposited Au/Cu/Ag/Pt/Au ultrathin (10 nm total thickness) metallic multilayer. Thickness of the individual metallic layer is altered based on their skin depth using standard equations. The Au/Cu/Ag/Pt/Au multi-layer presents a considerable transmittance of 44 % (at 500 nm) with nearly uniform trend over the complete visible region of the electromagnetic spectrum. Electrical transport measurements of the multi-layer yielded 60 $\Omega/\square$ sheet resistance and a carrier mobility of 2.02 $cm^2V^{-1}s^{-1}$. The transition of bare PET from hydrophilic (73.85°) to hydrophobic (99.83°) upon depositing the metallic multi-layer is observed from contact angle measurements. The surface features explored using atomic force microscope and optical profiler showed uniform topography, and free of cracks. The metallic multi-layer exhibits high mechanical strength of sheet resistance withstanding up to 50,000 bending - twisting sequences with only marginal variation in sheet resistance. The measured surface work function of Au/Cu/Ag/Pt/Au metallic multi-layer is 5.01 eV. The sputter deposited ultrathin Au/Cu/Ag/Pt/Au metallic multilayer is tested as top and bottom electrode in an ACEL device and as top electrode

in a PENG device. The fabricated ACEL and PENG devices show appreciable performance and the results are discussed in detail.

iv) **Chapter 4** Based on the observations of chapter 3, in order to further enhance the optoelectronic properties, this chapter describes the details of sputter deposited Au/Pt/Au ultrathin (6 nm total thickness) metallic tri-layer transparent conducting electrode deposited over flexible PET substrate. The tri-layer shows considerably better transmittance of 55 % at 500 nm and it presents nearly flat behavior of transmittance in the entire visible spectrum. Electrical transport properties of Au/Pt/Au layer show sheet resistance of 66 $\Omega/\square$ and mobility of 8.32 $cm^2V^{-1}s^{-1}$, respectively. The contact angle measurement indicates that plain hydrophilic PET (62.6°) to turn into hydrophobic (94.2°) upon coating with Au/Pt/Au tri-layer. The surface properties analyzed using atomic force microscopy and optical profilometry indicate a crack-free, and closely packed homogenous film. The tri-layer film shows mechanical stability of up to 50,000 bending and twisting cycles. The obtained surface work function of Au/Pt/Au tri-layer film is 4.97 eV. The ultrathin flexible Au/Pt/Au tri-layer explored as top electrode in a piezoelectric nano generator (PENG) and as top and bottom electrodes in an alternating current driven electroluminescent (ACEL) device exhibits appreciable performance and the results are discussed by correlating with the measured optoelectronic properties.

v) **Chapter 5** This chapter presents the effect of solvent on the optimization of F-doped tin oxide (F:SnO_2) (FTO) thin films using facile spray pyrolysis technique deposited onto glass substrates over an area of 5×5 cm^2 by varying solvent concentration of 2-methoxyethanol (2ME) and ethylene glycol (EG). The volume of EG is varied as 0, 25, 50, and 100 ml in the 2ME admixture. The XRD patterns reveal successful formation of tetragonal SnO_2 lattice without any structural change. Upon changing the volume of EG in 2ME, the textured growth changes from (110) direction to (211) direction. The film thickness is found to vary significantly with varying volume of the mixed solvents. Transmittance is found to increase and reach a maximum value of 75 % (at 550 nm) for the film deposited using only EG. The photoluminescence emission data reveals that the overall intensity of violet emission is found to quench upon increasing the volume of EG in the solvent mixture. The sheet resistance is found to decrease gradually with increasing the volume of EG and is found to be the lowest with a value of 6.34 $\Omega/\square$ for complete 100 ml of EG solution. The surface wettability nature of the thin films obtained from contact angle measurements indicate changeover from

hydrophobic to hydrophilic nature (104.4° to 52.2°) with increasing EG volume in the admixed solvent. Among all these samples, the film prepared with 100 % EG solvent shows highest figure of merit value of $3.02 \times 10^{-3}\ \Omega^{-1}$. The optimal film prepared with complete EG solvent has surface work function of 4.69 eV.

To further enhance the optoelectronic properties of optimal FTO, co-doping of niobium (Nb) and fluorine (F) into SnO_2 (NFTO) lattice as cationic and anionic dopants, respectively, is explored. A fixed 10 wt.% F and varying Nb concentration from 0 to 5 wt.% is incorporated into the SnO_2 lattice. X-ray diffraction reveals substitution of Nb and F into the SnO_2 lattice without altering the structure and without any secondary phases. Optical transmittance is found to increase with Nb content up to 4 wt.% of Nb (77.59 %), and it decreases thereafter. Scanning electron microscope and optical profiler imply a relatively smooth surface with sharp-tipped particles which is found to vary with Nb concentration. Sheet resistance decreases up to 3 wt.% of Nb doping and increases thereafter. Contact angle measurement indicates that upon doping with Nb, the films to turn hydrophilic. Among the deposited films, 4 wt.% Nb-doped film shows the highest figure of merit of $5.01 \times 10^{-3}\ \Omega^{-1}$. The surface work function of the 4 wt.% Nb-doped SnO_2 film is 4.687 eV. The optimal films are tested as electrodes for their performance in dye sensitized solar cells and the results are discussed in detail.

vi) **Chapter 6** This chapter presents the deposition and characterization of Sb and Nb co-doped SnO_2 thin films by spray pyrolysis technique. Researchers identified, Sb-doped SnO_2 (ATO) as an exceptional alternative contender but it is restricted by its low optical transmittance due to inherent gray tinge attributed by the presence of Sb in +5 charge state. In this study, the computational simulations of the Nb (0, 1, 2, 3 wt.%) and fixed Sb (5 wt.%) co-doped SnO_2 were performed based on the Density Functional Theory (DFT), and the same were experimentally deposited in thin film form by spray pyrolysis technique over an area of $5 \times 5\ cm^2$ glass substrate. The XRD measurement revealed formation of tetragonal crystal structure of SnO_2 without any secondary phases. The variation in surface morphology of SnO_2 films upon co-doping of Nb and Sb is analyzed using FESEM, exhibits tetragonal shaped particles with sharp edges. The analyzed topography from AFM indicates the roughness to increase with co-doping of Nb upto 2 wt.% and then it decreased for further increase in Nb concentration. The contour mapping of sheet resistance (Rs) is also performed for the entire $5 \times 5\ cm^2$ area for all the deposited samples using linear

four-probe technique. Optical transparency improved overall upon co-doping of 2 wt.% Nb and 5 wt.% Sb into SnO_2 lattice (NATO2) and it has shown highest transparency of 88.33 % which reduced thereafter for further increase in dopant concentration. The XPS spectra revealed the existence of Sn in +4, Sb in +5, and Nb in +5 charge state. Sheet resistance stability of the films with varying annealing temperature indicated NATO2 film to be stable up to 400 °C for 30 minutes annealing duration. The co-doping of Nb and Sb into the SnO_2 lattice might play a synergistic effect for enhancing the optoelectronic properties of the film. Consequently, a significant power conversion efficiency of 5.45 % was attained for DSSC device fabricated using NATO2 thin film as photoanode/counter electrode. The ACEL device is also demonstrated using NATO2 electrode. Based on these results, it is identified that 2 wt.% Nb and 5 wt.% Sb co-doped SnO_2 is one of the promising alternative materials for supplementing the existing ITOs/FTOs for various optoelectronic device applications.

vii) **Chapter 7** This chapter summarizes the results obtained from the core chapters. The optoelectronic properties of metallic multi-layers and doped SnO_2 based TCEs are tabulated for comparision to highlight the key findings. The scope for future work is also outlined in this chapter briefly.

Contents

List of Figures

List of Tables

List of Acronyms

TCE	Transparent Conducting Electrode
TCO	Transparent Conducting Oxide
ITO	Indium Tin Oxide
TO	Tin Oxide
FTO	Fluorine doped Tin Oxide
NFTO	Niobium and Fluorine co-doped Tin Oxide
ATO	Antimony doped Tin Oxide
NATO	Niobium and Antimony co-doped Tin Oxide
RMS	Root Mean Square
BM-Shift	Moss–Burstein Shift
VBM	Valence Band Maxima
CBM	Conduction Band Minima
FoM	Figure of Merit
XRD	X-Ray Diffraction
JCPDS	Joint Committee on Powder Diffraction Standards
FESEM	Field Emission Scanning Electron Microscope
EDS	Energy Dispersive X-ray Spectroscopy
UV-Vis	Ultraviolet-Visible
PL	Photoluminescence
AFM	Atomic Force Microscopy
KP	Kelvin Probe
OLED	Organic Light Emitting Diode
DSSC	Dye Sensitized Solar Cell
EIS	Electrochemical Impedance Spectroscopy
PENG	Piezoelectric Nanogenerator
ACEL	Alternating Current Electroluminescent Device
OSC	Organic Solar Cells

PeLED	Perovskite Light Emitting Diode
PePV	Perovskite Photovoltaics
PSC	Perovskite Solar Cells
HEL	Hole Extraction Layer
HTL	Hole Transport Layer
ETL	Electron Transport Layer
CNT	Carbon Nanotube
NWs	Nano wires
MNWs	Metallic Nano wires
DC	Direct Current
UHV	Ultra High Vaccum
PET	Polyethylene Terephthalate
CA	Contact Angle
DFT	Density Functional Theory
EQE	External Quantum Efficiency
ZSC	Cu doped Zinc Sulfide

List of Symbols

η	Power conversion efficiency
σ	Conductivity
β	Full Width at Half Maximum (FWHM)
θ	Diffraction angle
d	Inter-planar spacing
$a, b, and\ c$	Lattice constants
TC_{hkl}	Texture coefficient
T	Transmittance
R	Roughness
t	Film thickness
I_{0hkl}	Standard peak intensity
I_{hkl}	Observed peak intensity
α	Absorption coefficient
h	Planck's constant
E_g	Band gap
E_{optg}	Optical band gap
m_e	Effective mass of electron
m_h	Effective mass of hole
E_F	Fermi Energy
Φ	Surface work function
I_0	Incident light intensity
ρ	Resistivity
n_c	Carrier concentration
e	Charge of the electron

μ	Mobility
R_S	Sheet resistance
λ	Wavelength
V	Voltage
I	Current
$\Omega/\square$	Ohm per Square
N	Defect density
V_{OC}	Open circuit voltage
J_{SC}	Short circuit current density
FF	Fill factor
V_{AC}	AC Voltage

Chapter 1

Transparent Conducting Electrodes: Fundamentals and Review of Alternative Materials

This chapter provides a general introduction on the Transparent Conducting Electrode (TCE) materials. An extensive literature review on the reported TCEs and its classification based on the non-oxide and oxide-based materials, elucidating their basic properties and performance. Requirement of various properties of thin film TCEs for the application in devices like dye sensitized solar cells (DSSCs), piezoelectric nanogenerators (PENG) and alternating current electroluminescent (ACEL) devices are also outlined briefly. The strategy for identifying and optimizing the alternative TCE materials to supplement for the existing ITO and FTOs are outlined. This chapter is concluded with objectives and scope of the thesis work.

1.1 Introduction

Transparent conducting electrodes (TCEs) are essential parts of numerous types of organic and inorganic electronic devices, including touch screen based display devices, and solar cells [1] . Transparent conductive oxides (TCOs), such as indium-tin oxide (ITO), [2] and fluorine-doped tin oxide (FTO), [3] constitute the majority of these electrodes. The increasing demand imposed by the rapid manufacturing and the scarcity of these component elements lead to high prices for these TCEs. The demand vs supply of indium in the last decade is shown in Fig. 1.1. (a). The material's brittleness also makes them unsuitable for cutting-edge designs of flexible electronic devices [4–6]. Since indium is a rare material, it cannot keep up with the growing demand for the next wave of electronic gadgets. Figure 1.1. (b) shows the end use applications of indium [7]. The liquid crystal display (LCD) sector, which includes flat-panel, touch-screen, and plasma displays for televisions, computers, and handheld electronic devices, has consumed about 1,550 tons of indium in the recent past. In the last ten years, this market expanded rapidly to 56 % of the total annual requirement of ITO. About 8 % of total consumption was accounted for PV applications. The

remaining 36 % of indium is utilised in a number of products, including light-emitting diodes (LEDs), batteries, solders, thermal interface materials, and other products like corrosion inhibitors, and as compound semiconductors for fabricating laser diodes.

Naturally, metals are highly conducting owing to high number of free electrons and overlapping of conduction and valance bands. Insulators and semiconductors are fully/partially transparent due to empty or partially filled conduction band and completely filled valance bands. TCE materials demonstrate an excellent synergy of electrical transport capabilities with high optical transparency (> 85 %) in the visible region of the spectra. It is difficult to achieve higher optical transparency with acceptable electrical conductivity in the same host. Understanding the fundamentals of these materials, like their structural, surface, electrical and optical properties are important for emerging applications. Researchers have gained good understanding of the physical/chemical features underlying these transparent conducting materials via computational and theoretical approaches [8, 9]. A variety of optoelectronic devices, notably those used in the field of renewable energy to capture/convert energy from solar radiation [10–12], as well as in storage devices [13, 14] can benefit greatly from these special class of materials. A variety of TCEs are used by low-energy converting devices based on the sheet resistance of TCEs including LCDs/LEDs, display units, touch screens, smart windows, smartphones, sensors, etc. [15–18]. Due to aspects like, low power consumption, compactness, and comparatively low production costs, alternative TCEs are expected to be widely employed in optoelectronic devices.

1.2 Evolution of TCEs

The majority of TCEs have a wide band gap ($> 3.1\ eV$) that allows for higher transmittance in the visible spectrum and an improved free carrier concentration ($> 10^{20}\ cm^{-3}$) that results in conductivity that is metallic-like [19]. In many of the

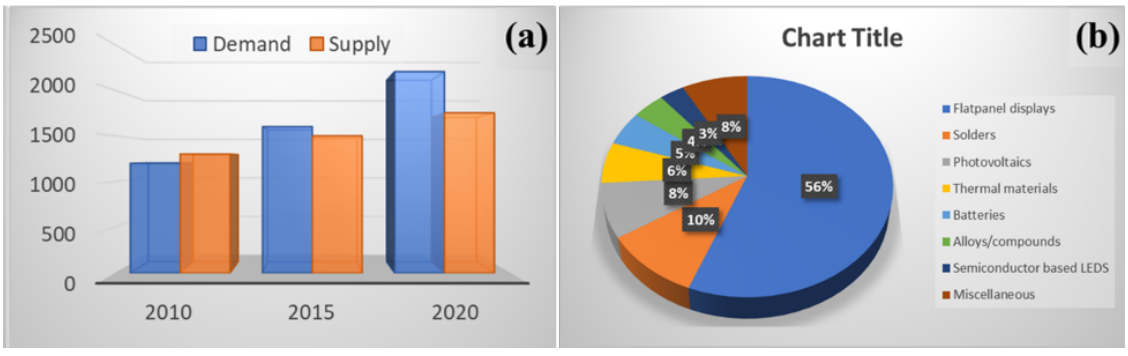

Figure 1.1: (a) Indium demand vs supply forecast in the last decade in tons and (b) its applications. Adapted from Lokanc et al. [7].

current day devices, thin film electrodes are made from a range of TCE materials [20]. Figure 1.2 shows the several low power consumption devices that are incorporated with TCEs based on their sheet resistance values [21]. To impart the necessary optical and electrical properties, all of these gadgets require specific TCE materials with the requisite dopants.

A German Physicist Karl Badeker first identified the CdO TCE in 1907 and he developed n-type cadmium oxide (CdO) film with high conductivity by merely post-annealing a "Cd" metal film in air [22]. The oxygen vacancies were found to increase the concentration of free carriers, which enhanced metallic-like conductivity in CdO, however due to its toxicity, it was not widely used commercially. Other TCEs such as Cu_2O and PbO, were also reported by Badeker et al. prepared using sputtering process and subsequent oxidation. Quantum mechanics has been helpful in the rapid advancement of TCE materials by enabling the fundamental comprehension of their physical and chemical behavior. Tin oxide (SnO_2) thin film was later patented by American inventor Harold McMaster in 1947 as a TCE that was developed using the chemical spray pyrolysis process [23]. During World War II, translucent heater films based on SnO_2 were utilised as aircraft wind screens [24]. During tests on the production of metal oxide insulators in the 1930s [25], Corning laboratories created the first indium-tin oxide alloys (90 % In_2O_3 : 10 % Sn) also called as indium-tin-oxide (ITO) as a TCE material, which was subsequently patented in 1947 [26]. Fraser and Cook [27] reported that the best ITO films had a resistivity of 1.77×10^{-4} Ωcm and a visible transmittance of about 85 %. Rupperecht launched the first commercial production of ITO materials in 1954 [28].

After a few decades, researchers identified the insufficiency of indium in the earth's crust, and also due to limited and complicated mechanisms involved in recycling of

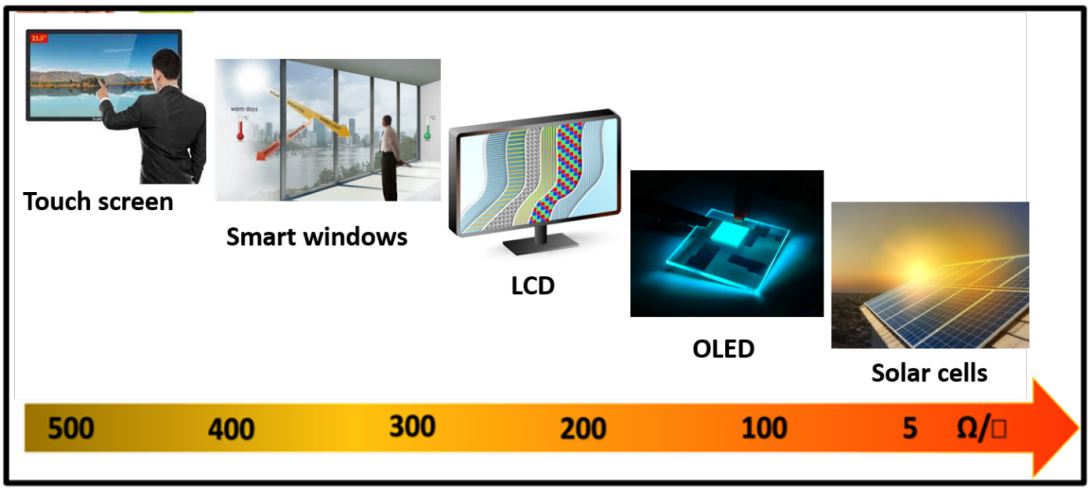

Figure 1.2: Applicability of TCEs for various optoelectronic gadgets based on its sheet resistance value.

indium [7]. Therefore, presently research on TCEs is on the high for finding suitable alternatives for ITO material. A number of research reviews on alternative TCEs has been published until now [29–32]. In 1953, Holland et al., wrote an exhaustive evaluation of TCO film's early work [33]. In 1970, Haacke [34] published the review article entitled "Transparent conducting coatings". In 1982, Jarzebsk et al., [35], reported preparation and physical aspects of transparent conducting oxides. In 2010, Akshay Kumar et al., [36] published a review article entitled "The race to replace tin-doped indium oxide: which material will win". Roy G. Gordon et al., [37] provided a thorough evaluation of the TCEs' deposition procedures, characterization methodologies, material characteristics, and applications. Computational methods were also used to resolve the theoretical model and a few important TCE material concerns [38]. Some significant limitations of the ITO thin film electrode, such as the scarcity of indium precursor and the high cost of manufacture, necessitate the creation of newer, alternative TCE materials. Figure. 1.3. shows the plausible alternative TCEs for ITO (a) and its cost vs conductivity comparison (b).

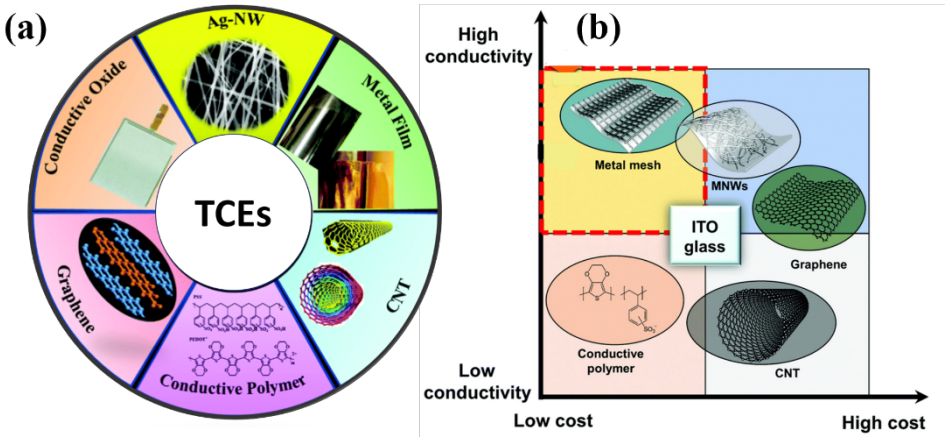

Figure 1.3: (a) ITO replacement materials, and (b) its comparison of cost vs conductivity. Adapted from Xu et al. [39].

1.3 Basic requirements for effective TCEs

According to basic electromagnetic theory, a material cannot exhibit both high electrical conductivity and optical transparency in the same host. Due to their wider bandgap ($> 3\ eV$), optically transparent materials are often electrical insulators. Metals serve as very good conductor but do not possess any transparency. However, TCEs need to have both these characteristics in the same host. It is essential to comprehend the fundamentals of TCOs in order to further investigate them and adjust their qualities as needed. The electronic band structure of the relevant material affects

the charge transport aspects (charge carrier type, concentration and mobility), as well as the optical characteristics (transparency and band gap) [40]. The hybridization of the O 2p state and metallic 3d state is necessary to comprehend the electrical band structure of the metal oxide host [41]. Donor and acceptor dopants raise the charge carrier concentration, which may cause the Fermi level for the n-type system to shift towards the conduction band rather than the valence band for the p-type system. The way charges are transported also matters a lot in the metal oxide host. In metal oxide lattice, charge transfer only takes place between the O 2p state and the metal 3d state. In doped metal oxide hosts, charge transfer occurs on an intermetallic level in addition the O 2p and the metal 3d states. The following sections gives valuable information about the other required properties for an effective TCE.

1.3.1 Electrical transport properties

The electrical transport parameters are carrier concentration (n_c), sheet resistance (R_s), electrical conductivity (σ), and mobility (μ). Intrinsic semiconductors produce electrical conductivity mainly due to free carrier concentration induced by native oxygen vacancy. In the case of extrinsic semiconductors, conductivity arise due to free charge carrier concentration and mobility. Hall co-efficient gives the information about the nature of semiconductor based on the hole and electron charge carrier density, based on the majority charge carriers the material is termed as p-type or n-type semiconductor. The electrical conductivity (σ) of a semiconducting host is expressed as [42],

$$\sigma = qn_e\mu_n + qn_p\mu_p \tag{1.1}$$

where, σ is the electrical conductivity expressed in Scm^{-1}, n_p and n_e are the concentration of the holes and electrons, respectively, and μ_p and μ_n are the mobility of the holes and electrons, respectively. The charge of the respective carrier is 'q'. The electrical resistivity, expressed in $\Omega\ cm$, is simply:

$$\rho = \frac{1}{\sigma} \tag{1.2}$$

A TCO material should have the highest possible charge carrier mobility (typically $\mu = 50\ to\ 70\ cm^2V^{-1}s^{-1}$), the lowest possible electrical resistivity (ideally $\rho = 10^{-4}\ to\ 10^{-5}\ \Omega\ cm$), and an optimal carrier concentration (around $2\ \text{x}\ 10^{21}\ cm^{-3}$) in order to minimise unwanted free carrier absorption and scattering. Fig. 1.4. makes it clear that inorganic materials can be divided into three groups based on their electrical properties: semiconductors (low carrier density, high mobility; lower right), highly conductive metals (both high carrier density and mobility; top right), and semimet-

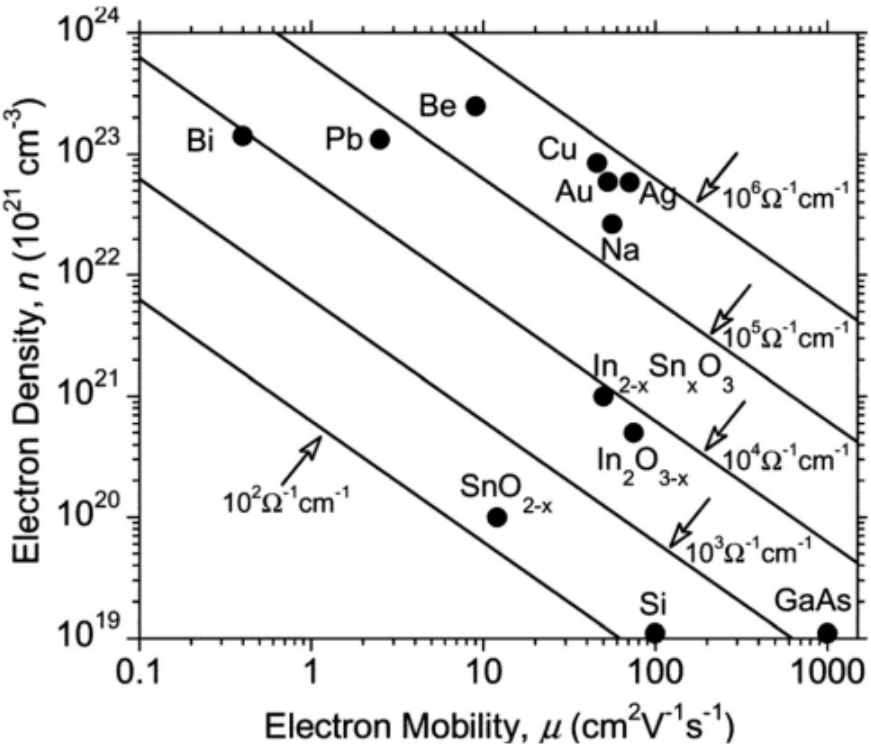

Figure 1.4: Categorizing of conducting solids at 300 K: metals, semimetals, transparent conductors and semiconductors based on electron carrier density and mobility, respectively. Constant conductivity contours are shown as straight lines. Adapted from Edwards et al. [41].

als (high carrier density, low electron mobility) [41]. The free carrier concentration is further improved by oxygen vacancies and stoichiometry deviation, but the free carrier mobility is constrained. Scattering by defects, including grain shape, grain boundaries, dislocations, and phonons, may potentially have an impact on the free carrier's mobility [43]. While the donor levels introduced near the conduction band enables a wide optical band gap from the VBM to the CBM. The optical absorption related to the transfer of electrons from the CBM to the available levels in the CBM, such that the TCO's absorption coefficient (α) is proportional to the density of free electrons 'n_c' given by,

$$\alpha = \omega n_c \tag{1.3}$$

where ω is the cross-section of absorption. Therefore, considerable optical absorption results from thick or highly doped TCO films [44], which must be taken into account while developing TCO components. In addition, as the TCO film's dopant concentration rises, an increasing density of defect (dopant) sites are introduced. As a result, the electron scattering effect caused by higher amount of defects gradually outweighs the increased conductivity provided by the donor dopant's properties. Film resistivity

rises when the mean free path of charge carriers decreases and, as a result, the free carrier relaxation time, decreases. ITO has the best conductivity among oxide-based TCOs, by the host material In_2O_3 doped with donor SnO_2. In addition to SnO_2, ZnO is also a potential alternative TCO host when properly doped with Al/Ga and is presently a subject of considerable research as well as recent commercialization.

1.3.2 Optical properties

The light that strikes TCO material interacts in a number of ways, including transmission, refraction, reflection, and absorption. Light can pass through or reflect off the surface if the substance does not absorb it. Surface abrasion and material flaws that affect the material's micro-structural integrity can also disperse light. The nature of the material will affect each of these characteristics. In the visible region, TCO materials should have enhanced transmittance and low absorption. Optical band gap is crucial for the transparency of the medium in order for a TCO to be practical, which implies that in an n-type TCO, conductivity can be enabled by injecting electrons from a neighbouring donor defect level straight into the conduction band. In n-type TCOs, lattice defects such as oxygen vacancies, proton interstitials, and some substitutional defects result in excess of electrons around the defect sites. The Fermi level will shift above the CBM if there is enough orbital overlap to allow for the delocalization of electrons from the defect sites, filling the electronic states at the CBM (see Fig. 1.5. (a)). This results in the Moss-Burstein shift effect, which effectively increases the optical band gap.

$$E_g = E_{CBM} - E_{VBM} \tag{1.4}$$

$$E_g^{opt} = E_g^{MB} + E_g = E_F - E_{VBM} \tag{1.5}$$

$$E_g^{MB} = E_F - E_{CBM} \tag{1.6}$$

Where, E_g^{MB} is the Moss-Burstein shift, E_F is the Fermi level, and E_g is the fundamental energy gap between the CBM and VBM. E_g^{opt} is the optical band gap relative to the shortest permitted optical transition from VB to the CB. In TCOs, lattice defects enable simultaneous enhancement of electrical conductivity and optical transparency. The optical band gap is one of the factors that must be taken into account in a TCO's band structure. Band gaps of familiar TCO hosts are shown in Fig. 1.5.(b), with the vacuum level set at $E = 0\ eV$. Other parameters include the distance between the host material's CBM and the vacuum level, often known as the CBM depth or electron affinity (EA), which has an impact on the 'dopability' of the TCO. A

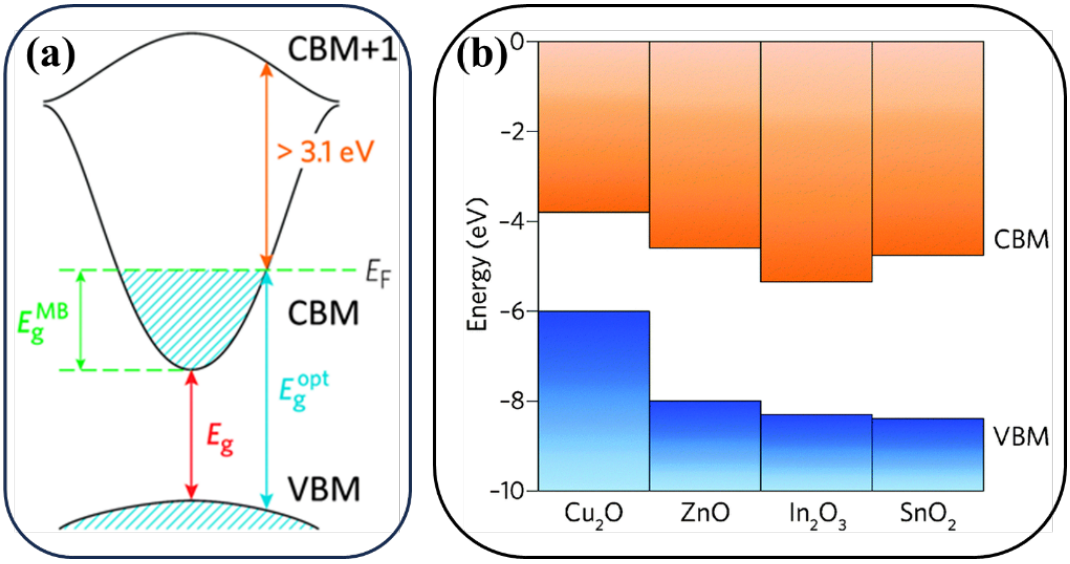

Figure 1.5: (a) Optical bandgap widening effect of the Moss–Burstein shift and (b) band gap values of familiar TCO host structures. The vacuum level is set at E = 0 eV. Adapted from Ganose et al. [46]

higher value of EA denotes greater dopability, or the ease with which charge carriers can be introduced. The excitation of electrons to higher levels inside the conduction band, which may otherwise lead to undesirable optical absorption, is prevented by a substantial gap ($E_g > 3\ eV$) between the Fermi level in the conduction band and the following electronic energy level. Free carrier absorption is a term used frequently to describe this process. These aspects are evident in Fig. 1.6., where Sn doping of In_2O_3 results in the Fermi level rising above the CBM (i.e., the conduction band becoming partially filled), while the separation between the CBM and the CBM + 1 level tend to be around 3 eV upon doping (also note that the basic band gaps are typically underestimated by the density functional theory) [45].

1.3.3 Figure of merit

The Figure of Merit (FoM) parameter is utilized to assess the use of the TCE for various optoelectronic applications, including solar cells, displays etc. FoM can be estimated using sheet resistance and transmittance (at 550 nm) values. In 1972, Fraser et al. [47] identified the FoM as a ratio of transmittance and sheet resistance. Later in 1976, Haacke [48] modified the FoM relation such that it may be applicable for transmission greater than 90 %. Excellent electrical conductivity and increased optical transmittance in the visible region are essential characteristics of TCE materials. The revised FoM relation (equation 1.7) is given below,

$$FoM = \frac{T^x}{R_s} \tag{1.7}$$

where T is the transmittance (at 550 nm) and R_S is the sheet resistance of the film. With different transmittance ranges, the exponential 'x' value changes. For instance, if the transmittance is from 90 % and 95 %, then "x" has multiple values of, 10 and 20, respectively. The TCE necessity of a specific gadget determines the requirement of the FoM value.

1.3.4 Surface work function

The electron affinity or work function of TCOs decide their suitability for use in various devices. The performance of optoelectronic devices is significantly influenced by the metal oxide layer's surface work function. Early display devices consisted of an organic semiconductor layer sandwiched between a low work function metal cathode (often Ca, Au, or Ag-Mg) and a relatively high work function TCO anode (typically ITO), with hole (HTL) and electron (ETL) transport layers in between. However, the optical transparency can only be as high as 50 % when even a thin metallic cathode layer is used [49]. So, the search is still on for a TCE host material with an optical transparency and electrical resistivity that are comparable to ITO but with lower surface work function for effective electron transfer.

Work function is the term used to describe the energy difference between the Fermi level and the vacuum level. A semiconductor's work function (Φ) depends on the Fermi level's position in relation to the vacuum level ($\Phi = E_{vac} - E_F$). While the Fermi level in a non-degenerate n-type semiconductor is below the conduction band minimum, it may be above the conduction band in the case of a doped degenerate n-type semiconductor. In general, techniques such as the Kelvin probe force microscope (KPFM) or

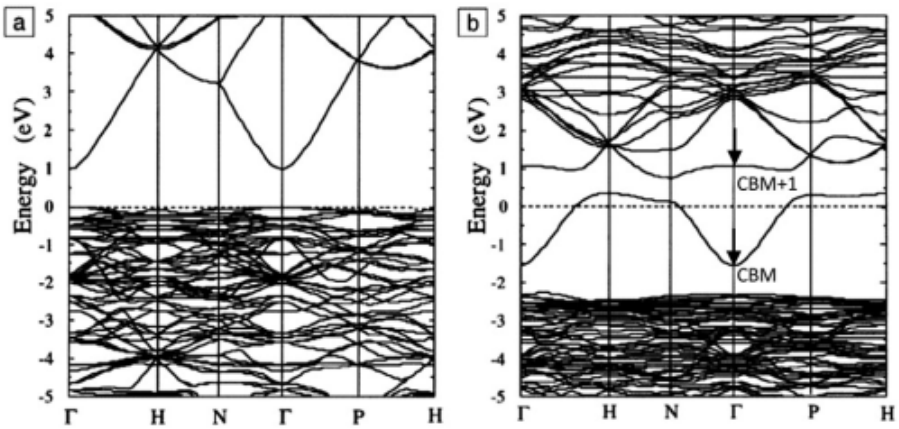

Figure 1.6: Band structures of (a) SnO_2 and (b) In_2O_3Sn. The Fermi level is set at E = 0 eV. The Brillouin zone centre is indicated by Γ, while H, N and P indicate points at the Brillouin zone along high symmetry k-vectors in the reciprocal lattice. The energy curves indicate permitted electronic states at given k-points. Adapted from Freeman et al., [45].

ultraviolet photoelectron spectroscopy (UPS) are used to evaluate a material's work function (Φ) [50]. Since its invention by Nonnenmacher et al., in 1991 [51], the KPFM technique is a distinctive non-contact approach for determining the contact potential difference between the film's surface and the reference electrode tip. Regarding the tuneability of the work function of doped TCO materials, much has been understood recently through computational and experimental approaches [46, 52]. It is envisaged that the ongoing relationship between computational and experimental approaches will deliver tangible progress to this rapidly evolving field.

1.3.5 Chemical, mechanical and thermal stability

Another prerequisite is the stability of transparent conducting electrodes in optoelectronic devices under high relative humidity conditions with good mechanical stability. The deposited electrodes need to have stable sheet resistance at various thermal, chemical and mechanical conditions. When high-temperature sintering or annealing processing is needed during device fabrication, like in the case of CdTe-based and dye sensitized solar cells (at roughly 450 °C for 30 min in air), the thermal stability of the electrode's characteristics is particularly crucial. The reduction of oxygen vacancies in the ITO film coincides with increasing resistivity [53–55]. The oxygen from ambient air permeates into the ITO layer during annealing and fill the oxygen vacancies. Due to the fact that an oxygen vacancy can produce two free electrons, the compensation of oxygen vacancies also causes a reduction in the number of free electrons, increasing the resistivity of the ITO film. The performance of DSSC photovoltaic systems is greatly diminished by the rise in ITO's resistivity caused by the material's thermal instability.

Another commercial electrode is FTO, which has better thermal stability than ITO. However, it has higher sheet resistance than ITO, since fluorine is substantially less soluble in SnO_2 than tin is in In_2O_3. FTO's optical characteristics are likewise inferior than that of ITO [56]. As a result, when ITO is replaced by FTO, even though its thermal stability is significantly high, due to lower optical electrical properties of FTO, ITO is still a good choice for various applications based on the aforementioned perspectives. The commercial ITO is stable only up to 250 °C, above which the sheet resistance of the electrode increases rapidly. For making ITO more stable, researchers followed many strategies. The coating of Sb doped SnO_2 (ATO) on the ITO layer (as a bilayer), Guillen et al., reported that the visible transmittance haze of ITO/ATO electrodes has been demonstrated to increase from 6 to 14 % as the ATO layer thickness increases from 80 to 200 nm, and sheet resistance for the 500 °C air-annealed bilayers is below 10 $\Omega/\square$. Sputtered coatings have also been shown

to enhance the thermal stability of ITO/ATO electrodes [57]. When it comes to mechanical stability, all the metal oxide electrodes are brittle in nature and need of high temperature to deposit very good crystalline materials, but it is difficult to coat metal oxide on PET due to low melting point of flexible PET (about 180-200 °C). Usually, ITO electrodes on pliable PET substrate coated at lower temperatures, lead to the lower transparency and conductivity. Even though it has very good flexibility, the sheet resistance is increased within few hundreds of bending or twisting cycles. To increase its mechanical stability instead of brittle metal oxides, ductile metals (Ag and Au) were tested as ultrathin metal layers architecture and shown very good mechanical stability even after thousands of bending or twisting cycles [58, 59].

1.4 TCE materials and its classification

The host TCE material's oxidation state, crystalline structure, work function, surface topology, optical transparency, and electrical transport aspects are the key factors that must be taken into account in order to attain the desired "contradicting properties" [60]. TCE materials can be split into two major groups: non-oxide-based TCEs and oxide-based TCE materials. Fig. 1.7 displays a categorization of various TCE materials. TCE host materials are selected for a variety of potential applications depending on the specific need of a combined electrical and optical characteristics. For example, p-type TCE materials are especially helpful for LED applications, while combined n-type and p-type semiconductors offer special features that make it suitable for use in invisible electronics [61]. The n-type TCE semiconductors are essential for applications involving the use of renewable energy sources in photovoltaics [62].

1.4.1 Non-oxide based TCE materials

Flexible displays, solar cells, and storage devices are examples of advanced developments in optoelectronic devices that call for TCE materials with specific properties in addition to high conductivity and transparency [63]. These properties include flexibility, hardness, tensile strength, elasticity, and elongation. When it comes to the usability of non-oxide TCE films in advanced devices, nanostructure (nanorods, nanowires, and nanosheets), crystallinity, surface topology (roughness, pores, and smooth surface), work function, resistance, and chemical stability are other important factors to consider. Due to their brittleness and low electrical conductivity (in comparison to metallic based TCEs), the use of currently available oxide-based TCO materials is restricted to specific applications. Several emerging materials such as con-

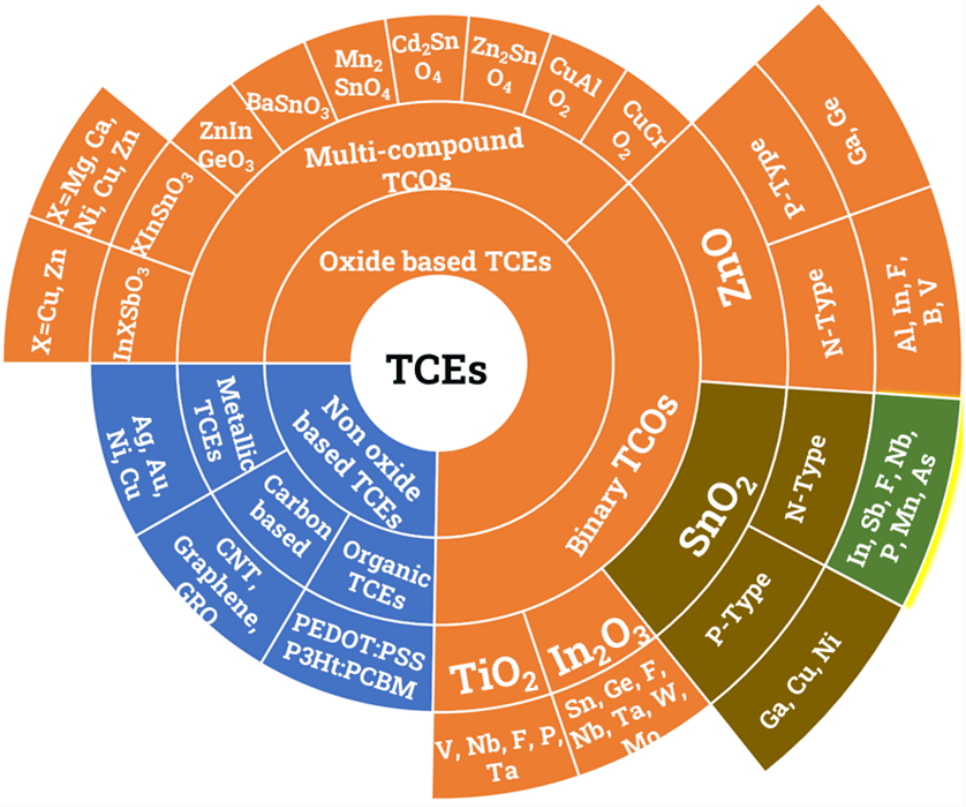

Figure 1.7: Classification of non-oxide and oxide based TCE materials.

ducting polymers [64, 65], carbon nanotubes [66, 67], graphene [68, 69], and metallic nanowires [70, 71] show potential as replacements for ITO electrodes.

1.4.1.1 Organic TCEs

The three most significant conducting polymers are polyaniline (PANI), polypyrrole (PPY), and poly(3,4-ethylenedioxythiophene): poly(4-styrenesulfonate) (PEDOT:PSS). PEDOT:PSS is one of the most widely used conductive polymers in the market. Pohl et al.,stabilized conjugated semiconducting polymers with better conductivity in the late 1960s and early 1970s [72]. Heeger et al., [73] reported an enhancement in polyacetylene's electrical conductivity in 1977 by doping it with arsenic pentafluoride (AsF_5) and the halogens chlorine, bromine, or iodine in small concentrations. Subsequently, they also created highly conducting films using polyacetylene, (CH)x derivatives, and demonstrated how the conductivity of the created films could be systematically and consistently changed across a broad range, with up to 10^{11} times the conductivity [74]. The research represented a newer milestone in the development of conducting polymers. The creation of electrically conductive polymers won the Nobel Prize in Chemistry for the year 2000 [75]. After that, due to their numerous potential applications as shown in Fig. 1.8, and as a transparent conducting electrode material, conducting polymers gained wide attention from researchers.

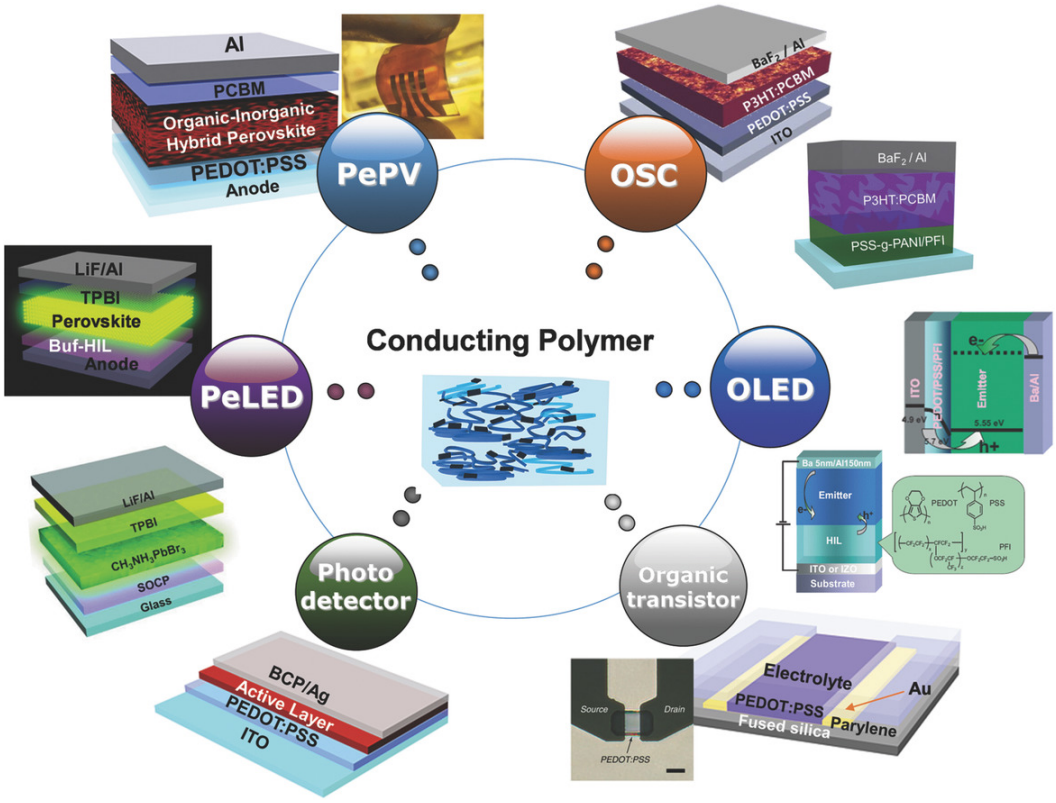

Figure 1.8: Applications of conducting polymers in organic and organic–inorganic hybrid perovskite electronics such as organic solar cells (OSCs), organic light emitting diodes (OLEDs), perovskite light emitting diodes (PeLED), perovskite photovoltaics (PePV), photo detectors and organic transistors. Adapted from Ahn et al. [76].

PEDOT and PSS are ionically linked together and are dissolvable in water, which is advantageous to all solution-processed solar cells [77–79]. In recent years, stratagies like doping, altering the organic solvent in the precursor, or enhancing processing conditions have all been used to create PEDOT:PSS with high conductivity [77, 80]. The PEDOT:PSS thin films can be produced using solution processing techniques like spin-coating and roll-to-roll techniques and have a number of benefits, including a higher match of the donor's highest occupied molecular orbital (E_{HOMO}) energy level, high mechanical flexibility, and high transparency in the visible range [81]. At an instance, hole extraction layer (HEL) made of PEDOT:PSS is frequently utilized in perovskite solar cells (PSC) devices. Many efforts have been made to increase the conductivity of PEDOT:PSS, and a number of methods have been suggested to do so significantly. Since high conductivity is noted for PEDOT doped with various anions, it is plausible to increase the conductivity of PEDOT:PSS on par with that of ITO [65]. A lot of effort was put into for improving PEDOT:PSS's conductivity. Early efforts were concentrated on switching the solvents for PEDOT:PSS. It was found that by treating it with a polar organic substance, such as ethylene glycol, glycerol,

d-sorbitol, or dimethyl sulfoxide (DMSO), its conductivity may be increased from 0.1 to approximately 200 Scm^{-1} [40, 82–85]. Using weak acids like acetic acid, propionic acid, butyric acid, oxalic acid, sulphureous acid, or hydrochloric acid, the conductivity of PEDOT:PSS can be improved. The final PEDOT:PSS film's conductivity was discovered to have increased from 0.2 to over 200 Scm^{-1}, or by a factor greater than 1000 [79]. Besides polar organic molecules, the conductivity of PEDOT:PSS can be greatly improved by adding ionic liquids [86], anionic surfactants [87], or carboxylic or inorganic acids [79] to the PEDOT:PSS aqueous solution. The durability of the PEDOT:PSS film under UV exposure, high temperatures, and extremely humid environments is one of its main weaknesses [88–90].

1.4.1.2 Carbon based TCEs

Due to its extraordinary physical and chemical properties, graphene, the thinnest two-dimensional carbon substance, has received a lot of interest since its discovery [91,92]. Novoselov et al., first reported graphene sheets in 2004 by mechanical exfoliation method [93]. For their achievement, they were awarded the "Nobel Prize" in Physics in the year 2010 [94]. Due to its remarkable transparency and conductivity, as well as its exceptional chemical stability and mechanical flexibility, graphene has been extensively researched for transparent conductive electrodes in the solar cell area and also in several other applications as shown in Fig. 1.9. High carrier mobility (4000 cm^2/Vs) [95], exceptional optical transparency (97.7 %) [96], and a high Young's modulus (1.0 TPa) [97] are a few noteworthy properties. Interest in exploiting graphene for practical applications has grown as a result of its amazing characteristics. Transparent electrodes made of graphene have been successfully used in organic solar cells (OSCs) and perovskite solar cells (PSCs) [98–101]. Many techniques, including mechanical exfoliation [102, 103], high temperature annealing of SiC [104], chemical reduction of graphene oxide [105–108], and chemical vapour deposition [109–111], have been used to create graphene films. Many improvements and modifications have been made to graphene's characteristics since its discovery in order to use it in a variety of electronic applications, such as transistors [112], photonic devices, and optoelectronic devices. The usage of graphene, however, could be constrained by a number of issues. The creation of high quality graphene is complex and expensive process. The primary disadvantage of graphene as a catalyst is that it is detrimental to oxidizing conditions and toxic chemicals are involved at higher temperature to produce it. Creation of graphene layers that are larger in size and pure enough to be employed in devices are some of the challenges that needs to be overcome. Even though there are numerous ways to create different types of graphene, none of them are practical for mass man-

ufacturing and cost is yet another significant barrier. Graphene's price has decreased dramatically since its initial market debut, despite these aspects. Still, one disadvantage of graphene is its expensive initial material cost and fabrication over a larger continuous area.

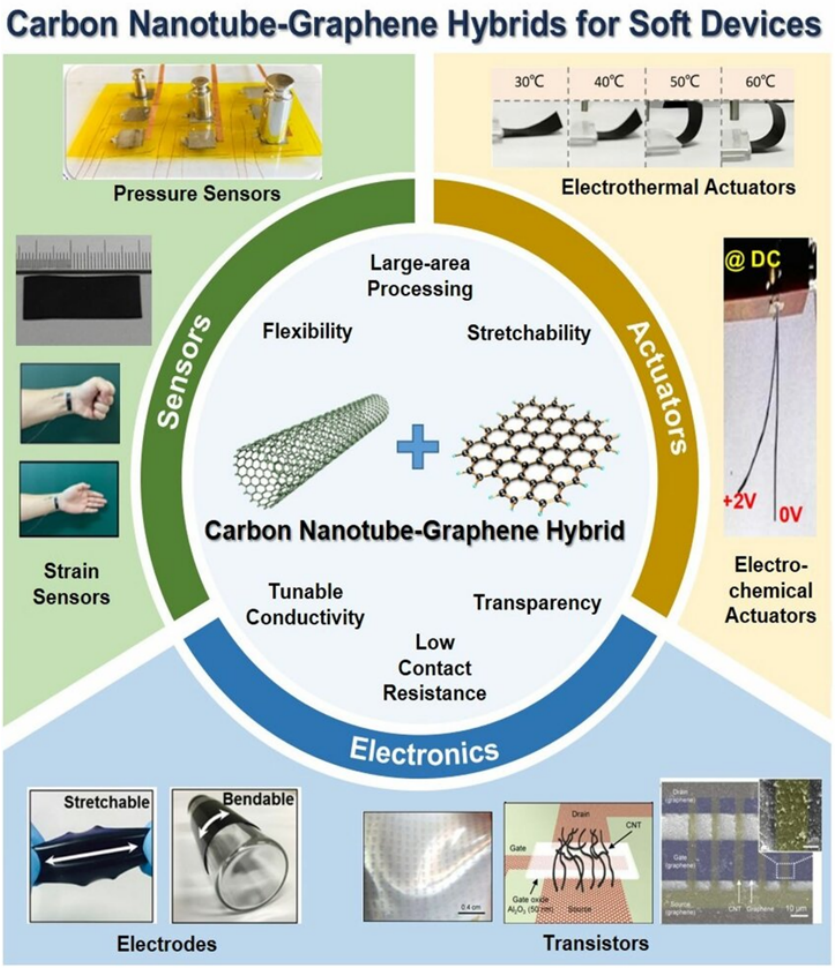

Figure 1.9: Utilization of carbon nanotube (CNT)-graphene based hybrids for soft electronic sensors and actuators. Superior characteristics of these electronic multidimensional carbon-based hybrids significantly enhance the performance of soft devices. Adapted from Pyo et al. [113].

Carbon nanotubes (CNTs) are cylinder-shaped nanoscale materials CNT is an excellent material for transparent electrodes in optoelectronic devices due to its extremely high mechanical strength, flexibility, and conductivity with exceptional work function. The multi-wall CNT (MWCNT) was initially demonstrated by Iijima et al., [114] in 1991, followed by the single-wall CNT (SWCNT) in 1993 [115]. However, Saran et al., [116] and Wu et al., [67] first described the transparent CNT conducting film in their study in 2004 and from then, CNTs underwent extensive research to enhance their characteristics for use in a variety of applications. For the development of SWCNT film on polyethylene terephthalate (PET) substrate, Kuan-Ru Chen et

al., separately used slot, dip, and blade coating processes [117]. All of these methods revealed almost the same transparency, which was above 85 %, and sheet resistance, which was near to 1000 $\Omega/\square$. For the purpose of creating highly transparent and electrically conductive films on plastic substrates, X. Yu et al., showed the usage of acid-treated SWCNT (a mixture of strong sulfuric acid and nitric acid). The produced SWNT film had a thickness of 100 nm, a surface resistivity of 6 $k\Omega/\square$, and a visible range transmittance of 88 %, which was thrice better than the untreated SWNTs films while maintaining a high resistance [118]. Despite having exceptional mechanical properties (failure tensile strain exceeding 11 %), carbon nanotube (CNT) films are limited in sheet resistance due to high contact resistance between the nanotube bundles [119]. CNT, on the other hand, has higher sheet resistance and roughness, which limited carrier mobility and device lifetime [118, 120]. Therefore, a viable technology of producing a highly conducting and transparent CNT film in large quantities is still need to be identified.

1.4.1.3 Metallic TCEs

A viable contender for flexible optoelectronic devices, is metal based TCEs which have achieved significant advancements in the recent decade owing to the development of nanomaterials and nanotechnologies. Recent developments in the field of metal nanostructures have led to the development of materials utilized in TCEs such as metal nanowires [77], metal meshes [121], ultrathin metal films [122], and composite electrodes [123]. Numerous applications for these nano dimensional materials have been made possible by a variety of their features in various fields. NWs are suitable for large-scale applications and are compatible with existing planar technologies owing to their tiny size, light weight, and low cost. In optoelectronic devices, such as photovoltaic cells, OLEDs, transparent heaters, touch panels, electronic circuits, and so forth, metal NW TCEs have a number of promising applications as shown in Figure. 1.10. due to their advantages, such as low sheet resistance, high optical transparency, and better mechanical flexibility. Cu, Ag, and Au metals have been identified as highly conductive materials with low sheet resistance [124–126]. Cu metal with an electrical conductivity of $5.96 \times 10^5\ Scm^{-1}$, which is quite near to that of Ag ($6.30 \times 10^5\ Scm^{-1}$), has the second highest intrinsic conductivity compared to all other metals. A number of research groups have shown scalable syntheses of copper nanowires (Cu NWs), as well as their coating from solution to produce films with characteristics similar to ITO [127–130].

Currently, Cu NW films have been shown to have best combination of sheet resistance (100 $\Omega/\square$) and transmittance (95 %) [132]. However, maintaining film per-

formance on par with ITO while stabilizing the Cu NWs against oxidation continues to be difficult. With recent efforts to address the low stability of Cu nanowires, Ag nanowires have become the most extensively studied form of metallic nanowires (MNWs) as TCEs. Since Cu NWs are prone to oxidation under ambient circumstances, Ag NWs have been the most extensively studied form of MNWs. Other MNWs development includes using metals like Au and Ni to increase the stability of Ag or Cu. [133] As diameters get closer to the electron mean free path (λ), MNWs' small diameters cause them to increase the resistivity. The typical MNW sizes described in the literature range from 40-150 nm, for example Ag (53.3 nm) and Cu (39.9 nm), [134] are reported. The resistance of MNW networks rises as a result of individual MNW degradation, which can also occasionally lead to inhomogeneity in the network's electrical and thermal aspects. The impacts of temperature, electrical current, gaseous species that cause deterioration, and mechanical failure can all be observed by probing failure mechanisms at the single-wire level. However, there are a number of disadvantages to NW films as well, including significant surface roughness, high junction resistance, and very small contact area [1, 123, 135].

Unless these are flattened or coated by thick buffer layers like conducting polymer PEDOT:PSS or metal oxides, randomly arranged metal NW networks are highly prone to induce short circuit due to their non-uniform and uncontrolled topologies. Furthermore, the conductivity of entire film degrades due to the high NWs junction

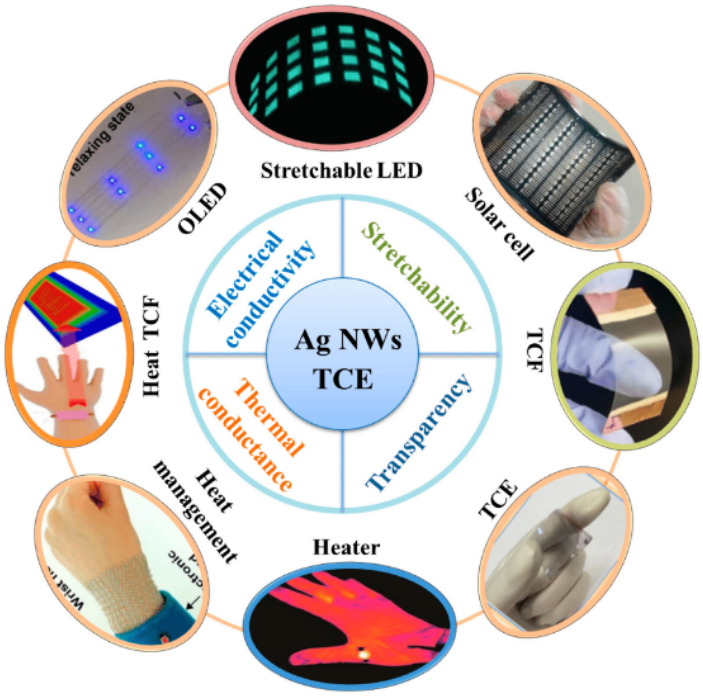

Figure 1.10: Properties and applications of devices developed based on Ag NWs based TCEs. Adapted from Shi et al. [131].

resistance caused by the inhomogeneous shape, and the heat produced at the junction may significantly impair the performance of the associated device. These obviously would restrict its potential for use as TCEs. Metallic mesh and ultrathin patterned electrodes with aligned morphologies have received a lot of interest recently since they successfully prevent junctions, naturally enhancing sheet resistance and mechanical stability. Metallic mesh thin film electrodes frequently have a grid topology, and the printing method can be used to accurately control the thickness variation. In contrast to NWs, metal mesh electrodes can demonstrate desirable electrical characteristics and surface morphology without the help of additional bulky inter-layers. Metal mesh electrode is a viable electrode choice for use in flexible electronic devices due to its straight forward fabrication and controlled shape. A reverse-offset printing technique was recently disclosed by Jiang et al., [136] for printing a homogeneous and ultrathin Ag mesh (100 nm) on extremely flexible substrates. The distance between neighboring lines allows for effective tuning of the conductivity and transparency of Ag mesh transparent electrodes. Finally, 93.2 % transmittance and a sheet resistance of 17 $\Omega/\square$ were concurrently attained, outperforming sputtered ITO electrodes in terms of performance. With just a 16.6 % rise in sheet resistance about 50 % compression and a 10.6 % increase in sheet resistance after 500 stretch/release strain cycles, the Ag mesh electrode with a buckling structure also demonstrated greater mechanical durability. Based on these aspects, the subsequent organic solar cells (OSCs) produced using it showed a PCE of 8.3 %. In addition to moulding, sintering is another technique that may be used to create metal mesh. Silver nanoparticles must be pre-coated first on the substrate before the annealing process can produce Ag mesh. Ink containing metal nanoparticles was selectively laser-sintered by Hong et al., [137] to create a metallic grid transparent conductor on a flexible substrate. The resulting transparent metallic grid electrode had a low sheet resistance of 30 $\Omega/\square$ and a high transmittance of $>$85 %. It is important to note that the customizable laser parameters and the programmable sintering process allowed the patterned electrode to exhibit significant potential on glass and polymer substrates on a broader scale.

Even though the aforementioned metallic nanomaterials are significant TCEs for optoelectronic devices, their drawbacks, such as rough surface, poor adherence, and poor surface coverage, need to be addressed. As a result, composite electrodes that combine metal nanoparticles with other conductive materials are used [77,138]. In this case, it is important to take into account the strong bending endurance and high electrical conductivity and transmittance. In order to obtain smooth electrodes, metal nanoparticles were typically coated on polymer matrix with excellent transparency and high flexibility. To create a transparent conducting film, Lu and colleagues im-

planted the AgNWs network in the PVA layer of the transparent polymer matrix [139]. The final electrode displayed an optical transmission of 87.5 % (at 550 nm) and a sheet resistance of 63 Ω/□ [139]. This technique was able to considerably lower the RMS of the electrode from 75 to 1.27 nm. The sheet resistance of the composite electrode increased 2-3 times after 250 cycles of compression folding, and the flexible OLED using this electrode was still able to maintain a greater efficiency (2.43 lm/W) than the ITO-based device (1.62 lm/W). However, due to the polymer matrix's insulating properties, the low quantity of conductive component in the composite electrode may not only result in an unfavorable electrical contact but also lower the active area of the solar cells. AgNWs and exfoliated graphene (EG) were mixed by Blom et al., to create a full coverage composite electrode [140]. The resultant composite electrode's sheet resistance may be decreased to 13.7 Ω/□ while retaining a high transmittance owing to the excellent conductivity of EG. Additionally, the two components' strong compatibility allows for a significant betterment in the mechanical and chemical stabilities. After 250 bending cycles, the ideal AgNWs/EG-based OSC achieved a PCE of 6.57 % with almost similar photovoltaic parameters.

Due to its variable electrical characteristics, inherent flexibility, high conductivity, and solution processability, the PEDOT:PSS conducting polymer, one of the few commercially available conducting polymers, has attracted considerable attention. To improve the electrode coverage, Li et al., spin-coated highly-conductive PEDOT:PSS onto PET/Ag-grid film. The resulting PET/Ag-grid/PEDOT:PSS composite electrode was capable of drastically lowering the sheet resistance at a 150 nm thick PEDOT:PSS to as low as 1.2 Ω/□ [141]. Large-area solar cells benefit from TCE's incredibly low sheet resistance. A PCE of 5.85 % was delivered by the pliable OSCs with a 1.21 cm^2 area, which is equivalent to their small area counterpart. However, only 80 % average transmittance in the 400–800 nm range was actually attained, which was attributable to the parasitic absorption of PEDOT:PSS in the longer-wavelength region, which would severely restrict the use of sunlight. Kim et al., developed a multilayer coating technique to create a high-performance AgNWs/PEDOT:PSS composite film in order to address the issue. The resulting AgNWs/PEDOT:PSS film presented low sheet resistance of 19.3 Ω/□ and an enhanced transmittance of 84 % at 550 nm due to the improved uniformity leading to alignment between AgNWs that can reduce light scattering and haze. Even though, PEDOT:PSS's natural parasite absorption was still not eliminated fully. To further enhance the transmittance of the composite electrodes, scientists have worked on the replacement of PEDOT:PSS with metal oxides like TiO_2, and ZnO. Kang et al., developed a composite electrode made of AgNWs and ZnO by combining solution-processed ZnO and AgNWs. At 550 nm, the

AgNWs/ZnO conductive film's transmittance achieved 93 % while also displaying a low sheet resistance of 13 $\Omega/\square$ and exceptional mechanical pliability [142]. The PCE of the ITO-based device was equivalent to that of the flexible OSCs based on this composite electrode. Similarly, ZnO and TiO_2 were combined with AgNWs by Tang et al., [143] Although the AgNWs/ZnO/TiO_2 pliable composite electrode showed a little lower transmittance of 84.5 % at 550 nm (along with PET substrate) than the AgNWs/ZnO composite electrode, the uniformity of TCE could be greatly increased. From the above, it is clear that flexible composite electrodes offer a number of benefits, including a homogeneous surface, good conductivity, and exceptional mechanical stability. However, there is still a problem that needs to be solved regarding the intricate manufacturing process of the composite electrodes. Simple fabrication of composite electrodes need to be improved with a view towards low cost and mass production.

Present day micro- and nanoelectronics, optoelectronics, and photonics, use of thin metal films is crucial. These films are extensively used in a wide range of applications, including transparent coatings for smart windows, solar cells [144], catalytic coatings [145], and an active layer of surface plasmon resonance-based biosensors [146]. The most common metals used in the TCE applications are noble metals, which have one electron in the final shell and a fully filled penultimate shell for example Cu, Ag, and Au. Ultrathin metallic films may form discontinuous, island-like structures that aid excitation of localized plasmon–polaritons upon illumination [147–149]. Key variables impacting the electrical and optical properties of metal films, including the effectiveness of plasmon-polaritons excitation, type of the deposited metal, thickness, grain size, and nuclear density of the formed metallic islands. The technique used to deposit the metal film on a certain substrate has a significant impact on its structure, optical, and electrical aspects. Axelevitch et al., [147] reported the dependance of these properties on the transmittance of the noble metals at different thickness. For in-situ monitoring of the optical characteristics of thin metallic films during the coating process, numerous approaches have been proposed. Real-time monitoring of the formation of Ag nanoparticles in a polymer matrix [150] and the magnetron sputtering of noble metals on SiO_2 [151, 152], and Si [150] substrates were both obtained using the spectroscopic ellipsometry technique. Due to their innate qualities that resemble bulk metal, metal films often have a low sheet resistance and strong mechanical resilience.

When employing them as transparent electrodes, however, the transmittance should be taken into particular consideration since more light must travel through them. In order to achieve high transmittance using the thermal evaporation approach, the metal layer in this instance needs to be exceedingly thin (10 nm). Unfortunately, it

is difficult to produce an ultrathin metal film with excellent performance since the Volmer-Weber growth mode is likely to produce a rough surface topology with numerous island-like grains, which would reduce the optical transmittance and electrical conductivity [153–155]. As a result, it is crucial to systematically regulate the evaporation parameters, including evaporating temperature and evaporation rate [156]. Zhang et al., reported in 2009 [157] that decreasing the thermal evaporation temperature could weaken the extent of the Ag atoms' diffusion, which is advantageous for creating continuous Ag film. By tuning the temperature and the evaporation rate during the deposition procedure, Stefaniuk et al., [158] also produced an ultrasmooth Ag film with an extremely low root mean square (RMS) roughness of 0.22 nm. Therefore, it is beneficial to carefully manage the evaporation conditions in order to produce a smooth ultrathin metal coating. There are still some challenges that need to be resolved even though numerous techniques exist to improve the quality of the electrodes, such as tuning evaporation conditions and adding seed buffer layer. It is also essential to simultaneously enhance the transmittance, sheet resistance, and mechanical properties of ultrathin metals. To further enhance these properties, in this current thesis, noble metallic ultrathin multilayer deposition via sputtering technique is explored and discussed in the subsequent chapters.

1.4.2 Oxide based TCE materials

In oxide based TCE materials, the creation of defect energy levels that can either donate free electrons to the associated metal oxide conduction band (n-type conductor) or accept electrons from the valence band (p-type conductor) is one reason for imparting electrical conductivity to a transparent wide bandgap metal oxide. The intrinsic conduction band of these oxides is mostly made up of partly filled metal cation energy levels, while the valence band is made up of fully occupied oxygen anion energy levels. Dopants that can create energy levels close to the VBM or the CBM are chosen as dopants. Fig. 1.6 [159] depicts the wide range of host and dopant elements that can be used to create effective alternative TCE materials. Table 1.1 lists some of the host and dopant criteria for creating TCO materials with desired features. The valence, charge state, ionic radii, effective mass, and natural abundance of the dopant elements are considered while choosing a dopant [19]. The chemical composition of the binary oxide system is simpler to manage during film deposition than the ternary and multi-component oxide systems. P-block elements are used to synthesize majority of the binary oxide TCO materials that provide superior TCO characteristics [160].

1.4.2.1 n-type TCE materials

The generalization is that specific metal oxide systems that have been slightly reduced can exhibit n-type electrical conductivity if charge-compensating electrons can be transferred to the metal oxide's conduction band from defect energy levels that are close to the conduction band minimum. Since this initial discovery, significant electrical conductivity values have been seen in numerous binary, ternary, and quaternary metal oxide systems [161–164]. Even though these materials can transmit light relatively well in the visible spectrum, their electrical conductivity are still much lower than those of metals. The material must display a comparatively high electron affinity and consequent low CBM in order to attain n-type conductivity in a wide bandgap metal oxide. These factors, suggest that zinc, gallium, cadmium, indium, tin, and their binary or ternary combinations would make excellent TCO candidates. The post-transition metal oxides ZnO, In_2O_3, TiO_2 and SnO_2 and subsequent combinations of these, like tin- or zinc-doped indium oxide (ITO and IZO), are now the only TCOs that are widely used in the industry as a standard electrode. These metal-oxide's orbital overlap results in low electron effective masses and strong electron mobilities. These structures serve as essential host structures for TCOs due to their deep CBMs (high dopability) and wide band gaps. Doped zinc oxide and tin oxide TCO materials have attracted specific attention in recent years due to indium supply risk, often with such dopants creating n-type TCOs (e.g., SnO_2:F, [165] SnO_2:Sb, [166] ZnO:F, [167] ZnO:B, [168] ZnO:Ga, [169], ZnO:Al, [170] TiO_2:Nb [171] etc.).

1.4.2.2 p-type TCE materials

P-type conductivity has been observed in some materials when the defect energy levels are close to the metal oxide's valence band [172, 173]. Conductivity is boosted in these materials by electron transfer to these defect levels, which leaves holes in the valence band. Once again, strong transmission in the visible part of the spectrum is possible; nevertheless, measured conductivities are significantly lower than those demonstrated by n-type host due to constrained hole mobility in the material's valence band [174]. A substance with a relatively low work function is necessary to obtain p-type conductivity. For metal oxide systems, this presents a challenge since most of them are characterized by comparatively higher work functions based on the type of the metal–oxygen link. For p-type wide bandgap semiconductors, metal chalcogenides are preferable over oxides due to their slightly lower work functions. However, several transition metal oxides will frequently exhibit lower work functions when their d-shells being incomplete, even when optical transitions between the d-levels that are

only slightly permitted and can still slightly reduce visible transparency. More than 90 % of TCOs are n-type, with electrons making up the majority of the charge carriers. Due to the intrinsic electronic structure of the majority of the easily obtained metal oxides, it is challenging to create p-type TCO; as a result, only a small number of p-type TCOs have been explored. P-type TCO's usefulness as a transparent conductor for commercial applications are constrained by fabrication challenges. Kawazoe et al. reported the first p-type TCO of copper aluminium oxide ($CuAlO_2$) in 1997 [175]. Transparent p-n junctions employing TCO materials could be developed after the creation of p-type TCO [176]. The most often studied p-type TCOs are $SrCu_2O_2$, $CuAlO_2$, $CuInO_2$, $CuGaO_2$, and $CuCrO_2$ [173].

1.5 Applications of TCEs

As discussed earlier in section 1.1 there are many applications where the TCEs can be utilized, however, here few of them are discussed and which were tested for the optimised electrodes in this thesis like DSSC, ACEL and PENG devices.

1.5.1 Solar cells

A photovoltaic (PV) device can convert light energy from the Sun into electricity using the generated photoelectrons is called a "solar cell". In this regard, the Sun acts as a renewable and sustainable energy supply by providing an enormous, free, and inexhaustible energy source in the form of solar radiation. The total solar radiation per year is approximately 3×10^{24} J: and out of 1.7×10^5 terawatts (TW) solar energy which strikes on the surface of the earth, the overall annual solar energy received by the earth's atmosphere is 342 Wm^{-2}. Out of this, 30 % of solar radiation is lost in the form of scattering or by reflection back to space. The remaining 70 % (239 Wm^{-2}) of solar radiation is used as an energy source for converting into electricity [177], which is significantly huge energy obtained in one hour compared to the energy requirement of the entire world for one year. The energy consumption in the world is reported to be 18 TW per year which is estimated to increase to 27.6 TW in 2050 [10]. Based on these statistics, world energy consumption is continuously increasing with the population growth day by day, and utilization of renewable technology such as solar energy provides a clear vision of opportunities to meet the global energy demands for the present and future needs.

The mention of a photovoltaic cell can be traced back to nearly 150 years and was first introduced by the French Physicist Alexandre Edmond Becquerel in 1839 [178].

He observed that light incident on an electrode placed in an electrolyte solution resulted in a photo-voltage, and this phenomenon is called light energy conversion. Later, it was named as photovoltaic (PV) effect and this phenomenon could be understood more precisely based on the photoelectric effect which was theoretically explained by Albert Einstein in 1904. These photovoltaic devices were then assembled in Bell labs in 1954 with an efficiency of 4.5-6 % (Si-based solar cell) [179]. Solar cells are divided into three generations, Figure 1.11. shows the development of solar cells. The 1^{st} generation solar cells are silicon solar cells, 2^{nd} generation solar cells are thin-film solar cells like GaAs, CdTe, and $Cu(In, Ga)(S, Se)_2$ CIGS and the 3^{rd} generation solar cells constitute DSSCs, quantum dot sensitized solar cells (QDSSCs), organic photovoltaics (OPVs), and perovskite solar cells (PSCs).

1.5.1.1 Dye sensitized solar cells

In 1870, Vogel et al., first developed the idea of DSSC, and they demonstrated that silver halide emulsions may be sensitized by adding a dye that extended the photoactivity to longer wavelengths [181]. After several years, James Moser invented the idea of dye enhancement in applications ranging from photography to photoelectrochemical devices using the dye erythrosine on silver halide electrodes [182]. The same concept was implemented by Hishiki and Gerischer by using ZnO and dyes like rose

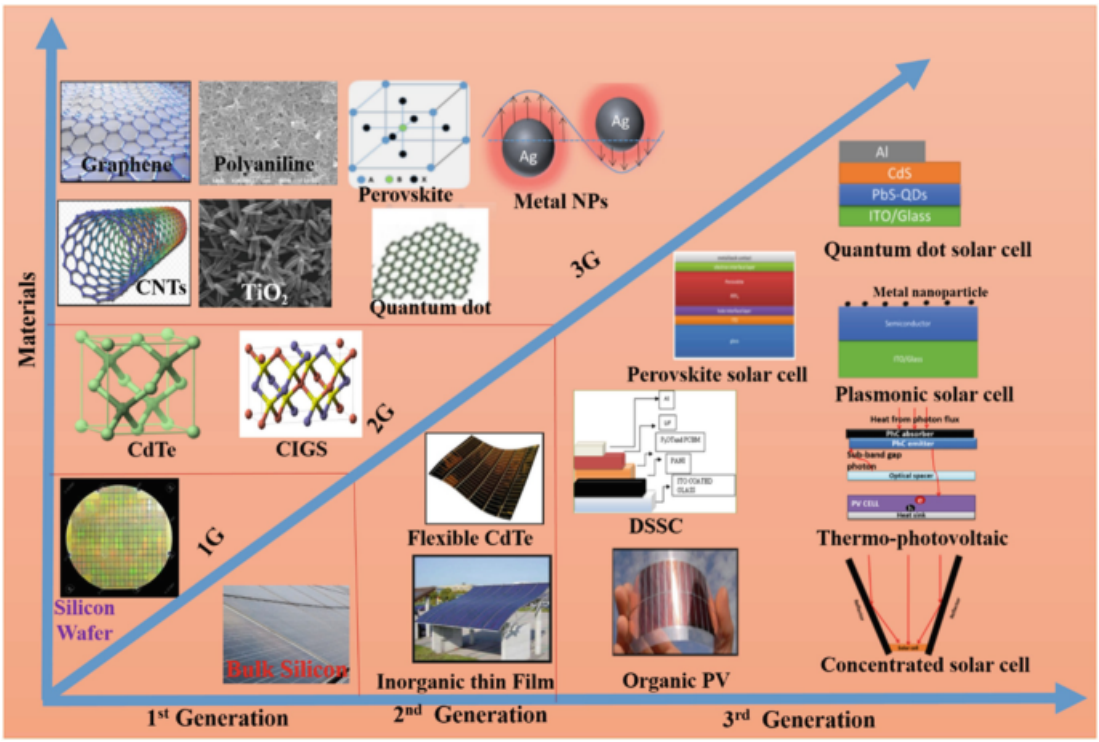

Figure 1.11: Development of solar cell structures and materials. Adapted from Rajbongshi et al. [180].

Bengal and cyanine [183, 184]. Daltrozzo and Tributsch introduced Rhodamine-B as a newer dye into the ZnO system, and subsequently, they observed electron transport to be the dominant mechanism for both photographic and photo-electrochemical sensitization phenomena [185]. In 1977, Spitler and Calvin replaced ZnO with TiO_2 in the cells and were able to elucidate the results of current density which was reported to depend on two factors of the dye, namely, the quantity of dye adsorbed on the TiO_2 surface and the pH of the dye solution [186]. From the late 1980s to the 1990s, newer research appeared in the field of solar cells initiated by Grätzel and his co-workers, reporting the use of synthetic dye series in the TiO_2 system. The DSSC first designed by O'Regan and Grätzel in 1991 attained 7.1 % power conversion efficiency using TiO_2 as a photoanode and ruthenium based synthetic dye. These solar cells were called Grätzel solar cells in honor of the inventor [187–189]. Later in 2014, researchers improved the device efficiency of these synthetic dye-based solar cells from 7.1 % to 13 % using porphyrin [190]. DSSCs are much easier to fabricate and are insensitive to environmental contaminants. They are also processable under ambient atmospheric conditions. Recently, the efficiency of DSSCs was enhanced to values exceeding 14 % using Triarylamine (TAA) based dyes as sensitizers [191].

1.5.2 Electroluminescent devices

A phenomenon known as electroluminescence (EL) is the non-thermal conversion of electrical energy (either a.c. or d.c.) to luminous energy. Thin films, single crystals, semiconductors, and impurity-doped ZnS have all been found to display the EL phenomena [193, 194]. Due to its solid-state design and intrinsic-emissive properties, which can increase performance for several display applications, EL displays are receiving a lot of interest as light sources these days (Fig. 1.12). Researchers from all around the world have been working to develop EL phosphors that have promising performance characteristics and are less expensive in terms of both cost and energy since they are useful for watches, digital assistants, cell phones, and illuminated signs. The most recent advancements in TCE materials, biological soft robotics, and stabilized device configurations are all advantages of these superbly built multipurpose EL devices (Fig. 1.12). In order to create TCE for a self-deformable EL actuator for a volumetric content display, Ag nanowires were used [15]. Extensible ionically conductive hydrogels have recently been used to demonstrate very flexible EL devices [15, 195, 196]. Wearable textiles and optically communicating sensors, respectively, have also been created using coplanar EL devices and fiber-shaped EL devices [13, 197, 198]. Due to enhanced resolution, high contrast and brightness, homogeneous light emission, and low power consumption [199], ACEL as a lighting and

display technology has attracted significant attention in the fields of liquid-crystal display [200], back-lighting, large-scale architectural and decorative lighting [201], among others. A phosphor layer, such as Cu-doped zinc sulphide (ZnS:Cu), and a structure sandwiched vertically between two insulators that are in contact with electrodes make up traditional ACEL devices.

1.5.3 Piezoelectric nanogenerators

Due to environmental concerns, carbon emissions, and the scarcity of fossil fuels, the majority of recent research has been on energy harvesting [202, 203]. The environment has a variety of energy sources, including mechanical, thermal, chemical, solar, nuclear, and much more. Unlike other forms of energy, mechanical energy is always accessible. It can originate from soft airflow, background noise, vibrations, human body motion, etc., all of which are appropriate for the aforementioned use. However, the mechanical energy source in the environment typically has random amplitude and frequency to overcome these challenges, a brand-new area of study called "nanogenerators" has appeared. In 2006, the piezoelectric nanogenerator (PENG) technology

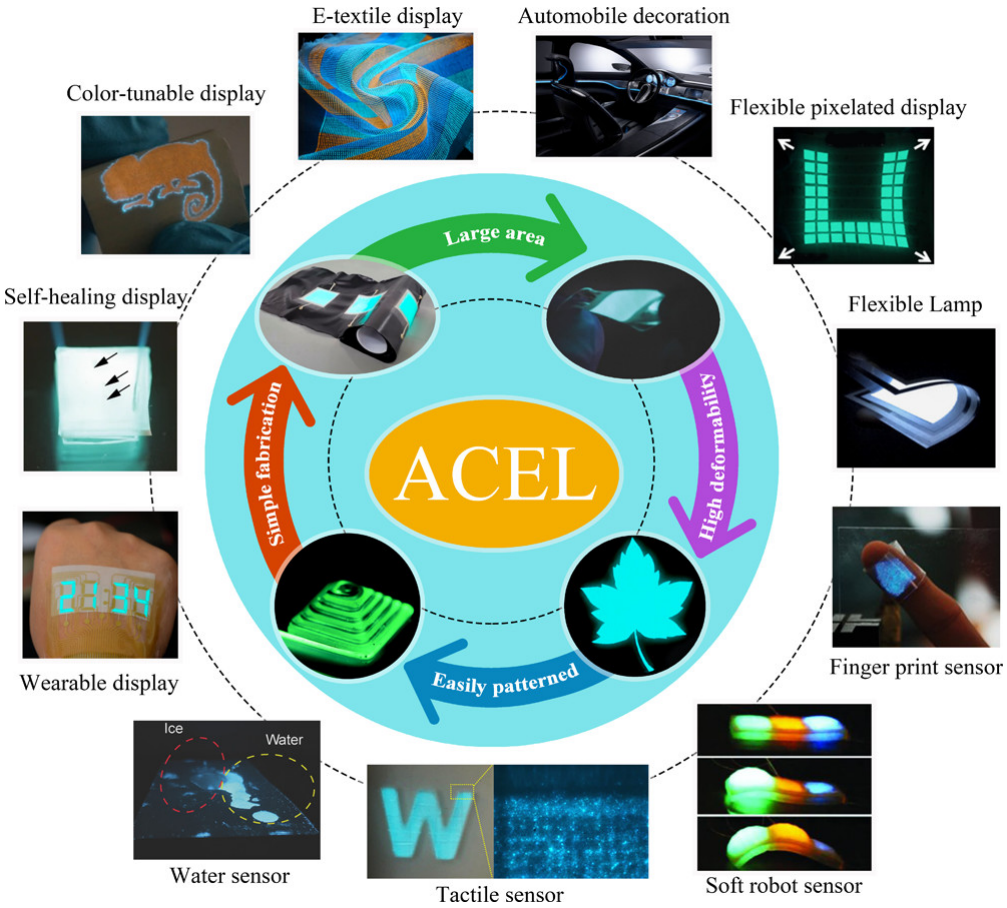

Figure 1.12: Advantages and applications of flexible ACEL devices. Adapted from Qu et al. [192].

was first put forth [204]. Using piezoelectric ZnO nanowires (NWs), which can be activated by extremely small physical motions and operate over a wide frequency range, it transforms random mechanical energy into electrical energy. ZnO is also biocompatible and non-toxic, which is essential for the sustainable energy technology utilised in our daily lives. This discipline makes use of piezoelectric materials to generate mechanical energy [204–206]. It is even more appealing and promising given how simple it would be to transform mechanical energy into electrical energy by using the well-known piezoelectric feature. The primary benefits of mechanical energy are always and everywhere in nature readily accessible.

Nanogenerators have been utilised as self-powered devices, sensors, photodetectors, and actuators [208–210]. At first, more interesting was the underlying science of the phenomenon [211, 212], and it was a long process to turn this technology from a theoretical one to practical one. For instance, increasing the open circuit voltage (V_{OC}) from the initial 9 mV to over 1 V has taken four years [213, 214]. Development of high-output piezoelectric nanogenerators since its inception from 2006 is shown in Figure. 1.13. However, the complex device fabrication process creates a roadblock for the advancement of this technology. The use of ZnO NWs allows for excellent mechanical stability and high-performance PENG device by a significantly facile fab-

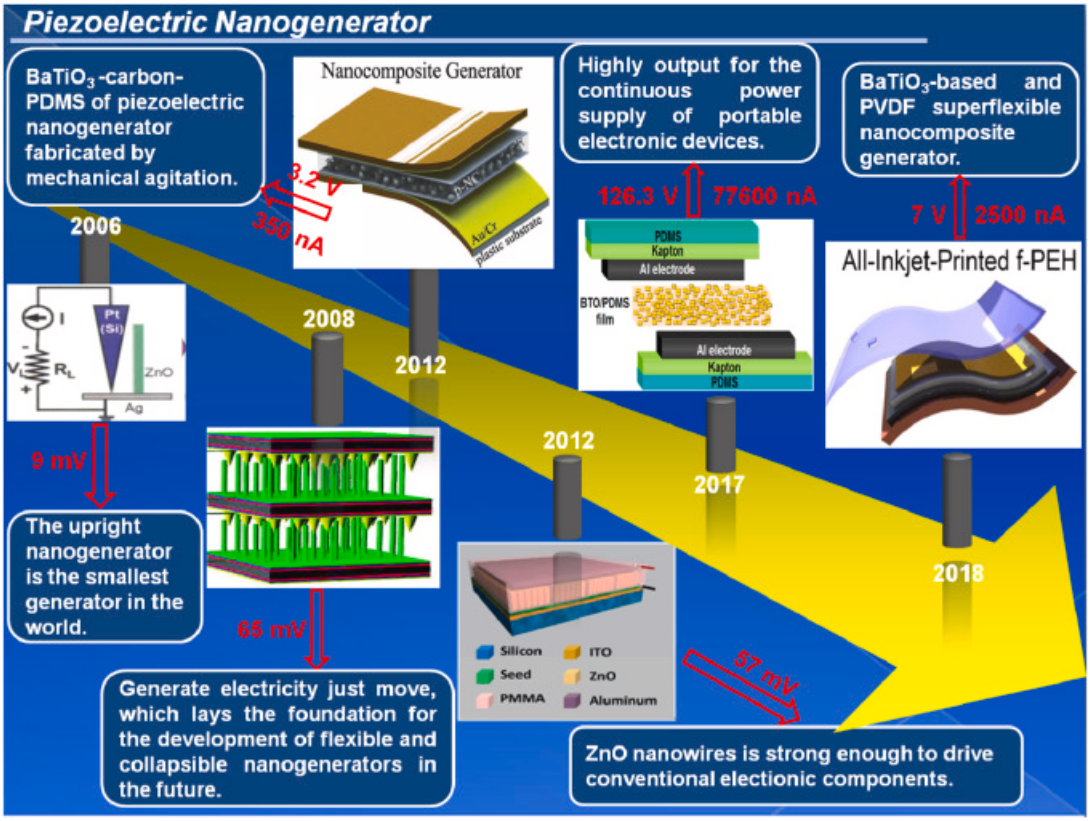

Figure 1.13: Development of high-output piezoelectric nanogenerators since its inception from 2006. Adapted from Hu et al. [207].

rication method. A new device design based on a sandwich construction has recently been developed. In most of the piezoelectric nanogenerators (PENG), there are two electrodes required, one is aluminum electrode used to grow the ZnO (bottom electrode) and second is flexible ITO electrode (top electrode). As we know the drawback of flexible ITO electrode leads to decrease in the stability of the PENG device, therefore, in this thesis the focus is to replace commercial flexible ITO with the alternative sputter deposited flexible metallic multi-layer electrodes.

1.6 Need for alternative TCEs

As it was discussed earlier, among all the TCEs, only ITO electrodes are frequently used as TCEs in several of the optoelectronic devices. However, the increasing demand of indium makes it very costly, leading to exploration of alternative TCEs. Especially in the case of flexible electrodes it needs to possess good electrical property and transparency along with very good mechanical stability. Considering all these factors, the present thesis is focused on developing the flexible electrodes with higher mechanical stability and good electrical and optical properties using noble metals in a thin metallic multi-layer structure. For the development of unpliable electrode, out of all the alternatives, doped SnO_2 is identified as good alternative for ITO, and therefore, the exploration of the SnO_2 based electrodes by various dopants is one of the trending research topics.

1.6.1 Flexible metallic TCEs

Earlier in section 1.4.1, possibility the non-oxide-based electrodes were discussed sufficiently. Metallic nanowires [215], metal meshes [216], and other types of alternative TCEs are investigated as potential replacements for ITO due to their abundant supply, high mechanical robustness, and considerable transparent conducting properties. Fundamentally, unlike ITOs, metal-based alternatives do not show better transmittance since bandgap do not exist. Although one cannot anticipate these alternatives to totally replace ITO since they do not have the same level of sheet resistance as conventional ITO and they do act as a supplement with a wide range of applications. In an attempt to get over these restrictions, interesting micro-structured networks of metallic nanowires and grid-like arrangements have been proposed as TCE substitutes [217]. The main barriers to mass production are electrical shorts caused by uneven surface characteristics and inherent optical haze, both of which are not desirable for display applications [218]. Due to its straight-forward and affordable de-

position method, high mechanical robustness, significant optical transmittance, and high electrically conducting features, stretchable ultrathin metallic multi-layers are a promising contender among the available options. After considering all these concerns, this thesis is focused on the development of the flexible TCEs using thin metal layers based on the concept of skin depth of a metal. These thin layers are placed in a multi-stack structure for the metallic constituents to work together synergistically to increase transmittance into a wider visible spectrum and electrical conductivity [156]. The highest transmittance of the corresponding metal components in a layer is more restricted to specific wavelengths [156]. Ag, Pt, and Au, which are noble metals, and their ultrathin layers (thickness lesser than skin depth) exhibit noticeable transparency in the visible range [219]. These noble metals are sandwiched into a multi-layer architecture and explored in order to attribute wider-range transparency in the visible wavelength domain, which serves as the inspiration for the current work.

1.6.2 SnO_2 based TCEs

The AO_2 binary oxide system provides excellent flexibility for the inclusion of donor or acceptor dopants at the 'A' or at the 'O' sites, and this insertion of dopants is highly helpful for drastically tunning the electrical and optical properties [13]. SnO_2 is one of the ideal host materials for TCO applications among the AO_2 compounds since it contains the 'Sn' cation element from group IV of the periodic table. The two main crystalline forms of tin oxide are stannic oxide (SnO_2) and stannous oxide (SnO). These two phases can be distinguished from one another primarily by their valence states. Sn occurs in a 2+ charge state in the SnO host, but a 4+ valence state in the SnO_2 system [111]. By using a variety of approximation techniques, density-functional theory (DFT) reveals the electrical band structure of a system [220]. For instance, a linear combination of atomic orbitals (LCAO) approximation is used to computationally determine the ground-state energy of the SnO_2 system [221]. The system's conduction and valence band energies were calculated using the tight binding approximation (TBA).

The SnO_2 system contains a variety of polymorph crystalline phases. According to research by Das and Jayaraman [222], these stages exhibit various chemical and physical behaviours. Cassiterite is a naturally occurring mineral that contains the rutile phase, which is the most stable of these phases. The P42/mnm space group is present in the tetragonal crystal structure of the rutile SnO_2 system. Two 'Sn' and four oxygen atoms are covalently bonded together in the tetragonal unit cell, which has the lattice constants a = b= 4.7374 (Å) and c = 3.1864 (Å) [111]. Structure of SnO_2 and Sb doped SnO_2 from DFT theoretical simulations are shown Fig. 1.14.

The coordination of each Sn atom is six-fold, compared to three for each oxygen atom. Chains of coordinated tin atoms with edge sharing are created along the [001] direction. The SnO_2 system exhibits insulating properties if it is fully stoichiometric. In general, metal oxides are not entirely stoichiometric in practice, which is caused by the crystal system's creation of oxygen vacancies, which are in charge of the electrical conduction process [223]. The fact that SnO_2 material has a high reflectance in the IR region is another crucial characteristics [224]. The applicability of undoped SnO_2 is limited because of its inferior electrical and optical properties in comparison to standard ITO system. According to Shanthi et al., [225], undoped SnO_2 has a poor electrical resistivity of $10^{-2}\ \Omega cm$, a carrier concentration of $6.42 \times 10^{19}\ cm^{-3}$, and a mobility of $7.5\ cm^2V^{-1}s^{-1}$. The donor/acceptor element serves as a dependable TCE electrode in a range of optoelectronic devices when it is doped into the crystal lattice of the SnO_2 system. The donor/acceptor can occupy the interstitial sites of the SnO_2 crystal lattice [226]. This donor/acceptor can significantly alter the sample's Fermi level, for both the undoped and doped SnO_2 systems. The underlying cause of the metal oxide system's coexistence of electrical conductivity and optical transparency is still not fully understood [8].

Under various chemical potential conditions in the SnO_2 host, first-principles calculations were reported to ascertain the formation energy and energy levels (donor and acceptor) for a variety of intrinsic defects, including oxygen/metallic vacancies, and interstitials [227]. The goal of this was to comprehend the coexisting conductivity and transparency phenomenon in doped SnO_2 systems. According to Maziar Behtash et al., [8], standard DFT calculations can be used to introduce acceptable TCO behavior into SnO_2 for a variety of dopants, including F, I, P, Sb, Nb, and Ta. Compared to the complicated p-type SnO_2 system, the n-type donor element doped

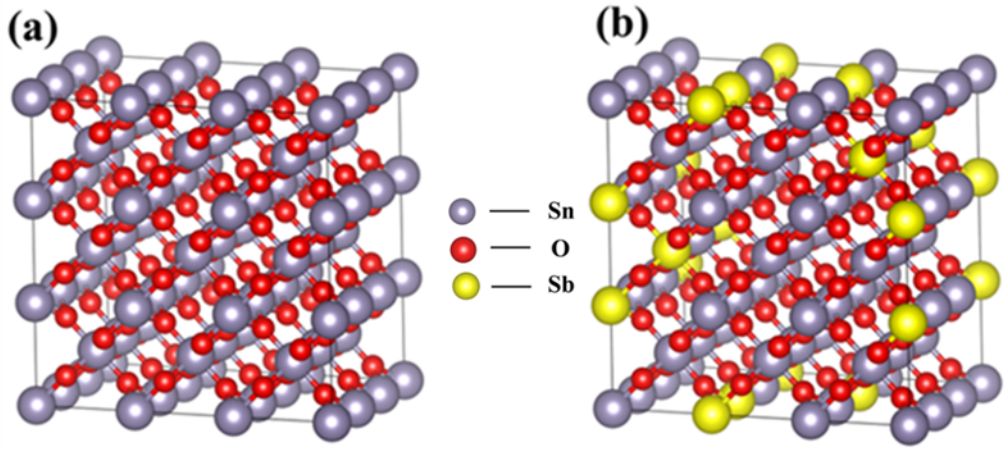

Figure 1.14: Structure of (a) SnO_2 and (b) Sb doped SnO_2 from DFT theoretical simulations

Table 1.1: Properties of the host and dopant materials that are crucial for constructing efficient TCOs (selected dopants are explored in this thesis by adopting co-doping strategy).

Group	Element	Oxidational state	Ionic radius	Coordination number
Host	O	-2	1.35/1.36/1.38/1.4/1.42	2/3/4/6/8
	Sn	+4	0.69/0.76/0.83/0.89/0.95	4/5/6/7/8
Donors/Acceptors	F	-1	1.285/1.3/1.31	2/3/4
	Al	+3	0.39/0.48/0.54	4/5/6
		+3	0.72	6
	Ta	+4	0.68	6
		+5	0.64/0.69/0.74	6/7/8
		+3	0.72	6
	Nb	+4	0.68/0.79	6/8
		+5	0.48/0.64/0.69/0.74	4/6/7/8
	In	+3	0.62/0.8/0.92	4/6/8
	Sb	+3	0.76/0.8/0.76	4/5/6
		+5	0.6	6
	Ga	+3	0.47/0.55/0.62	4/5/6
	P	+3	0.44	6
		+5	0.17/0.29/0.38	4/5/6
	As	+3	0.58	6
		+5	0.34/0.46	4/5
		+4	0.66	6
	W	+5	0.62	6
		+6	0.42/0.51/0.6	4/5/6

SnO_2 materials are more viable TCOs. There are various ways to deposit SnO_2 based alternative TCOs. The methods used in the several articles on doped SnO_2 thin films with different dopants are listed in Table 1.1. By adjusting a number of factors, including the deposition process, choice of precursor, substrate temperature, film thickness, rate of deposition, and post-annealing temperature, the optical and electrical properties of a donor doped SnO_2 lattice can be improved. Each approach has benefits and drawbacks of its own. For instance, the spray pyrolysis process makes it simple to adjust the electrical and optical properties, although the surface feature of the film is not as good as that of sputter deposited films [228]. Sputtering techniques need an ultra-high vacuum to produce a smooth surface, however spray pyrolysis does not require such a high vacuum and it relies heavily on the substrate temperature, type of precursor and solution concentration etc.

1.7 Scope and objectives of the thesis

The major goal of this thesis is to develop alternative pliable and unpliable electrodes as supplement for ITO electrodes that are currently available in the market and to demonstrate their usability in various optoelectronic devices. The specific objectives of the thesis are listed below,

i) To perform extensive literature survey for in-depth understanding of various metal and metal oxide based alternative materials, so as to identify the existing problems and to address it using appropriate strategy using relevant deposition techniques under optimal conditions and to explore them for its optoelectronic properties suitable for various device applications.

ii) To deposit ultrathin flexible metallic multilayer electrodes with higher mechanical stability with lower sheet resistance and considerable transmittance by employing various noble metals like Au/Ag/Pt/Cu based on their respective skin depth.

iii) To select suitable co-dopant elements for the SnO_2 and to optimize deposition conditions onto glass substrate by spray pyrolysis technique towards host material with higher transmittance and lower sheet resistance.

iv) To explore for their physico-chemical, optical and electrical transport properties by characterizing the optimized thin film electrodes using various techniques for their structural, optical, morphological, charge state, electrical transport, and surface work function properties.

v) To test the applicability of the optimal thin film electrodes in various optoelectronic applications like dye sensitized solar cell (DSSC), piezoelectric nanogenerator (PENG) and alternating current electroluminescent (ACEL) devices.

Chapter 2

Thin Film Deposition and Characterization Techniques

The fundamentals of thin film technology, formation of thin films, and thin film deposition methods are briefly outlined in this chapter. The instrumentation details of various characterisation techniques used for investigation in this thesis along with the basics of devices that are fabricated using the optimised films are also covered in this chapter.

2.1 Thin film technology

Modern society's rapidly evolving technological landscape necessitates the creation of newer, more efficient materials and sophisticated technologies for a variety of uses [229]. Due to its superior electrical, optical, surface, and luminescent properties, thin film technology has a significant advantage over bulk counterparts [230]. A thin film is a low dimensional material made by condensing individual ionic, atomic, and molecular species over a substrate. Mathematically, an ideal thin film is a homogeneous solid material that is enclosed between two parallel planes, extended infinitively in the x and y directions, and constrained along the third direction (z), which is perpendicular to the x-y plane [230]. Although thin films are typically less than one micron thick, their thickness can vary up to a few nanometers depending on the species, experimental parameters, and necessity. Due to high absorption, bulk material do not have the best optical transmittance, but the thin layer of materials does because of low absorption. Additionally, thin films have benefits over bulk materials such as compactness, improved performance, increased reliability, reduced production costs, and lighter packaging weight. In the 18^{th} century, Michael Faraday apparently invented the thin film of materials using an electrochemical process [231]. Several review articles on thin film technology have been published for a variety of advanced technological applications [26, 163, 232–235].

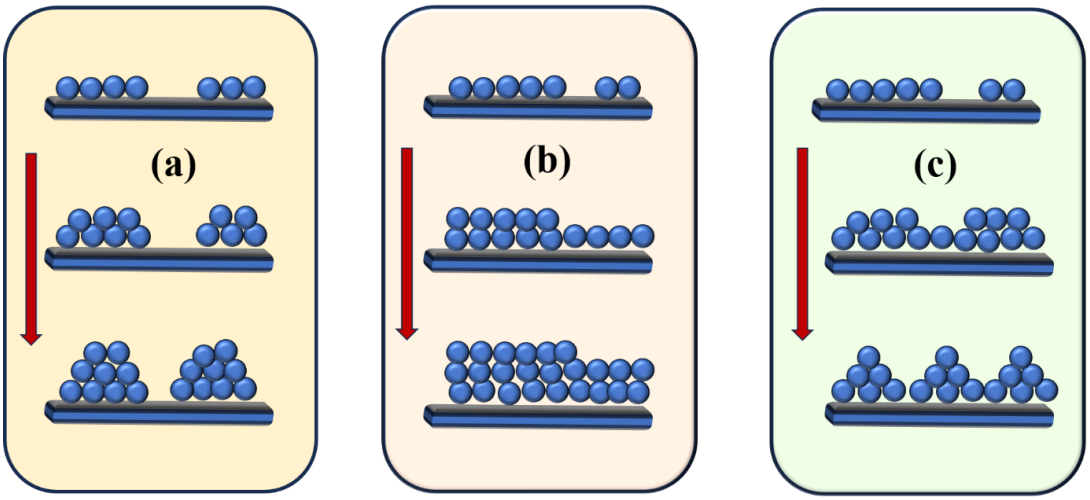

Figure 2.1: Thin film growth modes; (a) island growth (Volmer–Weber), (b) layer by layer growth (Frank–Van der Merwe), and (c) mixed growth mode (Stranski–Krastanov)

2.2 Thin film growth modes

Three main growth modes involved in thin film formation are island growth, also known as the Volmer-Weber mode (VW), layer-by-layer growth, also known as the Frank-Van der Merwe mode (FV), and mixed growth type, also known as the Stranski-Krastanov (SK) mode [236]. Figure 2.1 (a) depicts the island growth mode: The term "island growth" refers to a tiny nucleus that has grown in an arbitrary direction over the substrate [236]. The growth of the islands is caused by the relatively weak force of attraction (adherence) between the substrate and adsorbed species. This type of growth mode results in the deposition technique, which involve low vacuum, low substrate temperature, and diluted precursor solution concentration. The metal oxide semiconductor system, which is deposited in low vacuum, often follows the island growth mode. The layer-by-layer growth exhibits the island growth's opposite behaviour, as shown in Fig. 2.1 (b). The smallest nucleation growth happens in two dimensions when atoms, ions, or molecules are gradually added, creating a layer-by-layer growth mode. Compared to other growth modes, here the substrate and film interact to one another quite strongly. Typically, layer by layer growth mode lead to epitaxial thin films. High vacuum conditions and a slow rate of deposition are necessary for achieving this growth method. The layer-by-layer and island growth modes are combined to form the mixed growth mode, also known as the Stranski-Krastanov mode (Fig. 2.1 (c)). After forming one or two monolayers by the layer-by-layer mode, this growth mode becomes unfavourable, and island mode starts to take control. This growth mode occur during the thin film deposition of metal-metal and metal-semiconductor materials using technique like DC or RF sputtering [236].

2.3 Thin film deposition methods used in this thesis

Based on the growth modes, the two main categories of thin film deposition techniques are physical and chemical deposition techniques as depicted in Fig. 2.2, which are further divided into the liquid phase, gas phase, evaporation, and sputtering [161]. The oxidation and reduction processes are essential for the creation of films when using the chemical deposition method (CDM). Physical phenomena like evaporation, ejection, condensation, and sputtering are significant in the case of the physical deposition method (PDM). Both approaches, though, offer benefits and drawbacks of their own, the quality of the film and cost make the choice of method for film deposition [230]. The high vacuum deposition methods are much useful to fabricate films for commercial devices, but it is more expensive than a low vacuum deposition method. For large scale production, we require a cost-effective deposition method, but it is difficult to obtain high quality thin films by these methods. In this thesis, the flexible ultra-thin metallic multi-layer electrodes were deposited on flexible PET substrate using sputtering technique and the oxide electrodes were deposited on glass substrate using the cost-effective chemical spray pyrolysis method.

2.3.1 Sputtering

Sputtering is the process by which atomic or molecular species are ejected off the surface of the target as a result of the bombardment of positive ions as high-energy projectiles. The schematics of the sputtering process is shown in Fig. 2.3. An ener-

<table>
<tr><th colspan="4">Thin film deposition methods</th></tr>
<tr><th colspan="2">Chemical deposition methods</th><th colspan="2">Physical deposition methods</th></tr>
<tr><th>Liquid phase</th><th>Gas phase</th><th>Evaporation</th><th>Sputtering</th></tr>
<tr><td>Spray pyrolysis</td><td>Laser chemical vapor deposition</td><td>Thermal evaporation</td><td>Magnetron sputtering</td></tr>
<tr><td>Spin coating</td><td>Photochemical vapor deposition</td><td>Electron beam evaporation</td><td>RF sputtering</td></tr>
<tr><td>Sol-gel</td><td>Plasma enhanced chemical vapor deposition</td><td>Pulsed laser evaporation</td><td>DC sputtering</td></tr>
<tr><td>Electrodeposition</td><td rowspan="2">Metal organic chemical vapor deposition</td><td>Arc evaporation</td><td rowspan="2">Ion beam sputtering</td></tr>
<tr><td>Chemical Bath deposition (Dip coating)</td><td>Flash evaporation</td></tr>
</table>

Figure 2.2: Classification of chemical and physical thin film deposition methods

getic ion or atom collides repeatedly with the target, causing sputtering of the target species. The following are examples of typical cathode reactions that could occur as a result of ion bombardment [237]: the ion may be reflected, the ion's impact may cause the target to eject an electron, the ion may become buried in the target, causing the phenomenon of ion implantation, the ion's impact may cause some structural rearrangements in the target material, the ion's impact may set up a series of collisions between the atoms of the target (cascade collision process), all of these potentially causing the ejection of medium atoms from the surface of the target [238]. The mechanism explained here, cathodic sputtering, involves bombardment by positive ions produced by an electrical discharge in a gas. In order to get useful amounts of material that may be deposited directly onto the substrate, material is ejected from the target in a certain fashion direction at an optimal rate.

The incident ions also knock out several atoms during their transit through the material, which causes them to lose energy. A portion of the atoms will diffuse to the top and get sputtered out. Once again, before impacting the target surface, the incident positively charged ion undergoes auger neutralization and becomes a neutral atom. In other words, it takes an electron from the target [239, 240] and creates an energetic atom that shares momentum with the atoms of the target. The result is that the target atoms will be displaced from their regular lattice location when enough energy is attained from such numerous collisions caused by the energetic ions. The hot-spot evaporation theory, developed by von Hippel and Townes [241], has produced overwhelming experimental evidence that sputtering is not an energy-transfer process but rather one of momentum-transfer, as first proposed by Stark er al.[17] Numerous advancements have been made to the early momentum-transfer or collision theory by Kingdon and Langmuir [242], Herjschke's [243], proposed billiard-ball model, which was accurate at low energies, and takes into account that sputtering results from the ions colliding twice or thrice with the lattice atoms before being reflected back by the lattice. More complex ideas, like those put forth by Keywell [244] and Pease [21], viewed sputtering as primarily a radiation-damage process.

The sputtering yield is the quantity of atoms that are ejected from the target surface for each incident ion. The most crucial factor in defining the sputter process is the sputtering yield. The material bombarded, its structure and composition, the energy of the incoming ion, and the experimental geometry of the sputter cathode all affect the sputtering yield. The sputtering yield exhibits an undulatory characteristic as a function of the target's atomic number, and the periodicity of the undulations matches the groups of elements in the periodic table. With a reduction in vaporization heat, the yield increases significantly. The yield of a single-crystal target rises as

the crystal's transparency toward the ion beam decreases. The exact details of the interaction of an ion with the target atom, the momentum transfer, and the collision mean free path mainly depends on its energy. With increasing energy (E), the interaction changes from billiard-ball to coulomb and then to a nucleonic model The sputtering yield (Y) has the following formula according to Pease's [21] theory:

$$Y = An^{\frac{2}{3}} \left(\frac{E}{4E_d} \right) \left[1 + \left[\frac{ln\frac{E}{E_s}}{ln\ 2} \right]^{\frac{1}{2}} \right] \tag{2.1}$$

Where "E" denotes the average energy of the struck atom, "E_s" denotes the sublimation energy, and "n" denotes the number of atoms per unit volume, "A" denotes the cross section for imparting energy larger than E_d, the energy required to displace an atom from its lattice location.

2.3.1.1 Magnetron sputtering

The development of magnetron sputtering has complemented other vacuum coating methods such as e-beam evaporation, thermal evaporation, and pulsed laser deposition (PLD). However, these methods have some drawbacks, and refractory metals are problematic because of variations in the alloy constituent vapour pressure and their high melting points (the necessity to operate sources at extremely high temperatures, which has an impact on the coated objects). At the modest evaporation pressures utilized for depositing the material, compounds can also dissociate into their chemical components. Once more, their adaptability in industrial appliances is constrained by low area deposition and volatility in the deposit's stoichiometry. These issues are resolved by magnetron sputtering, which is superior to previous methods in the following aspects:

- Good control on nucleation and growth of thin films (by controlling atom to ion ratio reaching the substrate)
- Relatively low temperature process
- Good adhesion can be achieved (due to self-cleaning)
- Uniformity in thickness and composition
- Substrates of larger dimensions can be coated cost effectively
- Viable for industrial scale applications

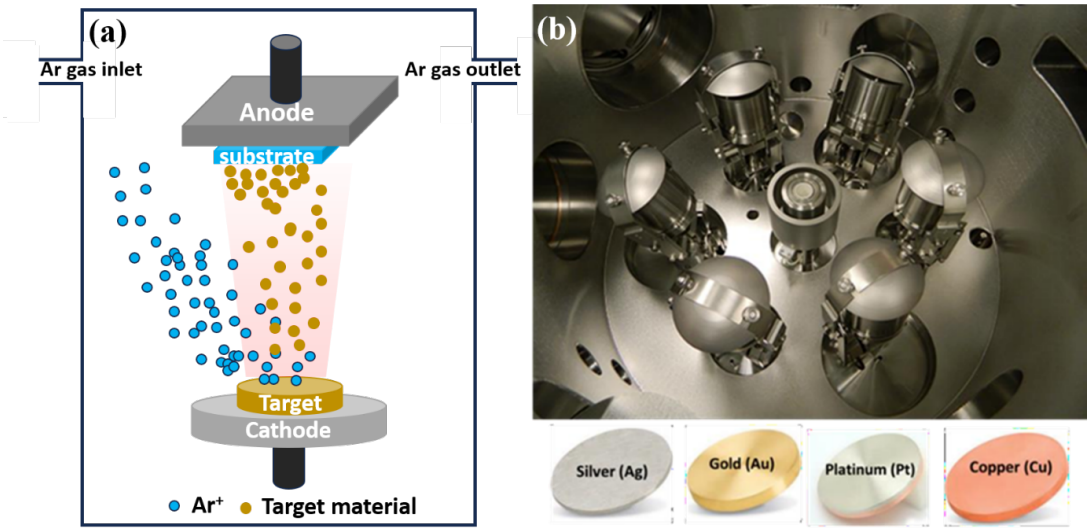

Figure 2.3: (a) Schematics of DC magnetron sputtering, (b) multitarget sputtering chamber along with Ag, Au, Pt and Cu targets

The sputtering process can be described by several terms, including cathodic sputtering, RF and DC sputtering, diode sputtering, reactive sputtering, and ion-beam sputtering all of which are variations of the same physical phenomenon. These arguments make it very evident that sputtering is a very potent technology with several uses.

2.3.1.2 DC magnetron sputtering

Since radio frequency (RF) power supplies require more complicated manufacturing methods than do DC power supplies are employed, the DC magnetron is a quite affordable and effective system for metals. The target may be operated up to currents of perhaps 70 Wcm^2 on an average over the target in the DC mode, however since it is direct conducting electricity and is subject to I-R losses. Power sources will be able to deliver up to 5 kW DC into the plasma for circular magnetrons with a diameter of 100 mm. This is suitable for high-production-rate applications because it can create deposition rates on static substrates of several micrometres per minute. Based on the size of the target, the necessary power can reach upto 50 kW for large magnetrons. The following is a list of some uses for DC magnetron sputtering:

- Metallizing for microelectronic circuits and chips
- Electrical resistance films, e.g. Ni-Cr for strain gauges
- Magnetic films (Fe, Co-Pt. Co-Cr, Cr-Ni etc.) for general magnetic storage devices, floppy discs, tapes and thin-film magnetic heads

- Opto-storage devices. e.g., compact discs and video discs
- Corrosion-resistant films (Cr-Ni)

Sputtering has become the most popular coating technique in microelectronic production processes due to its simplicity and versatility, especially when treating alloy-type materials as films and avoiding step coverage. Gas ions from plasma are propelled toward a target that contains the substance to be deposited during the sputtering process. Material is separated (or "sputtered") from the target and then deposited on a nearby substrate. The procedure is carried out in a closed chamber that is pushed down to a base vacuum pressure prior to the start of the deposition. Argon is typically fed into the chamber at pressures ranging from 1×10^{-3} to 0.1 mbar to facilitate plasma ignition utilizing residual ionized Ar^+ ions. A negative voltage V up to several hundreds of volts is applied to the target during DC sputtering. As a result, the Ar^+ ions are accelerated in the direction of the target and liberate the material; however, they also create secondary electrons due to which the gas becomes much more ionized. A breakthrough voltage V_D from which a self-sustaining glow discharge is determined by the electrode distance 'd' and gas pressure 'p' using the equation:

$$V_D = \frac{A \times pd}{ln\,(pd) + B} \tag{2.2}$$

A and B are the material constants in this equation. According to the above equation, as pressure rises, the likelihood of ionization rises as well, leading to an increase in ions and gas conductivity and a dramatic drop in voltage. A stable plasma is produced with an adequate ionization rate, which also produces enough ions for the material to be sputtered. In the magnetron sputtering, a ring magnet is placed beneath the target to further improve the ionization rate by the released secondary electrons which are entrapped in its field and move around the target surface in cycloids. They cause a prolonged dwell period in the gas, with greater probability of ionization and, as a result, creating a plasma ignition at pressures that can reach up to 100 times smaller than with traditional sputtering. Higher deposition rates can be achieved in this way and on the other side, the sputtered material experiences lesser impacts due to the lower pressure and kinetic energy at the substrate, in its journey towards the substrate. There is a greater impact on the substrate. The electron density and hence the number of generated ions is the highest, where the magnetic field is parallel to the substrate surface. The target area immediately beneath this region experiences a maximum sputter yield and a zone of erosion develops that mimics the magnetic field's shape.

Positive ions would charge the surface of a non-conducting object after bombarding it, which would then shield the electrical field and ion current would stop flowing. As a result, only conducting materials, such as metals or doped semiconductors, can be sputtered in DC magnetron sputtering. Currently, there are two methods for creating dielectric films: In RF sputtering, the target receives an AC voltage. Ions are accelerated in one phase and sputter material as they approach the target surface, the other phase reaches charge neutrality. This makes it possible for non-conducting materials to sputter as well. Alternately, to form oxidic or nitridic films during reactive sputtering, other gases such as oxygen or nitrogen are supplied into the sputter chamber in addition to argon. In this thesis work, Multi target (5 Nos.) ultra-high vacuum (UHV) DC magnetron sputtering equipment was used for deposition of the multi-layer using Ar gas (Fig. 2.3). All other sputtering parameters of elements are given in the respective chapters.

2.3.2 Chemical spray pyrolysis

Metal oxide semiconducting thin films can be deposited effectively via spray pyrolysis, a cost-efficient chemical vapour deposition technique. For producing distinct structural, surface, optical, and electrical transport features in thin films, the spray deposition conditions are more viable. A key benefit of the spray approach for producing a variety of oxide-based materials on a wide scale is how simple and straightforward it is to adjust the deposition parameters. In order to produce a thin film of reasonably good quality and uniformity, spray dynamics are of utmost importance. The size of the atomized droplet, spray flow rate and velocity, substrate temperature, and solution concentration are some of the variables that affect this. The inter-particle spacing in the films is used to evaluate the size distribution of the produced particles, and larger values of this parameter result in more inhomogeneity and uneven particle size in the films [245]. Since the droplets intended to reach the heated substrate are expected to contain enough solvent to form a largely homogeneous surface, the solution concentration also plays a key role in film development. Spray dynamics affect droplet size and probability of atomized droplet production [245]. By changing the distance between the substrate and gun nozzle, the thermal gradient that impacts film formation can be reduced. The coverage area increases with increasing substrate to gun nozzle distance, but at the expense of longer precursor droplet flight times, slower deposition rates, and non-continuous film development. Spray-coated thin film for use in a variety of devices has been the subject of numerous research papers and review publications [230].

2.3.2.1 Thin film formation mechanism in spray pyrolysis

Spray pyrolysis primarily involves three essential steps mainly: a) atomization of the precursor solution, b) transportation of the resultant aerosol, and c) decomposition and thin film formation over the substrate. To generate a thin film of good quality, these three processes are more crucial [246].

2.3.2.1.1 Atomization of the precursor solution : In atomization of the precursor solution, the solution and compressed air/gas combine to form an aerosol in the spray nozzle gun [247]. There are many theoretical, computational and empirical study reported for the formation of the aerosol. Spray nozzle size, solution concentration, and compressed air or gas pressure are the factors influencing the aerosol formation and its characteristics.

2.3.2.1.2 Aerosol transport : The microstructure, electrical, and optical properties of a film are significantly influenced by the aerosol's transportation. The key variables to govern aerosol transport are the ideal spray flow rate, velocity, and substrate location. All the droplet should reach the heated substrate without particle formation in order to produce a more homogeneous and uniform thin film. The solution velocity, nozzle diameter, and substrate temperature have a greater impact on aerosol size and its movement. Different forces, including gravitational, thermophoretic, and Stokes forces, have an impact on the droplet velocity. The temperature and pressure gradients during the growth of the film allow the thermophoretic force to come into play [245].

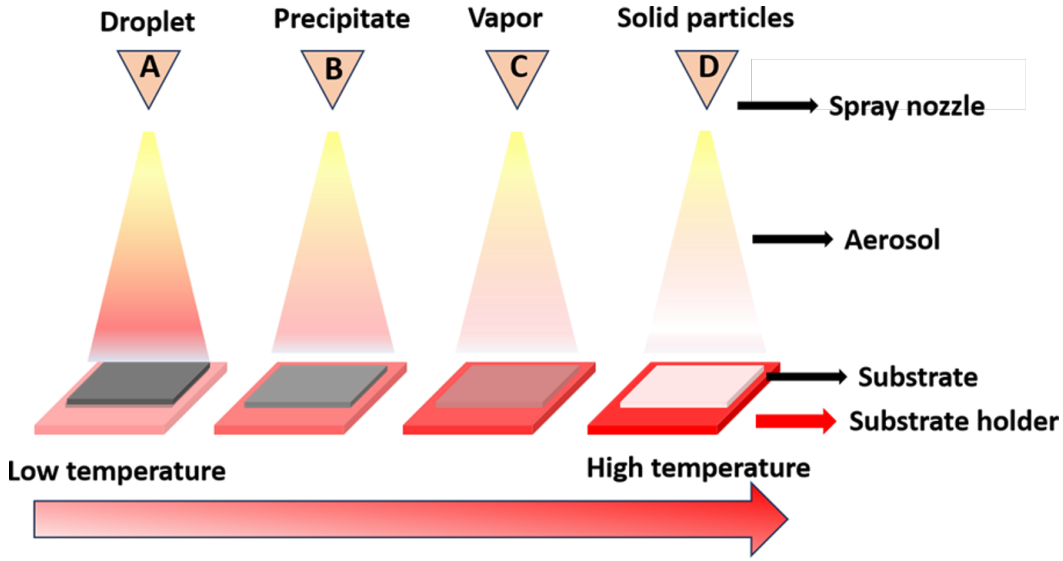

Figure 2.4: Viguie and Spitz mechanism of spray deposition and oxide film formation

2.3.2.1.3 Decomposition of the precursor aerosol : Aerosol decomposition on the heated substrate is a crucial step in the creation of thin films. Aerosol breakdown, droplet spreading, and solvent evaporation are a few of the simultaneous activities that take place when an aerosol impacts a surface. Viguie and Spitz provided a model that is simple to comprehend the thin film growth mechanism [248] among other theoretical and computational models for the droplet's decomposition. The Viguie and Spitz model, which provides comprehensive information on aerosol dynamics, is shown in various stages in Fig. 2.4. Additionally, the island growth mode is identified to occur for spray-deposited thin film formation. The film processes that happen with rising substrate temperature were proposed by Viguie and Spitz. Stage A: A droplet splashes onto the substrate under the conditions of the lowest substrate temperature without properly decomposing. Stage B: Dry precipitate strikes the substrate and begins to decompose when the solvent completely evaporates during the droplet's flight at moderate substrate temperatures. Stage C: The solvent also evaporates before the droplet reaches the substrate at higher substrate temperatures. It has been determined that stage C is where most of the chemical deposition of thin film creation occurs. Stage D: At the higher temperature, the precursor vaporises before it contacts the substrate; as a result, the solid particles are created even before reaching the substrate. Various TCO films were deposited in this thesis using a single static nozzle spray device using the setup shown in Fig. 2.5.

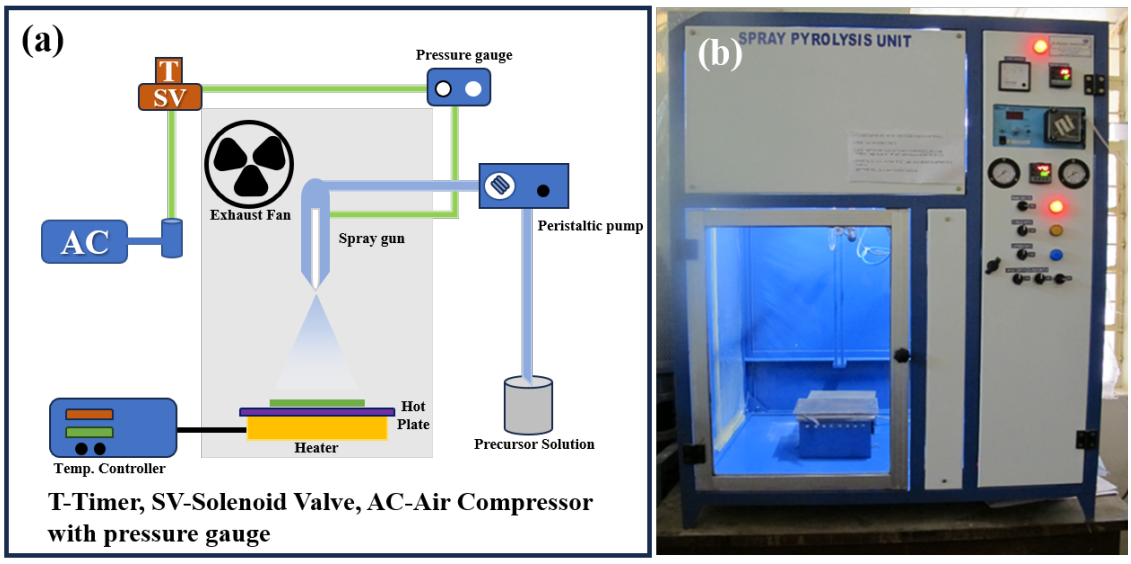

Figure 2.5: (a) Schematics of spray pyrolysis system and (b) photograph of the system used in this thesis

2.3.2.2 Precursor solution preparation

Variable donor (Sb, Nb, F) doped SnO_2 thin films have a variable precursor solution and concentration (molarity). The host material for each of the three donors doped TCO systems was tin chloride di-hydrate ($SnCl_2 \cdot 2\,H_2O$) salt. The same procedure was employed for making the solution, but different solvent was used to dissolve the various donor components. At room temperature, the precursor solutions are made by magnetic stirring. First host and donor element precursors were separately dissolved for 30 minutes by magnetic stirring in 10 ml of distilled water and 2-propanol (IPA). Following these steps, the two solutions were combined and stirred continuously for 30 minutes; the resulting mixture was turbid. To make the solution clear, an additional 2 drops of HCl was added [249]. The final precursor solution for spray pyrolysis was then created by adding the necessary amount of ethylene glycol. The exact composition of the precursor solution are elaborated in the respective chapters.

2.3.3 Substrate cleaning procedure

Glass slides from Zhuhai Kaivo, Optoelectronic Co. Ltd. with a high softening temperature (730 °C) were utilised as substrates. Acetone, IPA, soap solution, and distilled water were used to clean the substrate. An ultrasonic cleaner was used to clean the substrates according to regular substrate cleaning procedures. Various solvents are used to remove the oil and grease contaminants on the glass substrate during the coating process. The ionic impurities that are present on the ultrasonically cleaned substrates was also removed using a high energy plasma cleaner (model: PDC-002 Harrick plasma). Finally, cleaned glass substrate placed on substrate holder in the spray pyrolysis chamber.

2.4 Thin film characterization techniques

2.4.1 X-Ray diffraction

The non-destructive X-ray diffraction (XRD) technique is used to examine the sample's crystalline structure and phase purity, lattice parameter, and degree of crystallinity. Quantitative sample parameters including grain size (crystallite size), dislocation density, texture coefficient, and stress analysis/lattice strain could also be estimated from the XRD patterns. The spacing of the lattice grating must match the wavelength for X-rays that are to be diffracted. The usual interatomic spacing in crystals is 2-3 Å, which is appropriate for X-ray diffraction. Based on the interference

of the X-rays scattered by the crystalline material, X-ray diffraction pattern results. The Bragg's condition is need to be satisfied for X-ray diffraction, $2d_{hkl} \sin\theta = n\lambda$, where n is the order of diffraction, λ is the wavelength of the incident X-ray radiation, d_{hkl} is the inter-planar spacing of the respective hkl plane, and θ is the Bragg's angle. Due to several parameters, such as the instrumental effect, grain size, lattice strain, etc., the diffraction pattern has a non-zero width [250]. The inter-planar distance of a particular material is indicated by the Bragg's equation, which can be calculated using the diffraction angle and the wavelength's known value. The schematic representation of the X-ray diffraction process is shown in Figure 2.6. The following equations were used to measure the crystallite size, dislocation density, strain, lattice parameters texture coefficient and stacking faults.

$$D = \frac{k\lambda}{\beta cos\theta} \tag{2.3}$$

$$\delta = \frac{1}{D^2} \tag{2.4}$$

$$\varepsilon = \left(\frac{1}{sin\theta}\right)\left[\left(\frac{\lambda}{D}\right) - (\beta cos\theta)\right] \tag{2.5}$$

$$\frac{1}{d^2} = \frac{h^2 + k^2}{a^2} + \frac{l^2}{c^2} \tag{2.6}$$

$$TC_{hkl} = \frac{I_{hkl}/I_{0hkl}}{1/N\sum_{N=1}^{N} I_{hkl}/I_{0hkl}} \tag{2.7}$$

$$SF = \left[\frac{2\pi^2}{45\,(3tan\theta)^{1/2}}\right]\beta \tag{2.8}$$

where D is the crystallite size, k is the Scherrer constant (shape factor considered as 0.9), λ is the wavelength of the X-ray used in the experiment (1.5406 Å), β is fullwidth at half maximum (FWHM) (in radians), θ is the diffraction angle and δ is the dislocation density, ε is the strain, TC_{hkl} texture coefficient of a particular plane, and SF is the stacking faults in the film. In this thesis, Panalytical (X-pert powder) XRD equipped with Cu-$k\alpha$ radiation (wavelength 1.5406 Å), horizontal goniometer $(\theta - \theta)$, is used to take the diffraction patterns of the deposited thin films.

2.4.2 X-Ray reflectivity

Unlike the X-ray diffraction technique, X-ray reflectivity (XRR) is not dependent on the crystalline structure. The former can be applied to crystalline solids, amorphous materials, liquids, and biological specimens. The mass density, thickness, and surface roughness of the individual layers all have a significant impact on an XRR scan. The

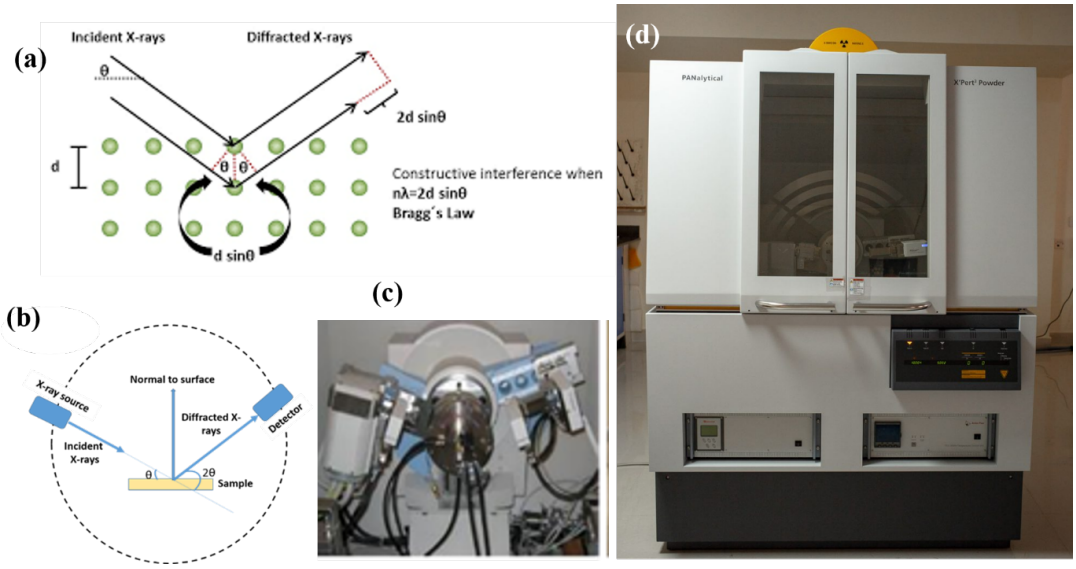

Figure 2.6: (a) Schematics of Bragg's law and (b) X-Ray diffraction, (c) schematics of XRD chamber, and (d) photograph of Panalytical XRD instrument

X-ray beam is completely reflected in a region of low incident angles for which the measured curves are characterized, and the reflected intensity rapidly decreases with increasing incident angle in an angular range above the critical angle. The drop of the reflected intensity presents a strong dependence on the surface roughness. Single layer XRR scans often show oscillations similar to the Fabry-Pérot effect, which are attributed to Kiessig fringes in reflectivity measurements. The optical interference phenomena resulting from reflection at successive atomic planes, or internal pseudo-interfaces with comparable physical and chemical properties, is what causes these oscillations. The individual layers and the averaged lattice parameter of the superlattice both contribute to the interference pattern that results when the layered complexity is increased to a periodic bilayer structure with a given number of periods (N). The thickness of multi-layer thin film is estimated using, using XRR. It is mandatory to know film thickness when the coating is only a few nanometres thick. Using the XRR technique, the thickness of the deposited film can be calculated accurately based on the critical angle and peak angle using equation 2.9.

$$t = \frac{\lambda}{2\sqrt{\alpha_{im}^2 - \alpha_c^2}} \tag{2.9}$$

where λ is the wavelength of the Cu-$K\alpha$ radiation (1.5406 Å), the α_c is the critical angle, and the α_{im} is the next peak angle after the critical angle.

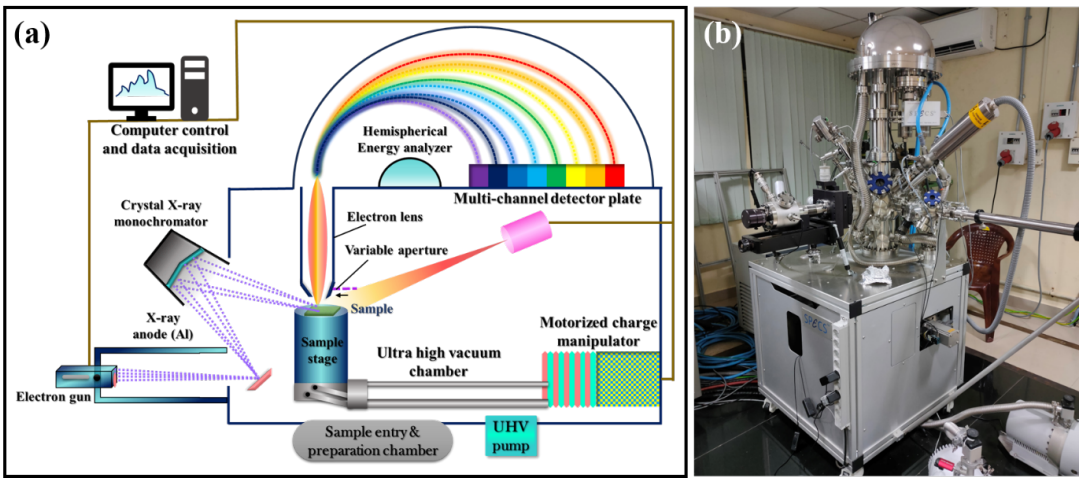

Figure 2.7: Schematics of X-ray photoelectron spectroscopy and the photograph of the actual equipment

2.4.3 X-Ray photoelectron spectroscopy

An advanced method to examine the binding energy and surface oxidation status of the samples elemental contents is X-ray photoelectron spectroscopy (XPS) [251], the most popular surface analysis method, also known as Electron Spectroscopy for Chemical Analysis (ESCA), which can be used on a variety of materials and yields useful quantitative and chemical state information from the surface of the material being studied. When the X-ray beam is incident on the sample, electrons absorb the X-ray energy and escape from the orbital with a maximum kinetic energy of $K.E = h\nu - E_B - e\Phi$, where E_B is the electron binding energy, ν is the photon frequency, and Φ is the work function, which is the electron's minimum free energy required to remove it from the material's surface [252]. The photoelectron that is expelled depends on its binding energy and is specific to the element from which it originates. This conversion's energy is regulated by the emission of either a distinctive x-ray spectrum or an Auger electron. XPS measurement can be used to study Auger electrons, since only the electrons created close to the surface escape and are measured, it is a surface sensitive technique. The photoelectrons have a low kinetic energy, the atomic structure of the sample prevents photoelectrons originating deeper than 20 to 50 Å from escaping with enough energy to be detected due to inelastic collisions. The photoelectron production unit, a detection unit, and an analyzer unit are the three main components of the XPS apparatus.

To explore the thin film's surface and structures, XPS measurements and ion milling (sputtering) can be combined to get depth distribution data. In order to do XPS, a sample's surface is typically excited with mono-energetic Al k_α x-rays, which causes the sample's surface to emit photoelectrons. The energy of the photoelectrons

released is measured using an electron energy analyzer. The elemental identification, chemical state, and amount of a detected element can be deduced from the binding energy and intensity of a photoelectron peak. The obtained XPS data is corrected for its background using gaussian function fitting. Ultra-high vacuum (UHV) conditions are necessary for XPS, which can be used to examine the surface chemistry of a substance in its "as received" state or following a variety of treatments, such as: cutting, scraping, or fracturing in air or UHV to reveal the bulk chemistry; ion beam etching to remove some surface contamination; exposure to heat to examine changes brought on by heating; exposure to reactive gases or solutions; exposure to ion beam implantation. The schematics of the XPS and photograph of the actual equipments are shown in Figure 2.7. The XPS used in the current thesis is ULVAC-PHI, Inc; PHI5000 (model) Version Probe III, High performance Micro-area analysis Ultimate depth resolution, with Ultra Photoelectron Spectroscopy (UPS) and X-Ray Photoelectron Spectroscopy (XPS).

2.4.4 Field emission scanning electron microscopy

The most popular method for studying the surface morphology of samples with high resolution and depth of focus is the field emission scanning electron microscope (FE-SEM) [253]. Both elastic and inelastic interactions between the sample surface and the highly accelerated electron beam are possible. The deflection of the incident electron beam by the sample by outer shell electrons with a similar energy produces elastic interaction. Backscattered electrons (BSE) are incident electrons that are elastically scattered at an angle greater than 90°. The incoming electrons interact with the sample, causing inelastic scattering, which causes the primary beam electron to transmit a significant amount of energy to that atom. Secondary electrons (SE) are produced

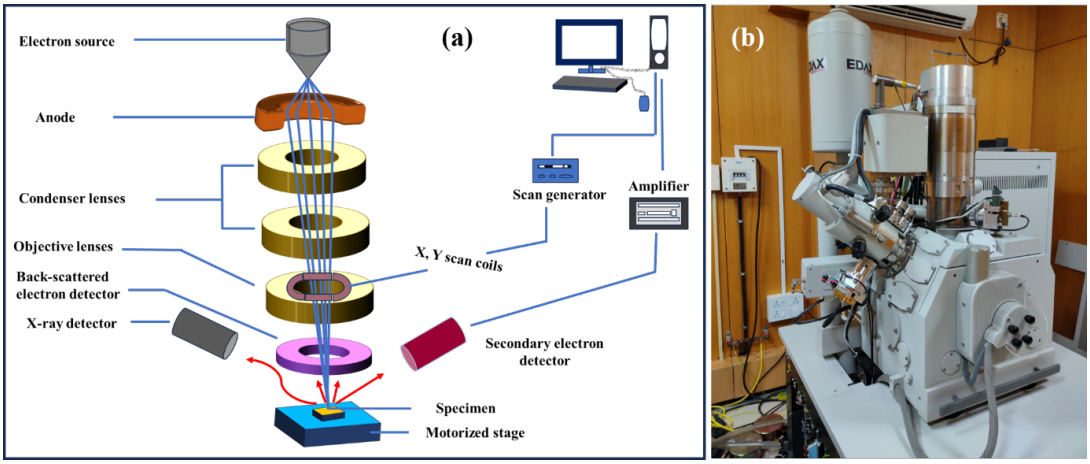

Figure 2.8: (a) Schematics and working principle of the FESEM instrument and (b) the photograph of the instrument

as a result of the specimen being excited during the ionisation of the specimen atoms. The surface morphology of the materials is imaged using these two types of electrons. The FESEM instrument's schematics and photographs are displayed in Figure 2.8. An electron gun uses field emission to create the electron beam. Using an anode grid, the generated electron is accelerated towards the sample surface at a voltage of 300 V to 30 kV. Various electromagnetic lenses and apertures are utilised to concentrate the accelerated electron beam on the sample's surface. Different kinds of signals are picked up from the sample surface as the electron beam is scanned across it. For a certain purpose, a variety of detectors can gather the emitted signal. By measuring the energy of the emitted X-ray radiation, the X-ray Energy Dispersive Spectroscopy (EDS) method can be used to determine the quantitative chemical composition of samples. In this thesis work, the surface morphology and chemical composition of the synthesized samples were analyzed using field emission scanning electron microscopy (FESEM) with energy-dispersive X-ray spectroscopy (EDX) (Hitachi, S-4300SE).

2.4.5 Atomic force microscopy

A very high-resolution surface scanning microscope with established resolution of the order of a nanometre is by the atomic force microscope (AFM). The cantilever bends or deflects away from the sample surface due to the force of attraction or repulsion between the tip and surface. The Van der Waals force of attraction between the interatomic species and the electrostatic force between the tip and sample both contribute to the cantilever deflection [254]. As the tip scans across the sample surface, a detector measures the cantilever movement. The cantilever's deflection measures

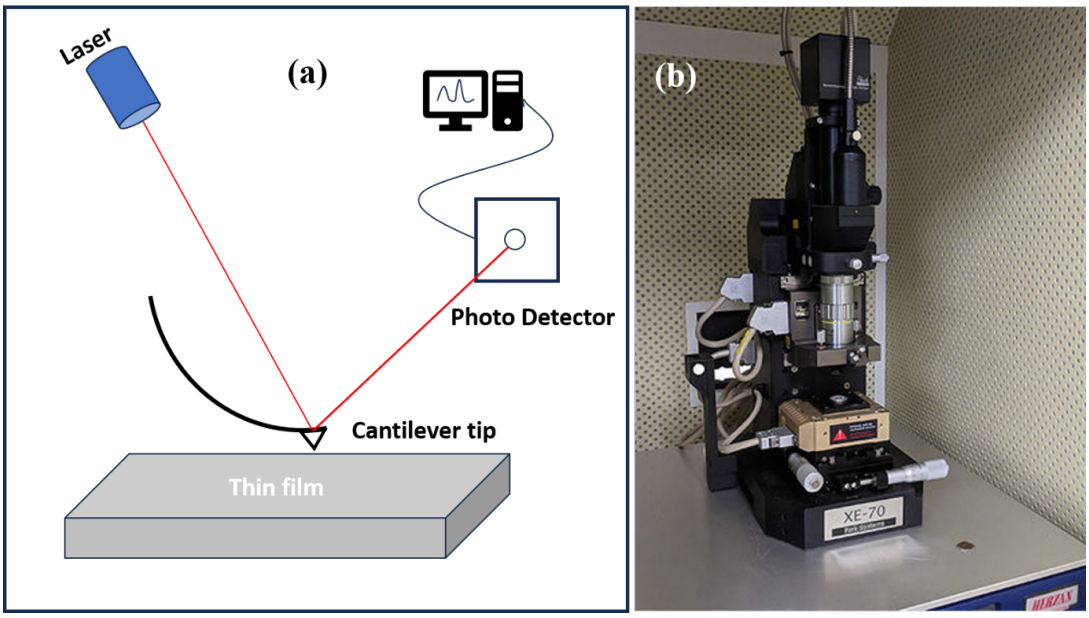

Figure 2.9: (a) Schematics of AFM and (b) photograph of the instrment

the topography of the surface. The three operating modes of the AFM instrument are contact, non-contact, and tapping-depending on how the tip interacts with the sample's surface. The schematics of the AFM instrument's operation is depicted in Fig. 2.9, and it is composed of three parts: a laser source, a cantilever, and a detector. In accordance with Hooke's law [255], the cantilever deflects when the tip is brought in close contact with the surface of the sample. A photodiode detects the laser light that is reflected when the cantilever is moving appropriately. Additionally, the feedback amplifier receives the reference signal and the detected light signal in order to analyse and document the surface variations on the sample. Topographical information of the thin films are taken using atomic force microscopy (AFM) measurements (Park Systems, NX10).

2.4.6 Optical profiler

An optical profilometer has been developed that offers a non-contact means to collect information on surface from the thin film. A piezoelectric transducer-driven Mirau interferometer, a linear array of photodiode detectors, a microcomputer, and a typical Leitz rejection microscope make up the system. The result of the combination is a system that accurately measures variation in optical height of surfaces. This height variation is processed by a computer to generate surface topographical and statistical information. A Leitz Mirau interferometer serves as the optical profiling microscope's brain. This interferometer is a reflection-based connection to the objective of a long-working distance microscope. Figure 2.10 (a) depicts schematics of the Mirau interferometer. The Mirau objective receives light from a tungsten light source, which pictures the field stop onto the surface being tested. A second optical channel is created by the Mirau beam splitter and ends at the reference surface, where

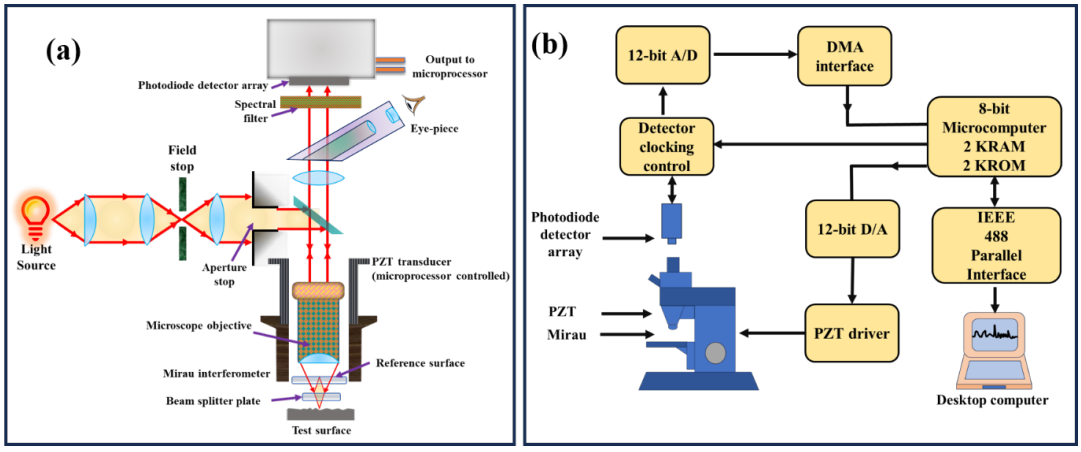

Figure 2.10: (a) Instrumental setup of Leitz Mirau interferometer and (b) block diagram of optical profiler

an image of the field stop is also created. By virtue of symmetry, if the test surface and the reference surface are both at the source's image, the optical path between the beam splitter and the test surface will be identical to the optical path between the beam splitter and the reference surface. Since both pathways are equivalent and produce white light fringes, a white light source can be employed. The photodiode detector array captures a second image of the test surface and the reference surface to quantify the intensity distribution of the interference fringes throughout a linear portion.

The piezoelectric transducer (PZT) is where the Mirau interferometer's objective, reference, and beam splitter plates are placed. The PZT transducer modulates the optical-phase difference between the test and reference arms of the Mirau interferometer to produce a phase modulation. The entire Mirau interferometer is pushed closer to the surface being tested while voltage is being delivered to the PZT transducer. This changes the relative phase difference between the interferometer's reference arm and test arm and the interference fringe's positions change as a result. Three steps of the PZT transducer are made, with each step corresponding to a 90° phase difference between the test and reference arms. The photodiode detector array records and stores the information in a microprocessor, after each step, the interference pattern from the interference of the wavefronts created by the test surface and the reference surface. NanoMap 1000WLI a non-contact optical profiler is used to study the topographical information of the deposited films.

2.4.7 Contact angle analyser

The contact angle (CA) measurement is a tool used to explore the surface characteristics of the film or any solid surface when it meets a liquid droplet, and is a key parameter in surface science. The shape of a liquid droplet on the solid's surface re-

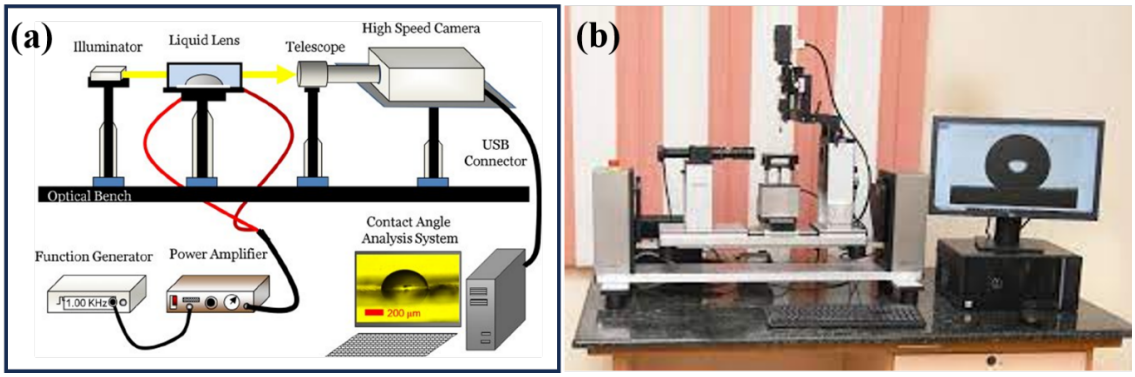

Figure 2.11: (a) Schematics of the experimental set up and (b) photograph of the equipment used to measure the contact angle

veals the aspects of surface wettability. It mainly depends on the interaction between the liquid and solid at the interface (or point of contact). Wettability provides a simple and reliable means for surface engineering. Surface wettability research can be used as a diagnostic method to evaluate beforehand the quality/performance of coated thin films when used as photoanode in DSSCs. This helps to understand indirectly the dye loading capacity or the electrolyte infiltration behavior of a photoanode film without actual device fabrication. The surface tension of droplets reflects the surface energy which is directly related to the surface properties. From the theoretical point of view, Young's equation remains the fundamental equation in the science of surface wetting [128]. Assuming an ideal solid surface, it relates the contact angle of a drop on a surface to the specific energies of the solid–vapor (γ_{sv}), the liquid-vapor (γ_{lv}), and solid-liquid (γ_{sl}) interfaces.

$$\gamma_{sv} = \gamma_{sl} + \gamma_{lv}\ cos\theta \tag{2.10}$$

$$cos\,(\theta') = r_W cos\,(\theta) \tag{2.11}$$

where θ' and θ are Wenzel's contact angle (measured) and young's contact angle (for ideal surface), respectively. r_W is Wenzel's roughness factor defined as the ratio of the actual area of a rough surface to the geometric projected area.

Several parameters can affect the contact angle value; those are surface roughness, functional groups present on the surface, porosity, surface energy, and impurities or cleanliness. Among these, surface roughness is considered to be a parameter controlling the surface contact angles. Based on the surface roughness values, the Wenzel and Cassie models are generally used to describe the contact angle [256]. The schematics of the contact angle instrument with the necessary components are shown in Fig. 2.11. The contact angle measurements were performed using a DSA25 Drop Shape Analyzer (KRUSS, Germany).

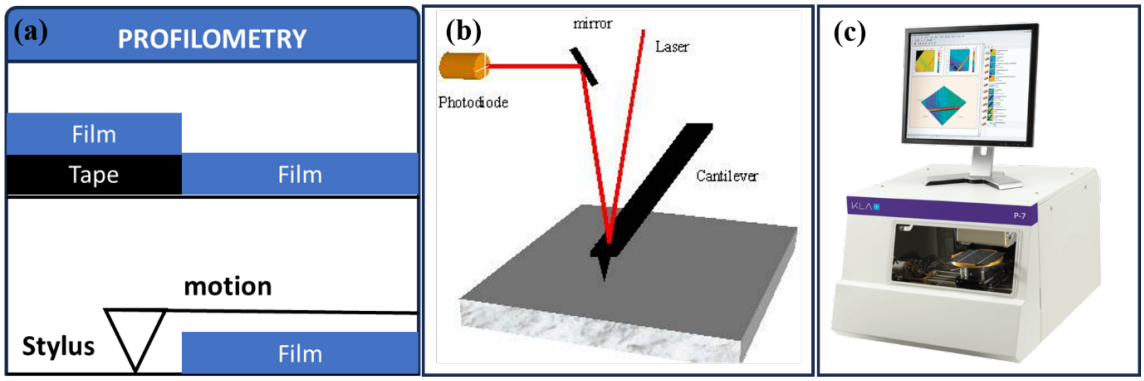

Figure 2.12: (a) Stylus profilometer tip on the step edge of the sample's surface (b) working principle, and (c) photograph of the Stylus profiler instrument

2.4.8 Stylus profiler

To estimate various thin film physical properties, including optical band gap and sheet resistivity, it is imperative to evaluate the film thickness [108]. Several optical techniques, such as ellipsometry, multiple beam interferometry, spectrophotometry, and stylus profilometry, are available to assess film thickness. One of them is the stylus profilometer measurement, which is more precise, trustworthy and straight forward. It is particularly crucial to quantify the thickness with a stylus profiler when a sharp-step edge forms in the thin film during deposition. The stylus profiler, which is scribed across the step edge over the uncoated and coated area, measures a slight change in vertical displacement as a function of the stylus location [257]. In contact mode, the stylus measures the thickness. Figure 2.12 shows the schematics of the stylus profiler with profilometry. The thickness measurements were performed using a stylus profilometer (Model: DektakXT, Bruker).

2.4.9 UV-Visible spectrometer

A potent method for determining a sample's optical characteristics, such as transmittance, absorption, reflectance, etc., is UV-Visible spectroscopy [258]. Higher transmittance in the visible range denotes lesser absorption and reflection from a substance. When the incident light intensity (I) and transmitted light intensity (I_o) are identical ($I = I_o$), the sample does not absorb the incident light for the specified wavelength range. I_o is always lower than $I (I_o < I)$ since in practice all materials do not have complete transmittance. According to Beer-Lambert's law, the relationship between absorption (A) and transmittance (T) is given, and the material's absorption is stated as $(A = -log(T) = -log(I_o/I))$ [259]. The layer thickness and material's band structure interface of the absorption coefficient (α). The absorption coefficient is a material's inherent quality. Considering the sample's thickness and absorbance, the optical band gap is determined. When incident light energy is absorbed by the

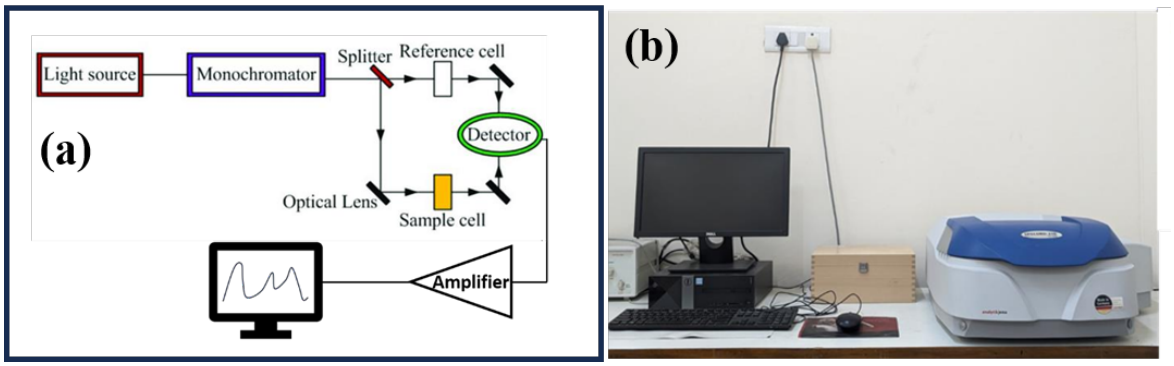

Figure 2.13: (a) Block diagram of UV-Vis spectrometer and (b) its photograph

semiconducting system, electrons may be stimulated from the valence band to the conduction band. There are two different kinds of optical transitions that can take place in a semiconducting system: direct and indirect transitions. The electromagnetic radiation's interaction with the crystal lattice causes both transitions to occur. The momentum vector of the photon with respect to the the position vector is used to compute the direct and indirect transitions. The Tauc relation is used to estimate the sample's direct and indirect band gaps [260]. Figure 2.13 is the schematics and photograph of the UV-Vis spectrometer. Transmittance spectra of the samples studied in this thesis were obtained using a UV–Vis spectrometer, Analytik Jena, SPECORD 210 PLUS (Germany).

2.4.10 Photoluminescence spectroscopy

An efficient method for comprehending different electronic transitions in materials is photoluminescence (PL) spectroscopy. Figure 2.14 (a) shows the block diagram of photoluminescence spectrometer and (b) its photograph. Based on the emission spectra, the luminescence study is helpful to determine the excitation and emission

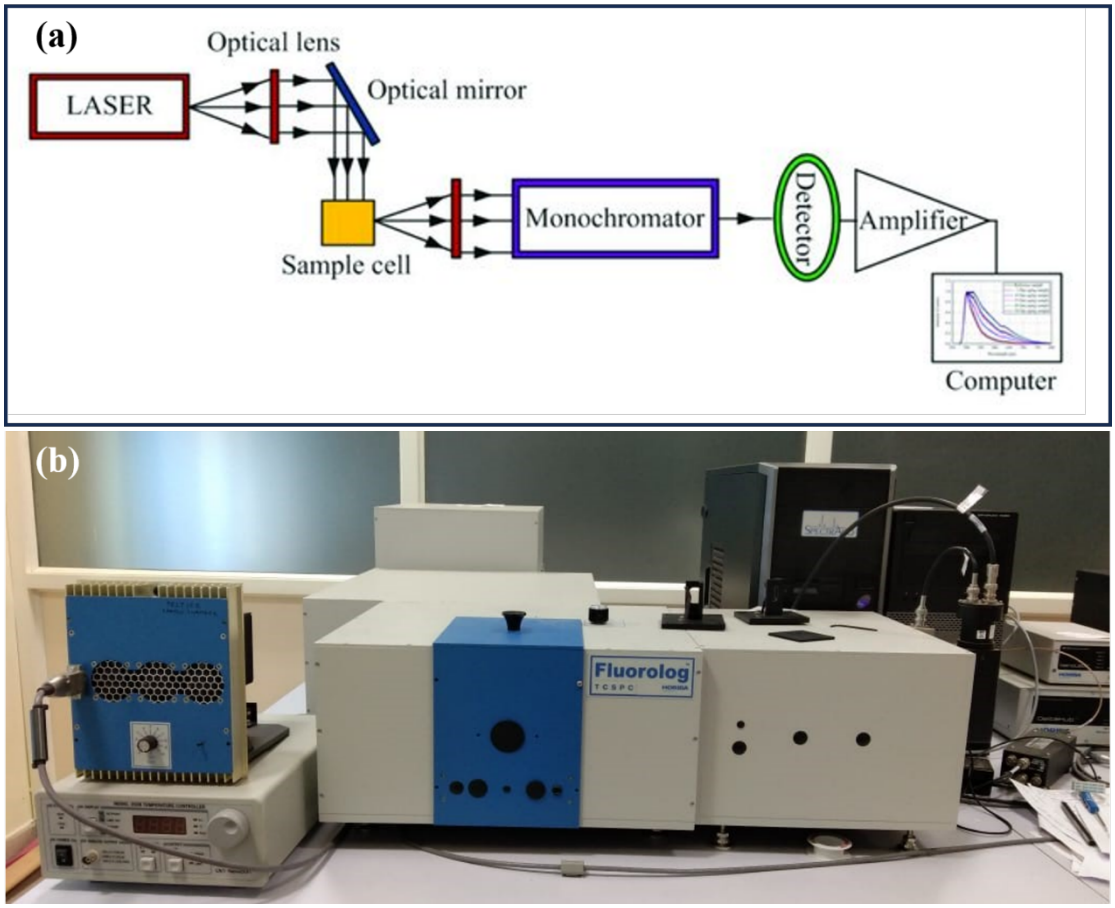

Figure 2.14: (a) Block diagram of photoluminescence spectrometer and (b) its photograph

process, band gap, and impurity defect levels of materials [261]. When the incident photon energy is equal to or greater than the band gap energy, light photons are emitted. During the absorption of incident photon, the electrons will be excited from the valence band to the conduction band. Since the excited state is not stable, the electrons radiate energy to return to the ground state. Non-radiative transfer from the excited state to the ground state is also conceivable. The photoluminescence emission spectrum that a material emits as a result of its system's defect state, localised impurity states, free electrons, valence electrons, and core electrons. Materials go through two different forms of electronic transitions: radiative and non-radiative transitions. The intrinsic states created by the impurities cause the radiative transition to occur. Band-to-band transitions, free exciton transitions, and free-to-bound transitions are only a few examples of the various radiative transitions that can occur in materials. Before or after the radiative transition, there is a non-radiative transition, during which no emission occurs [262]. Equation 2.12 is used to estimate the defect density in the deposited thin films. The smakulas relation is as follows, [263]

$$N = 1.29 \times 10^{17} \frac{n}{F\left(n^2+2\right)^2} \alpha W_{(1/2)} \tag{2.12}$$

where n is refractive index of SnO_2 (n=2), F is oscillator strength of optical transmission (F=1) $\alpha W_{(1/2)}$ is the Gaussian peak area obtained by fitting the PL emission peak. Photoluminescence emission spectra were recorded using a Horiba Jobin Yvon Flourolog-3-21 spectrofluorometer (a 450 W xenon arc lamp) with an excitation wavelength of 325 nm at room temperature.

2.4.11 Hall effect

From an applications standpoint, the assessment of TCEs electrical transport characteristics is very crucial. Investigations of the electrical transport properties of thin films show that they depend on their thickness as well as their structural and surface

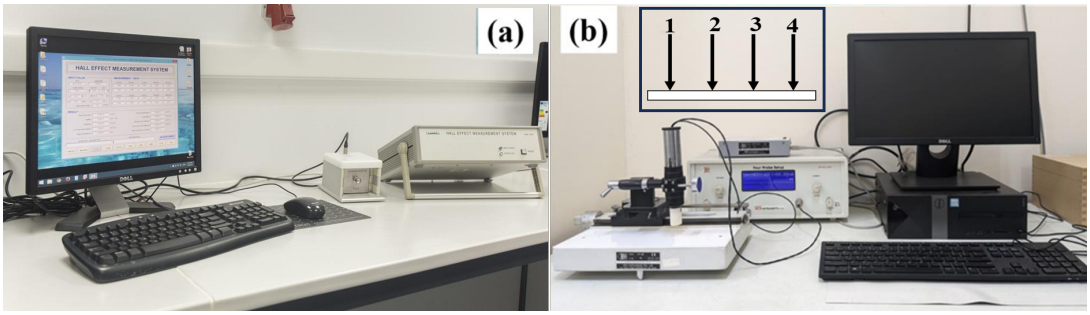

Figure 2.15: The photograph of (a) Hall-Effect and (b) four probe resistivity measurement instruments

characteristics. Using conventional Van der Pauw geometry, the Hall-Effect measurement was used to determine the electrical transport parameters like carrier concentration, mobility, and conductivity of semiconducting samples as well as for determining the type of conduction (n-type or p-type). Figure 2.15 (a) shows photograph of the room temperature hall effect equipment. The fundamental idea behind the hall effect is that, when a current carrying conductor (I_H) is placed in a uniform perpendicular magnetic field (B), a voltage develops in the direction opposite to these two plane directions. This voltage is known as the Hall voltage (V_H) [264]. In the present work, Hall Effect Measurement System HMS 5300 Ecopia, Working temperature: 80 K – 350 K Input Current : 1 nA - 20 nA, Resistivity Range: 10^{-4} to 10^{-7} Ωcm, Sample dimensions: 5×5 mm-20×20 mm, 0.51 Tesla magnetic field, spring loaded probes, is used to study the electrical transport parameters.

2.4.12 Linear four probe measurement setup

The most familiar method for determining the thin film's sheet resistance and resistivity as a function of temperature or at room temperature is the four-probe configuration. In the setup, the probes are positioned over the sample's surface at an equal distance (usually 1 mm). Equation $R_S = F(V/I)$ $\Omega/\square$ is used to calculate the sheet resistance. $F = 4.532$ is used as a correction factor, t is the film thickness, V is the voltage drop across any two probes, and I is the current applied between any two probes. Figure 2.15 (b) shows the photograph of the experimental setup of the linear four probe technique.

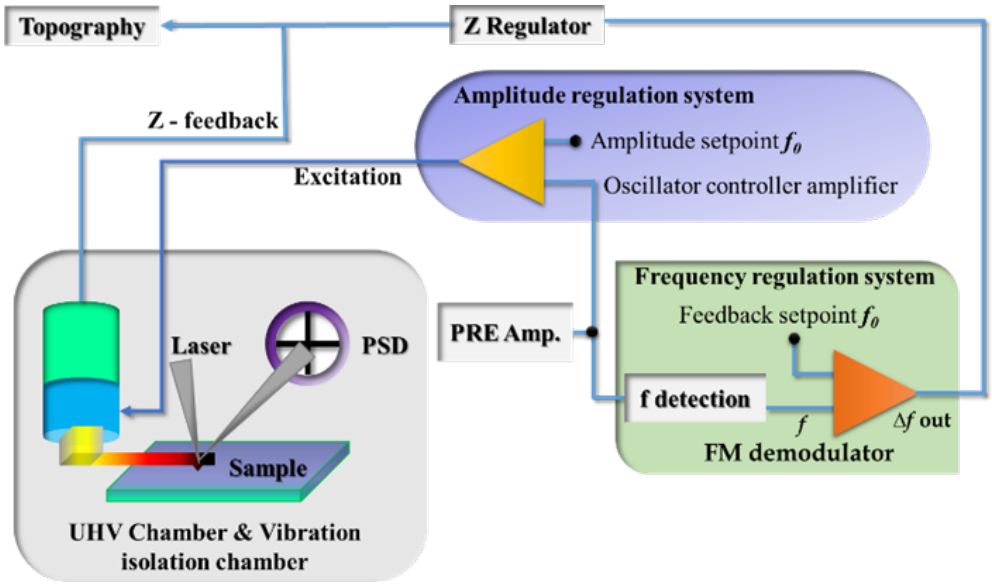

Figure 2.16: Block diagram of FM mode AFM system operated in UHV. The piezo scanner and the laser/PSD are enclosed in a UHV chamber system.

Table 2.1: Correction factors with respect to current and voltage probes position of linear four probe technique.

Current Probe	Voltage Probe	Correction Factor F
1-4	2-3	$(\pi/ln2) = 4.532$
1-2	3-4	$(2\pi/(ln4 - ln3)) = 21.84$
1-3	2-4	$(2\pi/(ln3 - ln2)) = 15.50$
2-4	1-3	$(2\pi/(ln3 - ln2)) = 15.50$
3-4	1-2	$(2\pi/(ln4 - ln3)) = 21.84$
2-3	1-4	$(\pi/ln2) = 4.532$

2.4.13 Surface work function by kelvin probe technique

A material's surface work function must be measured in order to evaluate its potential for use in optoelectronic device applications. Work function is the term for the energy level difference between a material's fermi level and vacuum level. Surface behaviour has a big impact on a material's work function. Both the Kelvin probe (KP) method and ultraviolet photoelectron spectroscopy (UPS) can be used to calculate a material's work function. Figure 2.16 shows the typical KP-AFM block diagram operated in UHV. The contact potential difference (CPD) between the actual probe and the sample's surface is provided by the KP method, whereas the UPS approach measures the absolute work function. To ascertain the contact potential difference between the sample and the reference electrode tip, the KP method is a special non-contact approach. It operates on a similar concept to a vibrating capacitor. The work function of the tip is then estimated using the following equations,

$$\Phi_{tip} = \Phi_{Au} - CPD\ (meV) \tag{2.13}$$

$$\Phi_{tip} = 5100 - CPD\ (meV) \tag{2.14}$$

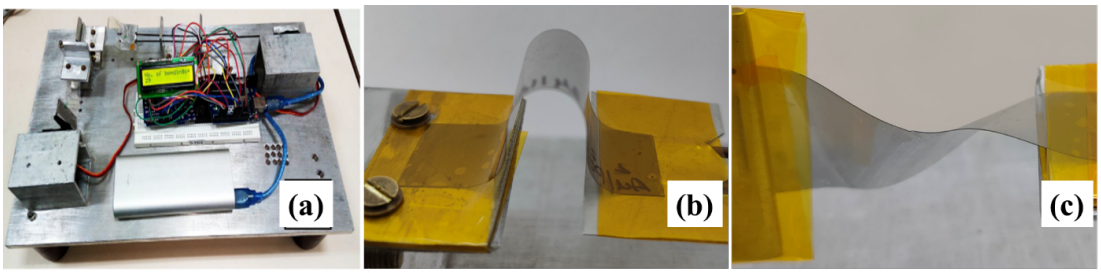

Figure 2.17: (a) Indigenously developed bending twisting apparatus, (b) bending position, and (c) twisting position of the sample

$$\Phi_{sample} = \Phi_{tip} + CPD\ (meV) \tag{2.15}$$

For the measurement, the work function (Φ) of the tip is estimated to be 4877.51±16.11 meV. Then, the sample is loaded and CPD between the sample and tip is also measured using equation 2.15. The surface work function of the samples was measured using Kelvin probe microscopy (KP Technologies APS04) operated in air with a 2 mm gold alloy tip.

2.4.14 Indigenous bending twisting apparatus

The advancement of bendable electronic components for compact and wearable gadgets needs a variety of highly robust and pliable TCEs suitable for a greater number of twisting and bending cycles, without considerable variation in sheet resistance, to prolong their efficient performance for longer lifetime. Hence, it is essential to explore sheet resistance stability of the pliable metallic multi-layer TCE for several bending-twisting cycles, which implies the layer sturdiness in resisting to external strain and stress. The mechanical stability of sheet resistance was executed using an apparatus developed indigenously with an ATmega328 microcontroller [265] (Fig. 2.17 (a)) for the stabilized pliable metallic multi-layers. The multi-layer samples placed in appropriate way for bending and twisting geometries, respectively, are shown in Figs. 2.17 (b) and (c).

2.5 Device testing using the TCEs

2.5.1 Piezoelectric nanogenerator

Over the last ten years, flexible piezoelectric nanogenerators have advanced rapidly and are now the technological cornerstone of next-generation, highly customized healthcare gadgets. These devices enable a multitude of innovative healthcare applications in the areas of electrical stimulation therapy, passive human biomechanical energy harvesting to power on-body devices from third parties, and highly efficient mechanical-to-electrical energy conversion. They are also simple to implement and self-powering. PENGs harvest the energy from body movements (e.g., jumping and walking) and it can power up the portable electronic gadgets. Lightweight, low cost, simple processing steps make PENGs promising for many energy harvesting applications. To be regarded as an effective means of energy harvesting, piezoelectric nanogenerators (PENGs) have to be able to endure heat, humidity, radiation, scratches, mechanical bearings, fatigue, and other contaminants.

The piezoelectric effect, which involves physically transferring mechanical strain to an electrical potential and is limited for specific materials depending on the distribution of ions, was originally identified by brothers Pierre and Jacques Curie in 1880. Materials with non-symmetric ion distribution have electric dipoles, which produce a piezoelectric signal. When positive and negative electric charges are in balance in the crystal structures of particular materials and there are no external forces acting upon them, the structure is referred to as neutral. When stress is applied, both cations and anions experience an instantaneous change at the center of charge, which causes the polarization to change. Direct effect and inverse effect are the two categories of piezoelectric effects. Materials that are polarized and produce observable voltages when subjected to an externally applied compressive or tensile stress are known as direct piezoelectric materials. This process is reversed for the inverse piezoelectric effect, when specific mechanical shifts in the material structure are triggered by the initial application of an electric potential. A substantial potential difference along the polarization direction is produced by the superposition of all the dipoles within the crystal, which is known as a piezo-potential. The commercially used electrodes in the PENGs is flexible ITO, but the durability of the ITO is very less, which can withstand only few hundreds of mechanical forces. Hence, in the present thesis, the exploration of flexible electrodes and its viability in the flexible PENGs devices is verified by replacing commercial ITO with the flexible metallic electrodes.

2.5.2 Alternating current electroluminescent device

The swift development of electronic technology has fueled the rise of stretchable electronics, which have flexible mechanical characteristics that allow them to endure a variety of bending, twisting, and stretching operations. Flexible alternating current electroluminescent (ACEL) devices are becoming more and more popular as wearable displays due to their excellent reliability, low power consumption, and uniform light emission. Recently, ACEL devices have gained attention as a possible option for wearable electronics, stretchable displays, electronic skin and next-generation smart lighting. In essence, stretchable light-emitting devices need all of their parts to have mechanically flexible qualities, such as strong deformation from rolling and stretching in addition to minor bending. Specifically, the simplified structure of ACEL devices which have an emission layer positioned between two electrodes makes them stand out for their appealing qualities, including an easy-to-manufacture process, exceptional durability, ease of integration, and stability in challenging environments. However, the fundamental need for stretchable ACEL devices is highly conductive electrodes with superior mechanical qualities. Many stretchable electrodes based on conductive

materials, such as single-walled carbon nanotubes (SWCNTs), silver nanowires (AgNWs), graphene, and MXene, which are combined with some soft substrates, such as polymers or elastomers, have been explored in order to achieve various mechanical deformations and high conductivity with conductive electrodes. However, when used with significant elongation, these techniques have the issue of abrupt resistance increases. Furthermore, the extensive use of luminescence in the realm of intelligent wearable devices is restricted by the high frequency and inexorably high driving voltage needed for it. Furthermore, electroluminescence (EL) devices' dynamic tunability and color diversity are essential for applications involving displays and communication. To overcome these problems, in the present thesis, the viability of various deposited electrodes are verified by replacing ITO in the fabrication ACEL device.

2.5.3 Dye sensitised solar cells

2.5.3.1 Device fabrication

In the photovoltaic (PV) industry, dye sensitized solar cells (DSSC) is one of the important topic. To create a DSSC, a variety of materials are used, such as dyes, electrolytes, counter electrodes (CEs), and photoanodes based on TiO_2 or other metal oxides. In addition to lowering the overall cost of DSSC fabrication, an effective TCE should be able to significantly enhance photovoltaic performance, or power conversion efficiency (PCE) and long-term stability. Grätzel and O'Regan derived a solid-liquid interface in the early 1990s using in semiconductor and electrolyte solutions in solar cells. These cells, known as Grätzel cells or DSSCs, are made up of mesoporous TiO_2 photoanode and ruthenium complex dye and Pt counter electrode. These cells can be produced using inexpensive materials and straightforward manufacturing processes. DSSCs have drawn a lot of attention because of their low cost, wide range of dyes, lightweight, packaging technology, eco-friendly materials, and comparatively high PCE. The use of two distinct materials for charge carrier transport and photon absorption distinguishes DSSC from traditional photovoltaic cells. The DSSC consists of a nanocrystalline TiO_2 electrode film deposited over a transparent conducting oxide sensitized with a dye, a Pt counter electrode, and an electrolyte containing dissolved iodide/tri-iodide ions. Pairs of these ions restore dye to its original state by acting as a redox couple. In this configuration, dye serves as an electron-generating layer and TiO_2 as the electron carrier layer. Electrons are produced when the dye absorbs incident photons. Electrons that have been photoexcited in TiO_2 are moved to the conduction band (CB). Electrons are transferred to the redox system by an external circuit, and the circuit is completed by counter electrodes. Device characteristics like

J-V plot and EIS analysis are explained in the following sections. A solar simulator is a device that can provide illumination approximate to natural sunlight for the measurement of current-voltage (J-V) characteristics of the fabricated DSSC devices.

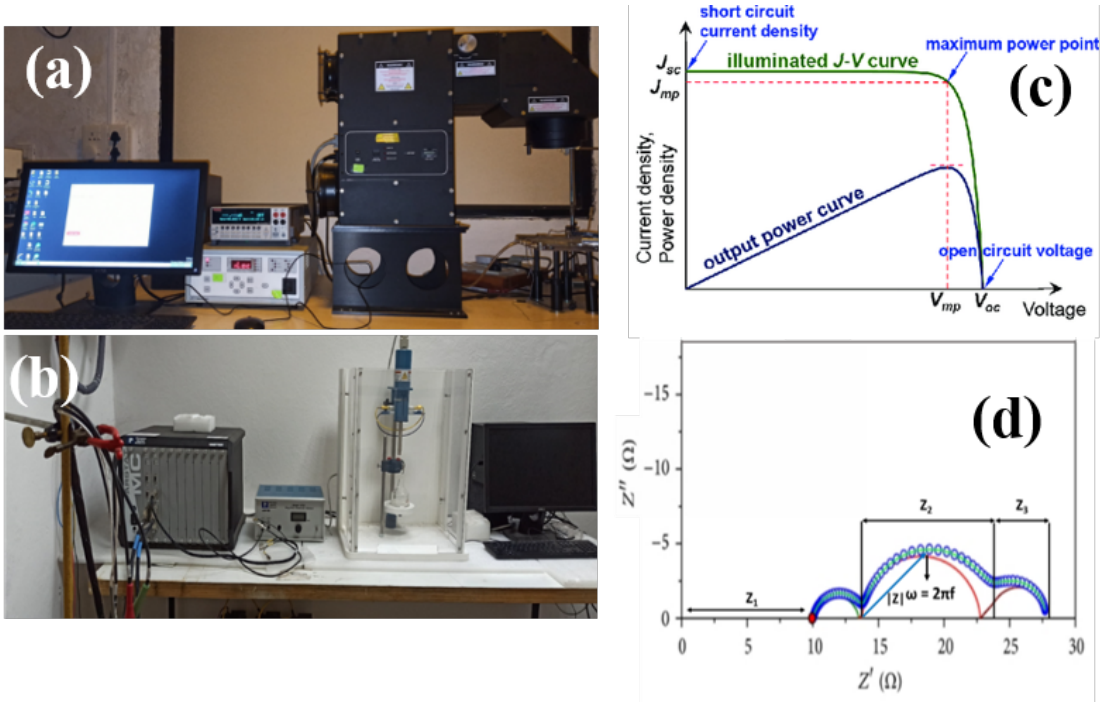

Figure 2.18: Photograph of (a) solar simulator, (b) EIS setup, (c) model J-V plot and (d) EIS analysis.

2.5.3.2 J-V characteristics of DSSC using solar simulator

The simulator constitutes a Xenon lamp arc with an output power of 300 W and an illumination area around 2 x 2 inches. The standard condition of illumination at AM 1.5 spectrum with incident power 100 mW/cm^2 at room temperature (298 K) is used for measurements. The Sun (source) is at an oblique angle of 48.2° which leads to a longer optical path length through the earth's atmosphere. J-V measurement is the most important tool to measure the photoconversion efficiency and figure of merit in solar cell devices. The J-V measurements yield parameters such as short circuit current (I_{SC}), current density (J_{SC}), open circuit voltage (V_{OC}), fill factor (FF), maximum output power (P_{max}), maximum current (I_{max}), maximum voltage (V_{max}) and efficiency (η) (Fig. 2.18 (b)). These parameters are compared with that of a reference cell to determine the spectral mismatch factors for different devices. The solar simulator is optimized using Newport standard silicon reference cell. In this thesis, J-V measurements of the fabricated DSSC devices were performed using Oriel class AAA solar simulator (Model: 94023A, Class AAA, IEC/JIS/ASTM, Xenon

lamp with 450 W power, illumination area is 2 x 2 inch). The photograph of the solar simulator is shown in Fig. 2.18 (a).

2.5.3.3 Electrochemical impedance spectroscopy

Electrochemical impedance spectroscopy (EIS) is an important technique to study electron transport kinetics and charge recombination processes occurring in the DSSCs. The experimental setup shown in Fig. 2.18 (b). To explore the charge transport kinetics of the fabricated DSSC devices, a frequency range from 10^{-1} to 10^{6} Hz was chosen with amplitude of 10 mV for measurement of Nyquist and Bode plots. The Nyquist plot consists of three semicircles attributed to the impedances at various interfaces of the device (Fig. 2.18 (d)). Three semicircles are in general observed in the conventional DSSCs; they are associated with the Warburg diffusion process [266] of I^{-}/I^{3-} and the electrochemical reaction at the Pt counter electrode. First semicircle at high frequency region (1 kHz to 100 kHz) is due to the charge transfer at the counter electrode and TiO_2, (R_{ct1}), second semicircle at intermediate frequency region (1 Hz to 1 kHz) is due to the TiO_2/dye/electrolyte interface (R_{ct2}), and third semicircle at low frequency region (0.2 Hz to 0.75 Hz) attributed to the Warburg impedance of tri-iodide ions present in the electrolyte [267, 268]. The series resistance (R_{series}) of the circuit connections is responsible for the high frequency intercept on the real axis. The value of R_{series}, R_{ct1}, and R_{ct2} depends on the sheet resistance of the electrodes that are used in the device. The life time of the electron can be calculated using equation 2.16.

$$\tau_e = \frac{1}{2\pi f_{max}} \tag{2.16}$$

In this thesis, EIS analysis of the fabricated DSSC devices was carried out using PARSTAT MC (Model: PMC–200) multichannel potentiostat instrument, and data analysis was done using ZSimpwin software.

Chapter 3

Sputter Deposition of Highly Flexible Metallic Au/Cu/Ag/Pt/Au Multi-layer Electrode

To explore for the alternatives for plausible metallic multi-layer, it is intended to deposit metals like Au, Cu, Ag, and Pt in a multi-layered alternative architecture. This chapter is focused on the optimization of sputtering parameters and thickness of each individual metal layer using XRR technique towards deposition of ultrathin Au/Cu/Ag/Pt/Au multi-layer on a PET substrate with a thickness of total 10 nm (each layer 2 nm). Exploration of its surface, optical and electrical transport properties using various characterization techniques are performed. Comparison of its mechanical stability of sheet resistance with commercial ITO for several thousand bending and twisting cycles is demonstrated. Demonstration of its applicability as a working electrode in devices like ACEL and PENG are also presented and discussed..

3.1 Introduction

Pliable transparent conducting electrodes (TCEs) form the foundation of current day optoelectronic gadgets like building integrated photovoltaics [269], organic LED-based displays [122,270], bendable photo-detectors [271], foldaway displays [272], electrochromic [273], piezoelectric power devices [274], pliable electro/tribo-luminescent device components etc. [275–279]. These devices typically utilize indium tin oxide (ITO) as TCE, owing to its superior visible light transparency (> 85 %) and low sheet resistance (10 $\Omega/\square$) [280]. Nevertheless, the continuous utilization of ITO over the years and the expanding need for its usage has resulted in deficiency of indium, eventually critically affecting the demand vs supply gap due to increased usage of display/interactive gadgets in various sectors. The brittleness of ITO, in combination with the need for higher processing temperature (> 400 °C) seriously affects the electrical properties [281], limiting its usage for bendable and stretchable gadgets. These shortcomings of ITO electrodes have accelerated the investigation of alternative materials to ITO for fulfilling requirements of the rapidly growing display and energy

sectors. Amongst alternative TCEs, metallic nanowires [215], metal meshes [216] etc. are explored as promising supplement for ITO, owing to their high availability and supply, high mechanical robustness, and significant transparent conducting aspects. As a fundamental aspect, unlike ITOs, metallic alternatives do not exhibit higher transparency due to absence of band gap. Whereas, they possess lower sheet resistance to match conventional ITO, and therefore one cannot expect these alternatives to completely replace ITO, but certainly they serve as a supplement with significant scope, depending on the type of application.

Interesting micro-structured networks of metal nanowires and grid-like structures have been put forth as an alternative for TCEs to circumvent these limitations [217]. However, the main hinderances in mass production are inherent optical haze, diffraction of light, and electrical shorts due to uneven surface features, which are undesirable for display-based requirements [218]. Among the existing alternatives, pliable ultrathin metallic multi-layer is a promising contestant viable for optoelectronic devices due to its simple and cost-effectiveness, good mechanical robustness, appreciable transparency and high electrically conducting aspects. These ultrathin layers are deposited in a multi-layer design such that the synergistic aspect of the constituent metallic components can improve the collective transmittance into a broader visible spectral domain and electrical conductivity [156]. In an individual layer, highest transmittance from respective metal components is more confined to particular wavelengths [156]. Ultrathin layers (thickness $<$ skin depth) of the noble metals (Ag, Pt and Au) are less sensitive and hold appreciable transparency in the visible range [219]. For the sake of attributing wider-range transparency within the visible wavelength domain, sandwiching of these noble metals is carried out into a multi-layer design (Fig. 3.2 (a)) and investigated, thereby serving a motivation for this chapter.

The thickness of the individual noble metal layer depends on its skin depth [282] which constitutes the selection of element for TCE multi-layers architecture. Usually, transmittance is lower for thicker samples and higher for thinner samples. Therefore, the thickness of individual metallic layer is critical while crafting a TCE. Apart from this, the key benefit of exploring an ultrathin metal layer is its outstanding mechanical stability, low cost (due to meager material utility), compactness, large area coating process via well optimized PVD methods, and compatibility with different types of substrates. Thin metallic bilayers/multi-layers can be designed to serve as TCE, for example, thermally evaporated ultrathin metallic tri-layer TCE in Au/Ag /Au (2/4/2 nm) architecture has been reported [265]. In this thermally deposited tri-layer, maximum transmittance of 62 % (at 550 nm) is witnessed, implying a balance between optical transparency and electrical conductivity [265]. According to litera-

ture, a metallic film with a thickness of 9 nm Au and 6 nm Cr exhibits significant transmittance with only a slight increase in resistivity when compared to samples with higher Au metal thickness (17, 26, and 34 nm), but it also has a higher electrical resistance of 766 $k\Omega/\square$. However, concerning the metallic grid configuration with Au thickness values of 17, 26, and 34 nm, decrement in sheet-resistance is witnessed for higher metallic layer thickness with no significant variation in the transmittance, mostly owing to pinholes in the layers [283]. This type of network layers is not viable for a variety of optoelectronic gadgets, owing to uneven work function due to existence of pinholes. The choice of film coating technique adopted to make this architecture is a key factor in deciding its optoelectronic properties, and DC magnetron sputtering technique is most suitable due to its potential in yielding large-area fine quality films [284].

In thin metal layers, it becomes challenging to simultaneously optimize the electrical conductivity and optical transparency since thicker layer exhibits high conductivity, but is less transparent. The thickness inclusive of all the constituent layers and the metal skin depth of individual layers determine the combined electrical properties and transparency. In this regard, the theoretical framework by Deng et al., [265, 284] for estimating the Au/Cu/Ag/Pt/Au multi-layer's effective skin depth (δ_{eff}) at 500 nm is given by the equations below,

$$\delta_{eff} = \sum_{i=1}^{N+1} d_i,\ i = 1, 2, - - - - N, N+1 \tag{3.1}$$

where

$$d_i = \int_{\sum_{j=0}^{i} t_j}^{\sum_{j=0}^{i-1} t_j} \left[\frac{\left[\prod_{j=0}^{i-1} (1+\Gamma_i)\right]}{\left[\prod_{j=0}^{i} (e^{\gamma_j t_j} + \Gamma_j e^{-\gamma_j t_j})\right]} \left(e^{-\gamma_i \left(Z - \sum_{j=0}^{i-1} t_j\right)} + \Gamma e^{\gamma_i \left(Z - \sum_{j=0}^{i} t_j\right)} \right) \right] \tag{3.2}$$

Propagation constant

$$\gamma_i = (1+j)\sqrt{\frac{\omega \mu_i \sigma_i}{2}} \tag{3.3}$$

Reflection co-efficient,

$$\Gamma = \frac{n_1 - n_2}{n_1 + n_2} \tag{3.4}$$

where n_1 and n_2 are the corresponding index of refraction of the i^{th} and $(i+1)^{th}$ layers, t is the thickness of the metallic layer, μ is the permeability of the metallic layer, ω is angular frequency, and σ is electrical conductivity. The estimated value (after iteration) of δ_{eff} using equation 3.1 for the Au/Cu/Ag/Pt/Au multi-layer is 7.957 nm. The crucial parameters of metallic layers in bendable and wearable opto-

electronic gadgets are high visible radiation transmittance, low electrical resistance, and compatibility to mechanical variations like twisting, folding, and bending. This chapter investigates the applicability of noble metals like Pt, Ag, Cu and Au in a multi-layer design coated on a pliable PET sheet as a TCE. Pt metal has steady temperature coefficient of resistance and high chemical stability [285] and Au is a classical metal suitable for electrode system [286]. The constituent layer of 2 nm thickness (dependent on skin depth as calculated using relation 3.1) is sputter coated on a pliable PET sheet in Au/Cu/Ag/Pt/Au multi-layer design. To reduce surface and interface roughness, safeguard the Pt layer from being oxidized, and improve the conductivity of the layers, the Au metallic layer is deposited as both seed layer and top layer. The pliability and transparent conducting aspects of the coated multi-layer TCE are investigated and exemplified by implementing them in alternating current electroluminescent (ACEL) and piezoelectric nanogenerator (PENG) devices to prove the concept of its applicability in luminescent and energy harvesting devices.

3.2 Experimental details

3.2.1 Materials used

Highly flexible 35 μm thick poly-ethylene terephthalate (PET) sheet was employed as substrate to coat the multi-layers. An ultra-high vacuum LJ5 DC magnetron sputtering unit was utilized to coat the multi-layers using high purity Au, Ag, Cu and Pt metallic targets. To build the ZnO layer for the PENG device, zinc nitrate [$Zn(NO_3)_2$] and NaOH (AR grade) were purchased from Sigma Aldrich (USA), and 0.1 mm of aluminum foil thickness was procured from Special Metals Pvt. Ltd., India. The ZnS:Mn phosphor used in the fabrication of the ACEL device was obtained using $ZnCl_2$, $MnCl_2$, and NH_4OH (AR grade Sigma Aldrich, USA).

3.2.2 Coating of Au/Cu/Ag/Pt/Au metallic multi-layer

Before coating, the PET substrate was washed by employing isopropanol and dried using a jet of nitrogen gas to eliminate any remaining debris on the surface. The metallic multi-layer (Au/Cu/Ag/Pt/Au) was coated using a DC magnetron sputtering process under argon gas at a substrate temperature of 70 °C and an ultra-high vacuum of 6×10^{-8} Torr. The Au/Cu/Ag/Pt/Au multi-layer has a total thickness of 10 nm, with each constituent layer being 2 nm thick. Figure 3.1 displays the calibration parameters of the metal constituent layers acquired using X-ray reflectivity (XRR) (Rigaku Smart Lab multifunctional). Figure 3.1 (a-f) depicts the room temperature

X-ray reflection (XRR) curves of the Au, Pt, Cu, and Ag (thickness of 5 nm and 10 nm) individual layers. It is evident that there exist peaks with oscillations which are fitted using cumulative fitting procedure. Further, thickness of the layer is determined using the equation 2.9. Using a fixed power of 25 W and an operating pressure of 5 mTorr under Ar inert gas, the individual metal layers were sputter coated. It took 34 s to coat the Au layers (seed and capping) at 0.058 nm/s with 2 nm thickness. A 2 nm thick Pt layer was coated for 72 s at a rate of 0.028 nm/s, a 2 nm thick Cu layer was coated for 56 s at a rate of 0.036 nm/s, and a 2 nm thick Ag layer was coated for 40 s at a rate of 0.050 nm/s (Tables 3.1 and 3.2). The schematic illustration of the

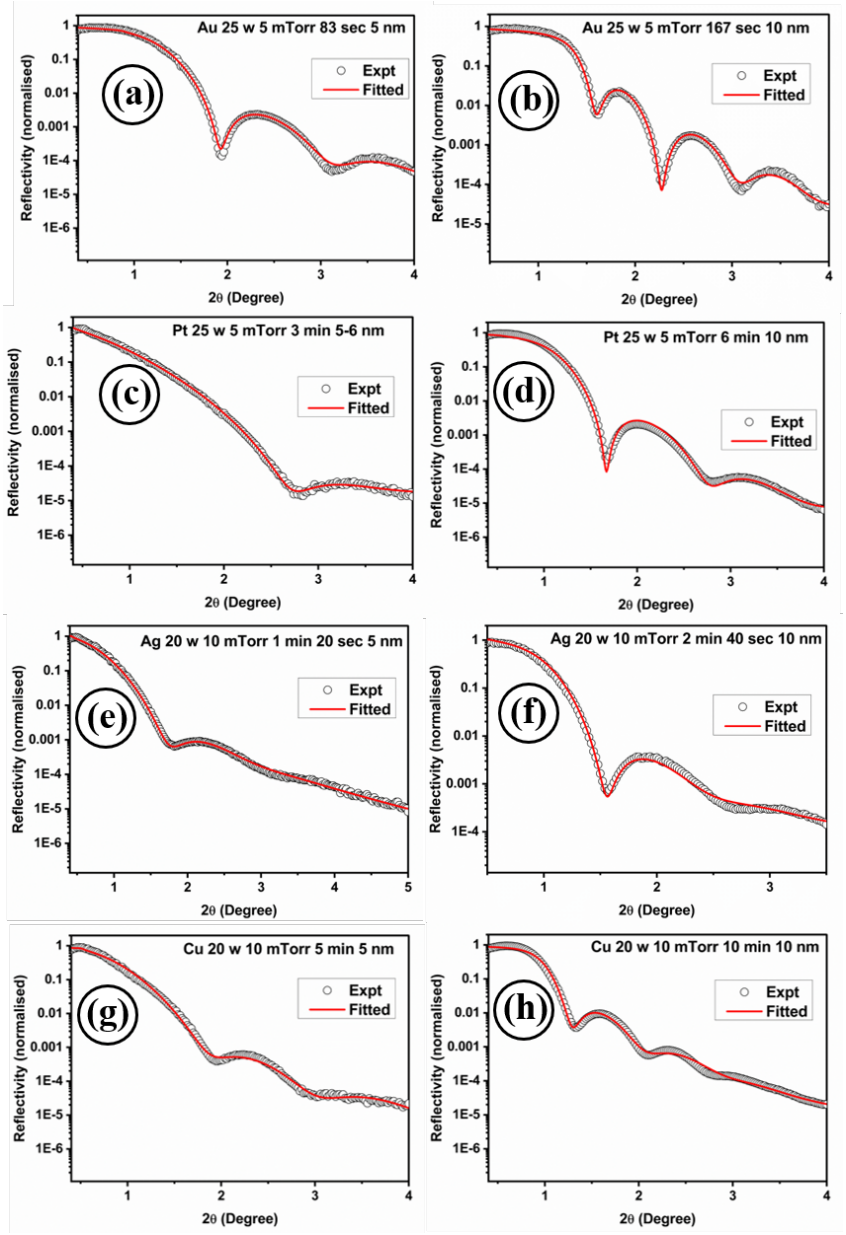

Figure 3.1: X-Ray reflectivity of Au film coated for 5 nm (a), 10 nm (b), Pt film coated for 5 nm (c), 10 nm (d), Ag film coated for 5 nm (e), 10 nm (f), Cu film coated for 5 nm (g), and 10 nm thickness (h).

Table 3.1: Thickness calibration parameters using X-ray reflectivity technique for the noble metals Au, Pt, Cu, and Ag.

Film	Sputtering power (W)	Argon pressure (mTorr)	Deposition time (s)	Film thickness (nm)	Deposition rate (nm/s)
Au	25	5	34	2	0.058
Pt	25	5	72	2	0.28
Cu	20	10	56	2	0.036
Ag	25	5	40	2	0.05

Table 3.2: DC Magnetron sputtering parameters for coating the noble metallic multi-layers.

Film	Deposition parameters	Thickness (nm)			Density (g/cc)	RMS Roughness (nm)
		Film	Oxides	Total		
Au	25 W 5 mTorr 83 s 5 nm	7.023	0	7.02	17.29	1.15
	25 W 5 mTorr 167 s 10 nm	10.94	0	10.94	19.3	1.15
Ag	20 W 10 mTorr 1 min 20 s 5 nm	6.42	0	6.42	7.25	1.54
	20 W 10 mTorr 2 min 40 s 10 nm	8.30	0	8.30	9.4	1.60
Pt	25 W 5 mTorr 3 min 5-6 nm	3.94	0	3.94	11.06	1.12
	25 W 5 mTorr 6 min 10 nm	7.89	0	7.89	12.58	1.23
Cu	20 W 10 mTorr 5 min 5 nm	3.77	2.80	6.57	8.02	1.14
	20 W 10 mTorr 10 min 10 nm	9.56	1.50	11.06	7.67	1.12

coated Au/Cu/Ag/Pt/Au multi-layer is shown in Figure 3.2 (a). The photograph of the multi-layer Au/Cu/Ag/Pt/Au on flexible PET sheet is shown in Figure 3.2 (b).

3.3 Results and discussion

3.3.1 Structural aspects from XRD

Figure 3.2 (c) shows the XRD patterns of uncoated PET and Au/Cu/Ag/Pt/Au coated PET, and both seem to be nearly the same. However, the major peak around 26.19° belongs to plain PET and is marginally shifted to 26.17° upon coating of Au/Cu/Ag/Pt/Au multi-layer. This observation indicates the presence of the Au/Cu/Ag/Pt/Au multi-layer on the plain PET sheet. The multi-layer is just 10 nm thick overall, and since the coating is done at 70 °C, the layers might have marginally crystallized with presence of smaller crystallites and very low density of grain boundaries; therefore, no other distinctive peaks of Au, Ag, Cu, or Pt are seen.

3.3.2 Surface morphology

The surface features of sputter-coated Au/Cu/Ag/Pt/Au multi-layer over PET sheet are studied through atomic force microscopy (AFM) and non-contact optical profiler measurements. It is difficult to perform AFM for the pliable Au/Cu/Ag/Pt/Au sputtered over PET sheet since the cantilever tip of the AFM is very fragile. Hence, the multi-layer film is sputter-coated parallelly over glass slide and PET sheet. Metallic layers above 100 nm thickness are not appropriate for optical components which need substantially higher transmittance and a smooth surface [136]. The 3D AFM image (Fig. 3.2 (d)) of the multi-layer over glass slide indicates that the surface is free from cracks and is closely packed. From Fig. 3.2 (d), the Au/Cu/Ag/Pt/Au multi-layer shows needle-like features on the surface with minimal RMS surface roughness of 0.645 nm. The non-contact optical profiler is used to explore the topology of the flexible Au/Cu/Ag/Pt/Au multi-layer over PET sheet. The 3D images (Fig. 3.2 (e)) vividly show a smooth surface with notably fewer spike-like aspects at that resolution on a relatively larger 1 mm x 1 mm region, hinting at its viability for large-area device capabilities. In general, the probable growth mode [287] in sputtering technique is Frank-van der Merwe (layer-by-layer) [288] which takes place when the smallest nuclei grow in two dimensions, leading to formation of disk-like features. In layer-by-layer growth mode, the coated ad-atoms are more firmly attached to the substrate than

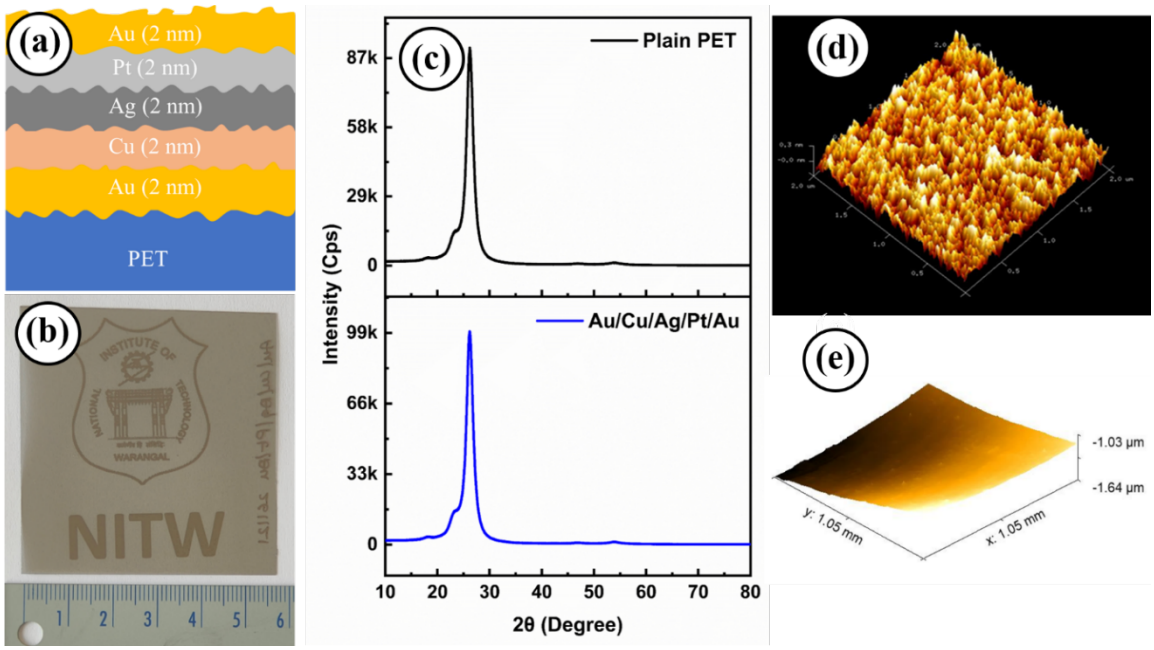

Figure 3.2: (a) Schematics of ultrathin Au/Cu/Ag/Pt/Au multi-layer structure, (b) photograph of the coated multi-layer, implying its transparent nature, (c) XRD patterns of bare and Au/Cu/Ag/Pt/Au multi-layer coated PET, (d) 3D AFM and (e) optical profiler images of the metallic multi-layer

to the ad-atom themselves, and each layer is progressively weakly bonded with the previous layer, and it extends until the bulk bonding strength is attained [289]. All these aspects result in a film with low RMS surface roughness of 0.645 nm.

3.3.3 Contact angle measurements

The contact angle (CA) measurement was done on the ultrathin Au/Cu/Ag/Pt/Au sputter-deposited pliable multi-layer employing D.I. water as a probe liquid. The CA provides information about the deposited film's surface wettability. In 1805, Young developed a relation (eq. 2.10) by considering all interfacial energies, namely solid-liquid boundary (γ_{sl}), liquid-vapor boundary (γ_{lv}) and solid-vapor boundary (γ_{sv}) energies as mentioned in section 2.4.7 [128]. In general, factors like surface tension of the probing liquid, surface roughness of the film, surface energy, functional groups and contaminants present over the film's surface, and film porosity have a significant impact on surface wettability [290]. The characteristics of de-ionized water droplets assessed on bare PET and sputter-coated Au/Cu/Ag/Pt/Au PET are presented in Fig. 3.3 (a) and (b), respectively. The contact angle of the bare PET sheet is 73.85°, indicating the substrate's hydrophilic character. After being coated with the Au/Cu/Ag/Pt/Au multi-layer, the contact angle increases to 99.83°, indicating the transition from hydrophilic to hydrophobic nature. The change in functional groups on the surface of the deposited multi-layer and the modification in surface roughness (0.645 nm) may be the reasons for the increased contact angle. The coated multi-layer's hydrophobic nature aids in the development of low-wetting characteristics, which may be beneficial for appropriate optoelectronic components with self-cleaning requirements.

3.3.4 Optical properties

Figure 3.3 (c) displays the transmittance spectra of commercially available pliable ITO film and the Au/Cu/Ag/Pt/Au sputter-deposited multi-layer in the 350–1000 nm range. The deposited multi-layer shows higher transmittance of 44 % at 500 nm, while the pliable commercial ITO shows a maximum transmittance of 58 % at 550 nm. In comparison to the coated Au/Cu/Ag/Pt/Au multi-layer, the commercial ITO demonstrates better transmittance in the visible range; nevertheless, the Au/Cu/Ag/Pt/Au multi-layer exhibits a nearly flat trend over the spectral range of 350–1000 nm. The observed transmittance is lower than the previously reported transmittance (62 %) of Au/Ag/Au tri-layer [265] coated by thermal evaporation technique, and better than the transmittance observed for Cu/Ag/Au tri-layer film (40 %) [291]. Alexander et al., showed that a 2 nm thick Au film coated over a glass

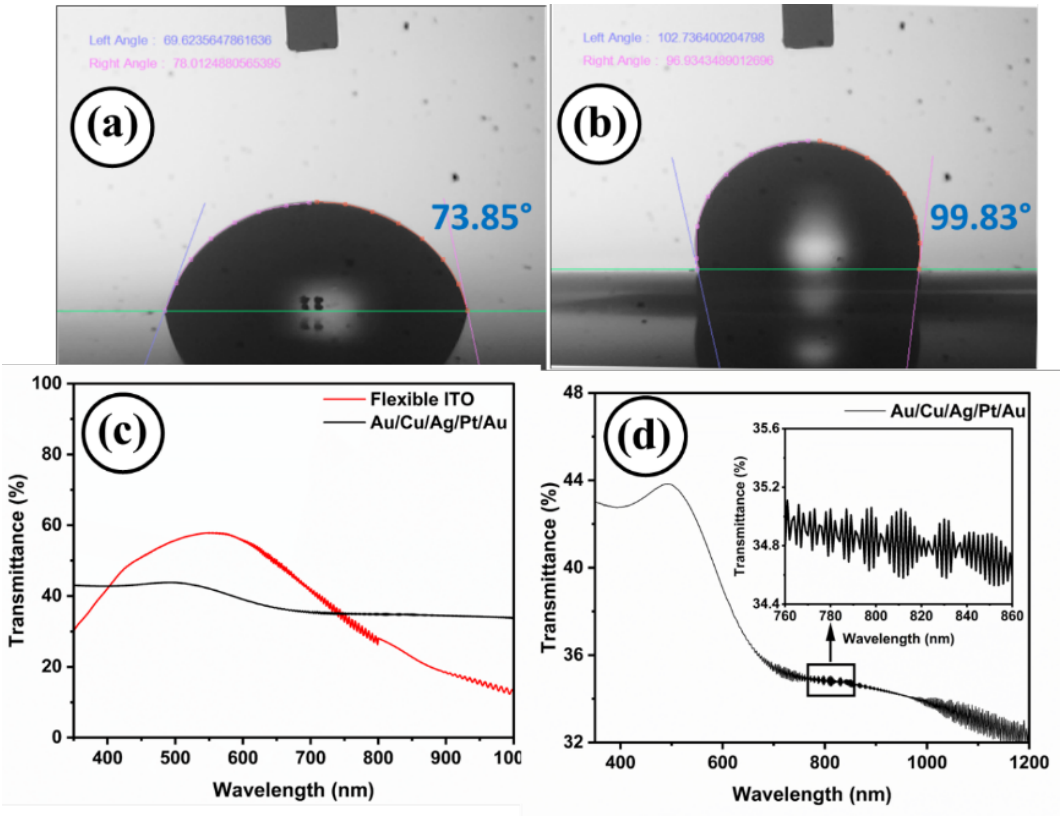

Figure 3.3: Contact angle images of water drop on the surface of (a) bare PET and (b) Au/Cu/Ag/Pt/Au sputter-coated PET. (c) Transmittance spectra of Au/Cu/Ag/Pt/Au-coated PET in comparison with flexible ITO film, and (d) expanded Au/Cu/Ag/Pt/Au multi-layer transmittance spectra (inset is the interference feature of elemental layer components in the multi-layer)

slide having a transparency of 70 % at 500 nm [147, 156]. The inclusion of extra 2 nm of Cu, 2 nm of Ag, 2 nm of Pt, and 2 nm of Au yielding Au/Cu/Ag/Pt/Au multi-layer, results in reduced transmittance. The flexible Au/Cu/Ag/Pt/Au multi-layer's optical transparency, on the other hand, displays a steady trend from the UV to near-IR region with values ranging from 32 % to 44 %. (Fig. 3.3 (d)). The near-flat trend in the entire region is mostly due to inclusion of four different metallic layers (Cu, Au, Pt and Ag) in the multi-layer architecture, revealing considerable variation in transparency compared to the bendable ITO. The transmittance peak around 500 nm with a value of 44 % is attributable to the presence of Au layer in the multi-layer stack [156]. The interference behavior around 800 nm due to the layered architecture with vivid and defined interface is shown in the inset of Fig. 3.3 (d). In the near-IR and far-IR regions, ITOs and FTOs exhibit low transmittance, which is well-documented in the literature and is generally brought on by plasmon resonance or intense absorption of free carriers [292–295]. Since there is a free-carrier plasmon edge, in the near-IR region, the transparency of the Au/Cu/Ag/Pt/Au multi-layer is more than that of ITO [295]. Apart from this, the transmittance of a metallic

multi-layer is also based on its percolation threshold limit [296]. A film forms islands when its thickness is below the percolation limit, and as thickness increases over the limit, continuous layer creation occurs, which reduces transparency [296].

3.3.5 Electrical properties

Hall effect measurement at room temperature was performed to determine electrical transport parameters of the Au/Cu/Ag/Pt/Au multi-layer thin film. All the transport parameters like sheet resistance (R_s), resistivity (ρ), free carrier concentration (n), and mobility (μ) of Au/Cu/Ag/Pt/Au multi-layer and commercially available ITO are given in Table 3.3. The layer typically creates islands at lower thicknesses, which causes discontinuous growth and high electrical resistance. The individual metal clusters create a continuous sheet when the film thickness is above the percolation threshold limit, improving the conductivity of metal layers [297]. In the multi-layer stack sample, 2 nm Au is coated as seed layer, 2 nm of Cu, 2 nm of Ag, 2 nm of Pt layer, followed by Au layer of 2 nm on the top as protective layer to prevent oxidation from the environment and for improved chemical robustness and surface work function. The coated Au/Cu/Ag/Pt/Au multi-layer exhibits 60 $\Omega/\square$ sheet resistance and resistivity of 6.02×10^{-5} Ωcm, which is slightly more than that of the commercially available bendable ITO electrode. The electrical resistivity of Au/Cu/Ag/Pt/Au multi-layer is significantly influenced by the free carriers scattered at the interfaces and grain boundaries [298]. However, the free carrier concentration of the coated Au/Cu/Ag/Pt/Au multi-layer is slightly better than the value for ITO (Table 3.3). Carrier mobility of the coated multi-layer is lower (2.02 $cm^2V^{-1}s^{-1}$) than that of ITO (10.18 $cm^2V^{-1}s^{-1}$), which is mainly because of the carrier scattering phenomenon that takes place due to phonon and grain boundary scattering, and free carrier confinement at the interfaces [299]. The Au/Cu/Ag/Pt/Au multi-layer has less mobility because of frequent collisions caused by the abundant free carriers, which results in a smaller mean free path. Apart from this, the surface morphology also influences the carrier mobility in the multi-layer.

3.3.6 Kelvin probe measurement for surface work function

The estimation of surface work function (Φ) of a TCE is essential for the operation of every optoelectronic device. The kelvin probe (KP) measurements are carried out under ambient conditions with gold plated tip (2 mm) attached to the system. Initially the tip is calibrated with a standard Au coated Al substrate (work function = 5.1 eV) (as per equations 2.13 and 2.14). The contact potential difference of

Table 3.3: Optical and electrical transport parameters of pliable Au/Cu/Ag/Pt/Au multi-layer in comparison with flexible ITO and existing literature.

Sample code	Carrier concentration n (cm^{-3})	Sheet resistance R_s ($\Omega/\square$)	Resistivity ρ (Ωcm)	Mobility μ ($cm^2V^{-1}s^{-1}$)	Transmittance T (%)	FoM (Ω^{-1})
ITO [265]	1.29×10^{22}	5	4.73×10^{-5}	10.18	55 (500 nm)	5.06×10^{-4}
$Cu/Ag/Au^a$ [291]	1.15×10^{23}	7.7	9.70×10^{-6}	5.58	40 (500 nm)	1.39×10^{-5}
$Au/Ag/Au^a$ [265]	2.48×10^{23}	10.42	7.46×10^{-6}	3.4	62 (550 nm)	5.20×10^{-4}
$Au/Cu/Ag/Pt/Au^b$	5.11×10^{22}	60.23	6.02×10^{-5}	2.02	44 (500 nm)	2.89×10^{-5}
a: thermal evaporation, b: D.C. magnetron sputtering (this work)						

Au/Cu/Ag/Pt/Au layer sample and tip were measured at different spot to estimate the work function of the sample (as per equation 2.15) [300]. The measurement of contact potential difference (V_{CPD}) between the Au layer and the tip is first carried out to standardize the Au tip with an Au-coated Al reference electrode (work function = 5.1 eV) [300]. The value of Φ_{tip} calculated (from eq. 2.14) is found to be 4.87 eV. The Au/Cu/Ag/Pt/Au multi-layer is then mounted, and V_{CPD} between the film and the tip is estimated applying the formula as per the equation 2.15 [300]. The calculated Φ value of the sputter-coated Au/Cu/Ag/Pt/Au multi-layer is 5.01 eV. The individual Φ values of Cu, Pt, Au, and Ag single metal layers are reported in the range 4.56-4.90, 5.53-5.91, 5.12-5.93, and 4.1-4.53 eV, respectively [301, 302]. The Φ value of ITO is reported in the range of 4.3-4.4 eV [303–306]. Even though the estimated Φ value of Au/Cu/Ag/Pt/Au pliable multi-layer is greater than that of ITO, it may be utilized for appropriate requirements, wherever this range is needed. Nonetheless, several display and energy devices need at least one TCE with a lower Φ value, which improves either the collection/injection of carriers from the lowest unoccupied molecular orbital (LUMO) or conduction band minima (CBM) of a particular organic/inorganic semiconducting material.

3.3.7 Mechanical stability of the sheet resistance by bending-twisting measurements

The advanced, bendable, compact and wearable gadgets needs a variety of highly robust pliable TCEs suitable for a greater number of twisting and bending cycles, without considerable variation in sheet resistance, to prolong their efficient performance for longer lifetime. Hence, it is essential to explore sheet resistance stability of the pliable Au/Cu/Ag/Pt/Au multi-layer TCE for several bending-twisting cycles, which implies the layer sturdiness in resisting to external strain and stress. The mechanical stability of sheet resistance was executed for commercially available ITO along with pliable Au/Cu/Ag/Pt/Au multi-layer using an apparatus developed indigenously with

an ATmega328 microcontroller [291] for large number of bending-twisting series. The multi-layer samples placed in bent and twisted geometries, respectively, are shown in the insets of Fig. 3.4 (a) and (b). The speed at which the bending-twisting sequences were carried out was 20 cycles of bending and 14 cycles of twisting per minute. For 5,000 bending and twisting cycles, the total time required was 250 and 350 min, respectively. The sputter-coated Au/Cu/Ag/Pt/Au multi-layer underwent a total of 50,000 bending and twisting cycles, each with a step size of 5000 cycles (Fig. 3.4 (a) and (b)). Due to lower stability of pliable ITO, bending-twisting cycles were performed at the same rate not exceeding 2,500 for the sheet resistance measured at an interval of 500 cycles.

The strain developed in the thin film mainly depends on the thickness of the substrate (d_s), bending radius (R), thickness of the metal layer (d_m), and Young's

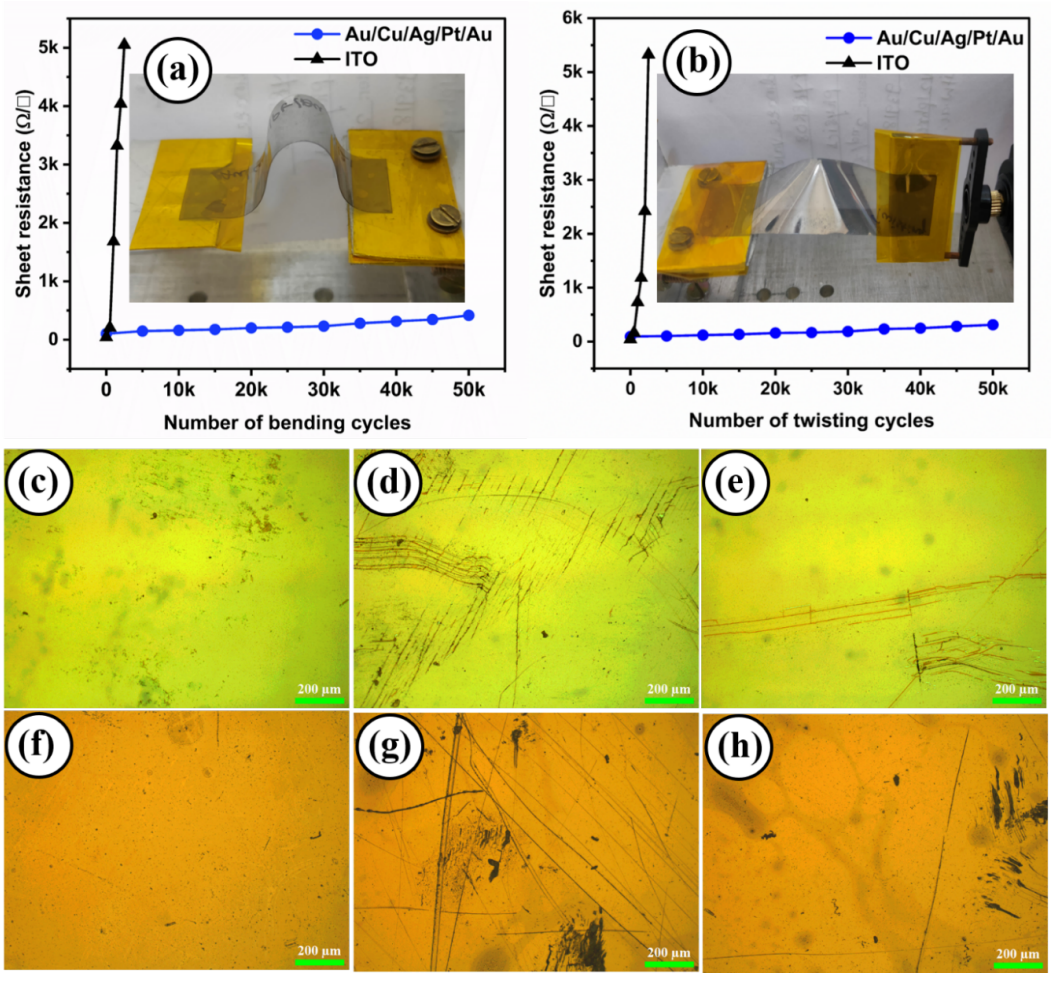

Figure 3.4: Comparing Au/Cu/Ag/Pt/Au multi-layer's sheet resistance stability to ITO for (a) bending and (b) twisting positions (Insets are the pictures of the respective positions). The bendable ITO film shown as microscopic images in (c) pristine condition, (d) after 2.5k bending cycles, and (e) after 2.5k twisting cycles. The Au/Cu/Ag/Pt/Au multi-layer deposited on PET is shown in (f) pristine condition, (g) after 50k bending cycles, and (h) after 50k twisting cycles

modulus of substrate (γ_s) and metal (γ_m) [307]. The estimation of strain in the deposited metal layer is done using the equation given below [307],

$$S = \left(\frac{d_m + d_s}{2R}\right)\left(\frac{1 + 2\eta + \chi\eta}{(1+\eta)(1+\chi\eta)}\right) \tag{3.5}$$

where η is the thickness ratio of metallic layer and substrate, and χ is the Young's modulus ratio of the coated layer and substrate. According to equation 3.5, the bending strain is directly proportional to the film thickness; as a result, if the film thickness is reduced, the layer's bending strain is decreased, thereby increasing the coated metal layer's bendability and stability. Thin metal layers are highly ductile and durable for many bending-twisting cycles. High durability of a bendable OLED constructed from Ag metal with an anode thickness of 80 nm (bending radius of 30 μm) was demonstrated by Yin et al., without sacrificing the device's performance [308]. In contrast to commercially available ITO, researchers have demonstrated a polymer-metal hybrid with high stability up to thousand bending cycles, and beyond which they noticed a decline in the performance of the device using ITO electrode in contrast to the device fabricated using Ag metal electrode which was showing almost no detriment in performance [309].

With a thickness of 10 nm, the flexible Au/Cu/Ag/Pt/Au multi-layer demonstrates exceptional mechanical durability up to 50,000 bending-twisting sequences. As shown in Figs. 3.4 (a) and (b), the Au/Cu/Ag/Pt/Au multi-layer has a hundred times greater pliability than that of the commercially available ITO. The pliable ITO electrode is not stable over 2,500 bending-twisting sequences as depicted in Fig. 3.4 (a) and (b), resulting in deterioration due to its fragile nature. The witnessed high sturdiness of the Au/Cu/Ag/Pt/Au multi-layer is mostly because of higher ductility of the constituent metal layers in comparison to that of the oxide TCEs, and due to lower layer thickness of the metals – Au, Cu, Pt and Ag. The sheet resistance of Au/Cu/Ag/Pt/Au multi-layer could not surpass more than 300 $\Omega/\square$ despite 50k bending-twisting sequences, while for flexible ITO, it exceeds more than 300 $\Omega/\square$ within a mere 500 bending-twisting sequences, and it rapidly shoots up to 5 $k\Omega/\square$ within 2,500 bending-twisting sequences (Fig. 3.4 (a) and (b)). Figure 3.4 (c-e) presents the images of optical microscopy for pristine ITO electrode and the one after 2,500 bending-twisting sequences where cracks due to rupture on the ITO electrode are seen vividly. They result in discontinuity over the electrode's surface lead to higher sheet resistance values. Whereas, for the sputter-coated Au/Cu/Ag/Pt/Au multi-layer, the surface images taken from optical microscope before and after 50,000 bending-twisting sequences (Fig. 3.4 (f-h)). Figure 3.4 (g) and (h) show only fewer

cracks even beyond 50,000 bending-twisting sequences.

Nevertheless, these minor cracks do not significantly influence the variation in sheet resistance of the Au/Cu/Ag/Pt/Au multi-layer. Apart from mechanical stability, it is essential to explore the adherence aspect of the coated Au/Cu/Ag/Pt/Au multi-layer by putting it through the tape test. On the multi-layer's film, a scotch tape is fixed firmly and manually removed, and this is performed for 100 trials at the same location and microscopic images were obtained at an interval of every ten tests. Examination of microscopic images at the location where tape test was carried out in comparison with the pristine multi-layer (Fig. 3.5 (a-k)) was intact without peeling off and any

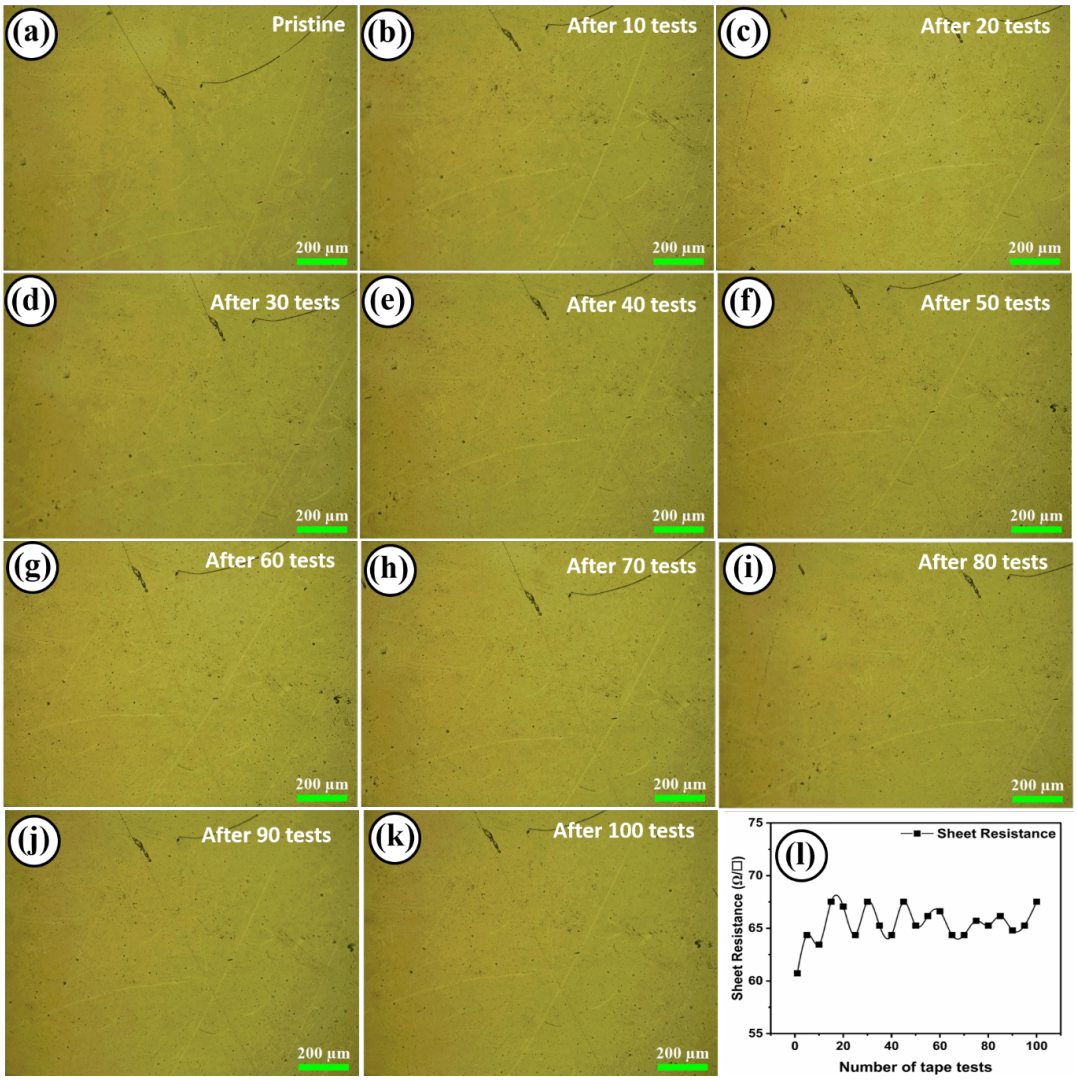

Figure 3.5: Tape tests performed to assess the quality of ultra-thin multi-layer film for a total of 100 trials with the observance of film's surface for inspecting adherence and measurement of sheet resistance stability. Optical microscopic images at the location where tape test was carried out in comparison with the (a) pristine multi-layer, and (b–k) at an interval of ten tests, and (l) Variation of sheet resistance of the pristine multi-layer with tape tests at the prescribed intervals show significant stability with only a marginal variation

significant visible signs of scratch. The variations in sheet resistance measured by linear four probe technique at the same intervals indicate only a marginal change, the pristine film having 60.72 Ω/□ increased to 67.52 Ω/□ after the 100^{th} test (Fig. 3.5 l) amounting to an increase of 11.2% from its initial sheet resistance. Therefore, from the tape test followed by optical microscope and sheet resistance measurements, the multi-layer is observed to indicate good adherence and sheet resistance stability. All these aspects indicate that the Au/Cu/Ag/Pt/Au multi-layer is a potential and electrically robust contestant for implementation in relevant bendable optoelectronic devices, leading to long-term stability.

3.4 Applications

3.4.1 Piezoelectric nanogenerator device

Al foil and an ultrathin, bendable Au/Cu/Ag/Pt/Au multi-layer coated PET were used as the top and base electrodes of a PENG device, respectively. ZnO active layer was grown over “Al” foil by chemical bath coating technique. Taking 0.5 g of $Zn(NO_3)_2$ and 0.3 g of NaOH diluted in deionized water, 160 ml of an aqueous solution was prepared. After being rinsed with acetone and placed in the solution, the "Al" foil was annealed for 4 h at 80 °C in a vacuum oven (10^{-3} bar) to encourage the formation of ZnO nanostructures on top of the foil. To remove the ZnO nanoparticles that are loosely attached, the ZnO grown over "Al" foil was rinsed in D.I. water. By tightly binding the 'Al' foil consisting of ZnO nanostructures to the stretchable ultrathin Au/Cu/Ag/Pt/Au layer with Kapton tape spacer, electrode short circuit is prevented. When finger tapping force is applied on the PENG device, a digital storage oscilloscope (DSO) (Tektronix-TBS 1102) connected to a computer picks up the piezo signal output. The polarity-switching experiments were also conducted by interchanging the connections of the electrodes.

The ZnO nanostructures-grown over Al foil shows flower petal-like morphology and is depicted in Fig. 3.6 (a). Figure 3.6 (b) displays the elemental composition of the synthesized ZnO along with the energy dispersive X-ray data. The PENG device is schematically represented in Fig. 3.6 (c). The flexible top Au/Cu/Ag/Pt/Au multi-layer electrode and the underlying 'Al' foil electrode are both clipped to a digital signal oscilloscope to assess the PENG device open-circuit voltage. The base "Al" electrode is clipped to the oscilloscope's negative terminal, and the top Au/Cu/Ag/Pt/Au multi-layer electrode is clipped to the oscilloscope's positive terminal. A mechanical force is applied across the ZnO nanostructures when the PENG device is slightly

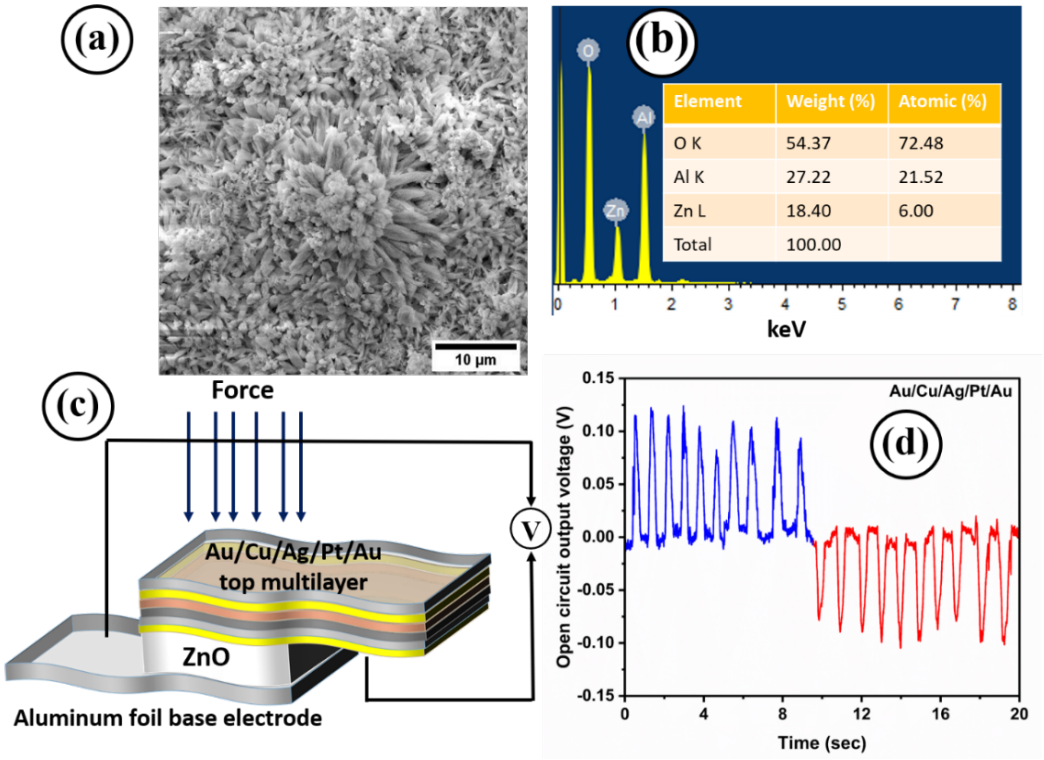

Figure 3.6: SEM image of (a) ZnO, (b) EDAX displaying weight and atomic percentage of ZnO grown on top of 'Al' foil, (c) design of a PENG device with a flexible Au/Cu/Ag/Pt/Au multi-layer as the top electrode, and (d) variation of open circuit voltage of the device with time.

tapped with a finger, yielding piezoelectric output voltage. The oscilloscope captures the output voltage produced by continuous finger tapping. The polarity-switching test which involves switching the connections can also be used to create the PENG device's output voltage. The polarity-switching test verifies that the output voltage is produced by tapping the PENG device with a finger rather than random instrument noise. In both forward and reverse bias, the highest output voltage generated for every pressing of the PENG device is 110 mV, (Fig. 3.6 (d)). The output voltage obtained is close to a value as that of commercially available ITO/PET as well as copper electrode-based ZnO nanogenerators published earlier [310, 311]. The applicability of Au/Cu/Ag/Pt/Au multi-layer as a top electrode leads to a device which is highly compact and pliable. Additionally, the top electrode's transmittance offers an additional degree of freedom that could be helpful to stimulate unique functionality by way of interaction with the incident photons.

3.4.2 Flexible alternating current electroluminescent device

Alkaline-produced ZnS:Mn nanoparticles that emit orange light were employed as phosphor [312]. The ammonia complex created when $ZnCl_2$ and NH_4OH reacts chem-

ically was then exposed to H_2S gas bubbles to produce the luminous ZnS precipitate. The next step was to combine $MnCl_2$, a soluble manganese dichloride salt, with a ppm concentration of ZnS precipitate before calcining it at 120 °C for five hours. The resultant precursor was extensively pulverized in a mortar and pestle before being sintered for 43 h at 950 °C in a sulphur gas environment to produce ZnS:Mn (0.01wt.% Mn) phosphor, which acts as a functional component in the ACEL device. To create a smooth ZnS:Mn paste, the produced ZnS:Mn phosphor was homogeneously disseminated in a dielectric matrix ($\epsilon_r = 5$). Two pieces of Au/Cu/Ag/Pt/Au multi-layers were employed as the bottom and top electrodes, respectively, and a thin layer of orange light emissive ZnS:Mn phosphor paste was sandwiched between them [15,313–315], and utilized to make the ACEL device. The base electrode's center was carved out into a rectangular pit, and double-sided transparent spacer tape was used to adhere it. The doctor blade approach was then used to apply the ZnS:Mn phosphor paste to the rectangular pit at the base of the Au/Cu/Ag/Pt/Au pliable electrode [15]. Double-sided tape plastic spacer was used to prevent electrical short circuit with the underlayer. Another portion of the Au/Cu/Ag/Pt/Au ultrathin sample was placed against the emissive phosphor layer as the top electrode. The top and bottom TCE electrodes were attached using copper tape that was double-side-bonded to allow clipping to the power source without piercing the flexible electrodes. The constructed ACEL device was powered up by a low-cost, indigenously developed power supply operated at a frequency of 5 kHz. Using a variable potentiometer, the input source voltage has been adjusted between 12-300 V_{AC} and the electroluminescent emission (EL) spectrum is measured using a fluorescence spectrophotometer (Hitachi, model: F-2710).

The flexible Au/Cu/Ag/Pt/Au multi-layer is used as the top and base electrodes of a bendable ACEL device. The primary benefit of such devices is their straightforward construction process, which may be completed fully in ambient conditions [316]. This enables their utilization to be increased in large-area displays, even using straightforward and inexpensive methods like drop casting or doctor blading. The ability of an ACEL device to be coated as an ultra-thin design with improved bendability and a consistent emission throughout the full surface area, benefiting for wider viewing angles, is one of its important features [317]. Figure 3.7 (a) shows the bendable electroluminescent device design. Figure 3.7 (b) shows the photograph of the constructed bendable ACEL device utilizing an Au/Cu/Ag/Pt/Au multi-layer and ZnS:Mn as the TCE and electroluminescent phosphor respectively. The detailed operation of the ACEL device is explained as follows: upon application of AC voltage between the top and bottom electrodes, the phosphor material's luminescence centers are excited,

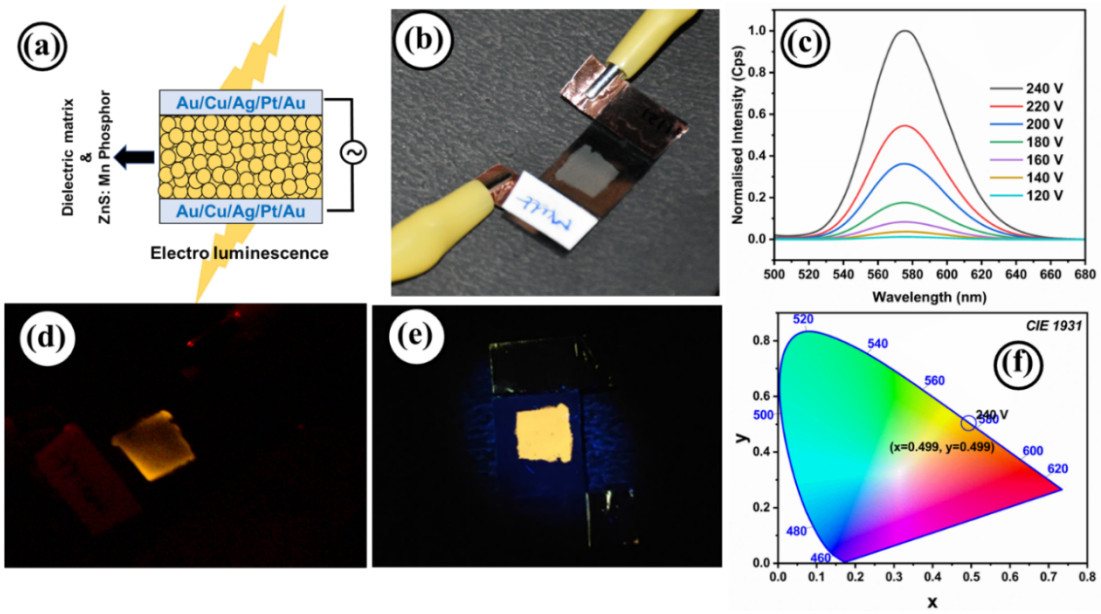

Figure 3.7: (a) The design of an ACEL device with Au/Cu/Ag/Pt/Au multi-layers as the top and base electrodes, (b) photograph of the device utilizing these pliable electrodes, (c) electroluminescence emission spectrum for varying applied voltage, (d) device response to 240 V_{AC}, (e) a potential-free glow in the presence of 365 nm UV light irradiation, and (f) the CIE chromaticity diagram of the orange emission for an applied voltage of 240 V_{AC}.

which causes photons to be released from the device. There are four steps that make up the entire process: Carrier injection, carrier transport, ionization of the luminescence centers due to impact, and carrier de-excitation through the phenomenon of radiative recombination via photon emission [317]. The Au/Cu/Ag/Pt/Au multi-layer electrodes used in the ACEL device assembly generate orange-colored emission in the 590-610 nm wavelength region (Fig. 3.7 (c)) [199, 318]. At low applied frequencies, luminescence emission initially flickers before stabilizing at higher applied frequencies. From the EL spectra (Fig. 3.7 (c)), as the applied voltage increases, the intensity of the orange emission rises to maximum for 240 V_{AC}. The threshold value of 120 V_{AC} is where the orange emission first appears. Figure 3.7 (d) shows the emission from the device at 240 V, which matches with the earlier reports for devices comprising of 'Al' and ITO as base and top electrodes, respectively [199].

Furthermore, as shown in Fig. 3.7 (e), the device is also evaluated using 365 nm UV light without any applied voltage. CIE chromaticity diagram of EL emission at 240 V_{AC} shown in Fig. 3.7 (f). According to published articles, the bottom electrode in ACEL devices is frequently seen to be important for innovation, and in certain instances, it consists of thicker opaque metallic layers with strong conductivity. Since the bendable ACEL device may produce light through both the top and base electrodes instead of the traditional design which only permits light emission from one

side, it is encouraging that both the top and base multi-layers in this case are transparent, conducting, and flexible. The sputter-coated Au/Cu/Ag/Pt/Au multi-layer appears to have high electrical conductivity and noticeable transparency based on the performance of the PENG and ACEL devices. This suggests that the multi-layer can potentially supplement flexible TCE for a variety of applications against external forces or applied potential. The bendability and sturdiness of the multi-layer electrode makes it appropriate for longer duration of functioning in optoelectronic devices, making it suitable for practical applications.

3.5 Conclusion

Pliable Au/Cu/Ag/Pt/Au multi-layer of total thickness 10 nm was sputter-coated on PET substrate. Au/Cu/Ag/Pt/Au multi-layer presents higher transmittance of 44 % at 500 nm and a uniform trend in the measured spectral region with transmittance ranging between 32 % and 44 %, implying its usage in UV-visible and near-IR regions suitable for bendable energy-harvesting applications. The multi-layer has low sheet resistance of 60 $\Omega/\square$, resistivity of 6.02×10^{-5} Ωcm, and surface work function of 5.01 eV. In addition to the considerable optoelectronic parameters that have been observed, the multi-layer exhibits increased mechanical strength of 50,000 bending-twisting sequences, which is significantly superior compared to commercial ITO, within the examined range. The commercially available ITO is stable only for a mere 500 bending-twisting sequences. The coated pliable Au/Cu/Ag/Pt/Au multi-layer is exemplified as a viable electrode for PENG and ACEL optoelectronic devices. The PENG device yields about 110 mV when force is applied by pressing with fingers. The ACEL device begins emitting orange light at 120 V_{AC}, and the brightness increases up to 240 V_{AC} with further increase in voltage. Both the exemplified devices indicate the sustainability of sputter-coated pliable Au/Cu/Ag/Pt/Au multi-layer as a viable electrode system for applicability in several bendable optoelectronic devices.

Although, the performance of the Au/Cu/Ag/Pt/Au multi-layer in PENG and ACEL devices are promising, it is necessary to further improve the optical transmittance by simplifying the multi-layer architecture which are presented in the following chapter.

Chapter 4

Sputter Deposition of Highly Flexible and Mechanically Stable Ultra-thin Metallic Au/Pt/Au Tri-layer TCEs

In this chapter, as a continuation of previous chapter on Au/Cu/Ag/Pt/Au multilayer electrode which has shown good electrical conductivity, but lower transmittance of 44 % (at 500 nm). Therefore, to increase its transmittance, the total thickness of the ultrathin multi-layer is decreased further by eliminating the Cu and Ag layers. Here, the ultrathin Au/Pt/Au tri-layer is deposited and explored for its optical, electrical, and mechanical properties. Finally, the deposited electrodes were also used in the fabrication of PENG and ACEL devices as active electrodes and demonstrated for its applicability.

4.1 Introduction

To further enhance the transparency of the flexible metallic multi-layer electrode, deposition of tri-layer architecture is carried out by eliminating Cu and Ag layers. Ultrathin metallic films are usually adapted in a multilayer architecture so that the synergistic effect of each metal layer can enhance the overall transmittance and conductivity into a wider visible spectral range [156]. In a single layer, the maximum transmittance from individual metals is only limited to specific wavelengths [156]. The metals Au and Pt are low-reactive noble metals and their ultrathin films (below their respective skin depth) possess transmittance in the visible region of the electromagnetic spectrum [219]. To induce wide-range transparency in the visible region, the combination is made into a tri-layer architecture Au (2 mm)/Pt (2 nm)/ Au (2 mm) (Fig. 4.1 (a)) and explored, for its optoelectronic properties. The thickness of individual layers based on their skin depth [282] forms the deciding factor for the transparent conducting property of multilayer TCEs. When the thickness of a thin film is high, its transmittance will be low, and when the thickness is low, the thin film possesses high transmittance. Hence, the thickness values of individual metal films become crucial when designing a TCE. In addition to this, the main advantage

of using ultrathin metal films is their excellent flexibility, cost-effectiveness (due to lesser material usage), compactness, ease of deposition due to well-established physical vapor deposition techniques, and compatibility with a variety of substrates.

In this chapter, the highly inert noble metals such as Au and Pt are explored in a tri-layer architecture by depositing on a flexible PET substrate for use as a TCE. Pt has good chemical stability and stable temperature co-efficient of resistance [285] and Au is also a typical metal for serving as stable electrode [286]. Each layer with a thickness of 2 nm (based on the skin depth) as estimated using the equation 3.1 is deposited on a flexible PET film using sputtering technique in Au/Pt/Au architecture. Au metal is coated as seed layer as well as capping layer to decrease the surface/interface roughness and to protect the Pt layer from native oxide formation, and it also aids to enhance the conductivity of the ultrathin film. The flexibility and transparent conducting properties of this TCE are explored and demonstrated in PENG and ACEL devices as a proof of principle validation of its viability in a variety of optoelectronic device applications. The same experimental conditions which were mentioned in the section 3.2.2 are followed for the deposition of the Au (2 mm)/Pt (2 nm)/ Au (2 mm) tri-layer (Fig. 4.1 a and b) and making of PENG and ACEL devices.

4.2 Results and discussion

4.2.1 Structural properties

X-ray diffraction patterns of plain PET and Au/Pt/Au coated PET are shown in Fig. 4.1 (c). Both the patterns are nearly similar, however, the main peak around 26.19° corresponding to PET substrate is shifted to 25.54° after deposition of Au/Pt/Au layers. This information gives an indication about the existence of the deposited Au/Pt/Au metallic tri-layers over the PET substrate. No other peaks corresponding to Au and Pt are observed since the total thickness of the tri-layer is merely 6 nm, and moreover, since the deposition temperature is only 70 °C, the layers might have crystallized marginally.

4.2.2 Surface topology

Surface topography of the sputtered Au/Pt/Au tri-layer on PET film is analyzed using AFM and optical profiler techniques. The surface analysis of the sputter coated flexible Au/Pt/Au PET film is highly challenging since the tip of the AFM instrument is extremely sensitive. Therefore, in the present work, the Au/Pt/Au tri-layer was

sputter-deposited simultaneously on both glass and PET substrates. Moreover, metal films over 100 nm thickness are not beneficial for use in optoelectronic devices which essentially require a smooth electrode surface [136]. The 2D and 3D AFM images (Fig. 4.2 a and b) of Au/Pt/Au tri-layer on glass substrate show that the film is crack-free and densely packed. From Fig. 4.2 (b), the Au/Pt/Au thin film clearly indicates the presence of needle-like particulates on the surface of the film with a lower RMS roughness of 1.04 nm. The topography of the flexible Au/Pt/Au sputtered on PET film was analyzed using optical profiler in non-contact mode and the 2D and 3D images are shown in Fig. 4.2 (c) and (d), respectively. Fig. 4.2 (e and f), shows the 2D and 3D images of plain PET surface and it is observed to be smooth. Also, the surface roughness calculated from AFM was reported to be 3.68 nm by K.G. Kostov et al., [319]. The 3D image of Au/Pt/Au film clearly shows a highly homogeneous film with significantly less spike-like features at that magnification over a larger area (1 mm $\times$ 1 mm), which implies its suitability in large-scale optoelectronic devices. In the present case, the ultra-thin tri-layer is deposited by sputtering technique at a rate of 0.058 nm/s for an individual layer thickness of 2 nm. Here, the most probable mode is Stranski-Krastanov, which is a mixed layer plus island growth mode [320,321].

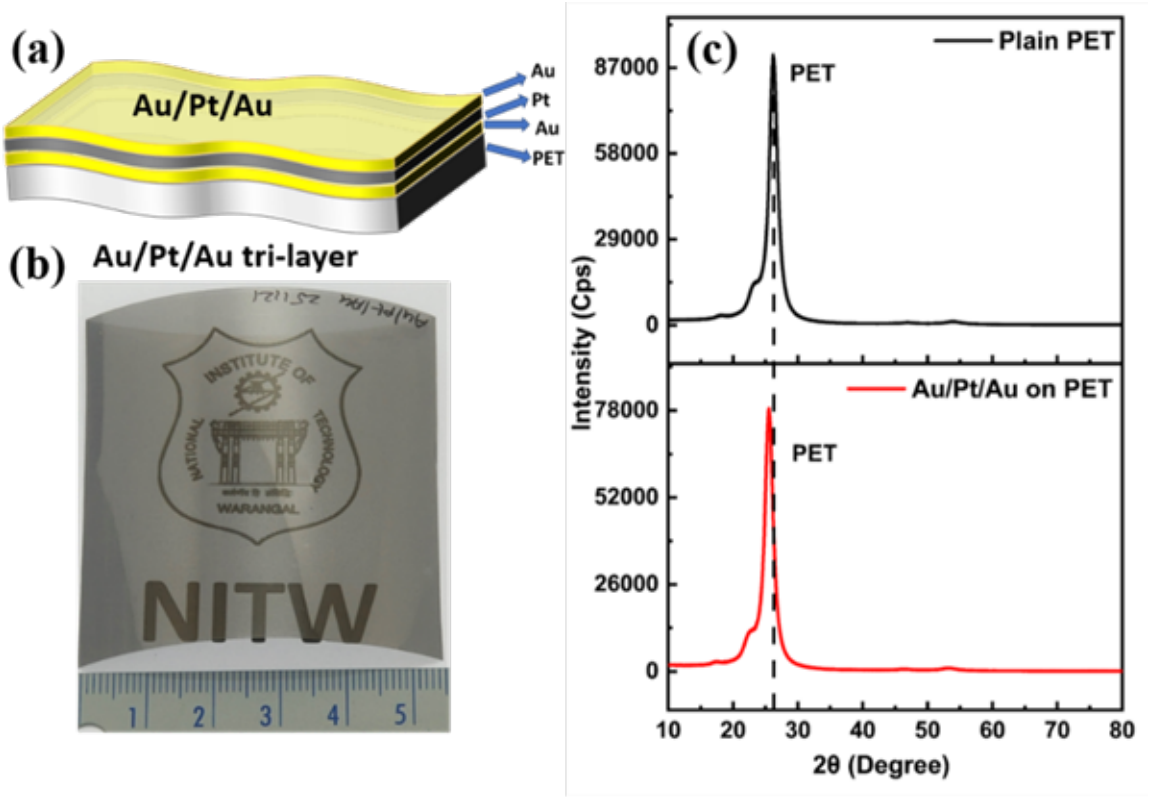

Figure 4.1: (a) Schematic 3D representation of ultrathin Au/Pt/Au tri-layer film architecture, (b) photograph of the deposited homogenous tri-layer indicating its bendable and transparent nature, and (c) X-ray diffraction patterns of plain PET and Au/Pt/Au sputter deposited over PET sheet.

Therefore, within a threshold limit, island formation may occur and upon depositing the Pt and Au overlayers, a considerably sharp interface exists, as evident from the X-Ray reflectivity data (see the Fig. 3.1) and from the interference pattern obvious in the UV-Vis transmittance data (see in the section 4.2.4, inset of Fig. 4.4 b). Therefore, the deposited ad-atoms or molecules are strongly bonded to the substrate and to each other progressively with the deposition of subsequent layers. All these factors lead to considerably uniform film formation with a moderate surface roughness of 1.04 nm.

4.2.3 Wettability of the Au/Pt/Au ultrathin flexible film

The wettability nature of the sputter-deposited Au/Pt/Au ultrathin flexible film is analyzed using contact angle measurement with de-ionized water as test medium.

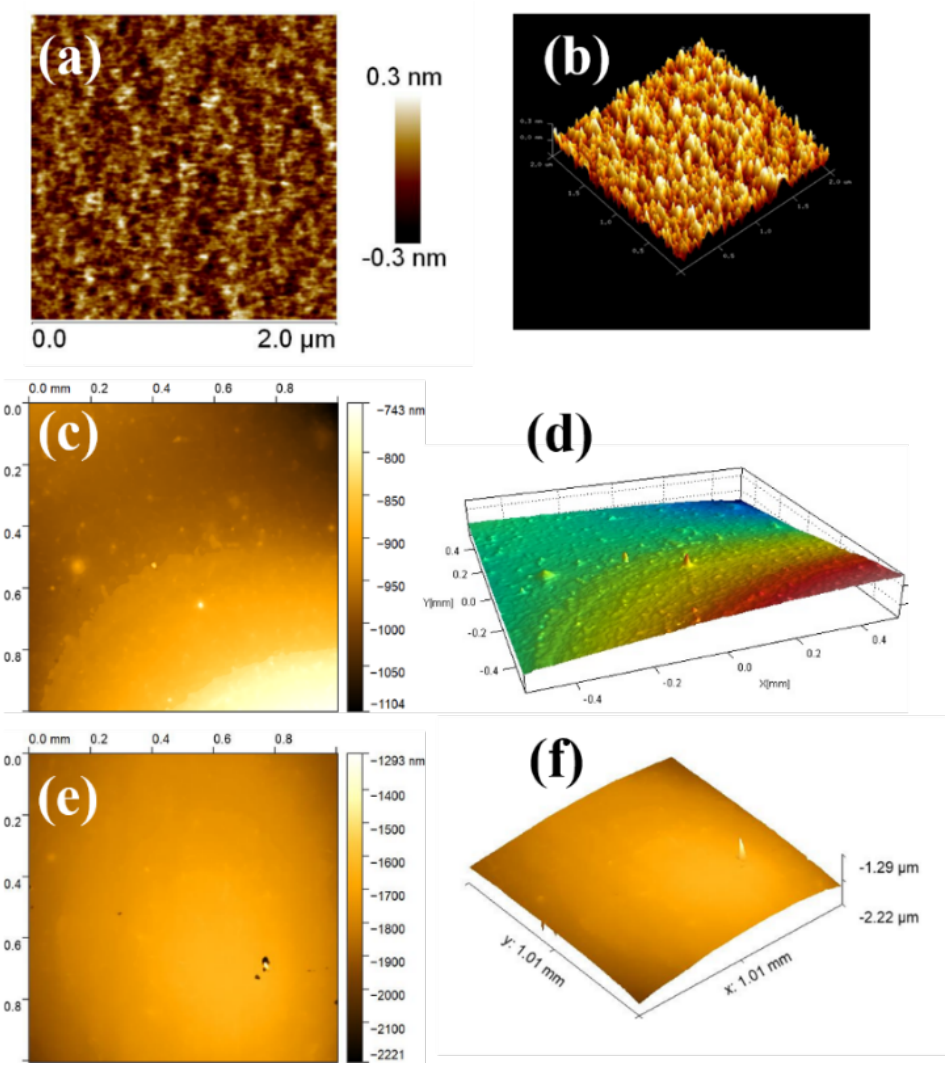

Figure 4.2: (a and b) The 2D and 3D AFM images of Au/Pt/Au tri-layers deposited on glass substrate, (c and d) the 2D and 3D optical profiler images of Au/Pt/Au tri-layer deposited on PET substrate, and (e and f) 2D and 3D optical profiler images of plain PET film.

Usually, the contact angle of a thin film is mainly dependent on aspects such as surface roughness, functional groups existing on the surface of the film, impurities present on the film's surface, porosity of the film, and surface energy [290]. In the present case, de-ionized water droplets tested on plain PET, Au/Pt/Au sputter deposited over PET and commercial ITO films are shown in Fig. 4.3 (a), (b) and (c), respectively. The plain PET substrate shows hydrophilic nature with a contact angle of 62.6°, and after deposition of the Au/Pt/Au metallic tri-layer, it turns hydrophobic with a contact angle of 94.2°. Here, the variation in the contact angle is mainly due to surface roughness and chemical nature of the film. The low surface roughness (1.04 nm) of the deposited ultrathin flexible Au/Pt/Au film with nano-dimensional needle-like features may be the cause for the change from hydrophilic to hydrophobic nature. The commercial flexible ITO also shows hydrophobic nature with a contact angle of 102.9°. Hydrophobic nature of the deposited thin film helps in low-wetting of the Au/Pt/Au ultrathin film, which may be useful for self-cleaning-like requirements of the deposited film.

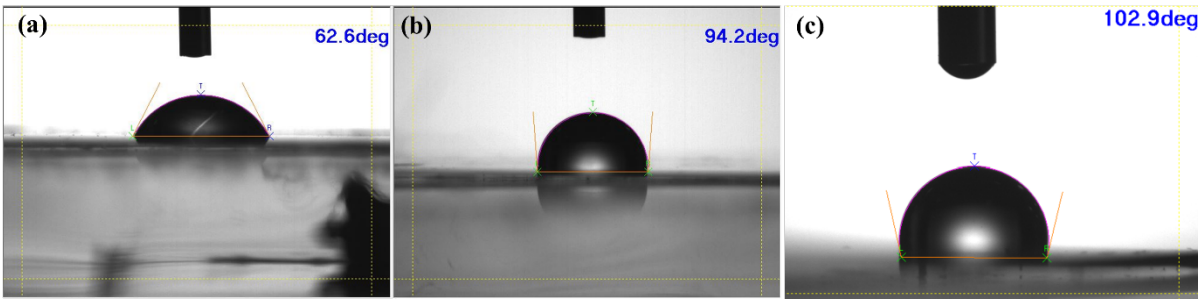

Figure 4.3: Contact angle measurement of water droplet on the surface of (a) plain PET, (b) Au/Pt/Au tri-layer film coated over PET, and (c) flexible commercial ITO

4.2.4 Optical transmittance

Figure 4.4 (a) shows the optical transmittance spectra of the deposited Au/Pt/Au tri-layer and commercial flexible ITO film (Zhuhai Kaivo Optoelectronic Technology Co., China). The Au/Pt/Au tri-layer film shows a maximum transmittance (T) of 55 % at 500 nm, whereas flexible ITO has slightly higher transmittance of 58 % at 550 nm. The transmittance of commercial ITO is marginally higher in the visible region, but in the case of the deposited Au/Pt/Au ultrathin flexible film, the transmittance shows near-flat behavior in the entire spectrum (350-1000 nm). However, this is lower than that of the Au/Ag/Au tri-layer (62 %) [265] and higher than the reported value for Cu/Ag/Au tri-layer film (40 %) [59] deposited by thermal evaporation technique. Alexander et al., reported the individual transmittance of 2

nm Au thin film deposited on glass substrate to be 70 % at 500 nm [147,156]. In the present case, the addition of another 2 nm of Pt and 2 nm of Au leads to decrease in the transmittance of the deposited Au/Pt/Au layer. However, the transmittance of the deposited Au/Pt/Au flexible thin film shows an extended behavior from ultraviolet region to near-infrared region, with a value ranging between 48 % and 55 % (Fig. 4.4 (b)). The flat behavior in the transmittance spectra is mainly due to the presence of two different metal layers (Au and Pt) in the tri-layer architecture, demonstrating significant change in transparency in comparison with that of commercially available flexible ITO from ultraviolet to near-infrared regions. The peak at 500 nm with transmittance value of 55 % is mainly due to the presence of Au layer in the tri-layer architecture [156]. The inset of Fig. 4.4 (b) shows an interference pattern around 800 nm, which is due to the layered structure of the sample with distinct and sharp interface. From the literature, it is well known that ITO and FTO films present very low transmittance in the near-infrared and infrared regions, which is mainly due to the presence of free electron plasmon resonance or strong free carrier absorption [292–295]. The optical transparency of the ultrathin Au/Pt/Au metal film dominates that of ITO in the near-infrared region, which may be due to the presence of free-carrier plasmon edge in the infrared region [295]. However, the transmittance of an ultrathin film is mainly dependent on its percolation threshold thickness of the respective material [296]. When the thickness of the film is below the percolation threshold, it forms a network of islands, whereas an increase in film thickness leads to continuous film formation, resulting in reduced transparency [296].

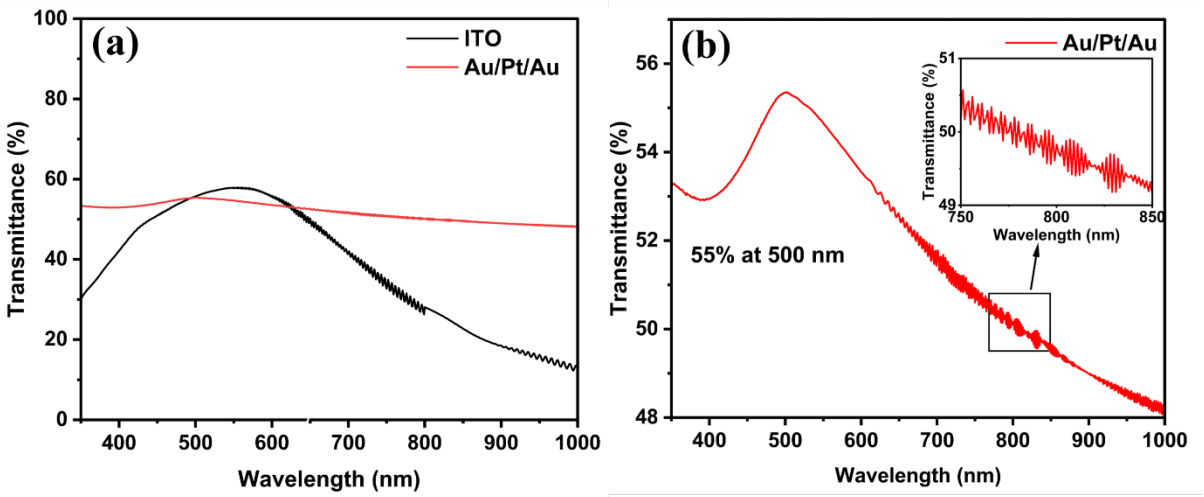

Figure 4.4: (a) Transmittance spectra of Au/Pt/Au coated PET and commercial flexible ITO films, and (b) enlarged transmittance spectra of the Au/Pt/Au flexible ultrathin metal film (inset is the interference pattern due to the constituent layers of the tri-layer architecture).

4.2.5 Electrical transport properties

The electrical transport properties of the Au/Pt/Au tri-layer film are evaluated using Hall effect at 300 K. The carrier concentration (n), sheet resistance (R_s), resistivity (ρ), conductivity (σ) and mobility (μ) values of Au/Pt/Au and commercial ITO are listed in Table 4.1. At lower thickness, the film grows into independent islands, leading to discontinuity, thereby causing high electrical resistance. If the thickness of the film surpasses the percolation threshold, then the discrete metal clusters further grow, forming a continuous metal layer, thereby increasing the conductivity of ultrathin metal films [297]. In the present case, 2 nm Au is deposited as seed layer to deposit Pt layer of 2 nm, followed by 2 nm of Au layer as capping layer to avoid oxidation and for better chemical stability and surface functionality. The deposited Au/Pt/Au layer shows a sheet resistance of 66 $\Omega/\square$ with resistivity of 3.72×10^{-5} Ωcm, which is slightly higher than that of commercial flexible ITO film.

The resistivity of ultra-thin Au/Pt/Au metal film is severely affected by electron scattering from grain boundaries and interfaces. The charge carrier concentration and conductivity of the deposited Au/Pt/Au ultrathin metal are marginally higher than that of commercial ITO (Table 4.1). The mobility of the deposited film shows slightly lower (8.32 $cm^2V^{-1}s^{-1}$) value than that of commercial ITO (10.18 $cm^2V^{-1}s^{-1}$), which may be due to the carrier scattering process that occurs in the thin film due to grain boundary scattering, phonon scattering and free carrier trapping at the interfacial defects [299]. The presence of a higher number of charge carriers leads to more frequent collisions, resulting in a decrease in the mean free path of electrons, in turn, contributing to lower mobility of the Au/Pt/Au ultrathin metal film. In addition to this, the surface features of the film also affect the mobility of carriers in the deposited film.

4.2.6 Surface work function

Surface work function (Φ) plays a very important role in the efficiency and performance of optoelectronic devices. Here, the work function of the sputtered Au/Pt/Au ultrathin flexible thin film is estimated from Kelvin probe measurement operated in ambient atmosphere with a 2 mm gold alloy tip [300]. Initially, the gold tip is calibrated with a standard Au-coated Al substrate (work function of Au-coated Al substrate is 5.1 eV) by evaluating the contact potential difference (V_{CPD}) between the Au film and the tip [300]. The value Φ_{tip} is estimated (from equation 2.14) to be 4.877±0.016 eV. The Au/Pt/Au ultrathin flexible film is then loaded, and V_{CPD} between the sample and the tip is calculated using the relation eq. 2.15 [300]. The

Table 4.1: Optoelectronic parameters of Au/Pt/Au ultrathin flexible tri-layer film in comparison with ITO and previously reported metallic tri-layer film.

Sample code	Carrier concentration n (cm^{-3})	Sheet resistance R_s ($\Omega/\square$)	Resistivity ρ (Ωcm)	Mobility μ ($cm^2V^{-1}s^{-1}$)	Transmittance T (%)	FoM (Ω^{-1})
ITO [265]	1.29×10^{22}	5	4.73×10^{-5}	10.18	55 (500 nm)	5.06×10^{-4}
$Cu/Ag/Au^a$ [291]	1.15×10^{23}	7.7	9.70×10^{-6}	5.58	40 (500 nm)	1.39×10^{-5}
$Au/Ag/Au^a$ [265]	2.48×10^{23}	10.42	7.46×10^{-6}	3.4	62 (550 nm)	5.20×10^{-4}
$Au/Cu/Ag/Pt/Au^b$	5.11×10^{22}	60.23	6.02×10^{-5}	2.02	44 (500 nm)	2.89×10^{-5}
$Au/Pt/Au^b$	2.01×10^{22}	62.08	3.72×10^{-5}	8.32	55 (500 nm)	3.39×10^{-5}

a: thermal evaporation, b: D.C. sputtering (this thesis)

estimated work function of the sputter-deposited Au/Pt/Au ultrathin flexible film is found to be 4.97 eV. The work function values of individual Au and Pt metals are reported to be in the range 5.31-5.47 eV and 5.12-5.93 eV, respectively [302]. The reported work function for ITO is around 4.3-4.4 eV [303–306]. Although the measured work function of Au/Pt/Au ultrathin flexible film is higher than that of ITO, it can be employed in specific applications, wherever this range of work function is necessary. Nevertheless, many optoelectronic devices need at least one electrode with a low surface work function. Low surface work function improves either the collection of electrons or the injection of electrons from the conduction band minima (CBM) or lowest unoccupied molecular orbital (LUMO) of a given inorganic/organic semiconductor.

4.2.7 Mechanical stability

The development of flexible electronic gadgets for portable and wearable devices requires a variety of transparent conducting flexible electrodes with good stability for several bending and twisting cycles without significant change in sheet resistance, to

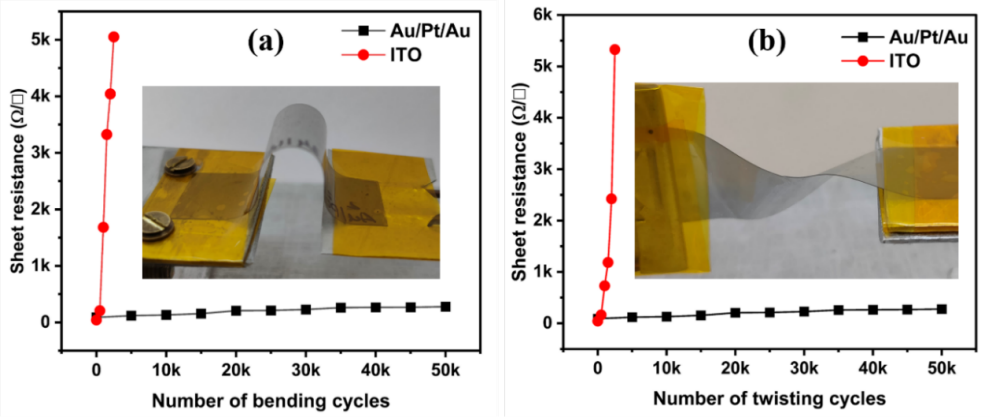

Figure 4.5: Stability of sheet resistance of Au/Pt/Au tri-layer film in comparision with commercial ITO for (a) bending and (b) twisting modes (insets are the photograph of the respective modes).

retain the efficiency and lifetime of the device. Therefore, it is necessary to study the stability of sheet resistance of the sputter-deposited Au/Pt/Au ultra-thin flexible electrode for several thousands of bending and twisting cycles, which shows the ability of the films to withstand applied stress and strain. The bending and twisting tests of commercial ITO along with Au/Pt/Au ultra-thin flexible film were performed using an indigenously designed apparatus employing an ATmega328 microcontroller [265]. Insets of Fig. 4.5 (a) and (b) show the films loaded in bent and twisted positions, respectively. The bending and twisting tests were performed at a speed of 20 bending cycles per min and 14 twisting cycles per min. The time taken for 5,000 bending and twisting cycles was 250 and 350 min, respectively. Sheet resistance stability measurements of total 50,000 bending (Fig. 4.5 a) and twisting (Fig. 4.5 b) cycles each with steps of 5000 bends and twists were performed on the sputtered Au/Pt/Au ultrathin flexible tri-layer film. The sheet resistance stability measurement of commercial flexible ITO was also performed at the same rate. Due to lower stability, a total number of 2,500 bending and twisting cycles with an interval of 500 cycles were performed.

The bending and twisting-induced strain in a metallic thin film is dependent on the thickness of the metallic film (d_m), thickness of the substrate (d_s), bending radius (R), and Young's modulus of the deposited metal (γ_m) and substrate (γ_s) [307]. The strain in the deposited film can be calculated using the equation 3.5 [307]. From the equation, the bending strain is proportional to the thickness of the deposited film, and so, if the thickness of the film is reduced, the bending strain of the film decreases, leading to increase in the flexibility and stability of the deposited metal film. Metal films are highly ductile and can withstand up to several thousands of bending and twisting cycles. Yin et al., demonstrated good stability of a flexible OLED fabricated using Ag (80 nm) as anode with bending radius of 30 μm, without degrading the device performance [308]. Kang et al., reported a polymer-metal hybrid electrode which showed good stability up to 1000 bending cycles compared to commercial ITO, and they observed decrease in device performance for the ITO electrode after 1000 bending cycles, whereas the device made with Ag electrode showed nearly no degradation of device performance [309]. A comparison between previously reported alternative flexible transparent conducting electrodes with the present work is given in Table 4.2. The Au/Pt/Au ultrathin flexible film with a thickness of 6 nm shows good mechanical stability up to 50,000 bending and twisting cycles. The flexibility of the Au/Pt/Au film is 100 times higher than that of the commercial flexible ITO as shown in Figs. 4.5 (a) and (b). The flexible ITO film is not stable even up to 2,500 bending and twisting cycles as shown in Figs. 4.5 (a) and (b), causing damage due to its brittle nature. The observed high stability in Au/Pt/Au film is mainly due to the ductile nature of

metallic layers compared to that of oxide films, and also because of low thickness of the Au and Pt layers.

The sheet resistance of Au/Pt/Au ultrathin flexible film does not exceed 300 Ω/□ even after 50,000 bending and twisting cycles, whereas in the case of commercial flexible ITO, it exceeds 300 Ω/□ within 500 bending and twisting cycles, and drastically increases to 5 kΩ/□ within 2,500 bending or twisting cycles (Fig. 4.5 (a) and (b)). Figure 4.6 shows the optical microscopic images of commercial ITO film before and after 2,500 bending and twisting cycles, where cracks on the ITO film are observed clearly. These cracks lead to discontinuity in the film surface, resulting in high sheet resistance. Whereas, in the case of sputter-deposited Au/Pt/Au ultrathin flexible film, optical microscopic images before and after 50,000 bending and twisting cycles are shown in Fig. 4.6 (d-f). Figure 4.6 (e) and (f) show only few cracks even after 50,000 bending and twisting cycles. However, these small cracks do not have much effect on the sheet resistance of the Au/Pt/Au ultra-thin film. In addition to flexibility, it is necessary to investigate the adhesion properties of the deposited Au/Pt/Au ultra-thin flexible film by subjecting it to scotch tape test. A scotch tape was placed and pressed on the film's surface, and then stripped away manually for about six trials. Upon visual inspection, the film was found to be intact, implying good adhesion, and the film was also electrically conducting as tested for its electrical continuity using a multimeter with almost no change observed in the sheet resistance after the tape test. All these properties suggest that the Au/Pt/Au ultrathin tri-layer is a promising and electrically stable candidate for appropriate flexible optoelectronic device applications with long-term robustness.

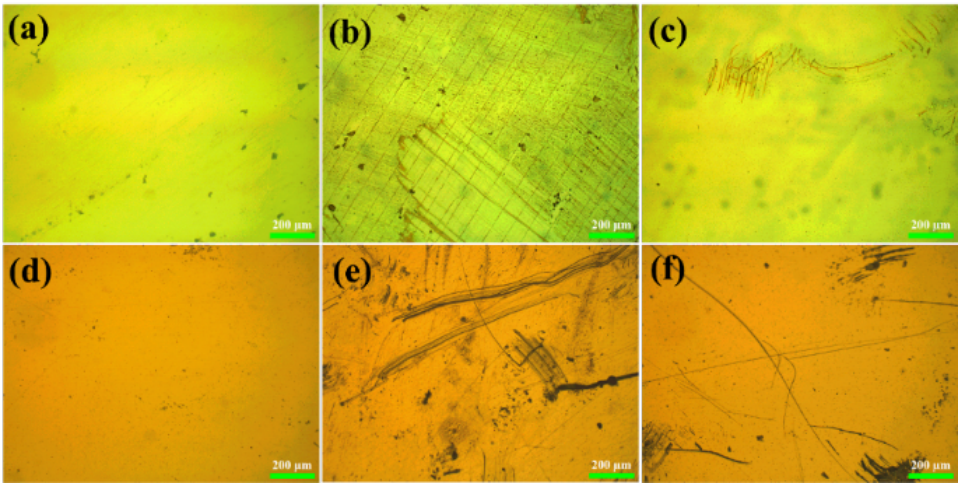

Figure 4.6: Microscopic images of commercial flexible ITO film: (a) pristine, (b) after 2500 bending cycles, (c) after 2500 twisting cycles; and Au/Pt/Au tri-layer coated over PET: (d) pristine, (e) after 50000 bending cycles, (f) after 50000 twisting cycles.

Table 4.2: Comparison of parameters of Au/Pt/Au tri-layer film with previously reported alternative transparent conducting electrodes.

Material	Thickness (nm)	T (%)	R_s ($\Omega/\square$)	Flexibility (Bending cycles or radius)	Application	Ref
Ag NWs	30	85	50	1-5 nm	ACEL	[322]
$ZnO/Cu/ZnO$	6.5	84	20	0-12 nm	OPV	[323]
Ta_2O_5/Al-doped Ag	4	75	46.8	200	OPV	[324]
Au	4.4	78.4	70.4	2000	OLED	[325]
Au	7	72	24	1000	OLED	[122]
Au	7	75	19	2000	OLED	[326]
Ag	12	69	10	1000	OPV	[327]
Au	6	28	766	3000	OLED	[283]
ITO	100	55	5	2500	-	[324]
$Au/Cu/Ag/Pt/Au$	10	44	60	50000	PENG & ACEl	Chapter 3
$Au/Pt/Au$	6	55	62	50000	PENG & ACEL	This work

4.3 Applications

4.3.1 Piezoelectric nanogenerator

Figure 4.7 (a) shows the schematic representation of a piezoelectric nanogenerator (PENG) device architecture. Figure 4.7 (b) shows flower-like morphology of the near-vertically grown ZnO nanostructures and Fig. 4.7 (c) shows the elemental composition of the same. To measure the open-circuit voltage of the nanogenerator, the bottom aluminum foil (Al) electrode and the top Au/Pt/Au ultrathin flexible electrode are both connected to a digial signal oscilloscope (DSO) using probes. In the forward connection, the top electrode (Au/Pt/Au ultrathin flexible film) is connected to the positive probe of DSO, and the bottom Al electrode is connected to the negative probe of the DSO. When a force is applied to the device by finger tapping, piezoelectric output voltage is generated due to mechanical deformation of the ZnO nanostructures. The generated output voltage for repeated finger tapping is recorded in the DSO. The output voltage of the device is also measured in reverse connection, which is called the switching-polarity test. The switching-polarity test confirms that the output voltage is due to the nanogenerator device, and not from any spurious signals/instrument noise. The maximum output voltage (in both forward and reverse bias) produced for each finger tap by the nanogenerator device is 150 mV, as shown in Fig. 4.7 (d). The generated output voltage is nearly at the same level as that of the commercial ITO/PET and copper electrode-based ZnO nanogenerators reported previously [310, 311]. The use of Au/Pt/Au ultrathin tri-layer as a top electrode makes the device very compact and flexible. Moreover, transparency of the top electrode contributes to additional degree of freedom which may be beneficial to induce novel functionality through interaction with incident light radiation.

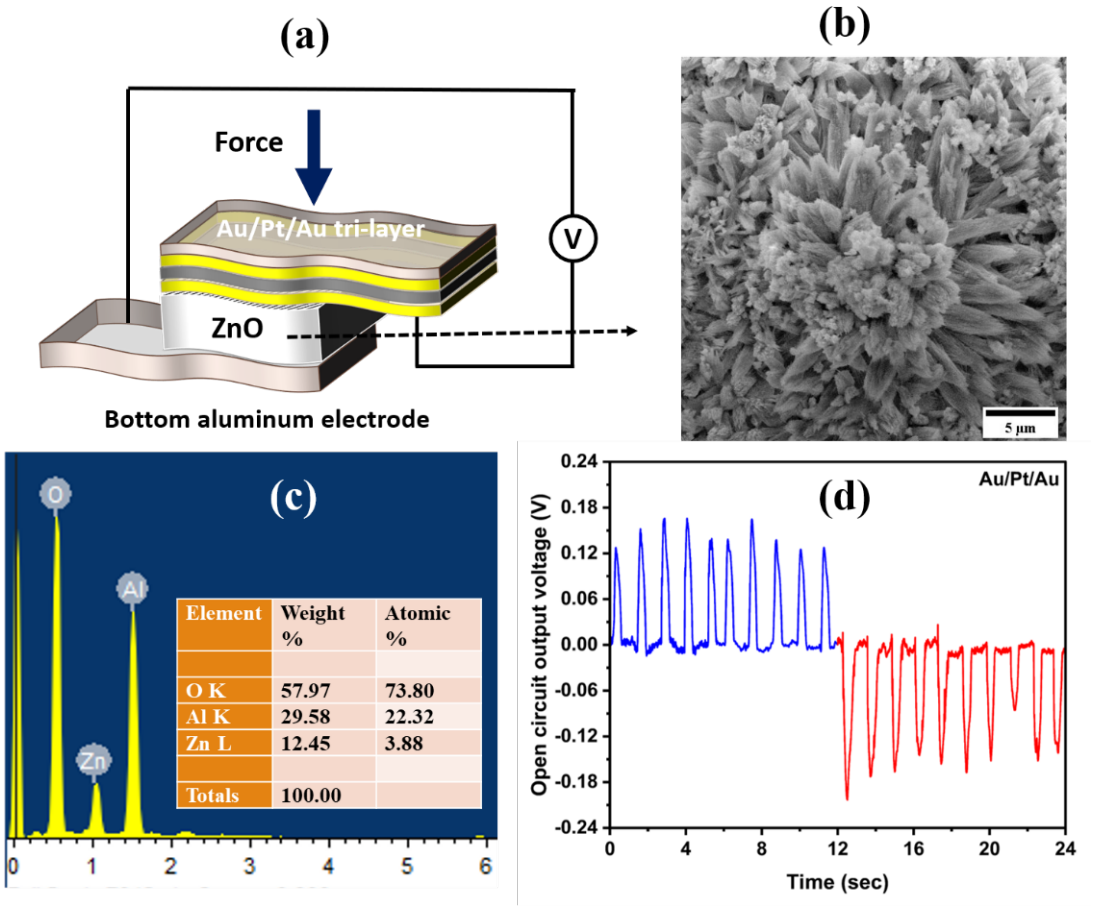

Figure 4.7: (a) Piezoelectric nanogenerator device architecture with Au/Pt/Au metallic tri-layer flexible transparent thin film as a top electrode, (b) SEM image, (c) EDAX spectrum of ZnO grown on aluminum foil (inset is the weight and atomic percentage of elements) and (d) time vs open circuit voltage response of the PENG device.

4.3.2 Flexible alternating current electroluminescent device

A flexible alternating current electroluminescent device (ACEL) is demonstrated using the ultrathin flexible Au/Pt/Au transparent conducting film as both top and bottom electrodes. The main advantage of ACEL devices is their facile fabrication process which can be executed in ambient environment [316]. One of the very essential characteristics of an ACEL device is its capability to be made into a very thin device architecture with enhanced flexibility and uniform emission across the whole surface area, leading to wider viewing angles [317]. Figure 4.8 (a) shows the flexible electroluminescent device architecture. The photograph of the fabricated flexible ACEL device using ultrathin Au/Pt/Au film as a transparent conducting electrode and ZnS:Mn as electroluminescent emissive material is shown in Fig. 4.8 (b). The working mechanism of ACEL device is as follows: When an AC voltage is applied between the two electrodes, light is emitted by the device due to excitation of luminescence centers

within the phosphor material. The entire procedure is divided into four steps: (a) electron injection, (b) electron transport, (c) impact excitation or impact ionization of the luminescence centers and (d) de-excitation of the excited electrons by radiative recombination process (Photon emission) [317].

The ACEL device fabricated using ZnS:Mn emissive layer and Au/Pt/Au ultra-thin film electrodes shows orange color emission in the range 590-610 nm [199, 318]. Initially, the luminescence flickers at low frequency and is eventually stabilized at higher frequency. The orange ACEL emission begins around 95 V_{AC} (threshold voltage), and when the applied voltage increases, the intensity of the device increases up to 180 V_{AC} (saturation voltage). Figure 4.8 (c) shows the ACEL emission at 180 V_{AC}, which is well matched with that of the previously reported ACEL device made from Al and ITO as bottom and top electrodes, respectively [199]. In addition to this, the device is also verified under UV light (365 nm) without any applied voltage as shown in Fig. 4.8 (d). Table 4.2 shows the comparison between reported and multi-layer electrodes optoelectronical properties. Literature reports show that in ACEL devices,

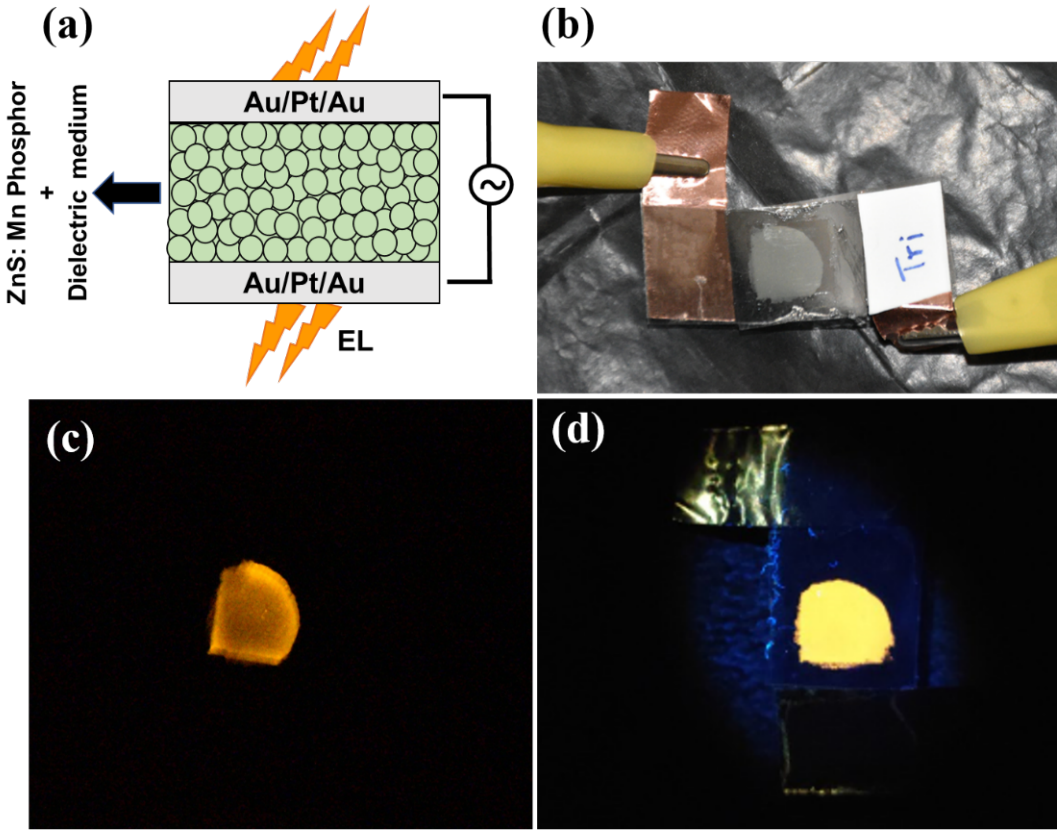

Figure 4.8: (a) Alternating current electroluminescent device architecture with metallic Au/Pt/Au film as top and bottom electrodes, (b) photograph of the electroluminescent device made using Au/Pt/Au flexible transparent film, (c) response of the device at 180 V_{AC}, and (d) response under UV light (365 nm) without any applied voltage.

the back electrode is given lesser attention for innovation, and in most cases, thick metallic layers possessing high conductivity but no transparency are used in general. In the present case, we have used both the top and bottom electrodes as transparent conducting and flexible ultrathin metallic tri-layers, which is impressive since the flexible ACEL device can emit from both sides of the electrodes, unlike conventional devices that permit only one-side light emission.

Both the PENG and ACEL devices demonstrate that the deposited Au/Pt/Au thin layers possesses high electrical conductivity as well as significant transparency, thereby indicating its viability as a potential alternative flexible transparent conducting electrode in a wide range of applications which may be comfortably wrapped around curvilinear surfaces and may respond seamlessly to applied potential or external forces. The flexibility and robustness of the metallic tri-layer electrode may be suitable for long period of operation when used in flexible ACEL devices, making them reliable for real-time usage.

4.4 Conclusion

Ultrathin Au/Pt/Au flexible tri-layer film is successfully deposited on PET substrate by sputtering technique. Au/Pt/Au film shows maximum transmittance of 55% at 500 nm and a near-flat behavior throughout the spectral range with transmittance between 48 % and 55 %, revealing its applicability for usage in UV-visible and near infrared regions, and it may be applicable for flexible energy-harvesting applications. It possesses low values of sheet resistance, resistivity, and work function of 62 $\Omega/\square$, 3.72×10^{-5} Ωcm, and 4.97 eV, respectively. In addition to the appreciable optoelectronic properties, it also exhibits very high mechanical stability of 50,000 bending and twisting cycles, which is far better than that of commercially available ITO, in this range of testing. The commercial ITO shows stability only for a mere 500 bending and twisting cycles. The deposited ultrathin Au/Pt/Au flexible film is demonstrated as an electrode in optoelectronic devices like piezoelectric nanogenerator and alternating current electroluminescent device. The piezoelectric nanogenerator produces nearly 150 mV on applying force by finger tapping. The ACEL device starts producing orange emission at 95 V_{AC}, and with increase in voltage, the brightness of the device increases up to 180 V. Both the demonstrated devices imply the potential of sputter-deposited ultrathin flexible Au/Pt/Au tri-layer film as a promising electrode system for use in various flexible optoelectronic devices. The ACEL device has an advantage of emitting light from both the top and bottom electrodes, and the trans-

parent top electrode may extend additional functionality of irradiation with UV light in the case of piezoelectric nanogenerator apart from finger tapping. However, further exploration is necessary on an effective strategy to minimize performance failure under mechanical deformations in order to extend the lifetime of the demonstrated optoelectronic devices.

The significant retention of optoelectronic properties even after several thousands of mechanical bends and twists indicates the electrical durability of the metallic-tri-layer. Researchers have reported formation of electrical double layers which behave as capacitors in metal-based conductors when combined with dielectric layer [284, 317]. Therefore, from this point of view, the ultrathin metal layers hava scope for further exploration as electrode system towards realizing bendable micro-supercapacitors. Being highly flexible, the ultrathin tri-layer over 30 μm PET can be tailored simply by cutting it using a pair of scissors or a stencil to make desired electroluminescent patterns of various geometrical shapes and designs for applications like diffuse indoor-lighting in buildings and automobiles, decoration/fashion designing, and also for see-through-flexible electronics. Owing to the low melting point of the 30 μm PET substrate, one can easily laminate it into wearable electronics as well as in safety jackets/traffic signs by suitably altering the phosphor material. Due to the facile and open air-process of the assembly protocol of the demonstrated devices without requirement for high temperature/vacuum, the robust metallic-tri-layer is highly suitable for scalability of various real-time optoelectronic devices for the current and future interactive-display-centric world.

Chapter 5

Deposition of Anionic F and Cationic Nb co-doped SnO_2 Thin Films by Chemical Spray Pyrolysis Technique

This chapter first discusses the optimization of F-doped SnO_2 (FTO) thin films by cost effective facile spray pyrolysis method. Main intention is to fine tune the deposition parameters for better optoelectronic properties of the FTO thin films. Secondly, the optimized deposition parameters have been selected for deposition of Nb and F co-doped SnO_2 (NFTO) film. Exploration of its structural, optical and electrical properties by several characterization techniques have been carried out. Finally, all the NFTO thin films were tested in a DSSC device as an alternative TCE electrode and the results are discussed in detail.

5.1 Introduction

Transparent conducting electrodes are developed using materials that possess high transparency and high electrical conductivity in the same host lattice. It is generally difficult to obtain both these properties in the same host material, since most of the transparent media are non-conducting in nature, like glass; whereas conducting materials are opaque in nature, like metals. Therefore, stabilizing these properties to the required value in the same host material is a cumbersome task. However, in 1930, Rupprecht found that In_2O_3 (90 %): Sn (10 %), also known as Indium Tin Oxide (ITO), is a transparent conducting medium with very good optical transparency and electrical conductivity [28]. Currently, ITO electrodes are widely used in almost every optoelectronic device [328]. However, the key problems they face are low availability of indium in the earth's crust, high processing cost [329], and low recycling-feasibility of the used ITO electrodes. From the demand vs supply forecast of indium (Fig. 1.1) [7], the necessity of indium is predicted to increase day by day, and hence there is an urge to identify alternative materials to indium to supplement its usage.

There are several types of transparent conducting oxide (TCO) materials that have been developed till date; however, only few of them like indium tin oxide (ITO), F

doped tin oxide (FTO), and Al doped zinc oxide (AZO) are commercialized. Appropriately doped SnO_2 has wide direct optical band gap (3.80 eV) and comparatively reasonable electrical conductivity which makes it a promising cost-effective TCO material with good chemical stability and high electron mobility (single crystal SnO_2 can attain maximum mobility of 250 $cm^2V^{-1}s^{-1}$) [330], indicating its suitability as a transparent conducting electrode (TCE) for various device applications [331]. Several deposition techniques have been employed to deposit doped transparent and conducting SnO_2 thin films, among which some are chemical methods like sol-gel, spin coating [332]], dip coating [333], doctor blading [334], chemical vapor deposition [335–338], inkjet printing [339] and spray pyrolysis [340–345]. Others are physical vapour deposition methods like reactive magnetron sputtering [346], electron beam evaporation [347], pulsed laser deposition [348]. Chemical spray pyrolysis is a facile deposition technique which is cost-effective and easily adaptable without the need for high vacuum. Spray pyrolysis technique is suitable for producing large-area thin film TCEs for a variety of applications [349].

Doping with tantalum (Ta) [350], niobium (Nb) [351], antimony (Sb) [352], and fluorine (F) [3] has been observed to convert intrinsic SnO_2 into an extrinsic semiconductor possessing high electrical conductivity without compromising transparency, which suggests that doped SnO_2 can be an excellent supplement to conventional ITO in appropriate optoelectronic devices. The ionic radius of F is nearly equal (1.28 Å) to that of O (1.35 Å); hence, it is used as dopant, resulting in an increase in carrier concentration of SnO_2 thin films. Here, both F and Sn are earth abundant materials possessing high mechanical, thermal and chemical stability, and are also lower in cost compared to ITO.

Highly transparent FTO for heat mirrors have been widely used over several decades in architectural windows for comfort and energy saving without sacrificing the "clear scenic view" and in recent years for energy efficiency in baking ovens. Textured FTO, which looks foggy, have been used for specific advantage in certain thin film solar cells. As a requirement for various applications and to aid researchers exploring alternatives by co-doping and other strategies, we intend to elucidate spray deposition of FTOs at lab scale on comparatively thinner glass substrates (1 mm) which may yield newer insights on the optimization parameters. Several reports exist on spray-deposited FTO thin films [15,345,353–357]; however, there are only very few reports investigating optical and electrical properties by varying the solvent type and solvent ratio while preparing the precursor solution for deposition [358–362]. Specifically, there is no report on varying the ratio of 2-methoxyethanol ($C_3H_8O_2$) and ethylene glycol ($C_2H_6O_2$) admixed solvent in depositing F-doped SnO_2 by spray py-

Table 5.1: Precursors, solvents and spray deposition parameters of the FTO thin films.

Parameters	Specifications
Precursors used	$SnCl_2 \cdot 2\,H_2O$ and NH_4F
Solvents used	2-methoxyethanol, Ethelyne glycol and HCl
Substrate and pyrolysis temperature	Glass slides ($5 \times 5\ cm^2$) at $410\ ^\circ C$
Carrier gas/pressure	Compressed moisture free air/ 30 kg cm^{-2}
ON/OFF Duration per spray	0.5 s/30 s
No of sprays/total spray duration	650 sprays, 5.41 min
Nozzle to substrate distance	35 cm

rolysis technique. In the present study, FTO thin films are deposited by varying the solvent volume ratio of 2-methoxyethanol ($C_3H_8O_2$) and ethylene glycol ($C_2H_6O_2$), and the admixed solvent effect on the optical and electrical transport properties are explored. The spray-pyrolyzed FTO electrodes are also tested as photoanodes by fabricating dye sensitized solar cells (DSSCs) and evaluating their performance. These results are elaborated in the following sections.

Part-A

Part-A of this chapter first stabilizes the optimal deposition parameters of the "F" doped SnO_2 thin films

5.2 Optimization of 'F' doped SnO_2 thin films

5.2.1 Experimental method

5.2.1.1 Precursor materials

In this section, to prepare FTO thin films, analytical grade chemicals $SnCl_2 \cdot 2\,H_2O$ and NH_4F were used as precursors (Finar). Ethylene glycol (Finar) and 2-methoxyethanol (TCI) were used for preparing the admixed solvent. Glass slides ($5 \times 5\ cm^2$) procured from Zhuhai Kaivo Optoelectronic Technology Co. Ltd. were used as substrates. Isopropyl alcohol (IPA) (Himedia), Acetone (Finar), ethanol, and deionized water were used in an appropriate sequence for cleaning the glass substrates ultrasonically. The DSSC was fabricated using standard TiO_2 paste (18NR-T) purchased from Grätzel Solar Materials Pvt. Ltd. as active material, and counter electrode was prepared using chloroplatinic acid (5 mM) solution. Redox couple was prepared from acetonitrile, 1-butyl-3 methylimidazolium iodide, 4-tert-butyl pyridine and iodine procured

from Sigma Aldrich. For sealing the DSSC device, Su®lyn spacer (SX1170-60, 60 µm thick from Solaronix) was used.

5.2.1.2 Optimization of F doped SnO_2 thin films

$SnCl_2 \cdot 2\,H_2O$ (90 wt.%) and NH_4F (10 wt.%), both of 0.5 M concentration, were dissolved in 2-methoxyethanol in two different beakers and stirred for 30 min. A few drops of HCl were added to both the beakers to obtain transparent solution, after which, both the solutions were mixed together. Finally, the admixed solution was loaded into the spray unit. Glass slides ($5 \times 5\ cm^2$) were cleaned ultrasonically using mild detergent, distilled water, acetone, and iso-propyl alcohol sequentially for 15 min each in order to remove dust particles and traces of oil/grease adhered to the surface. These cleaned glass substrates were then blow-dried with compressed and moisture filtered air. Plasma cleaner of higher energy (Harrick Plasma, Model PDC-002) was used to neutralize the ionic charge contaminants on the substrate's surface. Finally, the cleaned glass substrates were loaded into the spray chamber. The substrate temperature was kept at 410 °C. The substrate to spray gun nozzle distance was kept 35 cm, compressed and moisture filtered air with pressure of 30 kg/cm^2 was maintained, and the spray duration was 0.5 s with an interval of 30 s (Table 5.1). A double-walled glass spray gun with a tapered inner nozzle of diameter 0.3 mm was used for film deposition, and a total of 650 sprays were performed using a total volume of 100 mL admixed solution. The aerosols sprayed onto the heated substrate undergo the following reaction, leading to the formation of oxide thin film.

$$NH_4F + SnCl_2 \cdot 2\,H_2O + C_3H_8O_2 + \tfrac{19}{4}\,O_2 \longrightarrow SnO_{2-x}F_x + 2\,HCl + NH_3 + 3\,CO_2 + \tfrac{11}{2}\,H_2O$$
$$NH_4F + SnCl_2 \cdot 2\,H_2O + C_2H_6O_2 + \tfrac{13}{4}\,O_2 \longrightarrow SnO_{2-x}F_x + 2\,HCl + NH_3 + 2\,CO_2 + \tfrac{19}{2}\,H_2O$$

Similarly, four different solutions were used for film formation by changing the solvent volumes as 0:100 ml, 25:75 ml, 50:50 ml, and 100:0 ml of ethylene glycol: 2-methoxyethanol, respectively. The nomenclature of the deposited films for varying solvent mixture is given as FTO1, FTO2, FTO3, and FTO4, respectively, which is also mentioned in Table 5.2.

5.2.2 Structural properties

The structural properties of the deposited FTO thin films are analyzed using X-ray diffraction (XRD) (Fig. 5.1). All the XRD patterns of the FTO films could be matched to the standard JCPDS file #: 00-041-1445 with space group P42/mnm

of tetragonal crystal structure of SnO_2. The preferred orientation is observed to change from (110) direction to (211) direction with variation of solvent volume of 2-methoxyethanol and ethylene glycol. Films deposited using only 2-methoxyethanol (FTO1) and ethylene glycol (FTO4) show preferred orientation along the (110) plane. However, in the case of admixed solvents (FTO2 and FTO3), the preferred orientation of the films is along the (211) plane. In thin films, preferred orientation is generally observed due to relaxation of residual strain that occur during the growth process. The (110) plane is the thermodynamically stable orientation in SnO_2 crystal structure due to lower surface energy [363]. Here, the change of plane orientation is mainly because of the effect of admixed solvents. Das et al., [363] observed that the growth of SnO_2 nanorods occur along the (101) plane instead of the (110) plane. Murakami et al., [364] also confirmed that the preferred direction is influenced by the type of precursor solution for the film coated using dibutyltindiacetate (DBTDA)-based precursor solution and shows dominant growth along the (200) plane, while the film coated using tetra-n-butyltin (TBT) shows textured growth along the (110) plane. Liyanage et al., reported that addition of ethylene glycol leads to change in the preferred orientation from (110) to (101) direction. Nevertheless, it has also been reported that anisotropic growth along other plane directions may also take place due to slower rate of formation of nuclei by chemical reaction in an ionic medium [365].

The crystallite size (D) and dislocation density (δ) of the deposited FTO films are calculated using the equations 2.3 and 2.4. The crystallite size values calculated from the FWHM of the (110) peak using equation 2.3 are presented in Table 5.2. The film prepared using only 2-methoxyethanol (FTO1) shows least crystallite size value of 42.86 nm, and increasing ethylene glycol volume in the total admixed solution leads to increase in the crystallite size with a maximum value of 65.54 nm for the film made using only ethylene glycol (FTO4). The dislocation density values of all the deposited films calculated using equation 2.4 are given in Table 5.2. The strain (η) in the deposited films is calculated using the Williamson–Hall method (equation 2.5) and the values are listed in Table 5.2. The FTO1 film has a positive strain which is converted to negative strain upon addition of ethylene glycol solvent. Moreover, incorporation of F^- ions leads to an overall reduction in the unit cell volume (Table 5.2). These variations may be due to doping of relatively smaller-sized F^- (1.28 Å) ions compared to O^{2-} (1.35 Å) anion, mainly due to the usage of ethylene glycol which is more polar in nature than 2-methoxyethanol solvent. The lattice parameters (a = b and c) calculated using equation 2.6 (Table 5.2) are found to decrease marginally with increasing ethylene glycol volume. Significant variation in intensity of the XRD patterns of the deposited FTO films is observed due to the use of two

admixed solutions in the solvent. When the aerosol impinges on the pre-heated substrate, evaporation of the solvent takes place, and the precursor clusters hover over the substrate and get adsorbed upon pyrolysis. The nature of the precursor clusters influences the nucleation and growth of the FTO film. Hence, the variation in ratio of the admixed solvents may influence the growth of these precursor clusters, leading to formation of a variety of surface features that will be discussed in section 5.2.3. The growth orientation of the deposited films can be identified by calculating the deviation of the texture coefficient using equation 2.7 [366].

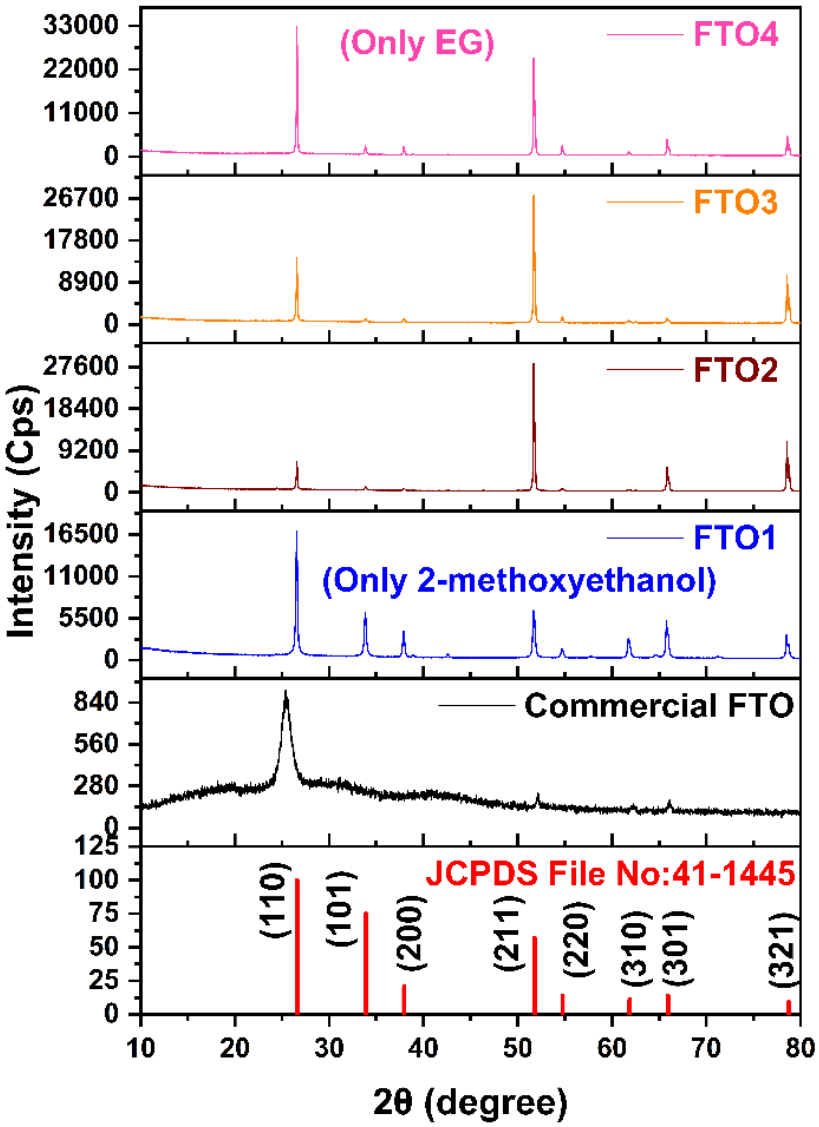

Figure 5.1: X-ray diffraction patterns of the FTO thin films deposited using admixed 2-methoxyethanol and ethylene glycol solvent with varying concentration in comparison with the commercial FTO and the standard cassiterite SnO_2 structure.

Table 5.2: Solvent admixture ratio, microstructural parameters and thickness of the spray-pyrolyzed FTO thin films.

Sample ID	Solvent mixture $C_2H_6O_2$:$C_3H_8O_2$ (ml)	Parameters ($a = b, c$) Å	Crystallite size (D) (nm)	Dislocation density (δ) (m^{-2})	TC_{110}	Volume (V) ^{3}	Micro strain (η)	Thickness (μm)
FTO1	0:100	4.742, 3.192	42.86	5.44×10^{15}	0.88	71.77	1.52×10^{-3}	2.91
FTO2	25:75	4.742, 3.188	54.07	3.42×10^{15}	0.22	71.68	-2.35×10^{-3}	1.24
FTO3	50:50	4.742, 3.186	57.54	3.02×10^{15}	0.52	71.64	-3.79×10^{-3}	1.90
FTO4	100:0	4.742, 3.188	65.54	2.33×10^{15}	1.26	71.68	-0.97×10^{-3}	0.40
Lattice parameters of cassiterite SnO_2 from JCPDS File No.: 41–1445: a = b = 4.7382 Å, c = 3.1871 Å								

The calculated TC_{110} values are given in Table 5.2. Deviation of the texture coefficient from unit value indicates a preferred growth along a particular orientation. The usual trend noted is that the use of a highly polar solvent (polarity parameter of ethylene glycol is 0.79) leads to the growth of a film which is considerably textured along the (110) direction. Similar type of trend using various solvents has also been observed and reported for other binary oxide systems [366–368]. The film FTO1 deposited using only 2-methoxyethanol solvent presents a thickness of 2.91 μm with a porous and mixed morphology (Fig. 5.2 a). Whereas, the film FTO4 deposited using only ethylene glycol solvent presents a thickness of 0.4 μm with uniform and

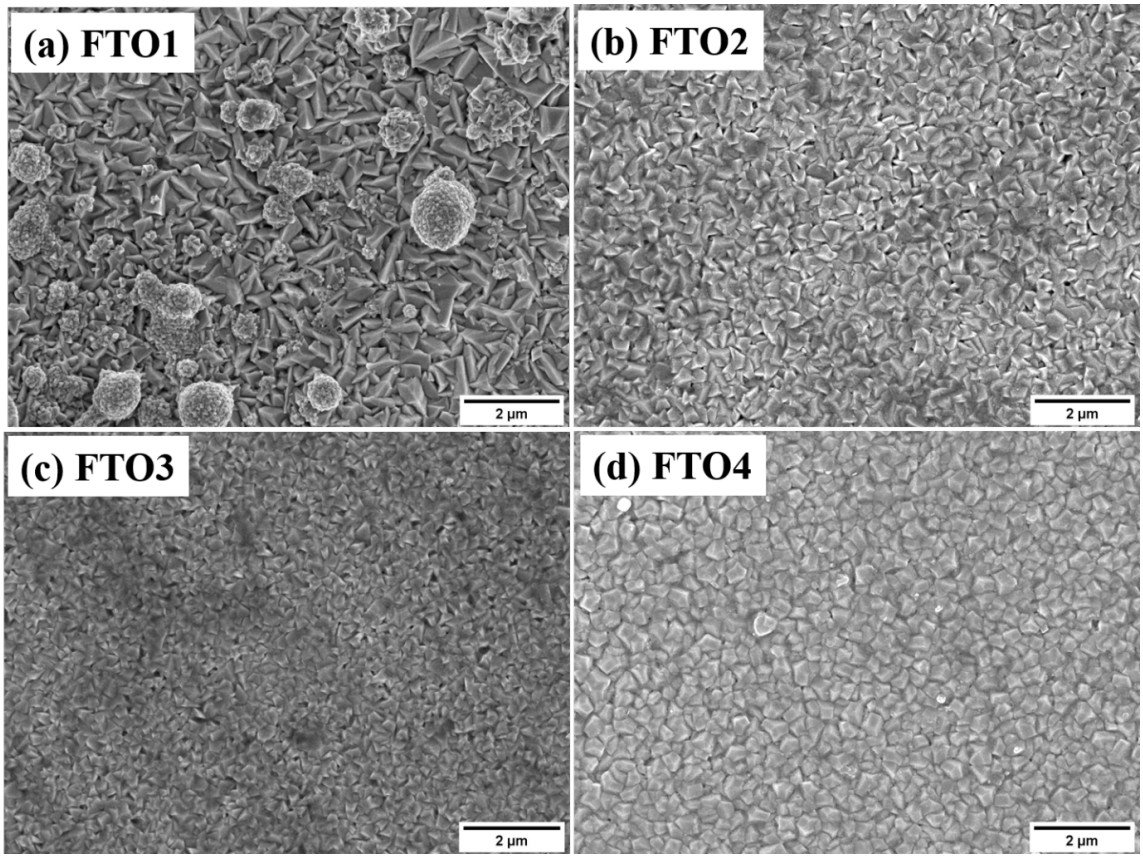

Figure 5.2: (a-d) SEM images of the spray-pyrolyzed FTO thin films by varying the admixed solvent ratio.

dense surface morphology (Fig. 5.2 d). This obvious variation in morphology has resulted due to the difference in boiling points of 2-methoxyethanol (135 °C) and ethylene glycol (197 °C) solvents during pyrolysis of the precursor aerosols based on the Viguie-Spitz mechanism [369]. Low boiling point (135 °C) of 2-methoxyethanol solvent leads to quick evaporation, resulting in a porous and mixed morphology for FTO1, while the ethylene glycol solvent (197 °C) evaporates at a slightly elevated temperature, leading to a dense and uniform morphology for the film FTO4. The choice of solvents result in films with distinct variation in morphology and porosity, leading to appreciable changes in crystallinity as evident from the XRD patterns. The intensity of diffraction peaks (Fig. 5.1) with nearly twice despite the film thickness being nearly seven times lower for FTO4 compared to that of FTO1.

5.2.3 Surface morphology and topology of the films

The surface features of the deposited FTO films analyzed using field emission scanning electron microscopy indicates changes with varying ethylene glycol ratio in the admixed solvent as shown in Fig. 5.2. All the films show smaller-sized particles without significant macroscopic defects like cracks and voids. The 2.91 μm thick FTO1 film (prepared with only 2-methoxyethanol) shows the microstructure of nearly-truncated pyramidal-shaped particles with certain aligned orientation and mild agglomeration with mixed morphology. Similar type of morphology for FTO has been observed by Vanna et al., [370] where there is slight change in film morphology with minimal agglomeration of particles due to the addition of ethylene glycol (Fig. 5.2 b-d). A decrease in particle size is observed for FTO2 and FTO3 films. For the film coated using only ethylene glycol solvent (FTO4), increase in particle size is observed with no sharp grain edges; and the nearly-equal sized grains without any pin holes are distributed uniformly (Fig. 5.2 (d)) where no mixed morphology is observed, and it has the lowest thickness (400 nm) among all the films. These improved homogenous surface features may eventually decrease the reflection loss of light, leading to an increase in transparency for FTO4 film, which will be discussed in section 5.2.5.

In the present work, the variation of solvent ratio vividly affects the surface morphology of the deposited thin films. Kumar et al., also observed change in film morphology by varying different solvents in the case of Al-doped ZnO [371]. From the XRD analysis, it is observed that the crystallite size increases with increase in ethylene glycol solvent volume, but in the case of SEM, the particle size of the film gradually decreases as the volume of ethylene glycol solvent increases. Similar type of observation based on solvent effects has been reported by Muruganantham et al., and Kumar et al., in the case of fluorine-doped SnO_2 and Al-doped ZnO, respectively [371, 372].

From the above results, it is evident that the crystallite size and particle size are not one and the same, since a particle may be made up of multiple crystallites [373]. Crystallites are coherently diffracting domains which are sensitive to incident X-ray radiation and peak broadening effects, whereas, particles which are bigger in size may consist of several such domains and are capable of being imaged by SEM. However, in some specific cases, if the grain is composed of a slightly bigger-sized single crystallites, then the crystallite size and grain size may be the same [374], which is also specific to the method and temperature conditions of preparation.

The surface topography analyzed using optical profiler and recorded over an area of $10 \times 10\ \mu m^2$ in non-contact mode showing the 2D and 3D images is presented in Fig. 5.3. The RMS surface roughness is higher for the thin films deposited using mixed solvents i.e., for FTO2 (b and f) and FTO3 (c and g), but the films FTO1 (a and e) and FTO4 (d and h) deposited using only individual solvents show lower RMS surface roughness. In particular, the film deposited using only ethylene glycol (FTO4) shows roughness around 109 nm which is the lowest value compared to the other deposited films (Table 5.3). This variation in surface roughness is mainly due to the subtle deviation in spray dynamics involved while growing the films. 2-methoxyethanol solvent has low boiling point (135 °C) compared to that of ethylene glycol (197 °C); and hence, it may evaporate before ethylene glycol, resulting in higher RMS surface roughness, and leading to significant variation in film thickness (Table 5.2) as discussed earlier in section 5.2.2 in corroboration with the surface morphology.

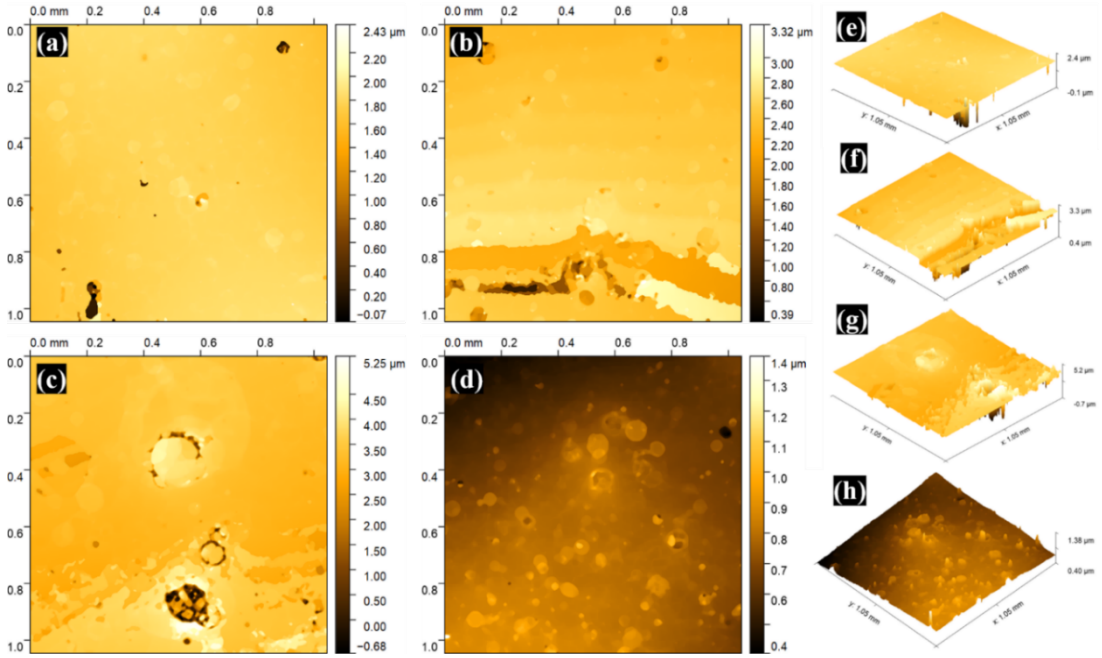

Figure 5.3: Surface topology from optical profiler (a-d) 2D images, and (e-f) 3D images of the FTO thin films spray-pyrolyzed by varying the 2-methoxy ethanol to ethylene glycol admixed solvent ratio from FTO1 to FTO4, respectively.

5.2.4 Surface wettability

The surface wettability nature of the deposited thin films is evaluated using deionized water droplets on their surface using a contact angle measurement unit. The films with increasing ethylene glycol volume turn from hydrophobic to hydrophilic in nature as shown in Fig. 5.4. The film deposited using only ethylene glycol solvent (FTO4) shows lowest contact angle of 52.2°, indicating hydrophilicity, whereas the film deposited using 2-methoxyethanol solvent (FTO1) shows highest contact angle of 104.4°, implying hydrophobicity. Generally, several factors can affect contact angle, namely surface features, functional groups present on the surface, impurities, porosity, surface roughness and surface energy of the films. With increasing surface roughness, the contact angle of hydrophilic material will decrease; whereas in the case of hydrophobic material, it will increase, i.e., hydrophobic material will turn more hydrophobic, and hydrophilic material will turn more hydrophilic with increasing surface roughness [290, 375]. Young's equation 2.10 is valid only for smooth surfaces [128]. For rough surfaces, Wenzel developed a model with a contact angle equation 2.11 as given in section 2.4.7 [256]. The variation in the contact angle may be because of porosity, surface roughness and surface features induced by change in ratio of the admixed solvent.

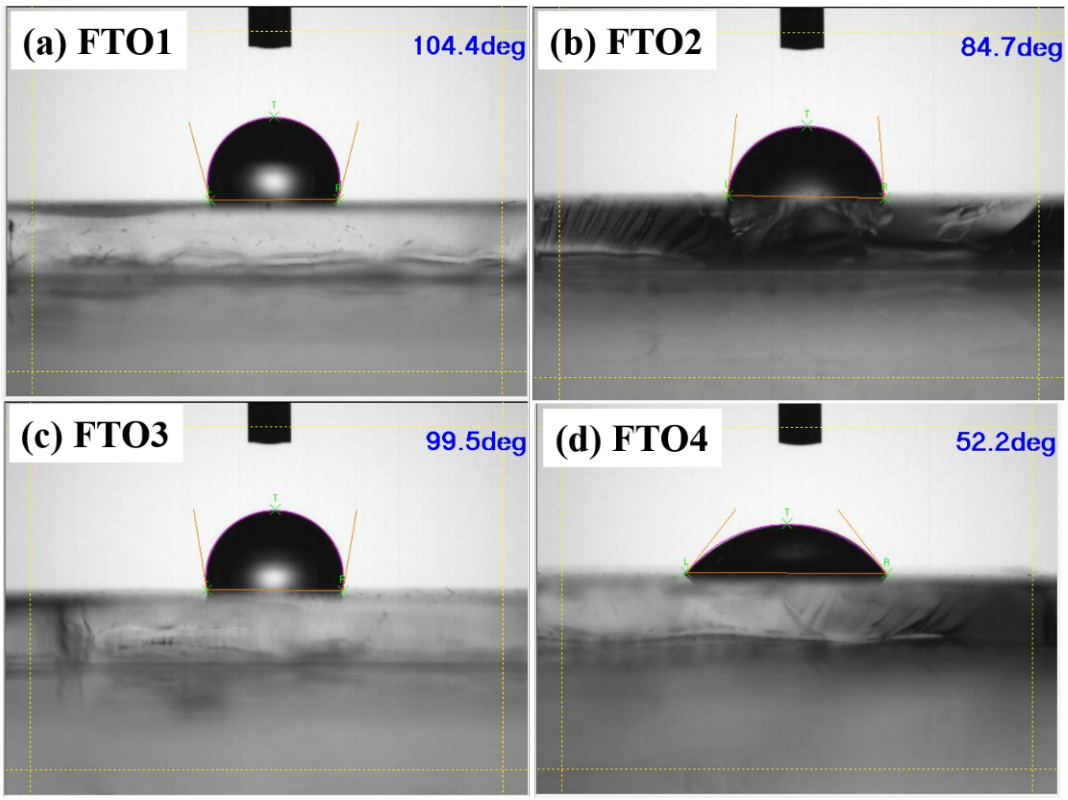

Figure 5.4: (a-d) Contact angle images of the spray-pyrolyzed FTO thin films with varying 2-methoxyethanol - ethylene glycol admixed solvent ratio.

5.2.5 Optical properties

The transmittance and absorbance spectra of all the spray-pyrolyzed FTO films measured using UV-Visible spectrometer are depicted in Fig. 5.5 (a) and (b). The transmittance (T %) values of all the FTO films at 550 nm are given in Table 5.3. From Fig. 5.5 (a), it is observed that the film prepared using only 2-methoxyethanol (FTO1) shows lowest transmittance of 29.62 % (at 550 nm). The variation of ethylene glycol solvent volume in the admixed solution leads to increase in transparency with a maximum value of 75 % for the film prepared using only ethylene glycol (FTO4). The increase in transmittance is mainly because of change in ethylene glycol solvent volume, leading to high transmittance due to low boiling point of 2-methoxyethanol (135 °C) compared to that of ethylene glycol (197 °C). There are three main steps involved in spray dynamics, namely a) atomization of precursor solution, b) transportation of aerosol, and c) decomposition and thin film formation. Among these three steps, decomposition of aerosol onto the preheated substrate is one of the crucial processes of thin film formation. Viguie and Spitz model gives complete information about aerosol dynamics [369]. Low substrate temperature leads to improper decomposition of droplets splashing on the substrate, whereas high substrate temperature leads to evaporation of solvent even before reaching the substrate, and at moderate temperature, the solvent evaporates soon and only the solute precipitate reaches the substrate. Here, the boiling point of 2-methoxyethanol (135 °C) is lower than that of ethylene glycol (197 °C) and therefore, the aerosol droplets evaporate before reaching the substrate, leading to uneven decomposition of the precursors, resulting in lower transparency of FTO1 film compared to that of the FTO4 film prepared using only ethylene glycol. The mixed morphology and considerable agglomeration of grains in FTO1 also result in relatively lower transparency. However, admixing of ethylene glycol in 2-methoxy ethanol results in drastic increase in transparency as observed for FTO2 to FTO4 samples. Eventually, the film prepared using only ethylene glycol solvent, i.e., FTO4, exhibits maximum transparency among the deposited films due to homogeneous film formation. The trend in variation of transmittance (at 550 nm) is depicted in Fig. 5.5 (d). In general, thickness is also one of the major factors that can affect the transmittance of the deposited films apart from factors like defects and morphology. As discussed earlier, the film thickness is found to vary significantly with varying volume of the mixed solvents (Table 5.2); hence, the variation in transmittance may also be attributed to variation in film thickness.

The bandgap of the deposited FTO thin films is calculated using Tauc plot (Fig. 5.5 c) and the variation of bandgap is shown in Fig. 5.5 (d). The bandgap is highest

for the film prepared using mixed solvents (FTO3) and lowest for the FTO4 film prepared using only ethylene glycol solvent. The calculated bandgap values are given in Table 5.3. The decrease in optical band gap value of FTO4 may be due to the existence of optimal concentration of localized defect states [376], and in addition to this, several other possible factors like structural distortions, charged defects, chemical disorder, etc. that contribute to a decrease in band gap have also been postulated [377, 378]. Luminescence emission properties based on defects of the deposited FTO thin films are studied from photoluminescence emission spectra. Fig. 5.6 (a) shows the photoluminescence emission spectra of all the deposited FTO thin films excited by 325 nm wavelength. Strong and highly intense violet emission peak is observed around 390 nm for all the films, representing the transition of electrons from the bottom of the conduction band (CB) to the top of the valence band (VB), which is also called as the near-band-edge (NBE) emission. Two minor peaks observed at 546 nm and 634 nm may be attributed to the presence of oxygen vacancies [379–381]. In metal oxide systems, the dominant defects are usually oxygen vacancies which act as luminescent centres. The types of oxygen vacancies are neutral oxygen vacancy (V_O), singly ionized oxygen vacancy (V_O^+), and doubly ionized oxygen vacancies (V_O^{2+}) with varying charge states. Among these, V_O^+ can act as luminescent centres, and in general, almost all

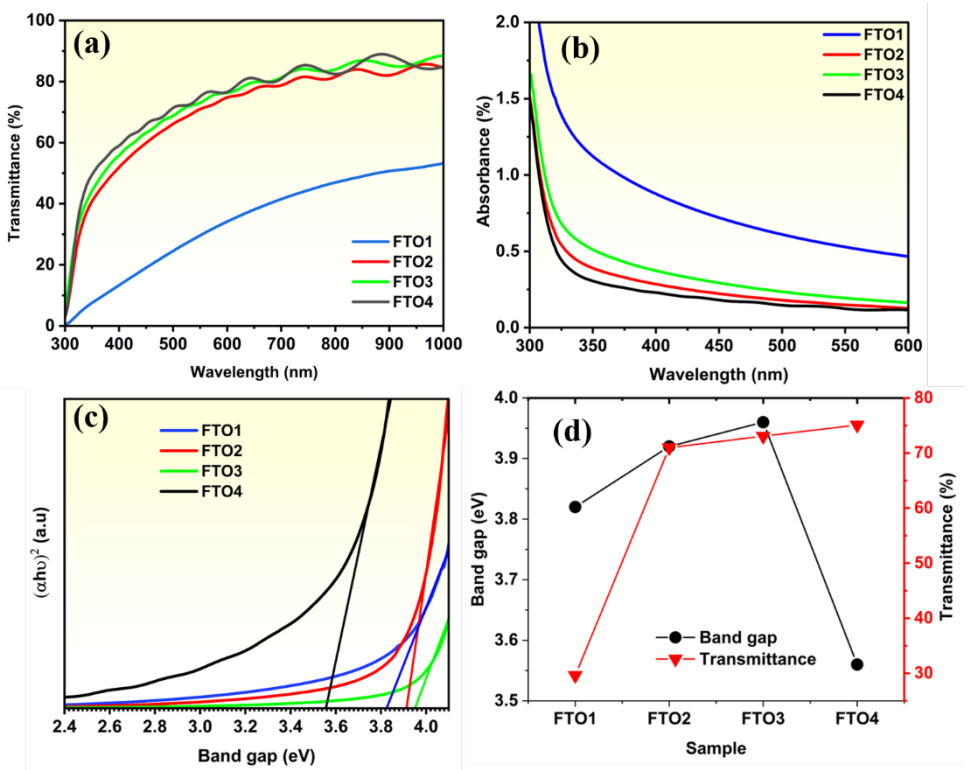

Figure 5.5: (a) Transmittance spectra, (b) absorbance spectra, (c) Tauc plot, and (d) variation of transmittance (at 550 nm) and bandgap of spray-pyrolyzed FTO thin films.

the oxygen vacancies may exist in V_O^+ charge state in SnO_2 lattice [195]. Usually, it is difficult to observe the band-to-band transition in SnO_2 lattice due to the presence of dipole forbidden gap transition [382], thereby limiting certain transitions between the defect levels and the band edges. In addition, the electrical conductivity of the deposited FTO films is n-type due to the presence of excess oxygen vacancy defects, and the position of these defects within the host material plays a critical role in the optoelectronic performance of the films. The defect density can be calculated from Smakula's formula using equation 2.12 [263]. Fig. 5.6 (b) shows the variation of defect density with changing admixed solvent ratio of the deposited FTO thin films. The variation of defect density is high for FTO1 and considerbly lower for FTO4 compared to FTO1, whereas it is much lower for films deposited using admixed solvents (FTO2 and FTO3).

5.2.6 Electrical transport properties

Electrical transport characteristics are analyzed using linear four probe and Hall effect techniques at ambient temperature of the spray-deposited FTO films are given in Table 5.3. Sheet resistance mapping of all the spray-pyrolyzed FTO thin films measured over $5 \times 5\ cm^2$ area is shown in Fig. 5.7, implying low and nearly-uniform resistance values in the middle region, and slight variation near the edges. This difference is due to subtle changes in the spray dynamics with respect to the middle region and the edges. The sheet resistance is measured from one edge to another edge of the deposited thin film. Spray dynamics variation may be due to changes in pressure, leading to variation in the aerosol reaching the substrate and due to temperature difference from the centre to the edges of the substrate. Among all the films, the sample

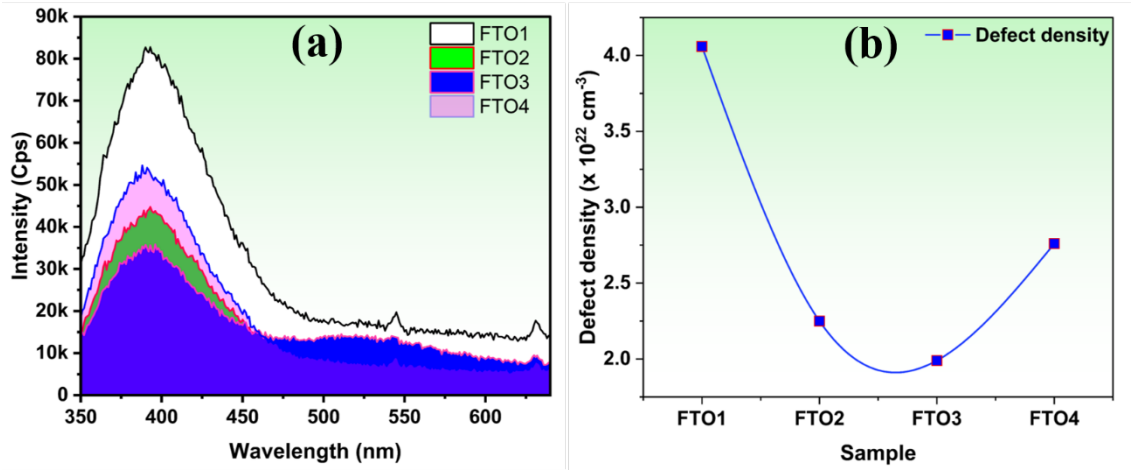

Figure 5.6: (a) Photoluminescence emission spectra and (b) variation of defect density of the spray-pyrolyzed FTO films by varying the admixed solvent ratio.

prepared using only 2-methoxyethanol (FTO1) shows lowest sheet resistance of 6.34 $\Omega/\square$, and the film prepared using only ethylene glycol (FTO4) shows highest sheet resistance of 18.61 $\Omega/\square$.

From the room temperature Hall effect data, all the films show n-type semiconducting nature. Sheet resistance is observed to increase with increasing ethylene glycol volume. However, the resistivity of the films decreases with increase in ethylene glycol volume, leading to increase in conductivity of FTO4 compared to FTO1 which is affected by the significant decrease in film thickness as shown in Table 5.2. Among all films, FTO2 shows the highest mobility of (37.37 $cm^2V^{-1}s^{-1}$), whereas FTO1 shows the lowest mobility (28.35 $cm^2V^{-1}s^{-1}$). FTO3 and FTO4 have moderate mobility of 30.08 and 31.47 $cm^2V^{-1}s^{-1}$, respectively. Change in the solvent from 2-methoxyethanol to ethylene glycol by admixing leads to decrease in film thickness (Table 5.2). The variation in surface morphology may be the reason for the observed variation in conductivity and mobility (Table 5.3). Resistivity change of an order of magnitude is observed from FTO1 to FTO4. The variation in electrical properties of these films may be due to the subtle change in crystallinity with low intensity peaks observed in XRD patterns (Fig. 5.1). Crystallographic defects and morphological features can decrease the carrier mobility, and eventually limit the transport properties. Figure of merit (FoM) is calculated using equation 1.7, and the deduced values are given in Table 5.3. Among all the spray-pyrolyzed films, FTO4 shows highest figure of merit, which indicates that the film prepared using only ethylene glycol solvent results in good crystallinity with significant optical and electrical transport properties.

5.2.7 X-ray photoelectron spectroscopy analysis

Based upon the structural, optical, and electrical properties as well as FoM values, X-ray photoelectron spectroscopy (XPS) is carried out to identify the charge state of constituent elements and to elucidate the chemical bonding states in the optimal FTO4 (prepared using only ethylene glycol) thin film. Figure 5.8 (a) is a wide scan of the FTO4 film which shows the existence of all the constituent elements like fluorine, tin and oxygen with respective charge states. The individual scans of each element are presented in Fig. 5.8 (b-d). From Fig. 5.8 (b), the subtle binding energy peak identified at 688.04 eV confirms the existence of fluorine in F^{-1} state. The peak intensity is very low because fluorine is lower in concentration compared to oxygen content (due to just one electron difference with fluorine), and may also be below the detection limit of the XPS instrument used [383–385]. During film formation at the substrate, F^- ions are promoted to interact with Sn^{4+}, leading to formation of Sn-F or Sn-O bonds [386, 387]. Figure 5.8 (c) shows the XPS spectra of O 1s core level

Table 5.3: Optical and electrical transport parameters of the spray-pyrolyzed FTO thin films by varying the admixed solvent ratio.

Sample ID	Transmittance at 550 nm (%)	Band gap (eV)	sheet resistance R_s ($\Omega/\square$)	RMS Roughness (μm)	Carrier concentration (n) cm^{-3}	Resistivity ρ (Ωcm)	Mobility μ ($cm^2V^{-1}s^{-1}$)	FoM (Ω^{-1})
FTO1	29.62	3.82	6.34	120	1.19×10^{20}	1.84×10^{-3}	28.35	8.19×10^{-7}
FTO2	70.98	3.92	11.05	227	1.21×10^{20}	1.37×10^{-3}	37.37	2.93×10^{-3}
FTO3	73.06	3.96	14.97	448	7.29×10^{20}	2.84×10^{-3}	30.08	2.89×10^{-3}
FTO4	75.09	3.56	18.61	109	2.66×10^{20}	7.44×10^{-4}	31.47	3.06×10^{-3}

obtained for the FTO4 thin film, which consists of three different peaks identified at 530.15, 531.73, and 534.09 eV belonging to metal oxides (Sn-O), oxygen vacancies (V_O), and hydroxyl (-OH) groups, respectively [388]. Fig. 5.8 (d) shows the Sn $3d_{5/2}$ and Sn $3d_{3/2}$ binding energy peaks located at 486.3 and 494.8 eV, respectively, indicating Sn to be present in +4 charge state, and may refer to the Sn-O and Sn-F bonding states in the SnO_2 lattice [339, 389].

5.2.8 Surface work function

Surface work function (Φ) of an electrode plays a pivotal role in the performance of various optoelectronic devices. In semiconductors, the band gap can be tuned with respect to the vacuum level by modifying the donor and/or defect level concentration,

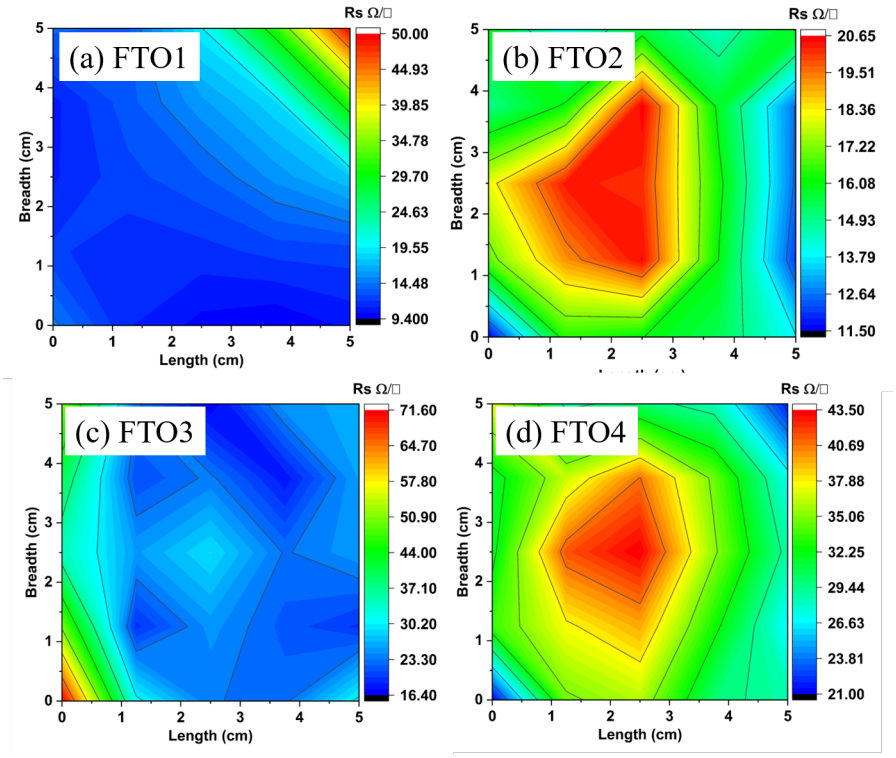

Figure 5.7: (a – d) 2D contour mapping of sheet resistance measured over 5×5 cm^2 of the spray-pyrolyzed FTO thin films by admixing 2-methoxyethanol and ethylene glycol solvents.

yielding a change in the work function [390]. The work function of a semiconductor is based on the Fermi level position with respect to vacuum level ($\Phi = E_{vac}$ - E_F) [391]. The surface work function of the FTO4 electrode is calculated using Kelvin probe measurement operated in ambient air with a 2 mm gold alloy tip [300]. Initially, the Au tip is calibrated with standard gold-coated aluminium substrate (known work function, 5100 meV) by measuring the contact potential difference (CPD) between the gold film and the tip. The work function of the tip is then estimated using the equations 2.13 and 2.14. Here, the work function (Φ) of the tip is estimated to be 4877.51±16.11 meV. Then, the FTO4 sample is loaded and CPD between the sample and tip is also measured using equation 2.15.

The surface work function values of undoped SnO_2 are reported in the range of 4.4 to 5.7 eV. The work function of SnO_2 can be tuned with effective dopants such as Sb, F, etc. Upon doping with appropriate donor element, SnO_2 turns into a degenerate semiconductor, thereby reducing the work function and enhancing the electrical conductivity. The spray-pyrolyzed FTO4 film is found to have a surface work function value of 4.69 eV. This value lies within the spectrum of values reported for doped

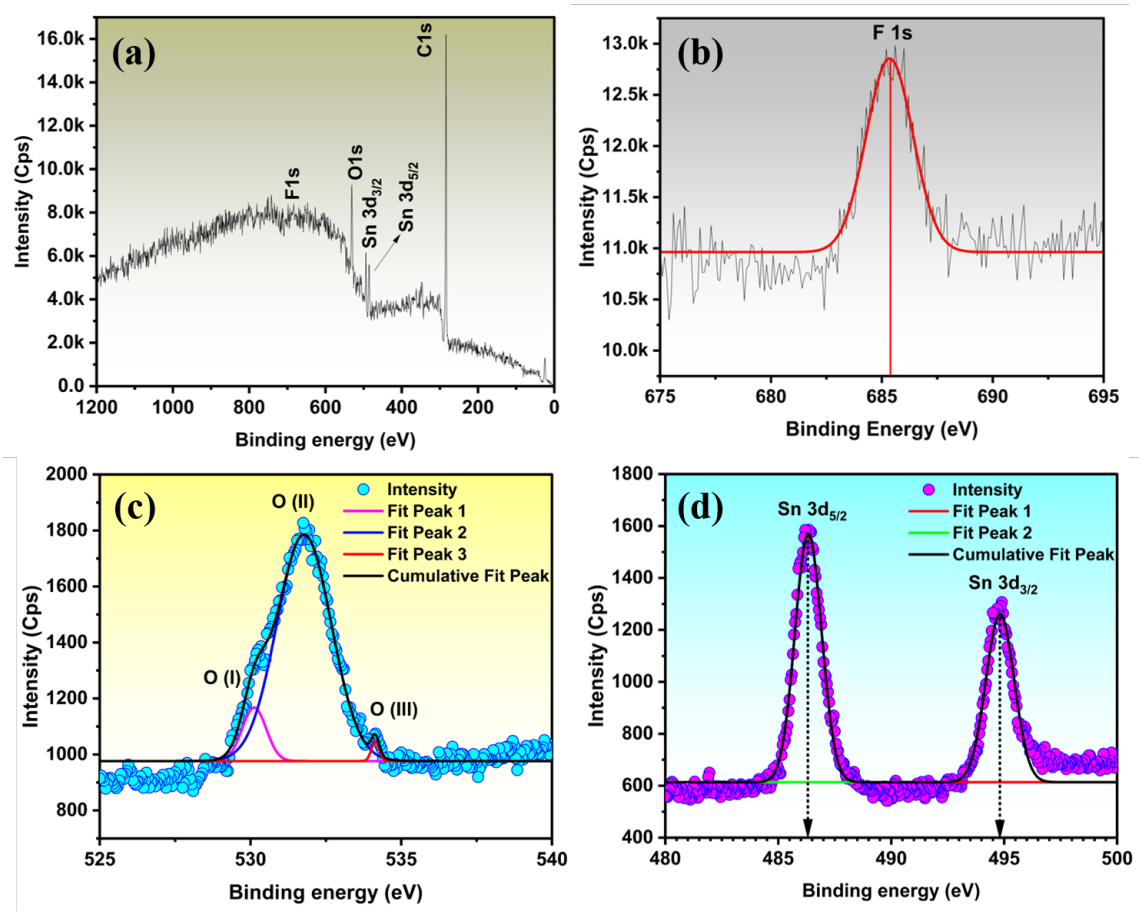

Figure 5.8: (a) Wide scan spectra depicting the presence of constituent elements, (b) F 1s, (c) O 1s, and (d) Sn 3d of optimal spray pyrolyzed FTO4 thin film.

degenerate SnO_2 films. However, the surface work function of FTO4 is higher than that of the standard ITO film which is around 4.3-4.4 eV [303–306] and the work function of FTO which is most cited as 4.4 eV [392–397]. Here, the deposited FTO4 film shows slightly higher work function (4.69 eV) compared to commercially available FTO (4.4 eV) electrodes. The role of work function of TCO in the performance of amorphous/crystalline silicon heterojunction solar cells has been studied through computer simulation [398, 399]. The surface work function of a degenerate semiconductor is also sensitive to factors like surface roughness, preferred orientation, and oxygen stoichiometry of the samples [43]. The variation of surface work function of SnO_2 based TCO is also reported to be dependent on oxygen stoichiometry [400]. However, most of the optoelectronic devices require at least one electrode with a work function sufficiently low to either inject or collect electrons from the lowest unoccupied molecular orbital (LUMO) or conduction band minima (CBM) of a given organic/inorganic semiconductor. Though the surface work function of FTO4 is slightly higher, it has the advantage of being employed in some specific optoelectronic device requirements, wherever this range of value is necessary.

Part-B

5.3 Deposition of anionic F and cationic Nb co-doped SnO_2 thin films

As discussed in earlier section, F is an efficient anionic dopant and several reports exist on F-doped SnO_2 thin films fabricated especially using chemical spray pyrolysis method [15, 345, 353–357, 401]. The ionic radius of O is 1.35 Å which is comparable to the ionic radius of F (1.28 Å). In addition, F has one electron excess than that of O, and therefore, F is used as an effective anionic dopant. Similarly, Nb is one of the cationic dopants explored for appropriate property modification in literature. It has been found that SnO_2 doped with individual Nb and F dopants at specific doping ratio to show excellent properties [402, 403]. Usually, higher doping concentration of F^- leads to increased interstitial impurities in F-doped SnO_2 thin films, which affects their optical and electrical properties [404]. Based on the literature, there is a feasibility to enhance the optical and electrical properties by co-doping SnO_2 in addition to F^- with an suitable element like Nb^{5+} with ionic radius of 0.64 Å, which is very close to that of Sn^{4+} (0.69 Å) [405].

This part of the chapter mainly focus on the deposition of Nb and F (cation and anion) co-doped SnO_2 thin films by using facile spray pyrolysis technique and the

Table 5.4: Precursors, solvents and spray deposition parameters of the NFTO thin films.

Parameters	Specifications
Precursors used	$SnCl_2 \cdot 2\,H_2O$, $NbCl_5$ and NH_4F
Solvents used	D.I. Water, IPA, Ethelyne glycol and HCl
Substrete and pyrolysis temperature	Glass slides $(5 \times 5)\ cm^2$ at $410\ ^\circ C$
Carrier gas/pressure	Compressed moisture free air/ 30 kg cm^{-2}
ON/OFF Duration per spray	$0.5\ s/30\ s$
No of sprays/total spray duration	650 sprays, 5.41 min
Nozzle to substrate distance	35 cm

exploration of their structural, optical and electrical properties as a function of Nb (1 to 5 wt.%) doping by maintaining F (10 wt.%) content as constant. The performance of the deposited thin films is tested as electrodes supplementing commercial ITO, and FTO electrodes in the fabrication of dye sensitized solar cells (DSSC).

5.3.1 Experimental

Materials and deposition conditions are same as part A, the conditions fixed for FTO4 is found to be good with better optoelectronic properties. Here, the additional cation co-dopant (Nb) is doped using $NbCl_5$ (Merck) by dissolving in IPA, all other conditions same like FTO4. A 0.5 M concentration solution of $SnCl_2 \cdot 2\,H_2O$ (89 wt.%), $NbCl_5$ (1 wt.%) and NH_4F (10 wt.%) each was dissolved in D.I water and IPA, in three individual beakers and stirred for 30 min. Few drops (roughly 3 mL) of HCl were introduced into all the beakers to result into a clear solution, and then, all were mixed in one beaker. Ethylene glycol was added to the final solution and then loaded into the spray unit. The cleaned glass substrates were positioned into the spray unit, and the films were deposited using the optimal parameters given in Table 5.4. The substrate temperature was maintained at 410 °C for all the thin films [406, 407]. The concentration of fluorine (10 wt.%) is kept constant and Nb is varied from 1-5 wt.% (1 wt.%, 2 wt.%, 3 wt.%, 4 wt.% and 5 wt.%) as cationic co-dopant into the SnO_2 lattice and the co-doped SnO_2 thin films will hereafter be referred to as NFTO1, NFTO2, NFTO3, NFTO4, and NFTO5, respectively. These co-doped samples are collectively referred to as NFTO thin films.

5.3.2 Structural analysis of NFTO thin films

It is essential to know the structural and crystalline aspects to confirm the phase purity and grain growth orientation of the deposited thin films in order to correlate with the

optical and electrical transport properties at a later instance. Figure 5.9 shows the X-ray diffraction patterns of all the spray-pyrolyzed NFTO thin films deposited at 410 °C over an area of $5 \times 5\ cm^2$, showing polycrystalline nature. The reflection planes of all the films, i.e. (110), (101), (200), (210), (211), (220), (310), (301) and (321), are identified against 2θ value at 26.61°, 33.89°, 37.95°, 42.63°, 51.78°, 54.75°, 61.87°, 65.93° and 78.71°, respectively. All these planes are in concurrent with the JCPDS file #: 00-041-1445 of tetragonal SnO_2 crystal structure with space group P42/mnm. Peaks corresponding to other plausible phases like Nb_2O_5, NbO_2F, NbF_5, metallic Nb, SnF_2, SnO, and SnO_3 are not observed. The crystallite size for all the spray-coated thin films is measured using the Scherrer formula given in equation 2.3 [250]. Though the FWHM is a collective contribution of grain size (i.e grains and boundaries), micro-strain and stacking faults. Here Scherrer formula is used to calculate the grain size from the X-ray peak broadening effects resultant from the grain boundaries and the micro-strain and stacking faults from Williamson-Hall (W-H) plot. The calculated crystallite size is found to decrease up to 3 wt.% of Nb co-doping and then increase for 4 and 5 wt.% of Nb co-doping (Table 5.5). A plausible explanation is that, up to 3 wt.% of Nb co-doping would have increased the nucleation density resulting into smaller sized crystallites and for further increase in dopant concentration the crystallite size increased and similar kind of observation was reported by Sayed et al., upon doping of cobalt into the SnO_2 lattice [408]. From Fig. 5.9 (b), all the films show a preferred orientation along the (301) plane. The change in preferred orientation is due to precursor solution chemistry, [409, 410] spray precursor solution molarity, [411] incorporation of Nb in the SnO_2 structure [412, 413] and substrate temperature of the sprayed SnO_2 [414]. In the present study, variation in texture coefficient is mainly due to the variation in Nb co-doping concentration in F-doped SnO_2 thin films. Dislocation density is estimated for all the films using equation 2.4, and it

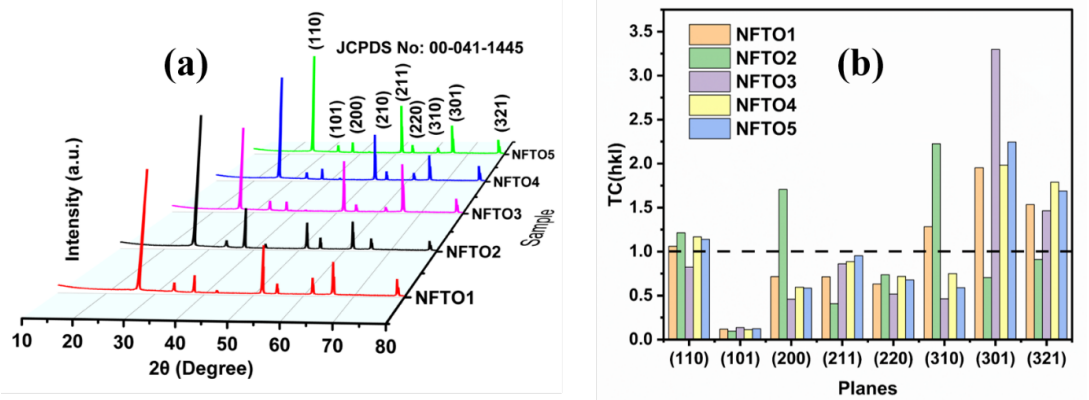

Figure 5.9: (a) XRD patterns and (b) variation of texture coefficient of spray deposited Nb and F co-doped SnO_2 thin films.

Table 5.5: Structural parameters and film thickness of the spray coated F and Nb co-doped SnO_2 thin films.

Sample ID	Nb:F:Sn composition ($Wt.\%$)	Lattice parameters (a=b,c) (Å)	Crystallite size (D) (nm)	Dislocation density (δ)(m^{-2})	Volume (^{3})	Stacking faults (SF)	Micro strain (ε)	Thickness (μm)
NFTO1	1:10:89	4.744, 3.189	60.16	2.76×10^{14}	71.77	3.67×10^{-3}	-1.48×10^{-3}	1.14
NFTO2	2:10:88	4.744, 3.186	59.28	2.85×10^{14}	71.70	3.73×10^{-3}	-2.18×10^{-3}	1.15
NFTO3	3:10:87	4.746, 3.191	54.90	3.32×10^{14}	71.87	4.02×10^{-3}	-1.42×10^{-3}	1.74
NFTO4	4:10:86	4.746, 3.191	57.93	2.98×10^{14}	71.87	3.81×10^{-3}	-0.5×10^{-3}	1.38
NFTO5	5:10:85	4.746, 3.189	58.22	2.95×10^{14}	71.83	3.80×10^{-3}	-1.8×10^{-3}	1.4

increases with Nb concentration. The microstrain of the deposited films is estimated from the W-H plot. All the films show negative strain since the substitution of F^- leads to a decrement in unit cell volume as seen in Table 5.5, which may be due to doping of relatively smaller ionic radius F^- (1.28 Å) compared to that of O^{2-} (1.35 Å). Negative value of strain indicates that the films are in a compressive state [415]. However, the strain is reduced upon co-doping of Nb and shows the least value for 4 wt.% Nb and F co-doped SnO_2. Lattice parameters (a = b, c) are calculated using equation 2.6, and the calculated values are well matched with standard values without much variation (Table 5.5). The stacking faults (SF) of the spray-deposited NFTO thin films are given in Table 5.5. Stacking fault is the fraction of layers that undergo sequential stacking faults in a crystalline lattice. It can be determined using the equation 2.8 [416]. All the structural parameters, including microstrain, dislocation density and stacking faults, increase with doping content up to 3 wt.%, and then decrease for 4 and 5 wt.% of Nb concentration (Table 5.5). The decrease in δ, ϵ, and SF for 4 wt.% Nb shows minimum defect concentration in NFTO4 film [415].

5.3.3 Surface morphology of NFTO thin films

The surface morphology measurements was performed to explore the dopant induced features and asperities, which will further help to correlate with the optoelectronic properties of the spray pyrolyzed films. The surface aspects of the spray-pyrolyzed thin films were analyzed using field emission scanning electron microscope (FESEM). Figure 5.10 shows the FESEM images of all the spray-deposited NFTO thin films. A vivid change in the surface features is observed with increasing Nb doping concentration in SnO_2: F (10 wt.%). For lower concentration of Nb doping (NFTO1), most of the grains appear to be irregular in shape, with some possessing pyramidal or prismatic surface morphology with a compact design and grain size of nearly 250–400 nm without any sharp edges. However, when the doping concentration is increased to >1 wt.% of Nb, a vivid change in morphology is observed with a decrease in average grain size, and all of them have a nearly truncated-pyramidal shape with sharp edges.

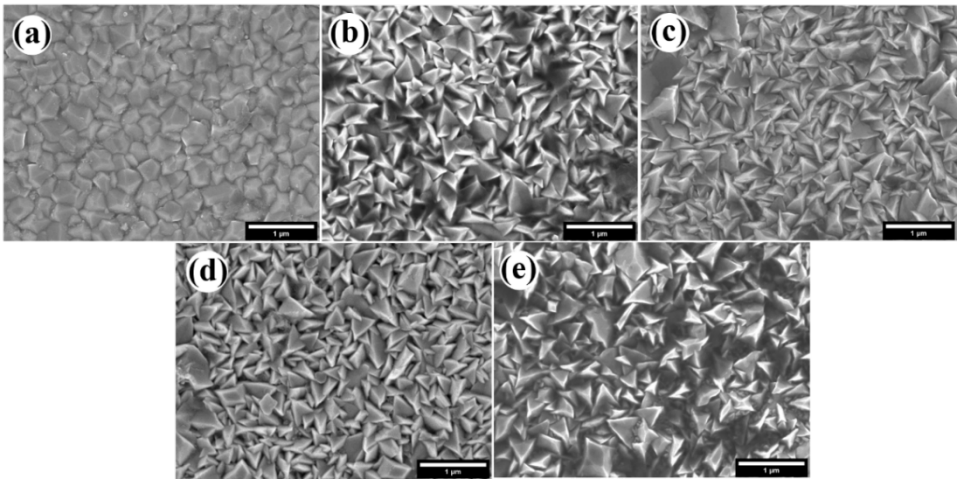

Figure 5.10: FESEM images of the spray-deposited (a) NFTO1, (b) NFTO2, (c) NFTO3, (d) NFTO4, and (e) NFTO5 thin films.

The particle size distribution of all the deposited films is shown in Fig. 5.11, and the average grain size decreases with increasing Nb co-doping concentration. Among the deposited films, NFTO4 shows dense distribution of well-structured particles within the 200-400 nm range (Figure 5.12 d and 5.11 d). Higher concentration of Nb leads to mixed (lower and higher) grain-sized particles from 100 nm to 600 nm.

Several authors have reported similar kind of needle-shaped morphology for F doped SnO_2 thin films deposited via ultrasonic spray pyrolysis technique [361,417,418]. Deyu et al., reported similar type of morphology for Al doped SnO_2 thin films deposited by ultrasonic spray pyrolysis [419]. Ramarajan et al., reported polyhedron shaped morphology for Nb doped SnO_2 thin films coated using spray pyrolysis technique [420]. In the case of higher doping concentration, the particles become more sharper and are randomly oriented which may lead to increased scattering

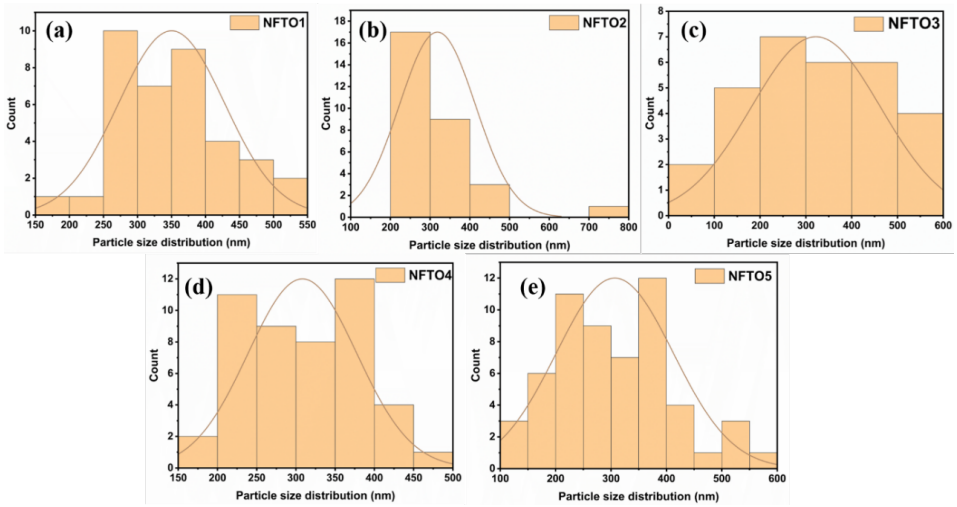

Figure 5.11: Particle size distribution of the spray-deposited (a) NFTO1, (b) NFTO2, (c) NFTO3, (d) NFTO4, and (e) NFTO5 thin films.

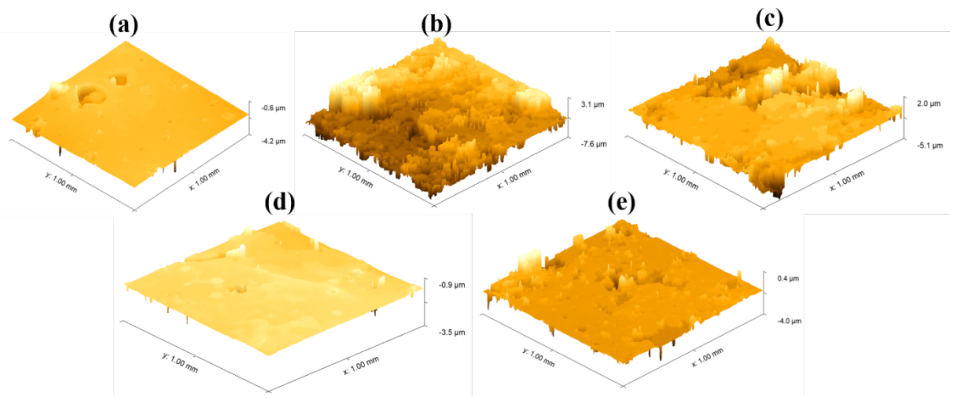

Figure 5.12: 3D images of spray-deposited (a) NFTO1, (b) NFTO2, (c) NFTO3, (d) NFTO4, and (e) NFTO5 thin films obtained from optical profilometer.

effect of light thereby influencing the transmittance of the films. In general, the grain/crystallite size and particle size are not one and the same, since a particle may be made up of multiple crystallites [372]. Crystallites are coherently diffracting region amidst the presence of grain boundaries which are sensitive to the incident X-ray radiation, and therefore peak broadening effects are dominant due to the defective nature of the grain boundaries. Particles that are bigger in size may consist of several such regions that are being imaged by the FESEM microscope. However, in specific cases, if the film is composed of a slightly bigger-sized crystallites, then the grain/crystallite size and particle size may be one and the same [373] as discussed in the section 5.2.2 Akbari et al., reported that the crystallite and particle size both are identical in the case of single crystal alumina nanoparticles [421]. However, the spray coated thin films are polycrystalline/granular in nature with significant grain boundaries.

Optical profiler measurements were performed to evaluate the surface topography aspects in addition to the SEM measurements which may help to correlate with the contact angle measurements which is also performed to elucidate the surface wettability properties with a liquid electrolyte when these spray pyrolyzed electrodes are utilized as components in a device. The surface topography of the spray-coated thin films is also characterized by an optical profilometer over a relatively larger area of 1 mm x 1 mm. The 3D images of NFTO thin films obtained from the optical profilometer are shown in Fig. 5.12. Figure. 5.12 (a) and (d) seems to be comparatively smooth than the other films whose roughness is primarily due to the increasing Nb concentration, that is influencing the nucleation and growth process of the film. The unintentional subtle deviation in deposition parameters can also affect the surface properties of the thin films and is inherent to spray pyrolysis technique. The large scale variation in surface topography must be related to other features, such as large sized particles resulting from subtle deviation in the spray deposition process.

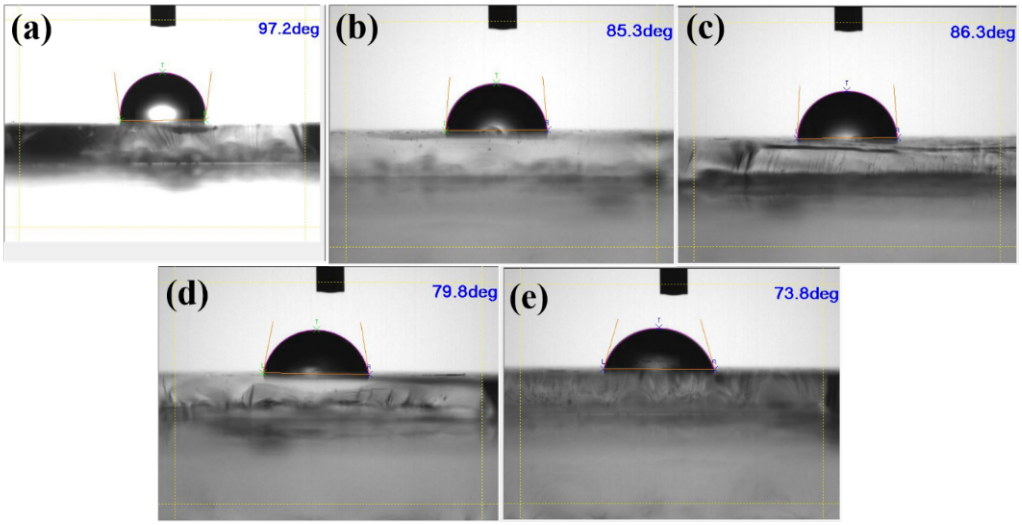

Figure 5.13: Contact angle images of spray-deposited (a) NFTO1, (b) NFTO2, (c) NFTO3, (d) NFTO4, and (e) NFTO5 thin films.

5.3.4 Contact angle analysis of NFTO thin films

Contact angle measurement is employed to obtain the surface wettability nature of the deposited NFTO thin films. Based on the contact angle value one may find the suitability of these films for appropriate applications. The wettability nature of the thin films mainly depends on the contact angle between solid, liquid and vapour interfaces. Here, the contact angle of the deposited thin films are analyzed using a deionized water droplet. The contact angle images of the water droplet on the surface of the deposited NFTO thin films are shown in Figure 5.13. From the figures, the contact angle is found to decrease with increasing Nb wt.%, and the film turns from hydrophobic (97.2°) to hydrophilic in nature (73.8°). However, the rough surface of the NFTO2 influences the decrease in contact angle compared to that of NFTO3. Overall, the increase of Nb concentration in the F-doped SnO_2 thin films results in the decrease of contact angle, representing hydrophilic nature.

5.3.5 Optical properties of NFTO thin films

The optical properties like transmittance, absorbance, and optical band gap of the spray-coated Nb and F co-doped SnO_2 thin films analyzed using UV-Vis spectrometer are shown in Figure 5.14. Figure 5.14 (a) shows the transmittance vs wavelength plot and Fig. 5.14 (b) shows the absorbance vs wavelength plot. The change in transmittance at 550 nm is shown in Fig. 5.14 (d). Transmittance increases with Nb concentration and reaches a maximum value for 4 wt.% of Nb and decreases for higher doping concentration ($>$ 4 wt.%). The transmittance of the thin films mainly depends on the type of dopant, doping concentration, film thickness, surface

roughness, deposition parameters and microstructure. From the surface analysis, it is evident that NFTO4 shows a relatively smoother surface, and therefore, presents higher transmittance since the reflection and scattering losses of the incident radiation are minimal. In the case of NFTO5, as shown in the FESEM image (Fig. 5.10 e), sharp edged particles are randomly oriented which leads to scattering of photons resulting in decrease of transmittance [422]. It can be seen from Fig. 5.14 (b) that the NFTO thin films begin to absorb light in the range of 300–350 nm, which is with the energy band gap of the material. The bandgap was calculated using tauc plot from the absorption coefficient 'α' by fitting the linear region and by extrapolating it to $\alpha = 0$ as shown in Fig. 5.14 (c). The calculated band gap values are given in Table 5.6 and are found to increase with Nb content up to 4 wt.%, and thereafter decrease. Figure 5.14 (d) shows the band gap variation with the increase in Nb wt.%, and it shows a systematic increase in the band gap up to Nb 4 wt.% (NFTO4), and it decreases for Nb 5 wt.% (NFTO5). The increase in band gap is mainly due to the Moss-Burstein effect, which occurs from the doping of an aliovalent element to the F-doped SnO_2 as empty states are filled in the conduction band and the Fermi level

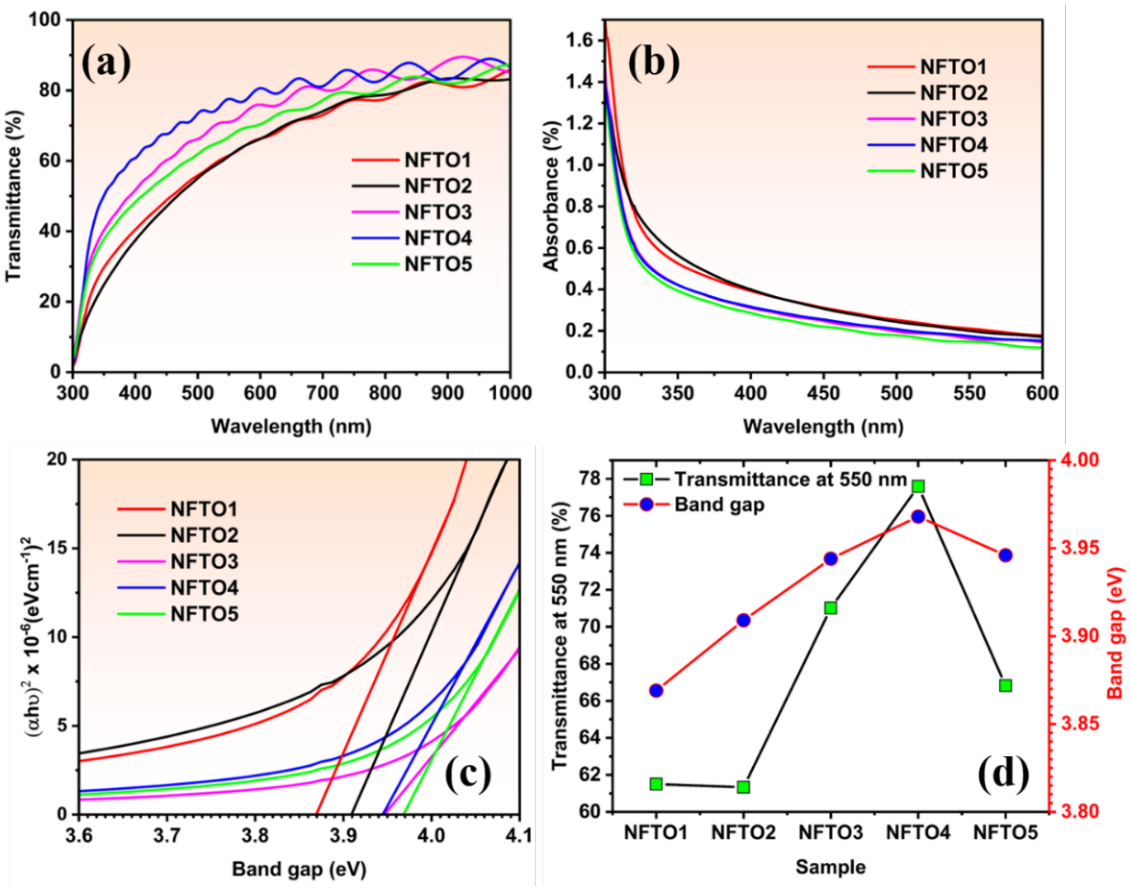

Figure 5.14: (a) Transmittance spectra, (b) absorption spectra, (c) Tauc plots, and (d) variation in transmittance and band gap of the spray-deposited Nb and F co-doped SnO_2 thin films.

rises. Likewise, when the doping concentration is increased to maximum, the band deformation would eventually occur, resulting in lowering of the band gap. Here, the decrease in band gap for doping concentration of 5 wt.% Nb (NFTO5) can be related to the deformation of the bands [423–425].

Photoluminescence (PL) emission properties were obtained at room temperature by exciting the films using 330 nm wavelength. The emission spectra of the deposited NFTO thin films are shown in Fig. 5.15 (a). A broad emission peak in the range of 350-450 nm with peak around 390 nm of energy 3.18 eV (violet emission) is observed in all the NFTO thin films. This emission represents the transfer of electrons from minima of the conduction band to maxima of the valence band, and it is also referred to as the near band edge emission (NBE). The broad violet emission peak also consists of two shoulder peaks at 365 nm (3.39 eV) and 451 nm (2.75 eV). Babar et al. reported similar results in spray-pyrolyzed undoped and Sb-doped SnO_2 thin films. Ramarajan et al. also obtained similar kind of results in spray-pyrolyzed Ba and Sb co-doped thin films [406,426]. The PL emission intensity of the NFTO thin films increases with an increase in Nb concentration and shows a maximum for 4 wt.% Nb (NFTO4); and thereafter, it decreases for further increase in Nb concentration. Usually, oxygen vacancies are the most common defects that can be observed in the deposited NFTO thin films. These defects existing in the films act as luminescent centres, giving rise to prominent defect level emission. The well-known oxygen vacancies are neutral (V_O), singly ionized (V_O^+), and doubly ionized oxygen vacancies (V_O^{2+}). In most cases, oxygen vacancies exist in singly-ionized (V_O^+) charge states in SnO_2 [195]. In addition, the n-type electrical conductivity of the deposited NFTO films is also due to excess of oxygen vacancy defects in the films apart from the dopant contribution of free electrons. The high PL intensity is mainly due to increase in trapped states within

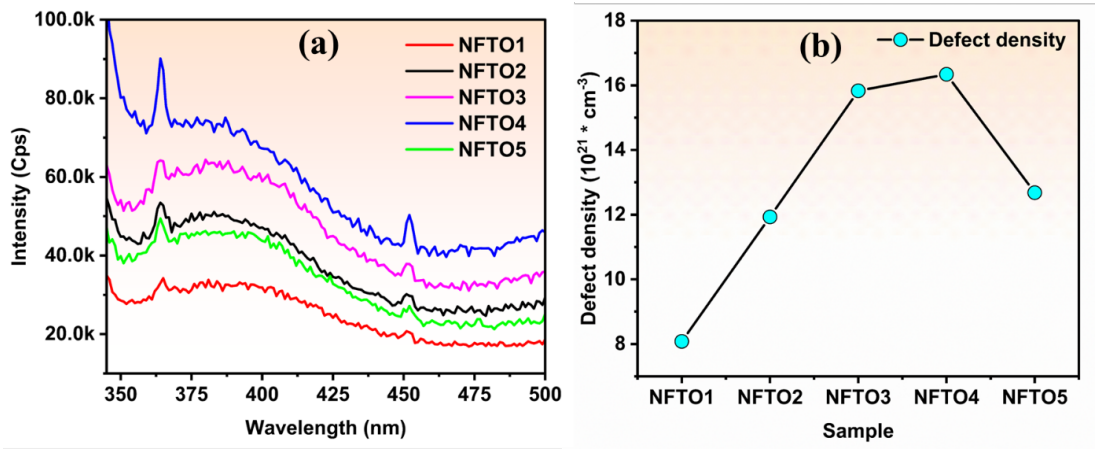

Figure 5.15: (a) Photoluminescence emission spectra and (b) variation in defect density of the spray coated Nb and F co-doped SnO_2 films.

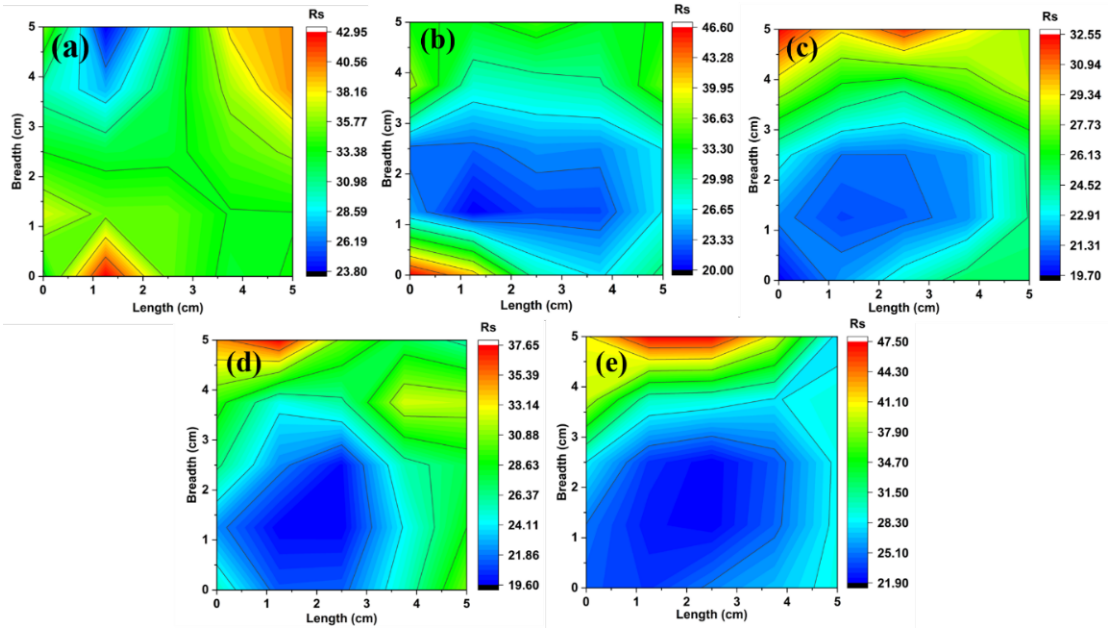

Figure 5.16: 2D contour mapping of the sheet resistance of spray deposited (a) NFTO1, (b) NFTO2, (c) NFTO3, (d) NFTO4, and (e) NFTO5 thin films.

the band gap because of interaction between high density of oxygen vacancies [426]. From the PL emission spectra, the defect density (cm^{-3}) of the coated NFTO thin films is estimated based on Smakula's equation 2.12 [427]. The defect density variation with Nb co-doping concentration is shown in Figure 5.15 (b), where NFTO4 shows highest defect density in the order of 10^{21} (cm^{-3}), similar range of defect density were reported in literature [263, 428–431]. The defect density increases up to Nb 4 wt.% (NFTO4 film), and it decreases for further increase in concentration, leading to a quenching effect. Moreover, the increasing free carrier absorption leads to quenching in luminescence properties [263, 406].

5.3.6 Electrical properties of NFTO thin films

The most important factor of an TCO is its sheet resistance and electrical transport parameters, for which the linear four probe and Hall effect measurements were performed respectively. The measured electrical parameters will indicate the sheet resistance range and its suitability for use in appropriate optoelectronic devices. In the present study, for the deposited NFTO thin films to be used as effective TCE in various applications, the electrical transport property measurements were performed at room temperature using linear four probe and Hall effect techniques in Table 5.6. Figure 5.16 shows the 2D contour mapping of sheet resistance tested over 5×5 cm^2 of the deposited NFTO thin films. The dark blue colour region shows the lowest sheet resistance of the films, and it changes with co-doping of Nb. There is a slight

increase in sheet resistance from the center to edges of the film which is mainly due to the spray-induced temperature gradient occurring due to lack of proper contact of the substrate with the hot plate compared to the center region, and also due to the pressure difference of the aerosol impinging on the substrate from the centre to the edges, leading to change in spray dynamics.

Among all the films, NFTO4 (Fig. 5.16 d) shows lowest sheet resistance with good uniformity at the centre. Stoichiometric SnO_2 (with very limited oxygen vacancy) has high sheet resistance, whereas, when higher concentration of oxygen vacancies are formed (without any donor element doping), the sheet resistance value decreases drastically, which is an indication that oxygen vacancies serve partly in contributing free carriers to the lattice aiding improvement in electrical conductivity [432, 433]. Also, oxygen vacancies are reported to act as electron traps thereby reducing the electrical conductivity [434–438]. However, in the literature, it is also widely reported from both these viewpoints, in some articles it is reported to act as electron traps, resulting in the lesser conductivity, whereas, several reports also claim that oxygen vacancies to increase the charge carrier density showing improved conductivity [439–443]. The importance of such oxygen vacancy induced intra-band defects, particularly in charge separation and transport, is thus still largely debated in literature [444]. As observed from the photoluminescence emission data, the oxygen vacancy is increased with co-doping of niobium leading to improved conductivity which was also reported previously [433, 445].

Further, the electrical transport properties of the deposited films were performed using hall effect measurements. Considering the sheet resistance deviations at the periphery of the spray pyrolyzed film, an area of $1 \times 1\ cm^2$ sample was chosen from the 'homogenous' region. Firm electrical contacts of the gold coated probes are ensured by obtaining the I-V curves prior to the actual electrical transport parameter measurements. The Hall effect experiment reveals that all the deposited NFTO thin films have n-type semiconducting behaviour. All the films show resistivity in the order of $10^{-3}\ \Omega cm$ and mobility above 40 $cm^2V^{-1}s^{-1}$. However, NFTO4 shows a higher carrier concentration of $7.42 \times 10^{19}\ cm^{-3}$ (Table 5.5) with a higher band gap (3.968 eV) and high figure of merit value ($5.01 \times 10^{-3}\ \Omega^{-1}$). In general, doping of Nb^{5+} into the Sn^{4+} sites increase the free carrier charge density resulting in enhanced conductivity of the film. In addition to this, increase in oxygen vacancy defects also helps increase in conductivity of the film, and this will also influence the mobility of the carriers [446, 447]. Similar kind of results were reported by Ramarajan et al., in Nb doped SnO_2 thin films deposited by spray pyrolysis technique [406].

5.3.7 Figure of merit of NFTO thin films

Figure of merit (FoM) is used to assess the applicability of the TCEs for various optoelectronic applications, including solar cells. FoM can be calculated using sheet resistance and transmittance (at 550 nm) values. In 1972, Fraser et al. [47] estimated the FoM as a ratio of transmittance and sheet resistance. Later in 1976, Haacke modified the FoM equation such that it can be applicable for transmission of more than 90 %. The revised equation 1.7 is used to calculate the FoM of the TCE thin films. The measured FoM values are given in Table 5.6, and it is found that NFTO4 has the highest value ($5.01 \times 10^{-3}\ \Omega^{-1}$). Based on the FoM value, further characterizations (Kelvin probe and XPS measurements) were performed only for the NFTO4 thin film.

5.3.8 Surface work function of NFTO thin films

The Kelvin probe measurement technique is used to calculate the surface work function of the deposited NFTO4 electrode [300, 390]. In general, pure SnO_2 has surface work function values in the range from 4.4 to 5.7 eV [397, 448, 449] and as discussed section 5.2.8, it can be modified by doping with suitable dopants such as F, Sb, Ta, etc. The measured surface work function of the spray-deposited NFTO4 electrode is found to be 4687.85 meV which lies within the reported surface work function values of doped degenerate SnO_2 thin films. Though the measured work function of NFTO4 is slightly higher compared to commercial ITO and FTO films (4.3-4.4 eV) [303–306, 392–397], it has the benefit of being used in specific optoelectronic device components, wherever this range of value is necessary. However, the measured work function is lower than the reported spray coated Nb doped SnO_2 thin film [406], which may be due to the effect of co-doping of fluorine. Most of the optoelectronic devices prefer low work function electrodes for either collection or injection of electrons from the CBM or LUMO of a given inorganic or organic semiconductor, respectively.

5.3.9 X-ray photoelectron spectroscopy of NFTO thin films

The X-ray photoelectron spectroscopy (XPS) measurement is carried out for the optimal NFTO4 thin film which shows highest FoM compared to other films. Figure 5.17 (a) shows the wide scan of NFTO4 thin film which consists of the constituent elements, namely Nb, F, Sn, and O. From Figure 5.17 (b), it is identified that the Sn $3d_{3/2}$ and Sn $3d_{5/2}$ are located at 495 eV and 486.52 eV, respectively representing the charge state of Sn^{4+} indicating the Sn-O and Sn-F bonding in the SnO_2 lattice [339, 389, 450, 451]. The core level XPS spectra of O 1s deconvoluted and fitted

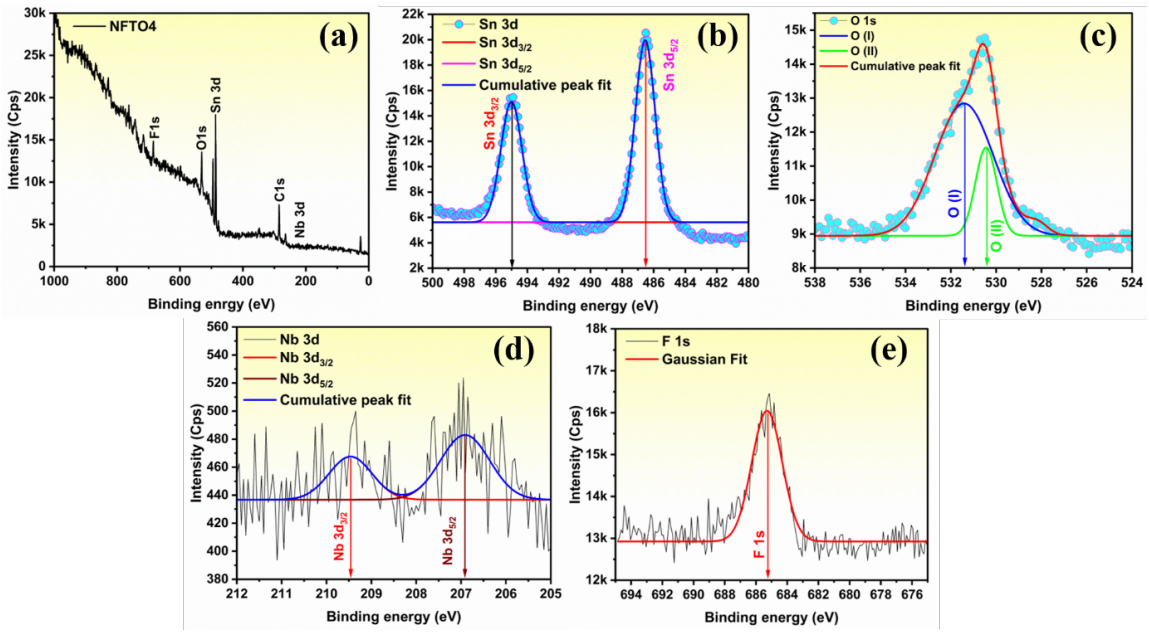

Figure 5.17: XPS spectra of spray coated NFTO4 thin film (a) survey scan, individual scan of energy levels of elements (b) Sn 3d, (c) O 1s (d) Nb 3d and (e) F 1s.

to a Gaussian profile is shown in Figure 5.17 (c). The deconvoluted peaks are located around 530.44 eV and 531.41 eV representing the hydroxyl (-OH) groups and oxygen vacancies (V_O), respectively [388, 406]. Figure 5.17(d) represents Nb in +5 charge state, and the peaks located around 206.9 eV and 209.46 eV represent the Nb $3d_{5/2}$ and Nb $3d_{3/2}$ levels, respectively [452]. The individual scan of F 1s level at 685.28 eV with the Gaussian fit, reveal the existence of F in the film in -1 charge state (Fig. 5.17 e) [383, 384, 453–455].

5.4 Application of the electrodes

In this section, all the FTO films stabilized in part-A and the films co-doped with F and Nb (NFTO) of part-B are combinedly presented and discussed.

5.4.1 Dye sensitized solar cell using FTO and NFTO thin films

DSSCs are cost-effective solar cells compared to conventional p-n junction solar cells. The working principle of DSSC is quite different from the conventional p-n junction photovoltaic devices. In p-n junction solar cells, light absorption and carrier transportation is performed by the semiconductor itself. However, in the case of DSSCs, light is absorbed by the dye (sensitizer), and then the charge carriers reach the semiconductor attached to the dye. Charge splitting takes place at the interface of the dye/semiconductor material via photo-induced electron injection from the dye to the

Table 5.6: Optoelectronic and transport parameters of the spray-coated NFTO films.

Sample ID	Transmittance at 550 nm (%)	Band gap (eV)	Sheet Resistance R_s ($\Omega/\square$)	Carrier Concentration (n) cm^{-3}	Resistivity ρ (Ωcm)	Mobility μ ($cm^2V^{-1}s^{-1}$)	FoM (Ω^{-1})
NFTO1	61.5	3.869	23.92	3.86×10^{19}	3.44×10^{-3}	46.91	3.23×10^{-4}
NFTO2	61.34	3.909	15.08	6.89×10^{19}	1.73×10^{-3}	52.14	5.00×10^{-4}
NFTO3	71.02	3.944	14.37	6.17×10^{19}	2.50×10^{-3}	40.39	2.27×10^{-3}
NFTO4	77.59	3.968	15.77	7.42×10^{19}	2.05×10^{-3}	40.98	5.01×10^{-3}
NFTO5	66.82	3.946	16.76	4.70×10^{19}	2.34×10^{-3}	56.59	1.05×10^{-3}

Table 5.7: The photovoltaic parameters of DSSC devices fabricated using the spray-pyrolyzed and commercially available FTO and NFTO thin film electrodes.

	Device ID	Open circuit (V_{oc}) (V)	Current density (J_{sc}) (mA/cm^2)	Fill factor (FF) (%)	Efficiency (η) (%)
Part-A	D_{CFTO}	0.68	9.77	44.85	2.99
	D_{FTO1}	0.67	5.36	21.46	0.77
	D_{FTO2}	0.68	7.27	26.54	1.32
	D_{FTO3}	0.68	5.44	47.69	1.78
	D_{FTO4}	0.70	7.53	41.95	2.21
Part-B	D_{NFTO1}	0.68	8.04	25.86	1.41
	D_{NFTO2}	0.65	6.31	36.64	1.51
	D_{NFTO3}	0.66	7.28	38.35	1.85
	D_{NFTO4}	0.68	9.29	34.15	2.17
	D_{NFTO5}	0.67	8.78	31.09	1.85

conduction band of the semiconductor. The semiconductor transports charge carriers to the charge collector electrode. The main advantage of DSSC is use of sensitizers to harvest a large fraction of sunlight (UV to the near IR) compared to semiconductor solar cells [456]. Recently Wang et al., reported incident photocurrent conversion efficiencies (IPCE) of 14 % using triarylamine (TAA) based dyes [457]. Although, ITO/FTOs are used as photoanode and counter electrodes to fabricate DSSCs, the present study attempts to supplement commercial FTO with an optimal alternative spray-deposited NFTO thin film.

The DSSCs were fabricated with an active area of 0.25 cm^2 using the spray-pyrolyzed FTO (samples of chapter 5, part-A) and NFTO (samples of chapter 5, part-B) electrodes and commercially available FTO electrodes using the device architecture: Spray coated FTO/NFTO/TiO_2/N719 dye+electrolyte/Pt/Spray coated FTO/NFTO as depicted in Fig. 5.18 (a). The DSSCs fabricated using commercially available FTO, and spray-pyrolyzed FTO1, FTO2, FTO3, FTO4, NFTO1, NFTO2,

NFTO3, NFTO4, and NFTO5 electrodes are denoted as D_{CFTO}, D_{FTO1}, D_{FTO2}, D_{FTO3}, D_{FTO4}, D_{NFTO1}, D_{NFTO2}, D_{NFTO3}, D_{NFTO4}, and D_{NFTO5} respectively. The J-V characteristics of all the devices under AM 1.5 G solar illumination are shown in Fig. 5.18 (b) and their corresponding photovoltaic parameters such as open circuit voltage (V_{OC}), short circuit current (J_{SC}), fill factor (FF) and power conversion efficiency (η) are listed in Table 5.7. From the photovoltaic parameters (Table 5.7), the device prepared using commercially available FTO (D_{CFTO}) shows highest power conversion efficiency (η) (2.99 %), and in the case of spray-pyrolyzed electrodes, the D_{FTO4} device shows a better efficiency of 2.21 % compared to other FTO electrodes. For device D_{CFTO}, V_{OC} is 0.68 V and J_{SC} is 9.77 $mAcm^{-2}$ with η of 2.99 %. However, for the device D_{FTO4}, V_{OC} shows slight increase to 0.7 V and J_{SC} decreases to 7.53 $mAcm^{-2}$, with efficiency of 2.21 %. The remaining devices D_{FTO1}, D_{FTO2} and D_{FTO3} show lower V_{OC} and J_{SC} values compared to that of D_{FTO4}, which may be due to the higher surface roughness and lower transmittance of the FTO1, FTO2, and FTO3 electrodes compared to that of FTO4 electrode (Table 5.7). In the case

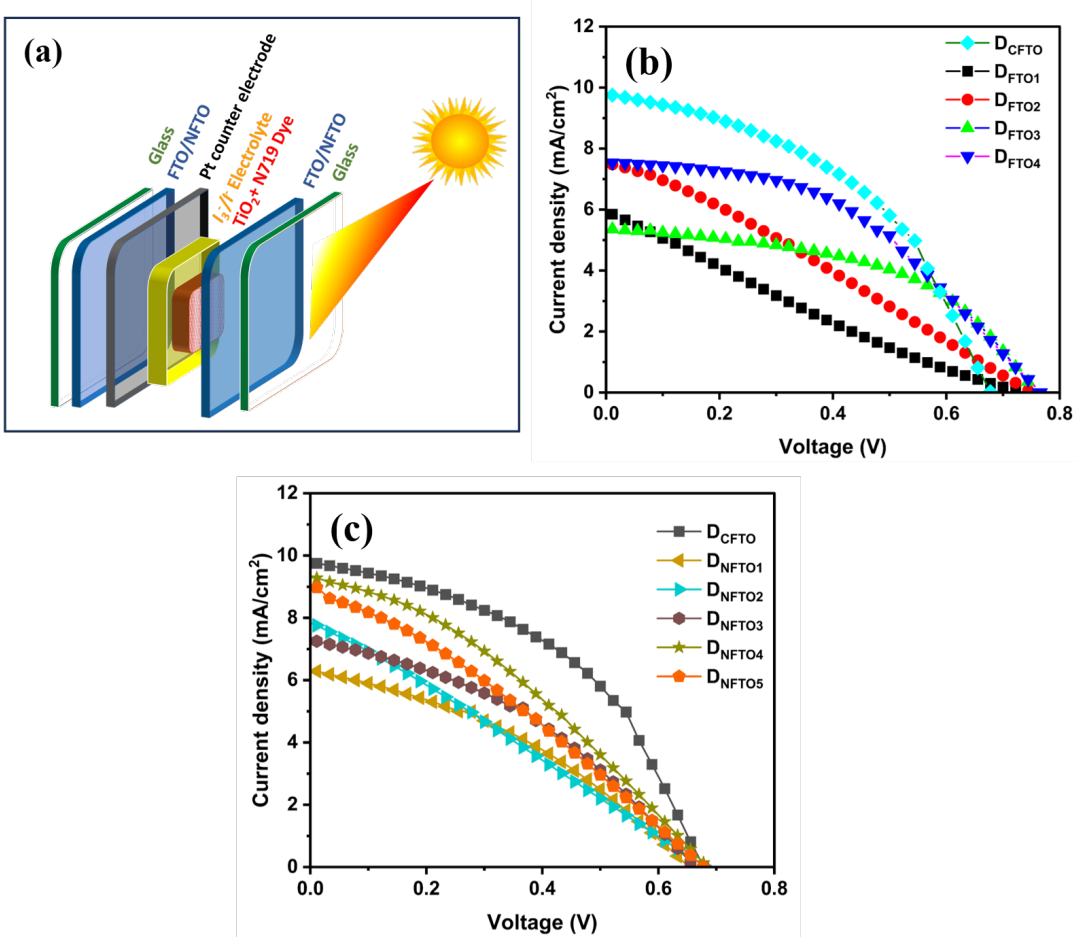

Figure 5.18: (a) Schematics of DSSC device architecture showing the constituent layers, J-V characteristics of DSSCs fabricated from spray-pyrolyzed (b) FTO and (c) NFTO thin films.

of FTO4, compared to commercial FTO, the lower current density and conversion efficiency may be due to slightly higher work function of FTO4 compared to that of commercial FTO, and slightly higher sheet resistance of FTO4 (18.61 Ω/□) than that of commercial FTO (10 Ω/□) (Zhuhai Kaivo Optoelectronic Technology Co. Ltd.). Moreover, the transmittance of commercial FTO is higher (85 % at 550 nm) than that of the spray-pyrolyzed FTO4 thin film (75 % at 550 nm), possibly due to the difference in deposition methodology, process parameters and precision in quality control. Generally, reverse leakage current in a solar cell is independent of light intensity. However, the device made with spray-deposited NFTO thin films shows the highest PCE of 2.17 % with a slightly higher V_{oc} of 0.68 V and a slightly lower current density of 9.29 $mAcm^{-2}$ for the device D_{NFTO4}. The decrease in the PCE of NFTO4 compared to that of D_{CFTO} device is mainly due to slightly higher sheet resistance and lower transparency with a rough surface of NFTO4 in comparison to that of commercially available FTO. These electrical and optical properties lead to the lower collection of photons and charge carriers (due to a slightly higher work function of 4.68 eV) of the NFTO4 electrode. All the other fabricated devices in this work show lower efficiency than that of NFTO4 device due to comparatively low figure of merit values than the NFTO4 film (Table 5.7).

5.5 Conclusion

The effect of admixing two different solvents, namely ethylene glycol and 2-methoxy ethanol, on the physicochemical properties of spray-pyrolyzed FTO thin films is explored. The film prepared using only 2-methoxy ethanol solvent yields low sheet resistance with lower transmittance with hydrophobic nature. Whereas, the film prepared using only ethylene glycol solvent yields high transmittance with moderate sheet resistance and hydrophilic in nature. In the case of admixed solvents, the preferred growth changes from (110) direction to (211) direction, leading to high surface roughness of the films. The film prepared using only 2-methoxyethanol solvent shows higher thickness with a porous and mixed morphology, whereas, the film deposited using only ethylene glycol solvent has seven times lower thickness with homogenous and dense surface features. This vivid variation in morphology and thickness resulting due to the difference in boiling points of the 2-methoxyethanol (135 °C) and ethylene glycol (197 °C) solvents leads to considerable changes in crystallinity as well as optical and electrical properties. Among all the deposited films, FTO4 (prepared using only ethylene glycol) shows higher figure of merit. In short, the analysis of the observed results implies that the choice of solvent is a crucial parameter while de-

positing FTO thin films with desired optical and electrical properties. Higher volume of 2-methoxyethanol solvent is favourable for obtaining low sheet resistance, whereas higher volume of ethylene glycol solvent leads to high transmittance, thereby allowing one to fix the ratio of the mixed solvents depending on the custom requirement of optical transparency and electrical sheet resistance for a desired optoelectronic application.

Cation (Nb) and anion (F) co-doped SnO_2 thin films were coated by fixing the optimal parameters of part-A and interestingly, it is found that with increasing the Nb concentration it enhances the transparency of NFTO thin films up to 4 wt.% of Nb, and then a further increase of Nb to 5 wt.% leading to a decrease in the transmittance. The sheet resistance decreases up to 3 wt.% of Nb concentration, then increases slightly for a higher doping concentration of Nb. However, among all the films, NFTO4 shows higher transmittance of 76 %, and with the highest figure of merit value of $5.01 \times 10^{-3}\ \Omega^{-1}$. The surface morphology is observed to change with variation of Nb concentration. The measured work function of NFTO4 (4.68 eV) is found to have slightly higher work function than that of the commercially available FTO (4.3-4.4 eV). Photoluminescence spectra reveal that NFTO4 has highest defect density of $16.34 \times 10^{21}\ cm^{-3}$ which leads to an increase in the carrier concentration of NFTO4 ($7.42 \times 10^{19}\ cm^{-3}$). The contact angle measurements show a changeover from hydrophobic (97.2°) to hydrophilic (73.8°) nature with increasing Nb concentration.

Among all the spray-pyrolyzed FTO electrodes, the D_{FTO4} device shows a better efficiency of 2.21 % compared to that of the devices fabricated using other electrodes deposited in this work. For device D_{CFTO}, V_{OC} is 0.68 V and J_{SC} is 9.77 $mAcm^{-2}$ with efficiency of 2.99 %. However, for the device D_{FTO4}, V_{OC} shows slight increase to 0.7 V and J_{SC} decreases to 7.53 $mAcm^{-2}$, with efficiency of 2.21 %. The remaining devices D_{FTO1}, D_{FTO2} and D_{FTO3} show lower V_{OC} and J_{SC} values compared to that of D_{FTO4}, which may be due to the higher surface roughness and lower transmittance of the FTO1, FTO2, and FTO3 electrodes compared to that of FTO4 electrode. The DSSC devices fabricated from spray-deposited NFTO electrodes show highest PCE of 2.17 % for the device fabricated with NFTO4 electrode. The lesser efficiency of FTO4, NFTO4 electrodes, compared to commercial FTO, the lower current density and conversion efficiency may be due to slightly higher work function and sheet resistance of FTO4 and NFTO4 compared to that of commercial FTO. From the present study, the NFTO4 electrode is found to have good optical and electrical properties; however, these values are lower compared to commercial FTO/ITO. The electrical and optical properties of NFTO4 can be further improved by fine-tuning the deposition parameters and adopting various other deposition techniques.

Chapter 6

First Principles Studies and Spray Deposition of 'Nb' and 'Sb' co-doped SnO_2 Transparent Conducting Electrodes for Optoelectronic Device Applications

Based on the observations of chapter 5, in order to enhance the optoelectronic properties further, co-doping of Nb and Sb into SnO_2 lattice is envisaged. Initially, first principles study is performed followed by spray deposition and exploration. Co-doping Nb and Sb into SnO_2 lattice is envisaged to enhance the optoelectronic properties. Although, ATO has very good electrical properties, the transparency of ATO is limited due to the grey tinge issue. To enhance the transmittance and also the thermal stability of ATO, this chapter focus on the deposition of Nb and Sb co-doped SnO_2 thin films using spray pyrolysis technique. The deposited electrodes are explored using several characterization techniques and finally, selected electrodes are tested in ACEL and DSSC devices as a TCE.

6.1 Introduction

The key properties of TCOs are, (i) High transparency in the visible region (>80 %); (ii) higher electrical conductivity ($\sigma > 10^4 S/cm$) [458]; In addition to these, few other conditions also need to be satisfied for achieving a near perfect TCO: (a) high thermal and chemical robustness that will permit the TCO to preserve its physical, chemical and optoelectronic properties enduring the complicated production process and environmental conditions during its service period [459]; (b) high earth abundance of the material [159]; and (c) low surface roughness.

From the previous chapter, it is found to be difficult to obtain optical and electrical properties by spray coated Nb and F co-doped SnO_2 beyond a limit due to the dominant haze induced by "F" doping. The co-doping of cation and anion into the same lattice may be one of the reasons, leading rise to higher defect states due to both the cationic and anion dopants, therefore, in the present chapter, co-doping of

two cation dopants is attempted. Numerous reports exist on the cation doped SnO_2 thin films with several dopants like In [28], Sb [420], Mo [460], Co [408], Mn [461], Nb [462], Ta [463], and W [464] etc., and co-doping with Nb:F [465–467], Nb:Sb [99], Ba:Sb [406], etc. Amongst all, Sb-doped SnO_2 is recognized as one of the promising supplement for ITO [468], even though the transparency and conductivity that do not surpass ITO. There are several reports on individual Nb doped SnO_2 and Sb doped SnO_2 films deposited by spray pyrolysis [228, 361, 406, 420, 453, 469–471], RF sputtering [472, 473], and pulsed laser deposition [462, 474, 475], plasma-enhanced chemical vapor deposition [476], plasma-assisted molecular beam epitaxy [477] and aerosol assisted chemical vapor deposition [478]. However, the conductivity and transparency of individual Nb doped SnO_2 and Sb doped SnO_2 films still need to be improved in order to enhance its optoelectronic properties so as to result in high figure of merit on par with that of ITO. Yude et al., published an article of individual doping of Sb, Nb, and Ta into SnO_2 lattice [435]. However, there are no reports available on Nb and Sb co-doped SnO_2 thin films coated by facile chemical spray pyrolysis method. In this chapter, Nb and Sb co-doped SnO_2 thin films deposited by facile chemical spray pyrolysis technique are investigated based on the output of first principle calculations. The Sb concentration is kept fixed at 5 % and the concentration of Nb (1 %, 2 %, and 3 %) is varied. The structural, optical and electrical transport properties of all the coated films are discussed in detail. The applicability of the spray coated thin films are demonstrated in dye sensitized solar cell (DSSC) device as an effective photoanode/counter electrode and in an ACEL device as both top and bottom electrodes.

6.2 Materials and methods

6.2.1 Preparation of precursor solution

The relevant precursor materials were weighed for 0.5 M concentration, to prepare a 200 ml solution. Three individual beakers were taken, two beakers were filled with 15 ml of D.I. water in each and the weighed $SnCl_2 \cdot 2\,H_2O$, and $SbCl_2 \cdot 2\,H_2O$ precursors added into it. Since, $SnCl_2 \cdot 2\,H_2O$ is having low solubility at room temperature, it was raised to 150 °C and stirred for 30 min. In another beaker in 10 ml of ethanol, the weighed $NbCl_5$ is added and dissolved. After mixing all the three solutions, 3 ml of HCl was added and stirred thoroughly for better solubility as well as to attain a clear transparent solution. Finally, 150 ml of ethylene glycol was added to the above solution and stirred for 3 h. Likewise, all the five different solutions for varying

concentrations were made, namely, pure tin oxide (TO), 5 wt.% Sb doped tin oxide (ATO), 1, 2, 3 wt.% of Nb, with constant 5 wt.% Sb co-doped tin oxide (NATO1, NATO2, NATO3) for a molarity of 0.5 M. The co-doped samples are denoted as NATO1, NATO2, and NATO3 and are collectively named as NATO hereafter in this chapter.

6.2.2 Spray deposition of thin films

To spray coat the Nb and Sb co-doped SnO_2 thin films, the glass substrates were cleaned by ultrasonication in the appropriate order of mild detergent solution, deionized water, acetone, IPA, and ethanol with 10 minutes each to eliminate traces of grease or oil stuck to the surface of the glass substrates. The cleaned glass substrates were then blown using nitrogen gas and then treated under UV light. Ionic charge contaminants on the surface of the substrates were eliminated using high energy plasma cleaner [Harrick Plasma, Model PDC-002] and then loaded to the substrate holder inside the spray pyrolysis instrument. The substrate holder temperature was ramped to 420 °C in 90 minutes and maintained same throughout the deposition. The substrate holder to spray tube nozzle distance was maintained at a height of 35 cm, and the moisture filtered compressed air pressure was 30 kg/cm^2. Each spray duration was 0.5 sec with a time interval of 30 sec, and the spray gun nozzle diameter was ≈ 0.3 mm, and a total of 650 number of sprays were performed for coating all the films using 200 ml of the total precursor solution. The optimal spray coating parameters are given in Table 6.1. Spraying aerosols onto a pre-heated substrate leads to formation of oxide thin film.

6.2.3 Fabrication of ACEL device

Zinc sulfide (ZnS) phosphor is prepared, by passing H_2S gas through a zinc ammonia complex created by reacting $ZnCl_2$ with NH_4OH, and it is identified that the resulting ZnS is of a luminous grade ZnS. Aluminum nitrate, and copper acetate was added in ppm level to ZnS precipitate, and then dried under an IR lamp illumination for 3 hours, and manually ground using a pestle and mortar. After thoroughly mixing the precursor, the material was heated for 3 hours under N_2 atmosphere at 1000 °C, the resulting ZnS: Cu (ZSC) phosphor that was crushed, passed through D.I. water and dried at 60 °C in an oven. To obtain the ZSC paste, the prepared ZSC phosphor was mixed uniformly with a semisolid dielectric medium of dielectric constant $\varepsilon_r \cong 5$.

The ACEL device was fabricated by sandwiching green emissive ZSC [479, 480] phosphor layer between the two optimized TCEs acting as the bottom and top elec-

Table 6.1: Optimal spray coating parameters of the Nb and Sb co-doped SnO_2 thin films

Parameters	Specifications
Precursor's used	$SnCl_2 \cdot 2\,H_2O$, $NbCl_5$ and $SbCl_5$
Solvents used	D.I. water, IPA, Ethelyne glycol and HCl
Precursor solution quantity	200 ml
Substrate and pyrolysis temperature	Glass slides $(5 \times 5)\ cm^2$ at $420\ ^\circ C$
Carrier gas/pressure	Compressed moisture free air/ 30 kg cm^{-2}
ON/OFF duration per spray	0.5 s/30 s
No of sprays/total spray duration	650 sprays, 5.41 min
Nozzle to substrate distance	35 cm

trodes. Using double side tape of thickness of $\cong$ 80 μm, the bottom electrode was covered, and an active region of $30 \times 20\ mm^2$ rectangular pit was engraved in the center part. The gap in the rectangular well at the bottom electrode was filled with the ZSC phosphor using doctor blade method without any air gap and bubbles. The top electrode positioned over bottom electrode without creating an electrical short circuit, ensuring that both the electrodes must have contact only through the ZSC emissive layer. The device was designed to be powered by an inexpensive indigenous portable power source that converts a direct current field into an alternating current field. This source's input voltage can be adjusted from 50 to 350 V_{AC} using a variable potentiometer.

6.3 First Principle calculations using Density functional theory

6.3.1 Computational methodology

The density functional theory (DFT) simulations were performed to correlate the theoretical results of Sb and Nb co-doping into the SnO_2 lattice with the experimental results of Sb and Nb co-doped SnO_2 thin films that are deposited via spray pyrolysis technique to understand and elucidate the co-doping effect on the optoelectronic properties. For theoretical simulations, Sb and Nb atoms were added as dopants into the Sn sites of the $3 \times 3 \times 3$ SnO_2 supercell. Doping concentration in supercell is nearly consistent with the experimental doping. These systems were studied by the first-principles calculation using WIEN2k code [481]. An exchange correlation of Perdew Burke and Ernzerhof (GGA) was used [482]. The RKmax value of 8 and the core/valence separation energy of -6 R_y is considered. A grid of $3 \times 3 \times 4$ k points was

used in the full-Brillouin zone. Though the theory considers only $3 \times 3 \times 3$ supercell, the calculated results may be extended to serve as a clue for the experiment and the analysis of the experimental data.

6.3.2 Discussion on the DFT output

The density of states (DOS) of the considered pure SnO_2 and Nb and Sb co-doped SnO_2 supercells are shown in Fig. 6.1. For pure SnO_2, the Fermi level (E_F) is situated near the valence band with a band gap of value 1.816 eV. Comparing with the reported experimental band gap value of 3.6 eV [483], theoretical band gap is significantly lower

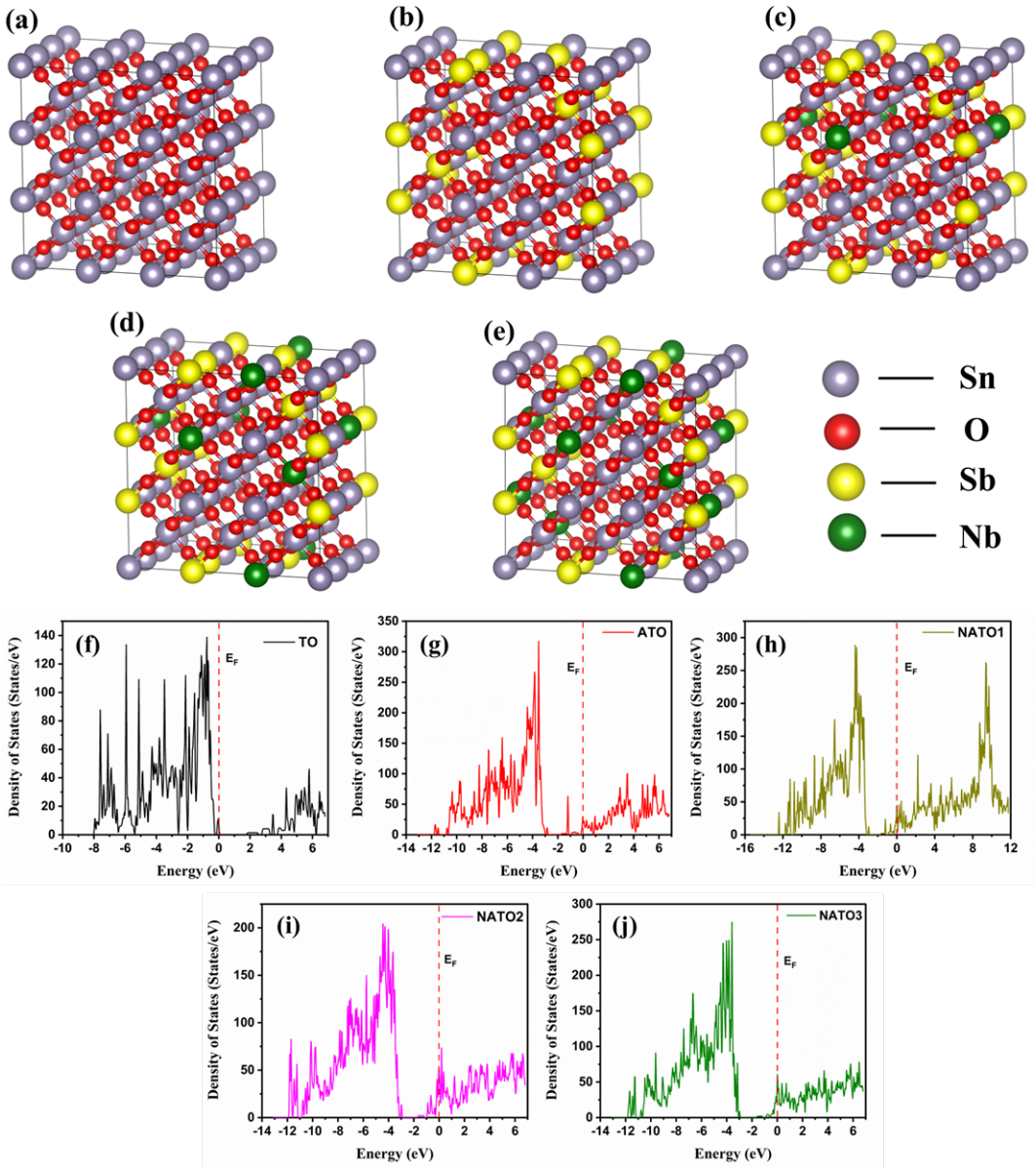

Figure 6.1: Pictorial representation of 3 x 3 x 3 supercells of (a) pure SnO_2 (TO) (b) ATO (c) NATO1 (d) NATO2, (e) NATO3, and (f to j) the respective density of states.

Table 6.2: Bandgap and optical bandgap of the pure and Nb and Sb co-doped SnO_2 films

Compound	Experimental Band gap (eV)	Calculated Band gap (eV)	Optical band gap from DFT simulations (eV)	Band gap from Tauc plot E_g (eV)
TO	3.6 [483]	1.816 [484]	-	3.888
ATO	-	-	2.725	3.779
NATO1	-	-	2.840	3.813
NATO2	-	-	2.859	3.821
NATO3	-	-	2.878	3.874

which may be due to the strong coulombic interaction between the electrons which are not taken into account [111, 485, 486] and also due to the supercell limitation. Sb and Nb were used as dopant elements in pure SnO_2 in which it occupies Sn position randomly. The composition of doping considered as SnO_2 95 % with Sb 5 %, SnO_2 94 % with Sb 5 % and Nb 1 %, SnO_2 93 % with Sb 5 % and Nb 2 %, SnO_2 92 % with Sb 5 % and Nb 3 % are pictorially represented in Fig. 6.1 (a-e). When the Sb atoms (5 %) were added into the SnO_2 lattice at the Sn sites, the E_F shifts above the conduction band minimum exhibiting n-type metallic character [111] and creating an optical bandgap of 2.725 eV. This shift is known as Moss-Burstein shift [487]. Similarly, Nb atoms co-doped with Sb atoms into the Sn sites furthermore widens the optical bandgap to higher values of 2.878 eV for Sb 5 % and Nb 3 % doped SnO_2 which are listed in Table 6.2. The optical bandgap of transparent conducting oxide (TCO) is crucial for determining its transparency in the visible region [487].

6.4 Experimental results and discussion

6.4.1 Structural properties

The X-Ray diffraction patterns of all the spray coated pure SnO_2(TO), ATO, and NATO thin films showed (Fig. 6.2) tetragonal cassiterite crystal structure with space group of P42/mnm (JCPDS file #: 00-041-1445) and no other secondary peaks are identified related to Sb_2O_3, Sb_2O_5 and Nb_2O_5 signifying successful formation of single phase of the samples. All the coated films exhibit preferred orientation along the (110) plane. There is no significant variations in peak positions, which due to nearly similar ionic radius of Nb^{5+} compare to ionic radius of Sb^{5+} (60 pm) and Sn^{4+} (69 pm). These results indicate that the crystallinity and preferred orientation are influenced by the Nb/Sb dopants and their concentration.

From the XRD patterns, the calculated unit cell volume is reduced for the ATO

film compared to TO. The contraction of the unit cell with decrement in volume may be due to substitution of smaller ionic radii Sb^{5+} (60 pm) at the Sn^{4+} (69 pm) sites. However, for lower concentration of Nb, the cell volume increased for 1 wt.% and then it decreased for higher concentration. On the contrary, the radius of Sn^{4+} (69 pm) is marginally higher than that of Nb^{5+} (64 pm) when Sn^{4+} ions are substituted by Nb^{5+} ions, a decrease in the volume is expected possibly due to contraction of the unit cell [**?**] (Table 6.3). Table 6.3 shows the structural parameters of all the coated NFTO films. Interplanar spacing is calculated based on Braggs-law, and the calculated 'd' spacing values were matching with the standard JCPDS card #: 41-1445 of tetragonal SnO_2 crystal structure. The crystallite size of the as-deposited thin film is calculated using Deby-Scherrer formula (eq. 2.3).

The crystallite size of pristine SnO_2 is found to be 55 nm, which upon doping of 5 wt.% Sb into the SnO_2 lattice decreased to 53.1 nm and with co-doping of 1 wt.% Nb it increased to 56.4 nm. It decreased with further increasing the Nb concentration. Dislocation density (δ), which is the number of dislocations per unit area present in the films was estimated using equation 2.4. The smallest value is obtained for NATO1 and highest value for NATO3 (Table 6.3). The micro-strain values of the spray coated films calculated using Williamson-Hall (W-H) plots, by plotting $\beta cos\theta$ Vs $4sin\theta$ [488]. The linear fit of these data yields the information about the residual strain in the samples. The main source of peak broadening is strain (ε), and more specifically inhomogeneous strain. If the crystallites are strained then the interplanar d spacings will be varying considerably. A compressive stress would make the d spacings smaller whereas a tensile stress would make the d spacings larger. As seen from Table 6.3, the calculated d values increased with co-doping of Nb and Sb into the SnO_2 lattice representing the presence of tensile stress in the films. The lattice constants (a and

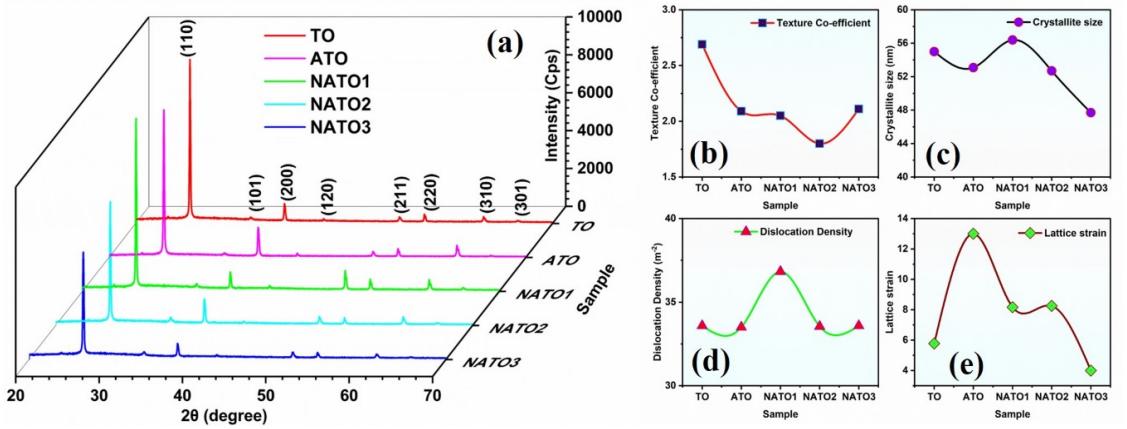

Figure 6.2: (a) The XRD patterns, (b) texture coefficient, (c) crystallite size, (d) dislocation density and (e) lattice strain of the as deposited TO, ATO and NATO thin films.

Table 6.3: Structural parameters and film thickness of the spray coated pure, Sb doped, and Nb and Sb co-doped SnO_2 thin films.

Sample code	Inter planar spacing (d) (Å)	Volume (V) ($Å^3$)	Crystallite size (D) (nm)	Dislocation density (δ) (m^{-2})	Lattice strain (η)	Texture coefficient (TC_{hkl})	Thickness (nm)
TO	3.3595	71.91	55	3.305×10^{14}	5.78×10^{-4}	2.69	320
ATO	3.3508	71.76	53.1	3.546×10^{14}	1.30×10^{-3}	2.09	510
NATO1	3.3683	72.23	56.4	3.143×10^{14}	8.17×10^{-4}	2.05	538
NATO2	3.3558	72.13	52.7	3.600×10^{14}	8.26×10^{-4}	1.80	490
NATO3	3.3595	71.75	47.7	4.395×10^{14}	4.00×10^{-4}	2.11	490

c) calculated using the equation 2.6, are marginally higher than the standard values of JCPDS card #: 00-041-1445 and are given in Table 6.3. The texture coefficient (TC_{hkl}) was estimated using equation 2.7. The calculated texture coefficient values for the (110) plane are given in Table 6.3 .

6.4.2 Optical properties of spray coated films

The transmittance spectra of the undoped TO, ATO, and NATO thin films are shown in Fig. 6.3 (a), inset is the variation of transmittance with doping of Sb and Nb into the SnO_2 lattice. Initially, the transmittance of TO is higher, with Sb doping it is decreased to 82.41 % after which it increased upon co-doping of Nb and reached a maximum transmittance value of 88.33 %, and it finally decreased to 85.24 % for 3 wt.% of Nb concentration (Table 6.5). Generally, the transmittance of TCOs by spray pyrolysis technique is restricted by: (a) reflection losses including scattered (diffuse) and specular components due to rough and textured orientation of grains and (b) inhomogeneities that exist in the film due to subtle deviation in the complex pyrolytic process [163], and (c) thickness variation of the film. The decrease in the transmittance of heavily doped semiconductors was explained by Drude's model [489]. For higher doping of Nb concentration (>2 wt.%), it leads to defect formation and hence scattering of photons is higher leading to decrease in transparency [169]. Fig. 6.3 (b) shows the Tauc plot of all the spray coated thin films and inset is the variation of the bandgap with co-doping of Sb and Nb into the SnO_2 lattice. From the inset of Fig. 6.3 (a) it is clear that the band gap to increase with Nb concentration. Initially it shows higher value for pure SnO_2 (3.888 eV) and with Sb doping it decreased to 3.799 eV, and then upon co-doping of Nb it increased to 3.874 eV (Table 6.5). The higher carrier concentration enhances the free carrier density which leads to shifting of the E_F towards the conduction band implying small variation in the bandgap, which is called as Moss-Burstein shift [490,491]. Although the band gap of pure SnO_2 from the theoretical simulations is lower with respect to the experimentally measured value, it

does not affect discussion of the results, since the same trend is observed in the DFT theoretical simulations with the insertion of Sb and Nb atoms into the SnO_2 supercell (Table 6.2).

Figure 6.3 (c) displays the defect-based photoluminescence (PL) emission characteristics of the TO, ATO, and NATO thin films. Radiation of wavelength 330 nm was used to excite the spray coated thin films. It is clear from Fig. 6.3 (c) that the UV emission occurs about 390 nm. The transition of electrons from the bottom of the conduction band to the top of the valance band is shown as the near band edge emission (NBE). The two sub-bands that make up the broad emission peak are spaced at 372 and 460 nm, respectively. Ramarajan et al, and Babar et al., reported similar type of emission peaks in spray pyrolyzed Ba and Sb doped SnO_2 and in only Sb doped SnO_2 thin films, respectively [352]. As seen from the PL emission spectra the intensity of the peak increased with Sb and Nb doping, however for higher concentration of Nb (>2 wt.%) it decreased due to concentration quenching effect.

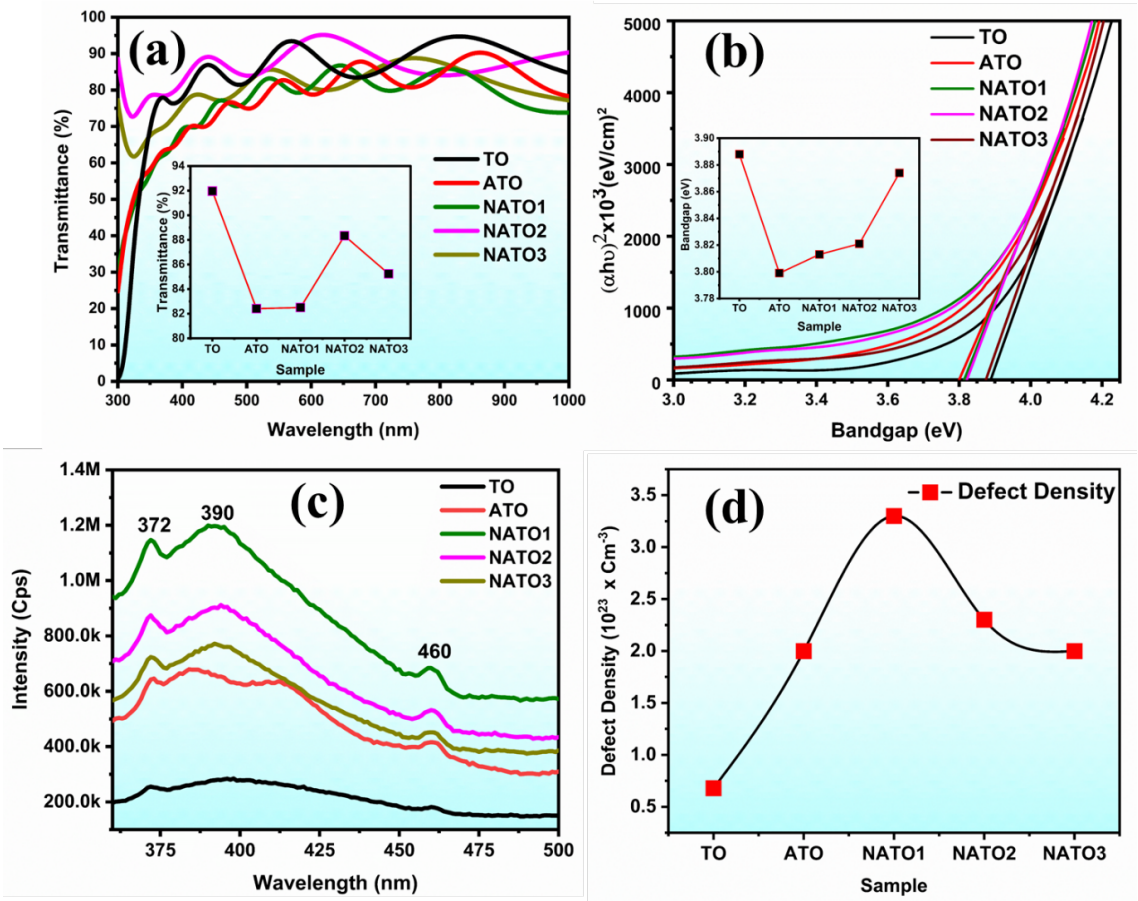

Figure 6.3: (a) Optical transmittance spectra (inset is the variation of transmittance at 550 nm upon doping of Sb and Nb for varying concentration), (b) Tauc plot (inset is the variation of bandgap with doping of Sb and Nb concentration), (c) photoluminescence emission spectra of TO, ATO, and NATO thin films and (d) variation of defect density upon doping of Sb and Nb into the SnO_2 lattice.

The most common defects are mainly due to complexes involving tin interstitials and oxygen vacancies caused by Nb and Sb insertion into the interstitial sites of the SnO_2 lattice, which generate defect energy levels close to the conduction band and are crucial for luminescence emission properties. There are three types of oxygen vacancies namely, (I) V_O neutral, (II) V_O^{1+} singly ionised, and (III) V_O^{2+} doubly ionised oxygen vacancy, among these three, singly ionised oxygen vacancy contributes more to defect level emission. The defect density can be determined from Smakula's relation (eq. 2.12) [427]. Fig. 6.3 (d) depicts the change in defect density upon doping with Sb and Nb into the SnO_2 lattice. Defect density is considerably increased with Sb and Nb co-doping and it eventually decreased for 2 and 3 wt.%. The decrease in defect density of the SnO_2 lattice is attributed to the dopants and the dopant-induced oxygen vacancies.

6.4.3 Surface features using FESEM

The surface morphology and asperities of the spray coated TO, ATO, and NATO thin films are shown in Figure. 6.4. All the deposited thin films have nearly homogenous surface morphology without any major cracks evident. The FESEM image of pure SnO_2 (Fig. 6.4 a) shows smaller grains without any defined edge morphology compared to the other spray coated films. All the Nb doped thin films are showing twisted metal sheet like features. The grains are distributed randomly with very sharp edges. Similar type of morphology in the Sb doped SnO_2 thin films coated by spray pyrolysis technique has been reported [492]. When the co-doping of Nb increases, the grain size is found to be decrease and the morphology also changed from twisted metal like shape to nano flake like morphology (Fig. 6.4 d and e). The decrease in the grain size with increasing Nb co-doping is mainly due to the induced heterogenous nucleation [493–495]. Deyu et al., reported decreasing of the grain size with increasing of Al doping into the SnO_2 lattice deposited by ultrasonic spray pyrolysis technique [493]. Khelifi et al., also reported similar type of morphology for F-doped SnO_2 thin films deposited by ultrasonic spray pyrolysis method [496]. Higher doping concentrations cause the particles to become sharper and more randomly oriented, which could enhance the effect of light scattering and affect the film's ability to transmit light.

6.4.4 AFM analysis

The 3D AFM images of the spray coated TO, ATO, and NATO thin films are shown in Fig. 6.4 (f-j). The surface topology seems to be denser and indicate good quality of the films. The RMS surface roughness values of the TO, ATO, NATO films are given

in Table 6.5. The RMS surface roughness increased upon doping of Sb and Nb into the SnO_2 lattice. The increasing surface roughness with increasing doping concentrations are also reported in literature for SnO_2 and Al doped ZnO thin films [497–499]. A reasonably rough surface is preferred for improving light scattering in the case of solar cell devices and thus the energy conversion efficiency is higher [15, 408]. A small percentage of elongated and irregularly shaped grains coexist with near spherical shaped grains. In contrast to irregularly shaped grains, which are grown in larger sizes, spherical grains are smaller in size. This type of size and shape variations are typically anticipated in high temperature heteroepitaxial growth conditions, which enhances the film's crystallinity by giving the surface species enough energy to result in near homogeneous surfaces [227]. The electrical resistance of thin films would be significantly influenced by carrier mobility, which is known to be dependent on grain boundaries [141].

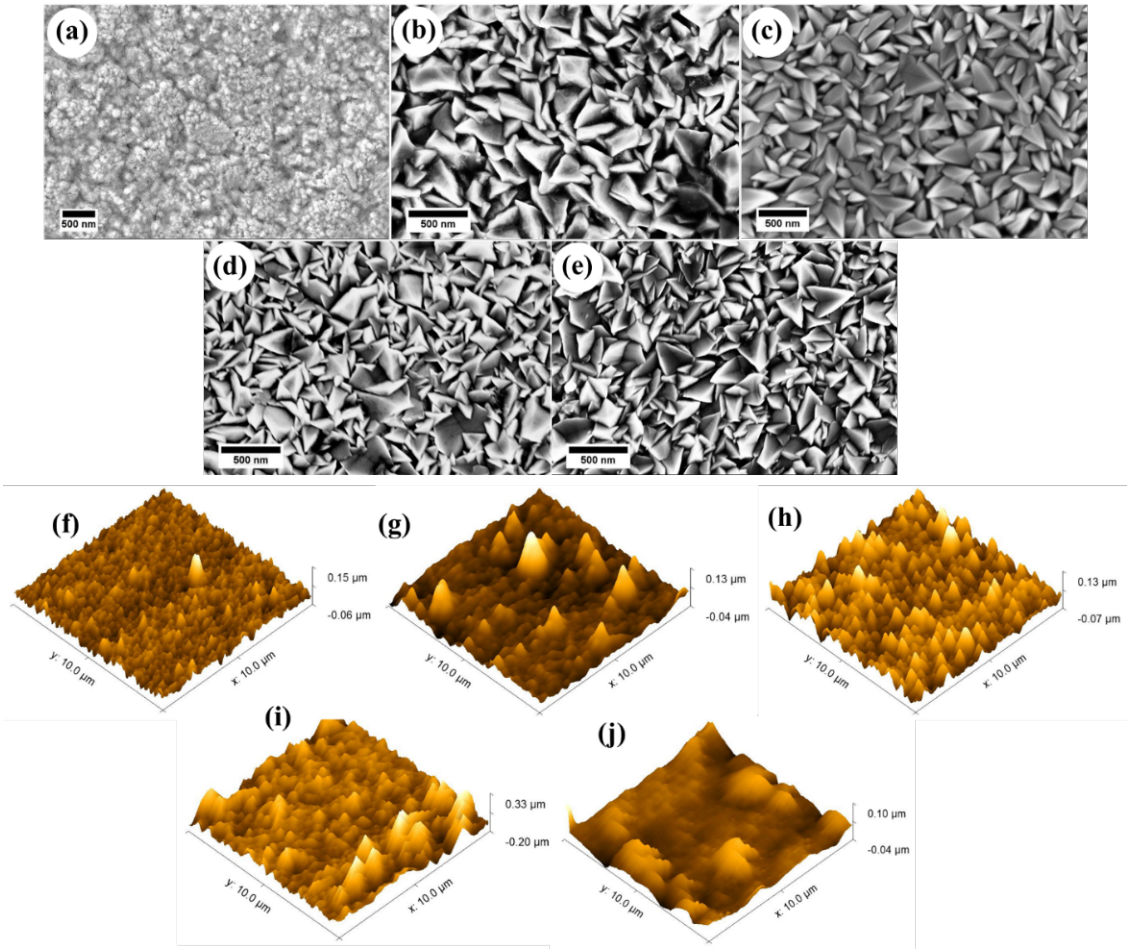

Figure 6.4: FESEM images (a-e) and 3D AFM images (f-j) of TO, ATO, NATO1, NATO2 and NATO3 thin films

6.4.5 Wettability nature

The surface wettability of the spray coated thin films was analysed by using contact angle (CA) measurement using de-ionised water as a probe liquid which reveals the interfacial contact of the liquid with the coated thin film surface depending on the contact angle between the solid, liquid and vapour interfaces. Fig. 6.5 shows the CA measurement images of all the spray coated thin films along with variation of contact angle for different doping concentrations. Among all the coated films, tin oxide (TO) shows lowest CA of 72° which upon doping with Sb increased to 89.5° and with further co-doping of Nb, it reduced for NATO1 and NATO2 from 86.7° to 77° respectively. However, for doping of 3 wt.% Nb, the surface turned from hydrophilic to hydrophobic nature. The lower CA of TO (72°) is due to low surface morphology of SnO_2 thin film, however with doping of Sb it increased to 89.5°. The increase of CA for ATO is due to increase in the surface roughness as seen from the AFM images of the thin film (Fig. 6.4 f-j). But, in the case of Nb and Sb co-doped SnO_2 thin films CA is found to decrease from 86.7° (NATO1) and 77° (NATO2), however, in the case of NATO3 the CA is increased to 96.7°. In case of pure SnO_2, the film's surface behaved as hydrophilic in nature but in case of doped NATO3 film's surface behaved as hydrophobic in nature.

6.4.6 XPS Analysis

The charge states of the constituent elements in the selected spray coated TO, ATO and NATO2 films were identified using their respective XPS spectra. The wide range XPS spectra of TO, ATO, and NATO2 thin films are shown in Fig. 6.6 (a). Fig. 6.6 (b) shows the Nb $3d_{5/2}$ peak centered around 206.43 eV confirming the donor Nb to be in +5 charge state [452, 500]. Fig. 6.6 (c) confirms the charge state of Sb to be in Sb^{5+} state for both the ATO and NATO2 films. The peak positions of Sb $3d_{5/2}$ and Sb $3d_{3/2}$ of ATO and NATO2 thin films are given in Table 6.4 with spin orbit split of 9.3 and 9.4 eV respectively. The close scan XPS spectra of Sn^{4+} is shown in Fig. 6.6(d), the Sn $3d_{5/2}$ and Sn $3d_{3/2}$ peaks clearly indicate shift in peak position with Sb and Nb doping indicating proper substitution into the SnO_2 host lattice (Table 6.4). The twin peaks exhibited spin orbit coupling with difference of 8.38, 8.38, and 8.45 eV for TO, ATO, and NATO2 respectively which is consistent with the reported literature [500]. Fig. 6.6 (e) shows a slight shift in the O 1s peak with doping of Sb and Nb to the SnO_2 lattice and corresponding binding energy values are given in Table 6.4. The O 1s can be further deconvoluted into two sub-bands of O (I), and O (II) which represents the Sn-O bond, and chemisorbed oxygen species, respectively [388, 500]. Thus, based on

the XPS spectra, it can be confirmed that the incorporation of Sb and Nb into the SnO_2 host lattice to exist in Sb^{5+} and Nb^{5+} charge states. These dopants provide free electrons and helps to increase the conductivity of the films.

6.4.7 Electrical transport properties

6.4.7.1 Sheet resistance

The sheet resistance contour mapping of the spray coated films over $5 \times 5\ cm^2$ glass substrate were measured using linear four probe method and are shown in Fig. 6.7. The variation in sheet resistance of the films upon doping with Sb and Nb into the SnO_2 lattice is shown in Fig. 6.7 (f). For the TO film, sheet resistance is very high since the free charge carriers are limited in pure SnO_2, whereas for ATO films it is showing lower sheet resistance since Sb in +5 charge state is replacing Sn^{4+} sites, and these excess electrons increase the conductivity of the film. Also, upon doping with Nb for 1 and 2 wt.%, it is nearly the same as that of ATO whereas for 3 wt.% of Nb the sheet resistance increased which may be due to high free carrier concentration leading to enhanced scattering due to which the conductivity is reduced. Apart from this, higher concentration of Nb leads to mixed charge states from Nb^{5+} to Nb^{4+} due to which the conductivity at higher concentration is decreased [501]. The change in sheet resistance at the edges of the films is mainly due to subtle deviation in spray dynamics and temperature gradient during the spray coating process leading to variation in the sheet resistance at the periphery of the films.

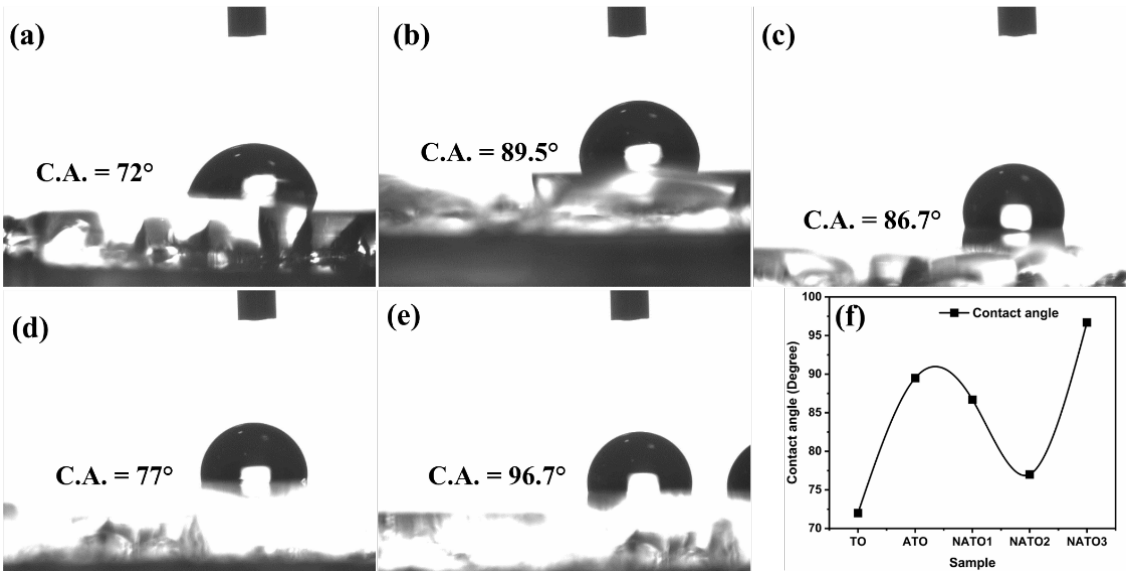

Figure 6.5: Contact angle measurement images of de-ionized water droplets on the surface of spray coated (a) TO, (b) ATO, (c) NATO1, (d) NATO2, (e) NATO3 thin films and (f) variation of contact angle with doping concentration.

6.4.7.2 Hall effect

The Hall effect measurements were performed at room temperature in Van-der Pauw geometry. From the negative Hall coefficient value, it is confirmed that all the films are of n-type semiconducting nature. The mobility, charge carrier density (bulk concentration), and resistivity values of pure tin oxide are 23.54 $cm^2V^{-1}s^{-1}$, 5.68×10^{19} cm^{-3}, and, 4.66×10^{-3} Ωcm respectively, and these typically fall within the range published in the literature [502, 503]. Since oxygen vacancies and interstitial Sn exist in the SnO_2 lattice, shallow donor levels are found to be the cause of the n-type conductivity [503]. The results depicted in Fig. 6.8 (f) indicate gradual variation in electron concentration upon doping of SnO_2 with Sb and Nb. The carrier concentration of

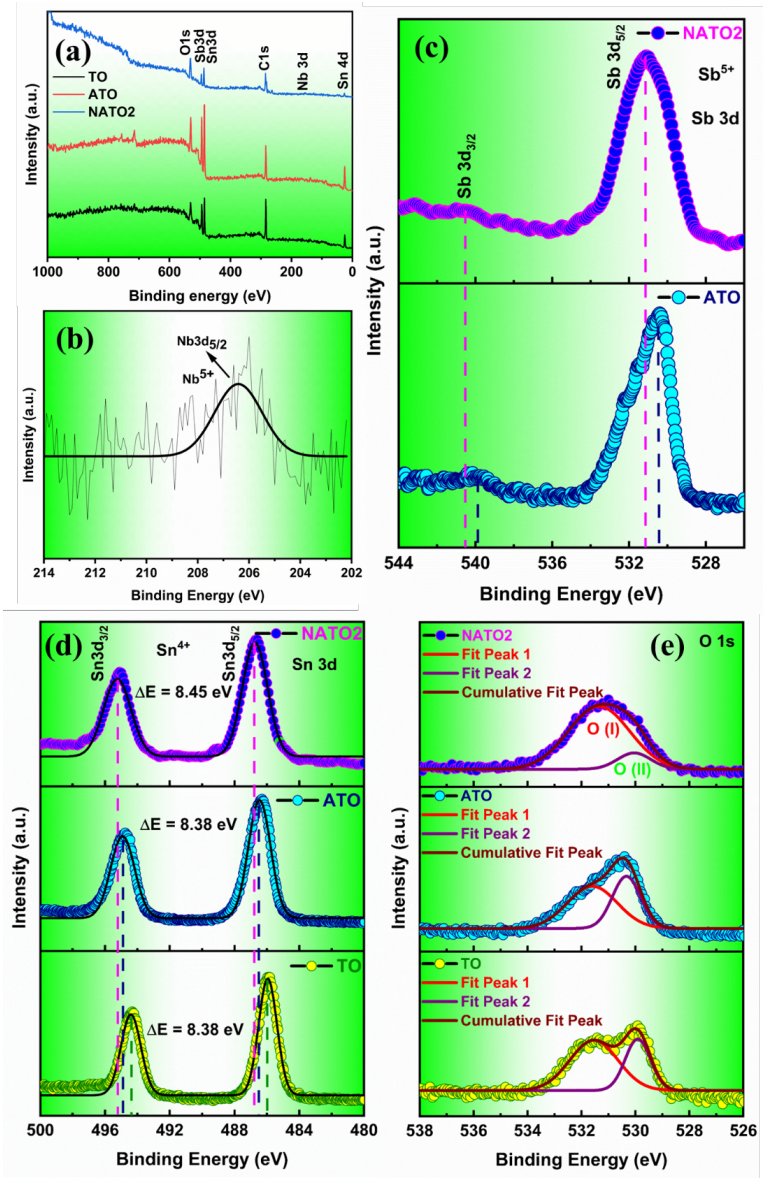

Figure 6.6: The XPS spectra of the spray coated TO, ATO, and NATO2 thin films showing the (a) wide scan spectra for all the elements, (b) Nb 3d, (c) Sb 3d, (d) Sn 3d, and (e) O 1s levels.

Table 6.4: Binding energy values of the constituent elements of the spray coated TO, ATO and NATO2 thin films

Sample code	Binding energy values (eV)						
	Sn^{4+}		O 1s		Sb^{5+}		Sb^{5+}
	Sn $3d_{3/2}$	Sn $3d_{5/2}$	O(I)	O(II)	Sb $3d_{3/2}$	Sb $3d_{5/2}$	
TO	485.97	494.35	531.34	530.04	-	-	-
ATO	486.50	494.88	531.59	530.32	540.58	530.70	-
NATO2	486.76	495.21	531.53	529.21	539.81	531.07	206.43

the spray coated films is found to be decreased from 5.66×10^{19} to 9.12×10^{20} cm^{-3} with doping of 5 wt.% Sb for ATO film compared to pure TO film. With co-doping of Nb upto 2 wt.%, the charge carriers increased thereafter and decreased for Nb 3 wt.% (NATO3). The sheet resistivity of the thin films decreased upon doping of 5 wt.% Sb (ATO), and with co-doping of 1 wt.% of Nb (NATO1) into SnO_2. However, further increase in doping concertation of 2 wt.% Nb lead to increase in the sheet resistivity of the film. The Nb^{5+} charge state increases the conductivity and carrier concentration by introducing excess of free electrons into the conduction band. The increase in resistivity for higher doping concentrations of Nb might be due to excess of Nb doping leading to mixed Nb^{5+} to Nb^{4+} charge states resulting in decrease of free carriers. When Nb atoms are localized at the interstitial lattice sites of the crystal lattice, they function as ionized scattering centres resulting in drop of mobility from 23.547 $cm^2V^{-1}s^{-1}$ to 8.533 $cm^2V^{-1}s^{-1}$ for TO to NATO3 [504,505] (Table 6.5). Scat-

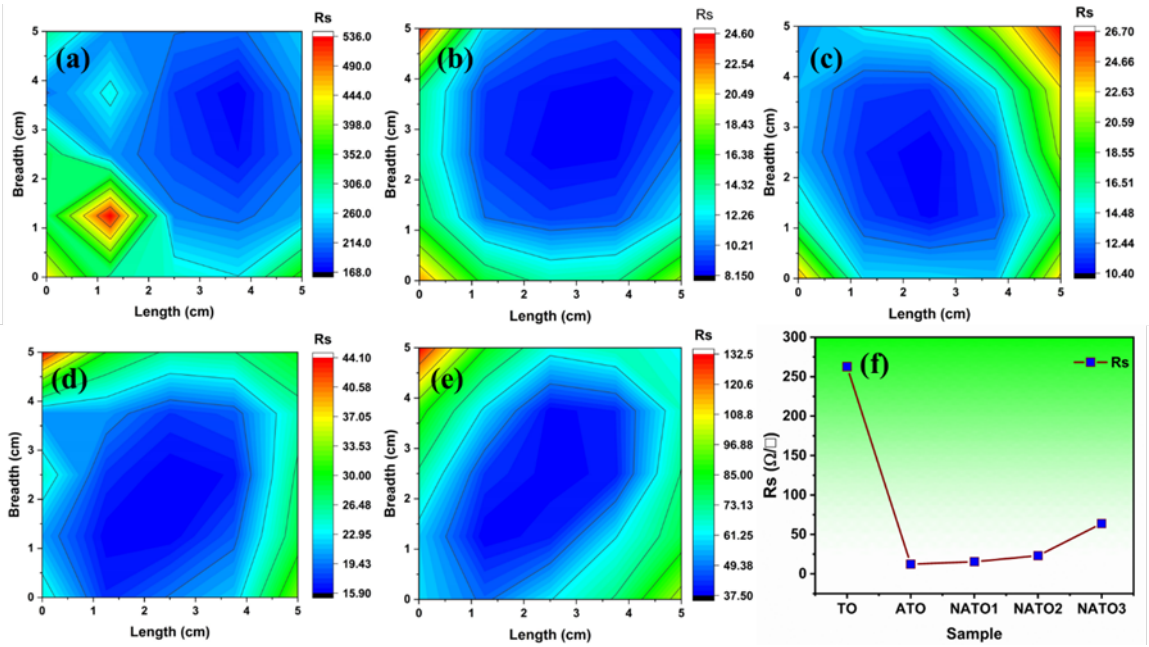

Figure 6.7: The 2D contour mapping of sheet resistance of the spray coated (a) TO, (b) ATO, (c) NATO1, (d) NATO2, (e) NATO3, thin films measured and plotted over 5×5 cm^2 area, and (f) the variation of average sheet resistance of the same.

Table 6.5: Optoelectronic and transport parameters of the spray-coated NATO thin films.

Sample ID	Transmittance at 550 nm (%)	Band gap (eV)	RMS Roughness (nm)	Sheet resistance (R_s) ($\Omega/\square$)	Carrier Concentration (n) (cm^{-3})	Resistivity ρ (Ωcm)	Mobility μ ($cm^2V^{-1}s^{-1}$)	FoM (Ω^{-1})
TO	91.96	3.888	16	262.7	5.68×10^{19}	4.66×10^{-3}	23.547	1.4×10^{-3}
ATO	82.41	3.799	20	12.2	6.20×10^{20}	6.09×10^{-4}	16.499	1.18×10^{-2}
NATO1	82.5	3.813	24	15.5	7.39×10^{20}	5.68×10^{-4}	14.857	0.91×10^{-2}
NATO2	88.33	3.821	57	23.01	9.52×10^{20}	8.19×10^{-4}	7.999	1.25×10^{-2}
NATO3	85.24	3.874	14	63.84	4.45×10^{20}	1.64×10^{-3}	8.533	0.31×10^{-2}

tering of the charge carriers limit its mobility in polycrystalline materials depending on the density of the grain boundaries [506]. For higher concentrations of Nb, the resistivity shows higher values due to low charge carriers and low mobility, therefore the, NATO2 film seems to be the optimal sample.

6.4.7.3 Thermal stability of the sheet resistance for spray coated films

The study of thermal stability of the R_s of the spray coated films is necessary to understand its potential for device applications. Here the thermal stability study has been performed by treating the samples at different temperatures and variation in R_s is measured by linear four-probe method. Thermal treatment was performed for 30 min from 200 °C to 500 °C with an interval of 50 °C. Fig. 6.8 shows the variation of R_s with annealing temperature for a duration of 30 minutes. From Fig. 6.8 (a) it is clearly identified that the variation of sheet resistance with annealing temperature from 200 °C to 250 °C, the values of sheet resistance decreased marginally. Above 250 °C (from 300 °C - 500 °C) it increased very rapidly. In the case of ATO (Fig. 6.8 b), the R_s decreased from 200 °C to 250 °C, with a marginal variation of 1 $\Omega/\square$, for above 250 °C it increased from 15 to 20 $\Omega/\square$ for every 50 °C. However, in the case of NATO2 (Fig. 6.8 c), it shows good stability upto 400 °C after which only a 5 $\Omega/\square$ is the variation for every 50 °C temperature, and all the samples indicate semiconducting nature with appreciably stable R_s. However, further increasing of annealing temperature results into a metallic like behavior of the films with drastic increase in R_s. These variation in the R_s of the films implies the defect formation while annealing the films. Among these three films, NATO2 has good temperature stability. Figure. 6.8 (d) shows the thermal stability of NATO2 films with different annealing duration. Four different sets of samples were taken and annealed for varying time duration, set A for 30 minutes, set B for 1 hour, set C for 1 hour 30 minutes and set D for 2 hours with a step size of 50 °C. Among all these, set A shows good thermal stability for 30 minutes of annealing duration in air atmosphere. The same set A samples were checked for thermal cycling for different annealing duration and no

significant increase in the resistance is observed even after two hours of annealing (Fig. 6.8 e). Suitability of any TCE for various optoelectronic applications, is evaluated based on the figure of merit (FoM) value. Utilizing R_s and % T (at 550 nm) data, FoM can be determined. The calculated FoM values using equation 1.7 are given in Table 6.5 and it was found to be highest for NATO2 ($12.5 \times 10^{-3}\ \Omega^{-1}$) due to higher transparency and lower sheet resistance values.

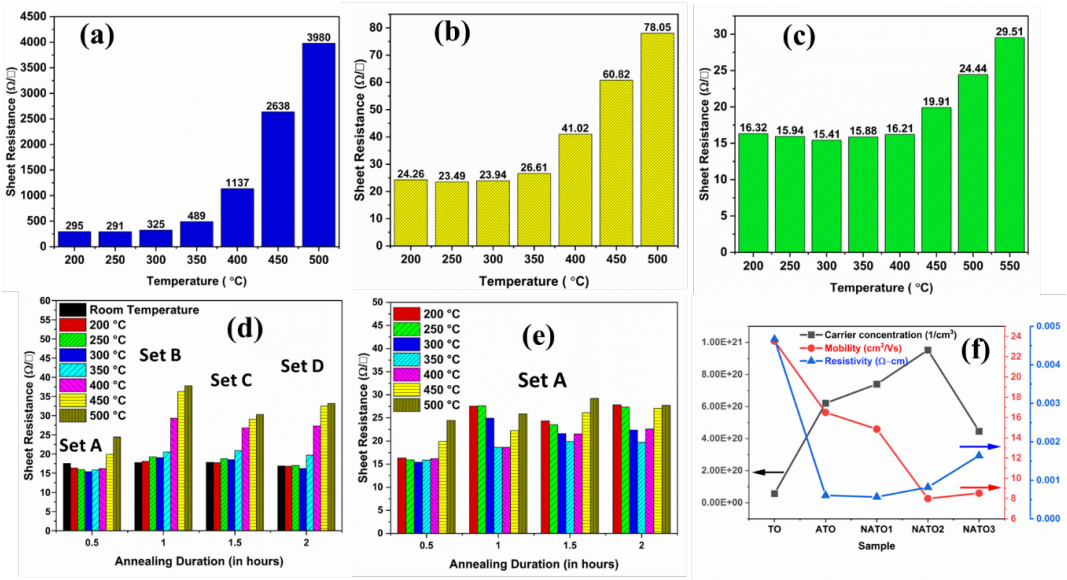

Figure 6.8: Variation of sheet resistance of (a) TO, (b) ATO, (c) NATO2 thin films with annealing temperature. (d) Stability of the optimal NATO2 thin film for varying annealing duration for different sets of the same sample (sets A, B, C, and D), (e) thermal cycling stability of NATO2 (Set A) thin film for different annealing duration and (f) the variation of resistivity, mobility, and carrier concentration of spray coated TO, ATO, and NATO thin films

6.4.8 Surface work function

The performance of an optoelectronic device mainly depends on the electrode's surface work function (Φ). TCEs are often chosen to enable effective carrier injection and extraction in functional optoelectronic devices in addition to regular light transmission. Transparency and conductivity are the two important criteria for efficient performance of devices, by means of alignment of energy levels between the electrodes and the involved active layers [507–509]. The charge-transfer barrier at the electrode interface may be significantly lowered by properly adjusting the effective surface work function of a particular electrode [510]. In most of the semiconductors the surface work function can be tuned by doping with suitable dopants at appropriate concentration [390]. The surface work function mainly depends on the position of its fermi level to its vacuum level ($\Phi = E_{vac} - E_F$) [391]. The surface work function of the

spray coated TO, ATO and NATO2 electrodes were measured based on the procedure discussed in our previous report [428], and the values are found to be 4.701, 4.778, and 4.756 eV respectively. The Φ value of pure SnO_2 are reported to be within the range 4.4 to 5.7 eV [397, 448]. The Φ value for the commercial FTO and ITO are reported to the in the range 4.3 to 4.4 eV [303, 306, 392, 394–396]. The sample TO shows the Φ value of 4.7 eV, and with Sb doping it increased to 4.778 eV, which upon co-doping of Nb it marginally decreased to 4.756 eV. Overall, the spray coated TO, ATO, and NATO2 films shows slightly higher surface work function than that of the commercially available FTO and ITO electrodes. The change in the Φ values may be due to increase in charge carriers upon doping of Sb/Nb and or change in the surface roughness, oxygen stoichiometry and preferred orientation of grains in the transparent conducting electrodes [43].

6.5 Applications

6.5.1 Performance of DSSCs fabricated using spray coated electrodes

Fig. 6.9 (a) shows the layer-by-layer representation of dye sensitized solar cell device (DSSC) architecture adapted in the present study. A total of six devices were fabricated including standard device using FTO electrode. The device made with TO electrode showed poor performance due to its higher sheet resistance and subpar electrical transport capabilities (Inset of Fig. 6.9 b). As shown in Fig. 6.9 (b) and Table 6.6, the photovoltaic conversion efficiencies are enhanced for ATO and NATO2 devices. Comparing all these devices, only NATO2 cell meets the performance comparable to that of the FTO based standard cell. The J_{sc} value of NATO2 device is 9.35 $mAcm^{-2}$ which is slightly lesser than the J_{sc} of standard device using FTO electrode, 11.45 $mAcm^{-2}$. The V_{oc} values of NATO2 device is 0.7598 V which is slightly higher than the V_{oc} of commercial FTO device (0.718 V). The higher J_{sc} for commercial FTO is mainly due to lower sheet resistance (10-12 Ω/□) compared to NATO2 electrode (23.01 Ω/□). Also, the surface work function of the NATO2 electrode (4.756 eV) is slightly higher than the FTO electrode (4.4 eV) leading to reduced charge carrier collection. The high surface roughness (57 nm) of the NATO2 film compared to the commercially available FTO electrode influences the contact resistance between the TiO_2 and NATO2 electrode layers. All these factors led to relatively lesser efficiency of the NATO2 device compared to commercial FTO device. The EQE spectra (Fig. 6.9 c) reveal improvement for NATO2 cell. Compared to ATO, NATO2 cell exhibits

Table 6.6: The J-V parameters and electrochemical impedance data of the DSSCs fabricated using the spray coated electrodes in comparison with standard device made from FTO.

Device ID	Open circuit (V_{oc}) (V)	Current density (J_{sc}) ($mAcm^{-2}$)	Fill factor (FF) (%)	Efficiency (η) (%)	Series Resistance (R_{series}) (Ω)	Charge transport resistance 1 (R_{ct1}) (Ω)	Charge transport resistance 2 (R_{ct1}) (Ω)	life time (μs)
$D_{FTO(c)}$	0.718	11.45	74.361	6.124	18.21	14.89	2.41	0.245
D_{TO}	0.669	0.218	25.460	0.037	-	-	-	-
D_{ATO}	0.686	9.134	64.094	4.018	59.93	24.12	7.20	0.34
D_{NATO1}	0.739	11.71	49.381	4.078	61.11	21.53	7.16	0.503
D_{NATO2}	0.759	9.35	76.670	5.452	121.8	39.56	14.4	0.633
D_{NATO3}	0.742	7.176	42.161	2.247	222.7	70.43	61.62	1.265

the highest EQE near to the standard FTO cell. The increase in EQE values for ATO and NATO2 are consistent with the variation of J_{sc}. The higher transmittance of NATO2 electrode enables more incident photons to fall on to the TiO_2 surface to result into a comparatively higher photo conversion efficiency compared to all other devices. In general, higher efficiency results when greater number of photo electrons are being injected into the conduction band of TiO_2 and thus lead to a higher J_{sc} of the cell. However, for further improving the device performance, it is needed to reduce the sheet resistance, surface work function and surface roughness of the NATO2 electrode by choosing other deposition techniques.

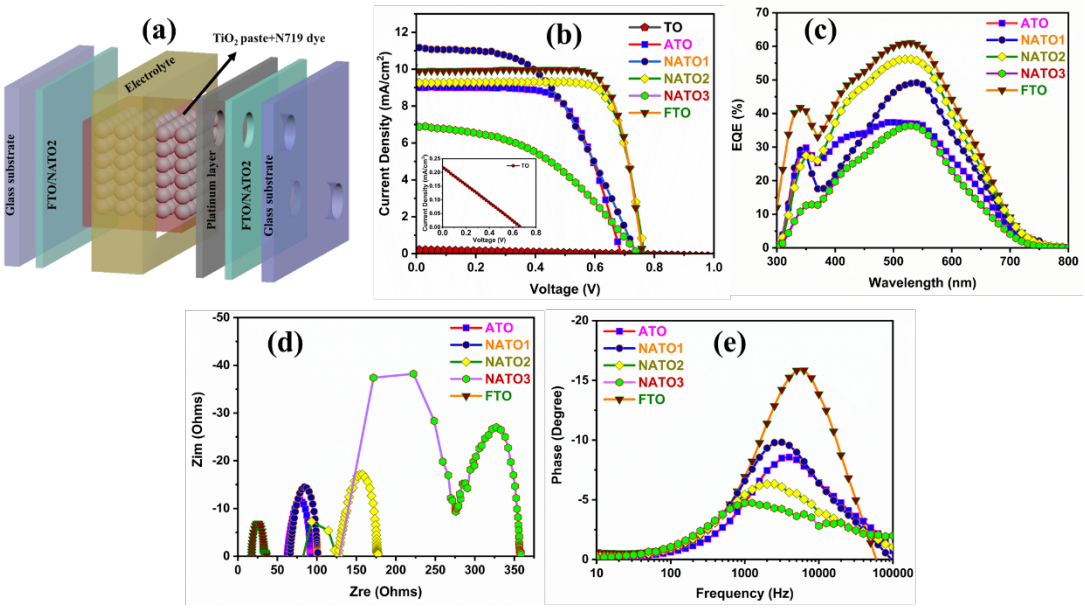

Figure 6.9: (a) Layer by layer representation of dye sensitized solar cell using all the spray coated electrodes. (b) J-V plots, and (c) external quantum efficiency (EQE), (d) Nyquist impedance spectra, (e) Bode plot of the DSSCs prepared from the spray coated electrodes in comparison with the standard device using FTO electrode (except for sample TO).

6.5.1.1 Electrochemical Impedance Spectroscopy analysis

The electrochemical impedance spectra (EIS) of the DSSCs made from the spray coated pure, Sb doped, and Nb and Sb co-doped SnO_2 thin films are depicted in Fig. 6.9 (d) as Nyquist plots. Fig. 6.9 (e) shows the bode plot and the electron life time (τ_e) is calculated from bode plot using the relation given in section 2.5.3.3 and equation 2.16 and all the obtained parameters are listed in Table 6.6. In general, the electron transport mechanisms within the electrochemical system of DSSCs are understood and analyzed using the EIS spectra. Three semicircles are in general observed in the conventional DSSCs; they are associated with the Warburg diffusion process [266] of I^-/I^{3-} and the electrochemical reaction at the Pt counter electrode. First semicircle at high frequency region (1 kHz to 100 kHz) is due to the charge transfer at the counter electrode and TiO_2, (R_{ct1}), second semicircle at intermediate frequency region (1 Hz to 1 kHz) is due to the TiO_2/dye/electrolyte interface (R_{ct2}), and third semicircle at low frequency region (0.2 Hz to 0.75 Hz) attributed to the Warburg impedance of tri-iodide ions present in the electrolyte [267, 268]. The series resistance (R_{series}) of the circuit connections is responsible for the high frequency intercept on the real axis. The value of R_{series}, R_{ct1}, and R_{ct2} depends on the sheet resistance of the electrodes that are used in the device. The sheet resistance of NATO2 electrode is slightly higher than the FTO, ATO and NATO1 electrode led to higher R_{series} resistance of the device. Although, the same layers (TiO_2 and Pt counter electrode) for all the devices, the various electrodes used have different sheet resistance so that there was a change in the R_{series}, R_{ct1}, and R_{ct2} with the trend of sheet resistance (Table 6.5).

6.5.2 Alternating current electroluminescent device

The first alternating current electroluminescent device (ACEL) device was demonstrated using Cu doped ZnS as an emissive layer by Destriau et al., in 1935 [511]. In this section, for demonstrating an ACEL device, the optimal NATO2 electrode with highest transmittance of 88.33 % and lower sheet resistance of 23 $\Omega/\square$ with higher FoM (1.25×10^{-2} Ω^{-1}) was utilized as both the top and bottom electrodes. The main advantage of an ACEL device is the facile construction process, which can be carried out at ambient conditions [316]. This feature makes it possible to extend them for large-area display devices using quick and cost-effective technique like doctor blading. The luminescence centres present in the phosphor material is activated when an ac voltage is supplied to the two terminals, producing light [512–514]. Based on the dopant material the emissive color of the phosphor will change. Several reports are available on green color emission phosphor, like ZnS:Cu, ZnS: Cu, Al, and

ZnS:Cl [480, 515, 516]. Tiwari et al., explained the operating principle of the ACEL device [199], in which when an AC voltage is applied to the two electrodes, luminescence centers within the phosphor material are excited, causing the device to emit light. The luminescence initially flickers at a low a.c frequency before stabilizing at a higher frequency. The threshold voltage for the green ACEL device emission is around 75 V_{AC}, and as the applied voltage rises, the device's emission intensity rises systematically up to 350 V_{AC} (saturation voltage). Figure 6.10 (a) exemplifies the schematics of an ACEL device. Figure 6.10 (b) shows the emission spectrum at different applied voltages between 75 and 350 V_{AC} with an interval of 25 V_{AC} at 1 kHz. The emission spectrum was centered at 525 nm, and the EL intensity increased with increasing voltage. The superior color and emission quality of an EL device is shown by the CIE 1931 chromaticity diagram (Fig. 6.10c), and the associated CIE coordinates for 100; 200; and 300 V_{AC} are 0.27,0.49; 0.24, 0.55 and 0.24, 0.58, respectively denoting the blue shift.

Fig. 6.10 (d) is the photograph of the fabricated ACEL device using ZSC phosphor as the EL emissive material and NATO2 as top and bottom TCEs. By supplying an AC voltage of 195 V, as illustrated in Figs. 6.10 (e-g), photographs of the EL device are also shown at ambient room light and total dark conditions. One of the

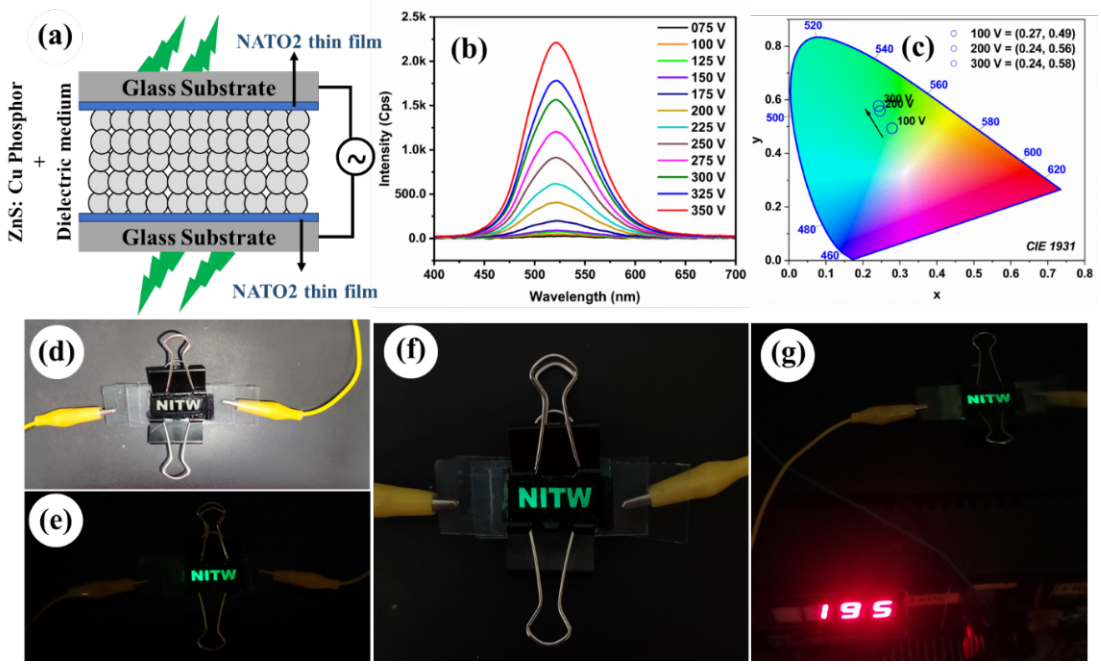

Figure 6.10: (a) Schematic representation of an ACEL device using the optimal NATO2 electrode, (b) EL emission spectra of fabricated ACEL device with ZSC phosphor, (c) CIE chromaticity diagram of the ZSC phosphor (d) ACEL device photograph at ambient room light condition without applied voltage (e) ACEL device in dark condition with applied V_{AC}, (f) ACEL device under room light with V_{AC}, and (g) ACEL device in dark condition with V_{AC} = 195 V.

most important characteristics of an ACEL device is its enhanced uniform emission throughout the entire surface area, resulting in broader viewing angles [317]. The rear electrode of an ACEL device generally receives less attention than the front electrode. Thick metallic coatings with strong conductivity but comparatively lesser transparency is typically used as rear electrode. In the present case, NATO2 electrode was utilized as both the top and bottom transparent and conducting electrodes since the ACEL device can emit light from both sides of the electrodes, unlike conventional devices that only permit one-side light emission.

6.6 Conclusion

A facile chemical spray coating approach was utilized to deposit TO, ATO, and NATO thin films based on the results of DFT simulation. The Nb and Sb co-doping into SnO_2 host lattice leads to synergic effect in tuning the optoelectronic properties of the deposited thin films. XRD results confirmed the doping of Sb and Nb into SnO_2 lattice without any secondary phases. FESEM images of all the deposited films have shown the twisted metal sheet like structure with tetragonal morphology. The overall change in contact angle form hydrophobic to hydrophilic with doping of Sb and Nb were observed. The XPS spectra of ATO and NATO2 revealed the existence of Nb and Sb in +5 charge state, enhancing the charge carrier concentration. Among all the deposited films, NATO2 film was found to have highest figure of merit value of 12.5×10^{-3} Ω^{-1} with highest transmittance of 88.33 % at 550 nm and lower sheet resistance of 23 $\Omega/\square$. The temperature stability of the sheet resistance is significant up to 400 °C for the NATO2 electrode. This enhancement in the optical and electrical properties improved the photovoltaic conversion efficiency of NATO2 to 5.452 % which is better than ATO (4.018 %) and is lesser than the commercial FTO (6.124 %) devices. In addition to this, the spray coated NATO2 electrode used in the ACEL device has shown promising results. Therefore, the spray coated Nb and Sb co-doped SnO_2 TCOs can serve as alternative electrodes for commercially available FTOs since it is a facile method to deposit large area thin films. The accomplishment of this work is the effective stabilization of an alternative transparent conducting electrode that is efficient and stable even at reasonably high temperatures of processing (up to 400 °C), thereby opening the opportunities for its expanded applications in optoelectronic sectors.

Chapter 7

Summary, Conclusions and Perspectives for Future Work

The findings of the pliable noble metallic multi-layer (chapter 3) and tri-layer electrodes (chapter 4) and unpliable Nb and F co-doped SnO_2 (chapter 5), and Nb and Sb co-doped SnO_2 (chapter 6) alternative TCEs, all compiled and discussed in this chapter. In this chapter: First, comparison of the four different TCE materials developed for their best optical and electrical transport parameters and second, a brief discussion of the stabilized material's prospects for follow up in the near future are presented.

7.1 Summary of the research work

This doctoral thesis work focused on developing the alternative TCEs for appropriate optoelectronic device applications. Exploring for its structural, optical, electrical characteristics and its mechanical and thermal sheet resistance stability. The applicability of these developed electrodes were also tested in devices like DSSC, ACEL, and PENG.

Chapters 3 and 4 focused on the deposition of metallic multi-layer and tri-layer electrodes on the pliable PET substrate using sputtering technique. The sputter deposited (chapter 3) Au/Cu/Ag/Pt/Au (total thickness of 10 nm) multi-layer has shown transmittance of 44 % at 500 nm and sheet resistance of 60 $\Omega/\square$, resistivity of 6.02×10^{-5} Ωcm with a surface work function of 5.01 eV. The multi-layer also shows higher mechanical strength of 50,000 bending-twisting sequences, which is way better than the commercially available pliable ITO electrodes within the studied range, which was only stable for a mere 500 bending-twisting sequences. The drawback of the deposited electrode is low transmittance compared to commercially available pliable ITO. To enhance the transmittance, the follow up work has been performed (chapter 4) with noble metallic Au/Pt/Au tri-layer electrode strategy. The thickness of the electrode was reduced from 10 nm to 6 nm, by excluding the Cu (2 nm) and Ag (2 nm) layers from the multi-layer architecture. The tri-layer was found to possess better transmittance of 55 % than compared to multi-layer's transmittance of 44

%. Moreover, it also possesses low resistivity and work function of 3.72×10^{-5} Ωcm and 4.97 eV, respectively. The mechanical stability of sheet resistance is very much stable even after 50,000 bending-twisting cycles similar to the multi-layer TCE. All these properties suggest that the noble metallic Au/Pt/Au tri-layer can be used as alternative to pliable ITO electrodes in similar aspects. The deposited multi-layer and tri-layer electrodes demonstrated as active TCEs in the fabrication of ACEL and PENG devices showed significant performance. When force is applied to the piezoelectric nanogenerator by tapping it, about 150 mV was generated. At 95 V, the ACEL device begins to emit an orange glow, and as voltage rises, the gadget's brightness rises to 180 V. The potential of sputter-deposited ultrathin flexible Au/Pt/Au tri-layer film as a promising electrode system for usage in diverse flexible optoelectronic devices is implied by both the tested devices.

In chapters 5 and 6, spray coated SnO_2 electrodes co-doped with appropriate dopants were explored. In chapter 5, optimization of F doped SnO_2 (FTO) electrode by varying the solvent ratio of ethylene glycol and 2-methoxyethanol. FTO4 (deposited only using ethylene glycol) found to have good transmittance of 75 % at 550 nm along with considerable sheet resistance of 18.61 $\Omega/\square$. Based on this, optimized (FTO4) parameters, further to improve the electrode characteristics by anion (F) and cation (Nb) co-doping strategy was followed. The Nb and F co-doped SnO_2 (NFTO) electrodes were spray deposited by keeping F concentration constant at 10 wt.% and by varying the concentration of Nb from 1-5 wt.%. The 4 wt.% Nb and 10 wt.% F has shown better optical and electrical properties of 77 % transmittance and sheet resistance of 15.77 $\Omega/\square$. In chapter 6, spray deposition of two cationic dopants Nb and Sb were co-doped into SnO_2 and explored for their optoelectronic properties. Other than FTO, ATO is identified as one of the alternative TCE, but due to gray tinge issue, the transmittance of ATO is much lesser than the ITO. Therefore, to enhance the ATO's optical and electrical properties, it was co-doped with Nb. Among all the deposited films, Nb 2 wt.% Sb 5 wt.% doped SnO_2 (NATO2) film was found to have highest figure of merit value of 12.5×10^{-3} Ω^{-1} with highest transmittance 88.33 % at 550 nm and a low sheet resistance of 23 $\Omega/\square$. The temperature stability of the sheet resistance of the NATO2 electrode is significant up to 400 °C for 30 minutes anealing duration. This enhancement in the optical and electrical properties improved the photo conversion efficiency of DSSC made with NATO2 to 5.452 % is better than DSSC made with ATO (4.018 %) device. In addition to this, the spray coated NATO2 electrode tested as top and bottom electrodes in the ACEL device has shown promising results.

Table 7.1: Comparison of pliable multi-layer and tri-layer electrodes in comparison with commercially available pliable ITO electrode.

Sample ID	Transmittance at 500 nm (%)	Sheet resistance (R_s)($\Omega/\square$)	Resistivity (ρ) (Ωcm)	Carrier concentration (n) (cm^{-3})	Mobility (μ) ($cm^2V^{-1}s^{-1}$)	FoM (Ω^{-1})	Surface work function (Φ) (eV)	Mechanical stability of sheet resistance bendings/twistings
Au/Cu/Ag/Pt/Au	44	60	6.02×10^{-3}	5.11×10^{22}	2.02	4.53×10^{-6}	5.01	50,000
Au/Pt/Au	55	62	3.72×10^{-5}	2.01×10^{22}	8.32	4.08×10^{-5}	4.97	50,000
Pliable ITO	55	5	4.73×10^{-5}	1.29×10^{22}	10.18	5.06×10^{-4}	4.4	500

Table 7.2: Comparison of unpliable spray deposited co-doped SnO_2 electrodes with commercially available ITO and FTO electrodes.

Sample ID	Transmittance at 550 nm (%)	Sheet resistance (R_S) ($\Omega/\square$)	Resistivity (ρ) (Ωcm)	Carrier concentration (n) (cm^{-3})	Mobility (μ) ($cm^2V^{-1}s^{-1}$)	FoM (Ω^{-1})	Surface work function (Φ) (eV)	DSSC efficiency (%)
FTO	75	18.61	7.44×10^{-4}	2.66×10^{20}	31.47	3.02×10^{-3}	4.69	2.21
NFTO4	78	15.77	2.05×10^{-3}	7.42×10^{19}	40.98	4.64×10^{-3}	4.68	2.17
NATO2	88	23	8.19×10^{-4}	9.52×10^{22}	7.99	0.12×10^{-3}	4.75	5.45
Commercial ITO	89	12.2	$> 10^{-5}$	$> 10^{22}$	-	0.25×10^{-3}	5.1	1.9
Commercial FTO	90	15	$> 10^{-5}$	$> 10^{22}$	-	0.23×10^{-3}	4.9	6.12

7.2 Conclusion

This section presents the comparison of key characteristics of the best-optimized pliable (Table 7.1) and unpliable alternative (Table 7.2) electrodes for their optical transmittance, sheet resistance, resistivity, mobility, carrier concentration, work function, and figure of merit.

The important conclusions are as follows,

1. The pliable metallic multi-layer and tri-layer electrodes shown nearly same sheet resistance (60 $\Omega/\square$) and the resistivity in the order 6×10^{-5} to 3×10^{-5} (Ωcm). However, with decreasing of film thickness from multi-layer (10 nm) to tri-layer (6 nm) by removing two metallic layers (Cu and Ag) leads to an increase in the transmittance of tri-layer from 44 % to 55 % at 500 nm. Both the electrodes have shown mechanical stability of sheet resistance even after 50,000 bending and twisting cycles. This is far better than the commercial ITO mechanical stability which withstands only about 500 bending and twisting cycles. Both these electrodes have shown promising results for ACEL and PENG device applications.

2. The non-pliable metal oxide electrodes deposited using spray pyrolysis has shown higher optical and electrical properties and thermal stability of sheet resistance up to 400 °C. Among all metal oxide electrodes Nb 2 wt.% and Sb 5 wt.% co-doped SnO_2 (NATO2) film was found to have highest figure of merit value of $12.5 \times 10^{-3}\ \Omega^{-1}$ and highest transmittance of 88.33 % at 550 nm and lower sheet resistance of 23 $\Omega/\square$. DSSC device made from these electrodes have shown a highest efficiency of 5.45 % for device made from NATO2 electrode. Although it is lesser than the commercial FTO (6.124 %) device but the variation is not very large and hence this electrode system is also promising. The NATO2 electrode can be used as efficient alternative unpliable electrode as a supplement of commercially available ITO and FTO electrodes.

7.3 Perspectives for future research work

There are several possibilities for expanding the materials explored in this thesis for the follow up work in the near future, some of them are listed below:

- The mechanical stability of the ACEL and PENG devices fabricated using flexible metallic tri-layer electrodes can be tested for several bending and twisting

cycles during its operation.

- The optimized metallic tri-layers can be coated on different substrates that are stable for higher temperature, so that the crystallinity will be improved, and the transmittance and sheet resistance may be improved further.

- The optimized spray coated co-doped SnO_2 films are to be further explored for use as an effective electrode in organic optoelectronic devices like OLED, and the currently trending perovskite solar cells.

- Due to uncontrollable film roughness of films coated using spray pyrolysis technique, the optoelectronic properties are not viable for devices with higher efficiency, therefore the same host and dopant concentrations may be explored by coating using RF sputtering technique.

*****

Dissemination of Research Findings

List of Publications:

[1] **Reddivari Muniramaiah**, Jean Maria Fernandes, M Manivel Raja, Dilli Babu Padmanaban, P Supraja, M Rakshita, Nandarapu Purushotham Reddy, Gouranga Maharana, M Kovendhan, Ganapathy Veerappan, Gangalakurti Laxminarayana, R Rakesh Kumar, D Haranath, D Paul Joseph. *Mechanically stable ultrathin flexible metallic Au/Pt/Au tri-layer as an alternative transparent conducting electrode for optoelectronic device applications*", ***Vacuum***, 2022, 206, 111487. **(SCI-indexed)**

[2] **Reddivari Muniramaiah**, Nandarapu Purushotham Reddy, Rompivalasa Santhosh, Jean Maria Fernandes, Dilli Babu Padmanaban, Gouranga Maharana, M Kovendhan, Ganapathy Veerappan, Gangalakurti Laxminarayana, Murali Banavoth, D Paul Joseph. *Solvent effect on the optoelectronic properties of fluorine doped SnO_2 thin films prepared by spray-pyrolysis*", ***Surfaces and Interfaces***, 2022, 33, 102174. **(SCI-indexed)**

[3] **Reddivari Muniramaiah**, Gouranga Maharana, Jean Maria Fernandes, M Manivel Raja, Dilli Babu Padmanaban, P Supraja, M Rakshita, Nandarapu Purushotham Reddy, M Kovendhan, Gangalakurti Laxminarayana, R Rakesh Kumar, D Haranath, D Paul Joseph. *Sputter-deposited highly flexible noble metal multi-layer electrode viable for energy and luminescent devices*", ***Surfaces and Interfaces***, 2023, 39, 102949. **(SCI-indexed)**

[4] **Reddivari Muniramaiah**, Nandarapu Purushotham Reddy, Rompivalasa Santhosh, Gouranga Maharana, Jean Maria Fernandes, Dilli Babu Padmanaban, M Kovendhan, Ganapathy Veerappan, Gangalakurti Laxminarayana, Murali Banavoth, D Paul Joseph. *Anionic fluorine and cationic niobium co-doped tin oxide thin films as transparent conducting electrodes for optoelectronic applications*", ***Physica Status Solidi a***, 2023, 220, 2200703. **(SCI-indexed)**

International conferences attended:

[1] "Sputter-deposited highly flexible noble metal multi-layer electrode viable for energy and luminescent device", ***International Conference on Nanoscience and Nanotechnology (ICONN-2023)***, SRMIST, Tamilnadu, India, 2023.

[2] "Optical and electrical properties of ultra-thin flexible Au/Cu/Ag/Pt/Au sputtered transparent conducting electrodes", ***ICAMMC-2021***, SRMIST, Tamilnadu, India, 2021.

[3] "Effect of solvent on the optical and electrical properties of the spray deposited FTO thin films",, ***ICAMMC-2021***, SRMIST, Tamilnadu, India, 2021.

[4] "Effect of Nb and F co-doping on the optical and electrical properties of the spray deposited Tin Oxide thin films", ***ICAMMC-2021***, SRMIST, Tamilnadu, India, 2021.

*****

Bibliography

[1] Pengfei Kou, Liu Yang, Cheng Chang, and Sailing He. Improved flexible transparent conductive electrodes based on silver nanowire networks by a simple sunlight illumination approach. *Scientific Reports 2017 7:1*, 7:1–11, 2 2017.

[2] Kosuke Sakamoto, Hiroyuki Kuwae, Naofumi Kobayashi, Atsuki Nobori, Shuichi Shoji, and Jun Mizuno. Highly flexible transparent electrodes based on mesh-patterned rigid indium tin oxide. *Scientific Reports 2018 8:1*, 8:1–8, 2 2018.

[3] Jaewon Kim, Sherman Wong, Gahui Kim, Young Bae Park, Joel Van Embden, and Enrico Della Gaspera. Transparent electrodes based on spray coated fluorine-doped tin oxide with enhanced optical, electrical and mechanical properties. *Journal of Materials Chemistry C*, 8:14531–14539, 10 2020.

[4] Yan Tang, Haibo Ruan, Hongdong Liu, Jin Zhang, Dongping Shi, Tao Han, and Liu Yang. Low-temperature solution processed flexible silver nanowires/ZnO composite electrode with enhanced performance and stability. *Journal of Alloys and Compounds*, 747:659–665, 5 2018.

[5] Kirill Zilberberg, Felix Gasse, Richie Pagui, Andreas Polywka, Andreas Behrendt, Sara Trost, Ralf Heiderhoff, Patrick Görrn, and Thomas Riedl. Highly robust indium-free transparent conductive electrodes based on composites of silver nanowires and conductive metal oxides. *Advanced Functional Materials*, 24:1671–1678, 3 2014.

[6] So Hee Lee, Sooman Lim, and Haekyoung Kim. Smooth-surface silver nanowire electrode with high conductivity and transparency on functional layer coated flexible film. *Thin Solid Films*, 589:403–407, 8 2015.

[7] Martin Lokanc, Roderick Eggert, and Michael Redlinger. The availability of indium: The present, medium term, and long term. 2015.

[8] Maziar Behtash, Paul H. Joo, Safdar Nazir, and Kesong Yang. Electronic structures and formation energies of pentavalent-ion-doped SnO_2: First-principles hybrid functional calculations. *Journal of Applied Physics*, 117:1–9, 2015.

[9] Paul Erhart, Andreas Klein, and Karsten Albe. First-principles study of the structure and stability of oxygen defects in zinc oxide. *Physical Review B - Condensed Matter and Materials Physics*, 72:1–7, 2005.

[10] Sining Yun, Yong Qin, Alexander R. Uhl, Nick Vlachopoulos, Min Yin, Dongdong Li, Xiaogang Han, and Anders Hagfeldt. New-generation integrated devices based on dye-sensitized and perovskite solar cells. *Energy and Environmental Science*, 11:476–526, 2018.

[11] Jérémie Werner, Jonas Geissbühler, Ali Dabirian, Sylvain Nicolay, Monica Morales-Masis, Stefaan De Wolf, Bjoern Niesen, and Christophe Ballif. Parasitic absorption reduction in metal oxide-based transparent electrodes: Application in perovskite solar cells. *ACS Applied Materials and Interfaces*, 8:17260–17267, 2016.

[12] G. R.A. Kumara, S. Kaneko, A. Konno, M. Okuya, K. Murakami, B. Onwonaagyeman, and K. Tennakone. Large area dye-sensitized solar cells: Material aspects of fabrication. *Progress in Photovoltaics: Research and Applications*, 14:643–651, 2006.

[13] Ye Zhang, Hao Li, Lidia Kuo, Pei Dong, and Feng Yan. Recent applications of graphene in dye-sensitized solar cells. *Current Opinion in Colloid and Interface Science*, 20:406–415, 2015.

[14] Dario Leister, Kristina Peters, Hasala N. Lokupitiya, Jiří Rathouský, Morgan Stefik, Mathias Labs, Alexander Kuhn, Mathias Pribil, David Sarauli, and Dina Fattakhova-Rohlfing. Nanostructured antimony-doped tin oxide layers with tunable pore architectures as versatile transparent current collectors for biophotovoltaics. *Advanced Functional Materials*, 26:6682–6692, 2016.

[15] Tzu Hui Wang, Tzu Wei Huang, Yu Chen Tsai, Ya Wen Chang, and Chien Shiun Liao. A photoluminescent layer for improving the performance of dye-sensitized solar cells. *Chemical Communications*, 51:7253–7256, 2015.

[16] Yiqing Sun, William D. Chemelewski, Sean P. Berglund, Chun Li, Huichao He, Gaoquan Shi, and C. Buddie Mullins. Antimony-doped tin oxide nanorods as a transparent conducting electrode for enhancing photoelectrochemical oxidation of water by hematite. *ACS Applied Materials and Interfaces*, 6:5494–5499, 2014.

[17] Matthias Batzill. Surface science studies of gas sensing materials: SnO_2. *Sensors*, 6:1345–1366, 2006.

[18] Monica Morales-Masis, Fabien Dauzou, Quentin Jeangros, Ali Dabirian, Herbert Lifka, Rainald Gierth, Manfred Ruske, Date Moet, Aïcha Hessler-Wyser,

and Christophe Ballif. An indium-free anode for large-area flexible oleds: Defect-free transparent conductive zinc tin oxide. *Advanced Functional Materials*, 26:384–392, 2016.

[19] Sebastian C Dixon, David O Scanlon, Claire J. Carmalt, and Ivan P Parkin. N-type doped transparent conducting binary oxides: An overview, 2016.

[20] Sukang Bae, Sang Jin Kim, Dolly Shin, Jong Hyun Ahn, and Byung Hee Hong. Towards industrial applications of graphene electrodes. *Physica Scripta*, 014024, 2012.

[21] Chang-Lae Kim, Chan-Won Jung, Young-Jei Oh, and Dae-Eun Kim. A highly flexible transparent conductive electrode based on nanomaterials. *NPG Asia Materials*, 9:e438, 2017.

[22] Karl Badeker. fiber de elelctrische leitfhdgkedt und die themnoelektrische e'raft eimiger sch wermetal luerbindungew ; von e. bcideker. *Ann. Phys.*, 22:749–766, 1907.

[23] Marcel Descamps, Henri Inion, and Laboratoires Labaz. United states patent office v-o. pages 3–6, 1970.

[24] The Royal Society. Constitution and mechanism of the selenium rectifier photocell. *Proceedings of the Royal Society of London. Series A. Mathematical and Physical Sciences*, 202:449–466, 2006.

[25] G Bauer. Elektrisches und optisches verhalten von halbleitern. XIII messungen an Cd-, Tl- und Sn-oxyden. *Annalen der Physik*, 422(5):433–445, 1937.

[26] Donald M Mattox and Vivienne Harwood Mattox. Review of transparent conductive oxides (TCO). 2007.

[27] D. B. Fraser and H. D. Cook. Highly conductive, transparent films of sputtered In_2SnO_3. *Journal of The Electrochemical Society*, 119:1368, 2007.

[28] Georg Rupprecht. Untersuchungen der elektrischen und lichtelektrischen leitfähigkeit dünner indiumoxydschichten. *Zeitschrift für Physik*, 139:504–517, 1954.

[29] R Ramarajan, D Paul Joseph, K Thangaraju, and M Kovendhan. *13 - Role of defects on the transparent conducting properties of binary metal oxide thin film electrodes*, pages 387–420. Elsevier, 2023.

[30] Mihaela Girtan and Beatrice Negulescu. A review on oxide/metal/oxide thin films on flexible substrates as electrodes for organic and perovskite solar cells. *Optical Materials: X*, 13:100122, 2022.

[31] Ankur Kumar, Mukesh Kumar, M. S. Goyat, and D. K. Avasthi. A review of the latest developments in the production and applications of ag-nanowires as transparent electrodes. *Materials Today Communications*, 33:104433, 2022.

[32] Adeniji E. Adetayo, Tanjina N. Ahmed, Alex Zakhidov, and Gary W. Beall. Improvements of organic light-emitting diodes using graphene as an emerging and efficient transparent conducting electrode material. *Advanced Optical Materials*, 9:1–23, 2021.

[33] L Holland and G Siddall. The properties of some reactively sputtered metal oxide films. *Vacuum*, 3:375–391, 1953.

[34] G. Haacke. Transparent conducting coatings. *Annual Review of Materials Science*, 7:73–93, 1977.

[35] Z. M. Jarzebski. Preparation and physical properties of transparent conducting oxide films. *Physica Status Solidi (a)*, 71:13–41, 1982.

[36] Akshay Kumar and Chongwu Zhou. The race to replace tin-doped indium oxide: Which material will win? *ACS Nano*, 4:11–14, 2010.

[37] Vincent Consonni, Germain Rey, Hervé Roussel, and Daniel Bellet. Thickness effects on the texture development of fluorine-doped SnO_2 thin films: The role of surface and strain energy. *Journal of Applied Physics*, 111:33523, 2012.

[38] R G Egdell, I Mckenzie, C F Mcconville, S F J Cox, and T D Veal. Shallow donor state of hydrogen in In_2O_3 and SnO_2 : Implications for conductivity in transparent conducting oxides. pages 1–4, 2009.

[39] Yuting Xu, Jingjing Wang, Lijuan Sun, Heng Huang, Jiaru Han, He Huang, Lanlan Zhai, and Chao Zou. Top transparent electrodes for fabricating semi-transparent organic and perovskite solar cells. *Journal of Materials Chemistry C*, 9:9102–9123, 2021.

[40] Alexandre Mantovani Nardes, René A.J. Janssen, and Martijn Kemerink. A morphological model for the solvent-enhanced conductivity of PEDOT:PSS thin films. *Advanced Functional Materials*, 18:865–871, 3 2008.

[41] P. P. Edwards, A. Porch, M. O. Jones, D. V. Morgan, and R. M. Perks. Basic materials physics of transparent conducting oxides. *Dalton Transactions*, 0:2995–3002, 9 2004.

[42] A.A. Maradudin V.M. Agranovich. *Modern Problems in Condensed Matter Sciences*. North Holland,, 10th edition, 1985.

[43] I. H. Kim, J. H. Ko, D. Kim, K. S. Lee, T. S. Lee, J. h. Jeong, B. Cheong, Y. J. Baik, and W. M. Kim. Scattering mechanism of transparent conducting tin oxide films prepared by magnetron sputtering. *Thin Solid Films*, 515:2475–2480, 12 2006.

[44] H. Peelaers, E. Kioupakis, and C. G. Van De Walle. Fundamental limits on optical transparency of transparent conducting oxides: Free-carrier absorption in SnO_2. *Applied Physics Letters*, 100:11914, 1 2012.

[45] A. J. Freeman, K. R. Poeppelmeier, T. O. Mason, R. P.H. Chang, and T. J. Marks. Chemical and thin-film strategies for new transparent conducting oxides. *MRS Bulletin*, 25:45–51, 8 2000.

[46] Alex M. Ganose and David O. Scanlon. Band gap and work function tailoring of SnO_2 for improved transparent conducting ability in photovoltaics. *Journal of Materials Chemistry C*, 4:1467–1475, 2 2016.

[47] D. B. Fraser and H. D. Cook. Highly conductive, transparent films of sputtered In_2O_3:Sn. *Journal of The Electrochemical Society*, 119:1368, 10 1972.

[48] G Haacke. New figure of merit for transparent conductors. *Journal of Applied Physics*, 47:4086–4089, 1976.

[49] X Zhou, M Pfeiffer, J S Huang, J Blochwitz-Nimoth, D S Qin, A Werner, J Drechsel, B Maennig, and K Leo. Low-voltage inverted transparent vacuum deposited organic light-emitting diodes using electrical doping. *Applied Physics Letters*, 81:922–924, 7 2002.

[50] A. Klein, C. Körber, A. Wachau, F. Säuberlich, Y. Gassenbauer, R. Schafranek, S. P. Harvey, and T. O. Mason. Surface potentials of magnetron sputtered transparent conducting oxides. *Thin Solid Films*, 518:1197–1203, 2009.

[51] M. Nonnenmacher, M. P. O'Boyle, and H. K. Wickramasinghe. Kelvin probe force microscopy. *Applied Physics Letters*, 58:2921–2923, 6 1991.

[52] Xueping Li, Fei Chen, Qiang Shen, Anxue Wang, and Lianmeng Zhang. Densification of ATO nanoceramics by spark plasma sintering. *Key Engineering Materials*, 508:230–234, 2012.

[53] Supachai Ngamsinlapasathian, Thammanoon Sreethawong, Yoshikazu Suzuki, and Susumu Yoshikawa. Doubled layered ITO/SnO_2 conducting glass for substrate of dye-sensitized solar cells. *Solar Energy Materials and Solar Cells*, 90:2129–2140, 2006.

[54] Yalan Hu, Xungang Diao, Cong Wang, Weichang Hao, and Tianmin Wang. Effects of heat treatment on properties of ITO films prepared by RF magnetron sputtering. *Vacuum*, 75:183–188, 7 2004.

[55] M. K. Chong, K. Pita, and S. T.H. Silalahi. Correlation between diffraction patterns and surface morphology to the model of oxygen diffusion into ITO films. *Materials Chemistry and Physics*, 115:154–157, 5 2009.

[56] Supachai Ngamsinlapasathian, Thammanoon Sreethawong, and Susumu Yoshikawa. Enhanced efficiency of dye-sensitized solar cell using double-layered conducting glass. *Thin Solid Films*, 516:7802–7806, 9 2008.

[57] C. Guillén, J. Montero, and J. Herrero. ITO/ATO bilayer transparent electrodes with enhanced light scattering, thermal stability and electrical conductance. *Applied Surface Science*, 384:45–50, 10 2016.

[58] R. Veera Babu, Jean Maria Fernandes, M. Kovendhan, Nandarapu Purushothamreddy, Reddivari Muniramaiah, R. Arockiakumar, N. S. Karthiselva, and D. Paul Joseph. Investigation of structural, optical, electrical and mechanical properties of transparent conducting 'Ag' electrodes. *Physica B: Condensed Matter*, 607:412690, 2021.

[59] Ch Surya Prakasarao, Slavia Deeksha D'Souza, Pratim Hazarika, S. N. Karthiselva, R. Ramesh Babu, M. Kovendhan, R. Arockia Kumar, and D. Paul Joseph. Fabrication and stability investigation of ultra-thin transparent and flexible Cu-Ag-Au tri-layer film on PET. *AIP Conference Proceedings*, 1942:080010, 4 2018.

[60] Claes G. Granqvist. Transparent conductors as solar energy materials: A panoramic review. *Solar Energy Materials and Solar Cells*, 91:1529–1598, 2007.

[61] Petru Lunca Popa, Jonathan Crêpellière, Pavan Nukala, Renaud Leturcq, and Damien Lenoble. Invisible electronics: Metastable cu-vacancies chain defects for

highly conductive p-type transparent oxide. *Applied Materials Today*, 9:184–191, 2017.

[62] Kirill Zilberberg, Jens Meyer, and Thomas Riedl. Solution processed metal-oxides for organic electronic devices. *Journal of Materials Chemistry C*, 1:4796–4815, 2013.

[63] Yugandhar Bitla, Ching Chen, Hsien Chang Lee, Thi Hien Do, Chun Hao Ma, Le Van Qui, Chun Wei Huang, Wen Wei Wu, Li Chang, Po Wen Chiu, and Ying Hao Chu. Oxide heteroepitaxy for flexible optoelectronics. *ACS Applied Materials and Interfaces*, 8:32401–32407, 2016.

[64] Stephan Kirchmeyer and Knud Reuter. Scientific importance, properties and growing applications of poly(3,4-ethylenedioxythiophene). *Journal of Materials Chemistry*, 15:2077–2088, 5 2005.

[65] Yung Hoon Ha, Nikolay Nikolov, Steven K. Pollack, John Mastrangelo, Brett D. Martin, and Ranganathan Shashidhar. Towards a transparent, highly conductive poly(3,4-ethylenedioxythiophene). *Advanced Functional Materials*, 14:615–622, 6 2004.

[66] Michael W Rowell, Mark A Topinka, Michael D McGehee, Hans-Jürgen Prall, Gilles Dennler, Niyazi Serdar Sariciftci, Liangbing Hu, and George Gruner. Organic solar cells with carbon nanotube network electrodes. *Applied Physics Letters*, 88(23), 2006.

[67] Qi Hui Wu, A. Thissen, W. Jaegermann, and Meilin Liu. Photoelectron spectroscopy study of oxygen vacancy on vanadium oxides surface. *Applied Surface Science*, 236:473–478, 9 2004.

[68] Zongyou Yin, Shuangyong Sun, Teddy Salim, Shixin Wu, Xiao Huang, Qiyuan He, Yeng Ming Lam, and Hua Zhang. Organic photovoltaic devices using highly flexible reduced graphene oxide films as transparent electrodes. *ACS Nano*, 4:5263–5268, 9 2010.

[69] Xi Chen, Baohua Jia, Yinan Zhang, and Min Gu. Exceeding the limit of plasmonic light trapping in textured screen-printed solar cells using al nanoparticles and wrinkle-like graphene sheets. *Light: Science Applications 2013 2:8*, 2:e92–e92, 8 2013.

[70] Chuan Fei Guo, Tianyi Sun, Feng Cao, Qian Liu, and Zhifeng Ren. Metallic nanostructures for light trapping in energy-harvesting devices. *Light: Science Applications 2014 3:4*, 3:e161–e161, 4 2014.

[71] Jung Yong Lee, Stephen T. Connor, Yi Cui, and Peter Peumans. Solution-processed metal nanowire mesh transparent electrodes. *Nano Letters*, 8:689–692, 2 2008.

[72] H. A. Pohl and E. H. Engelhardt. Synthesis and characterization of some highly conjugated semiconducting polymers. *Journal of Physical Chemistry*, 66:2085–2095, 1962.

[73] C. K. Chiang, C. R. Fincher, Y. W. Park, A. J. Heeger, H. Shirakawa, E. J. Louis, S. C. Gau, and Alan G. MacDiarmid. Electrical conductivity in doped polyacetylene. *Physical Review Letters*, 39:1098–1101, 1977.

[74] C. K. Chiang, M. A. Druy, S. C. Gau, A. J. Heeger, E. J. Louis, A. G. MacDiarmid, Y. W. Park, and H. Shirakawa. Synthesis of highly conducting films of derivatives of polyacetylene, (CH)x. *Journal of the American Chemical Society*, 100:1013–1015, 1978.

[75] The nobel prize in chemistry 2000.

[76] Soyeong Ahn, Su Hun Jeong, Tae Hee Han, and Tae Woo Lee. Conducting polymers as anode buffer materials in organic and perovskite optoelectronics. *Advanced Optical Materials*, 5:1600512, 2 2017.

[77] Chang Yeoul Kim and Doh Hyung Riu. Raman scattering, electrical and optical properties of fluorine-doped tin oxide thin films with (200) and (301) preferred orientation. *Materials Chemistry and Physics*, 148:810–817, 12 2014.

[78] Zhiyong Liu and Ning Wang. Effects of highly conductive PH1000 anode in combination with ethylene glycol additive and H_2SO_4 immersion treatments on photovoltaic performance and photostability of polymer solar cells. *Journal of Materials Chemistry C*, 6:9734–9741, 9 2018.

[79] Yijie Xia and Jianyong Ouyang. Anion effect on salt-induced conductivity enhancement of poly(3,4-ethylenedioxythiophene):poly(styrenesulfonate) films. *Organic Electronics*, 11:1129–1135, 6 2010.

[80] Ermioni Polydorou, Martha Botzakaki, Charalampos Drivas, Kostas Seintis, Ilias Sakellis, Anastasia Soultati, Andreas Kaltzoglou, Thanassis Speliotis, Mihalis Fakis, Leonidas C. Palilis, Stella Kennou, Azhar Fakharuddin, Lukas

Schmidt-Mende, Dimitris Davazoglou, Polycarpos Falaras, Panagiotis Argitis, Christoforos A. Krontiras, Stavroula N. Georga, and Maria Vasilopoulou. Insights into the passivation effect of atomic layer deposited hafnium oxide for efficiency and stability enhancement in organic solar cells. *Journal of Materials Chemistry C*, 6:8051–8059, 8 2018.

[81] Mikkel Jørgensen, Kion Norrman, Suren A Gevorgyan, Thomas Tromholt, Birgitta Andreasen, Frederik C Krebs, M Jørgensen, K Norrman, S A Gevorgyan, T Tromholt, B Andreasen, and F C Krebs. Stability of polymer solar cells. *Advanced Materials*, 24:580–612, 2 2012.

[82] Young Woon Kim, Sang W. Lee, and Haydn Chen. Microstructural evolution and electrical property of Ta-doped SnO_2 films grown on Al_2O_3(0001) by metalorganic chemical vapor deposition. *Thin Solid Films*, 2002.

[83] Jianyong Ouyang, Qianfei Xu, Chi Wei Chu, Yang Yang, Gang Li, and Joseph Shinar. On the mechanism of conductivity enhancement in poly(3,4-ethylenedioxythiophene):poly(styrene sulfonate) film through solvent treatment. *Polymer*, 45:8443–8450, 11 2004.

[84] Leif A.A. Pettersson, Soumyadeb Ghosh, and Olle Inganäs. Optical anisotropy in thin films of poly(3,4-ethylenedioxythiophene)–poly(4-styrenesulfonate). *Organic Electronics*, 3:143–148, 12 2002.

[85] S. K.M. Jönsson, J. Birgerson, X. Crispin, G. Greczynski, W. Osikowicz, A. W. Denier van der Gon, W. R. Salaneck, and M. Fahlman. The effects of solvents on the morphology and sheet resistance in poly(3,4-ethylenedioxythiophene)–polystyrenesulfonic acid (PEDOT–PSS) films. *Synthetic Metals*, 139:1–10, 8 2003.

[86] Markus Döbbelin, Rebeca Marcilla, Maitane Salsamendi, Cristina Pozo-Gonzalo, Pedro M. Carrasco, Jose A. Pomposo, and David Mecerreyes. Influence of ionic liquids on the electrical conductivity and morphology of pedot:pss films. *Chemistry of Materials*, 19:2147–2149, 5 2007.

[87] Benhu Fan, Xiaoguang Mei, and Jianyong Ouyang. Significant conductivity enhancement of conductive poly(3,4- ethylenedioxythiophene): Poly(styrenesulfonate) films by adding anionic surfactants into polymer solution. *Macromolecules*, 41:5971–5973, 8 2008.

[88] Udo Lang, Nicola Naujoks, and Jurg Dual. Mechanical characterization of pedot:pss thin films. *Synthetic Metals*, 159:473–479, 3 2009.

[89] Chang Yeoul Kim and Doh Hyung Riu. Texture control of fluorine-doped tin oxide thin film. *Thin Solid Films*, 519:3081–3085, 3 2011.

[90] Michael Vosgueritchian, Darren J. Lipomi, and Zhenan Bao. Highly conductive and transparent PEDOT:PSS films with a fluorosurfactant for stretchable and flexible transparent electrodes. *Advanced Functional Materials*, 22:421–428, 1 2012.

[91] Rongkang Yin, Zheng Xu, Ming Mei, Zhaolong Chen, Kai Wang, Yanlin Liu, Tao Tang, Manish Kr Priydarshi, Xuejuan Meng, Siyuan Zhao, Bing Deng, Hailin Peng, Zhongfan Liu, and Xiaojie Duan. Soft transparent graphene contact lens electrodes for conformal full-cornea recording of electroretinogram. *Nature Communications 2018 9:1*, 9:1–11, 6 2018.

[92] Yue Qi, Bing Deng, Xiao Guo, Shulin Chen, Jing Gao, Tianran Li, Zhipeng Dou, Haina Ci, Jingyu Sun, Zhaolong Chen, Ruoyu Wang, Lingzhi Cui, Xudong Chen, Ke Chen, Huihui Wang, Sheng Wang, Peng Gao, Mark H. Rummeli, Hailin Peng, Yanfeng Zhang, and Zhongfan Liu. Switching vertical to horizontal graphene growth using faraday cage-assisted PECVD approach for high-performance transparent heating device. *Advanced Materials*, 30:1704839, 2 2018.

[93] K. S. Novoselov, A. K. Geim, S. V. Morozov, D. Jiang, Y. Zhang, S. V. Dubonos, I. V. Grigorieva, and A. A. Firsov. Electric field in atomically thin carbon films. *Science*, 306:666–669, 10 2004.

[94] The nobel prize in physics 2010 - nobelprize.org.

[95] A. K. Geim. Graphene: Status and prospects. *Science*, 324:1530–1534, 6 2009.

[96] R. R. Nair, P. Blake, A. N. Grigorenko, K. S. Novoselov, T. J. Booth, T. Stauber, N. M.R. Peres, and A. K. Geim. Fine structure constant defines visual transparency of graphene. *Science*, 320:1308, 6 2008.

[97] Won Jae Lee, Easwaramoorthi Ramasamy, Dong Yoon Lee, and Jae Sung Song. Performance variation of carbon counter electrode based dye-sensitized solar cell. *Solar Energy Materials and Solar Cells*, 92:814–818, 2008.

[98] Guanguang Zhang, Xu Zhang, Honglong Ning, Huangxing Chen, Qiong Wu, Man Jiang, Conghao Li, Dong Guo, Yiping Wang, Rihui Yao, and Junbiao Peng. Tungsten doped stannic oxide transparent conductive thin film using

preoxotungstic acid dopant. *Superlattices and Microstructures*, 130:277–284, 2019.

[99] Aqing Chen, Shengjian Xia, Haiyue Pan, Junhua Xi, Haiying Qin, Hongwei Lu, and Zhenguo Ji. A promising Ti/SnO_2 anodes modified by Nb/Sb co-doping. *Journal of Electroanalytical Chemistry*, 824:169–174, 2018.

[100] Fei Pan, Chenkai Sun, Yingfen Li, Dianyong Tang, Yingping Zou, Xiaojun Li, Song Bai, Xian Wei, Menglan Lv, Xiwen Chen, and Yongfang Li. Solution-processable n-doped graphene-containing cathode interfacial materials for high-performance organic solar cells. *Energy Environmental Science*, 12:3400–3411, 11 2019.

[101] Sivasankar Nemala, Sateesh Prathapani, Purnendu Kartikay, Parag Bhargava, Sudhanshu Mallick, and Sivasambu Bohm. Water-based high shear exfoliated graphene-based semi-transparent stable dye-sensitized solar cells for solar power window application. *IEEE Journal of Photovoltaics*, 8:1252–1258, 9 2018.

[102] K. S. Novoselov, A. K. Geim, S. V. Morozov, D. Jiang, M. I. Katsnelson, I. V. Grigorieva, S. V. Dubonos, and A. A. Firsov. Two-dimensional gas of massless dirac fermions in graphene. *Nature 2005 438:7065*, 438:197–200, 11 2005.

[103] Yuanbo Zhang, Yan Wen Tan, Horst L. Stormer, and Philip Kim. Experimental observation of the quantum hall effect and berry's phase in graphene. *Nature 2005 438:7065*, 438:201–204, 11 2005.

[104] Konstantin V. Emtsev, Aaron Bostwick, Karsten Horn, Johannes Jobst, Gary L. Kellogg, Lothar Ley, Jessica L. McChesney, Taisuke Ohta, Sergey A. Reshanov, Jonas Röhrl, Eli Rotenberg, Andreas K. Schmid, Daniel Waldmann, Heiko B. Weber, and Thomas Seyller. Towards wafer-size graphene layers by atmospheric pressure graphitization of silicon carbide. *Nature Materials 2009 8:3*, 8:203–207, 2 2009.

[105] Sasha Stankovich, Dmitriy A. Dikin, Richard D. Piner, Kevin A. Kohlhaas, Alfred Kleinhammes, Yuanyuan Jia, Yue Wu, Son Binh T. Nguyen, and Rodney S. Ruoff. Synthesis of graphene-based nanosheets via chemical reduction of exfoliated graphite oxide. *Carbon*, 45:1558–1565, 6 2007.

[106] Inhwa Jung, Dmitriy A. Dikin, Richard D. Piner, and Rodney S. Ruoff. Tunable electrical conductivity of individual graphene oxide sheets reduced at "low" temperatures. *Nano Letters*, 8:4283–4287, 12 2008.

[107] Goki Eda, Yun Yue Lin, Steve Miller, Chun Wei Chen, Wei Fang Su, and Manish Chhowalla. Transparent and conducting electrodes for organic electronics from reduced graphene oxide. *Applied Physics Letters*, 92:47, 6 2008.

[108] Hee Kwan Lee, Myung Sub Kim, and Jae Su Yu. Improved device performance of AlGaInP-based vertical light-emitting diodes with low-n ATO antireflective coating layer. *Microelectronic Engineering*, 104:29–32, 2013.

[109] Qingkai Yu, Jie Lian, Sujitra Siriponglert, Hao Li, Yong P. Chen, and Shin Shem Pei. Graphene segregated on ni surfaces and transferred to insulators. *Applied Physics Letters*, 93:113103, 9 2008.

[110] Keun Soo Kim, Yue Zhao, Houk Jang, Sang Yoon Lee, Jong Min Kim, Kwang S Kim, Jong-Hyun Ahn, Philip Kim, Jae-Young Choi, Byung, and Hee Hong. Large-scale pattern growth of graphene films for stretchable transparent electrodes. 457, 2009.

[111] Dongmei Li, Da Qin, Minghui Deng, Yanhong Luo, and Qingbo Meng. Optimization the solid-state electrolytes for dye-sensitized solar cells. *Energy environmental science*, 2:283–291, 2009.

[112] Monika ., Kapil Bhatt, Cheenu Rani, Ankit Kapoor, Pramod Kumar, Sandeep Kumar, Shilpi ., Sandeep ., Randhir Singh, and Chandra Charu Tripathi. A facile approach to fabricate graphene based piezoresistive strain sensor on paper substrate. *Indian Journal of Pure Applied Physics (IJPAP)*, 56:361–366, 2018.

[113] Soonjae Pyo, Youngkee Eun, Jaesam Sim, Kwanoh Kim, and Jungwook Choi. Carbon nanotube-graphene hybrids for soft electronics, sensors, and actuators. *Micro and Nano Systems Letters*, 10:1–12, 12 2022.

[114] Sumio Iijima. Helical microtubules of graphitic carbon. *Nature*, 354:56–58, 1991.

[115] Sumio Iijima and Toshinari Ichihashi. Single-shell carbon nanotubes of 1-nm diameter. *Nature*, 363:603–605, 1993.

[116] Neerja Saran, Kunjal Parikh, Dong Seok Suh, Edgar Muñoz, Harsha Kolla, and Sanjeev K. Manohar. Fabrication and characterization of thin films of single-walled carbon nanotube bundles on flexible plastic substrates. *Journal of the American Chemical Society*, 126:4462–4463, 4 2004.

[117] Kuan-Ru Chen, Hsiu-Feng Yeh, Hung-Chih Chen, Ta-Jo Liu, Shu-Jiuan Huang, Ping-Yao Wu, and Carlos Tiu. Optical-electronic properties of carbon-

nanotubes based transparent conducting films. *Advances in Chemical Engineering and Science*, 2013:105–111, 1 2013.

[118] Rodrigo V. Salvatierra, Carlos E. Cava, Lucimara S. Roman, and Aldo J.G. Zarbin. ITO-free and flexible organic photovoltaic device based on high transparent and conductive polyaniline/carbon nanotube thin films. *Advanced Functional Materials*, 23:1490–1499, 3 2013.

[119] Hong Zhang Geng, Kang Kim Ki, Pyo So Kang, Sil Lee Young, Youngkyu Chang, and Hee Lee Young. Effect of acid treatment on carbon nanotube-based flexible transparent conducting films. *Journal of the American Chemical Society*, 129:7758–7759, 6 2007.

[120] Dachuan Shi and Daniel E. Resasco. Study of the growth of conductive single-wall carbon nanotube films with ultra-high transparency. *Chemical Physics Letters*, 511:356–362, 8 2011.

[121] Hock Beng Lee, Won Yong Jin, Manoj Mayaji Ovhal, Neetesh Kumar, and Jae Wook Kang. Flexible transparent conducting electrodes based on metal meshes for organic optoelectronic device applications: A review. *Journal of Materials Chemistry C*, 7:1087–1110, 2019.

[122] Yan Gang Bi, Jing Feng, Jin Hai Ji, Yang Chen, Yu Shan Liu, Yun Fei Li, Yue Feng Liu, Xu Lin Zhang, and Hong Bo Sun. Ultrathin and ultrasmooth Au films as transparent electrodes in ITO-free organic light-emitting devices. *Nanoscale*, 8:10010–10015, 5 2016.

[123] Shuai Wang, Liyi Shi, Guorong Chen, Chaoqun Ba, Zhuyi Wang, Jiefang Zhu, Yin Zhao, Meihong Zhang, and Shuai Yuan. In situ synthesis of tungsten-doped SnO_2 and graphene nanocomposites for high-performance anode materials of lithium-ion batteries. *ACS Applied Materials and Interfaces*, 9:17163–17171, 2017.

[124] Ian E. Stewart, Aaron R. Rathmell, Liang Yan, Shengrong Ye, Patrick F. Flowers, Wei You, and Benjamin J. Wiley. Solution-processed copper–nickel nanowire anodes for organic solar cells. *Nanoscale*, 6:5980–5988, 5 2014.

[125] Hyun Min Nam, Duck Min Seo, Hyung Duk Yun, Gurunathan Thangavel, Lee Soon Park, and Su Yong Nam. Transparent conducting film fabricated by metal mesh method with Ag and Cu-Ag mixture nanoparticle pastes. *Metals 2017, Vol. 7, Page 176*, 7:176, 5 2017.

[126] Anuj R. Madaria, Akshay Kumar, Fumiaki N. Ishikawa, and Chongwu Zhou. Uniform, highly conductive, and patterned transparent films of a percolating silver nanowire network on rigid and flexible substrates using a dry transfer technique. *Nano Research*, 3:564–573, 7 2010.

[127] Huizhang Guo, Na Lin, Yuanzhi Chen, Zhenwei Wang, Qingshui Xie, Tongchang Zheng, Na Gao, Shuping Li, Junyong Kang, Duanjun Cai, and Dong Liang Peng. Copper nanowires as fully transparent conductive electrodes. *Scientific Reports 2013 3:1*, 3:1–8, 7 2013.

[128] Haimin Zhang, Yun Wang, Dongjiang Yang, Yibing Li, Hongwei Liu, Porun Liu, Barry J Wood, and Huijun Zhao. Directly hydrothermal growth of single crystal Nb_3O_7 (OH) nanorod film for high performance dye-sensitized solar cells. *Advanced Materials*, 24:1598–1603, 2012.

[129] Aaron R. Rathmell and Benjamin J. Wiley. The synthesis and coating of long, thin copper nanowires to make flexible, transparent conducting films on plastic substrates. *Advanced Materials*, 23:4798–4803, 11 2011.

[130] Mingshang Jin, Guannan He, Hui Zhang, Jie Zeng, Zhaoxiong Xie, and Younan Xia. Shape-controlled synthesis of copper nanocrystals in an aqueous solution with glucose as a reducing agent and hexadecylamine as a capping agent. *Angewandte Chemie International Edition*, 50:10560–10564, 11 2011.

[131] Yue Shi, Liang He, Qian Deng, Quanxiao Liu, Luhai Li, Wei Wang, Zhiqing Xin, and Ruping Liu. Synthesis and applications of silver nanowires for transparent conductive films. *Micromachines 2019, Vol. 10, Page 330*, 10:330, 5 2019.

[132] Xingchen Ye, Jiayang Fei, Benjamin T. Diroll, Taejong Paik, and Christopher B. Murray. Expanding the spectral tunability of plasmonic resonances in doped metal-oxide nanocrystals through cooperative cation-anion codoping. *Journal of the American Chemical Society*, 136:11680–11686, 2014.

[133] Ian E. Stewart, Shengrong Ye, Zuofeng Chen, Patrick F. Flowers, and Benjamin J. Wiley. Synthesis of Cu-Ag, Cu-Au, and Cu-Pt core-shell nanowires and their use in transparent conducting films. *Chemistry of Materials*, 27:7788–7794, 11 2015.

[134] Daniel Gall. Electron mean free path in elemental metals. *Journal of Applied Physics*, 119:85101, 2 2016.

[135] Chang Lae Kim, Chan Won Jung, Young Jei Oh, and Dae Eun Kim. A highly flexible transparent conductive electrode based on nanomaterials. *NPG Asia Materials 2017 9:10*, 9:e438–e438, 10 2017.

[136] Qi Jiang, Xingwang Zhang, and Jingbi You. SnO_2: A wonderful electron transport layer for perovskite solar cells. *Small*, 14:1801154, 8 2018.

[137] Sukjoon Hong, Junyeob Yeo, Gunho Kim, Dongkyu Kim, Habeom Lee, Jinhyeong Kwon, Hyungman Lee, Phillip Lee, and Seung Hwan Ko. Nonvacuum, maskless fabrication of a flexible metal grid transparent conductor by low-temperature selective laser sintering of nanoparticle ink. *ACS Nano*, 7:5024–5031, 6 2013.

[138] Chuan Pei Lee and Kuo Chuan Ho. Poly(ionic liquid)s for dye-sensitized solar cells: A mini-review. *European Polymer Journal*, 108:420–428, 2018.

[139] Xiao Yan Zeng, Qi Kai Zhang, Rong Min Yu, and Can Zhong Lu. A new transparent conductor: Silver nanowire film buried at the surface of a transparent polymer. *Advanced Materials*, 22:4484–4488, 10 2010.

[140] Antonio Gaetano Ricciardulli, Sheng Yang, Gert-Jan A H Wetzelaer, Xinliang Feng, Paul W M Blom, A G Ricciardulli, S Yang, G j A H Wetzelaer, P W M Blom, and X Feng. Hybrid silver nanowire and graphene-based solution-processed transparent electrode for organic optoelectronics. *Advanced Functional Materials*, 28:1706010, 4 2018.

[141] Wenfeng Mao, Bangyun Xiong, Yong Liu, and Chunqing He. Correlation between defects and conductivity of Sb-doped tin oxide thin films. *Applied Physics Letters*, 103:1–5, 2013.

[142] Myungkwan Song, Jong Hyun Park, Chang Su Kim, Dong Ho Kim, Yong Cheol Kang, Sung Ho Jin, Won Yong Jin, and Jae Wook Kang. Highly flexible and transparent conducting silver nanowire/ZnO composite film for organic solar cells. *Nano Research*, 7:1370–1379, 9 2014.

[143] Teng Yu Jin, Wei Li, Yan Qing Li, Yu Xin Luo, Yang Shen, Li Peng Cheng, and Jian Xin Tang. High-performance flexible perovskite solar cells enabled by low-temperature ALD-assisted surface passivation. *Advanced Optical Materials*, 6:1801153, 12 2018.

[144] M. S.R. Khan and A. Reza. Optical and electrical properties of optimized thin gold films as top layer of mis solar cells. *Applied Physics A Solids and Surfaces*, 54:204–207, 2 1992.

[145] Jeong Ho Shin, Jae Yong Song, and Hyun Min Park. Growth of ZnO nanowires on a patterned au substrate. *Materials Letters*, 63:145–147, 1 2009.

[146] Jiří Homola. Present and future of surface plasmon resonance biosensors. *Analytical and Bioanalytical Chemistry*, 377:528–539, 10 2003.

[147] A. Axelevitch, B. Gorenstein, and G. Golan. Investigation of optical transmission in thin metal films. *Physics Procedia*, 32:1–13, 1 2012.

[148] S. Norrman, T. Andersson, C. G. Granqvist, and O. Hunderi. Optical properties of discontinuous gold films. *Physical Review B*, 18:674, 7 1978.

[149] R. Lazzari, J. Jupille, and Y. Borensztein. In situ study of a thin metal film by optical means. *Applied Surface Science*, 142:451–454, 4 1999.

[150] S. Marsillac, S. A. Little, and R. W. Collins. A broadband analysis of the optical properties of silver nanoparticle films by in situ real time spectroscopic ellipsometry. *Thin Solid Films*, 519:2936–2940, 2 2011.

[151] T. W.H. Oates and A. Mücklich. Evolution of plasmon resonances during plasma deposition of silver nanoparticles. *Nanotechnology*, 16:2606, 9 2005.

[152] H. T. Beyene, J. W. Weber, M. A. Verheijen, M. C.M. van de Sanden, and M. Creatore. Real time in situ spectroscopic ellipsometry of the growth and plasmonic properties of au nanoparticles on SiO_2. *Nano Research*, 5:513–520, 7 2012.

[153] Tobias Schwab, Sylvio Schubert, Simone Hofmann, Markus Fröbel, Cornelius Fuchs, Michael Thomschke, Lars Müller-Meskamp, Karl Leo, and Malte C. Gather. Highly efficient color stable inverted white top-emitting oleds with ultra-thin wetting layer top electrodes. *Advanced Optical Materials*, 1:707–713, 10 2013.

[154] Nadia Formica, Dhriti Sundar Ghosh, Tong Lai Chen, Christian Eickhoff, Ingmar Bruder, and Valerio Pruneri. Highly stable Ag–Ni based transparent electrodes on PET substrates for flexible organic solar cells. *Solar Energy Materials and Solar Cells*, 107:63–68, 12 2012.

[155] Kaiyong Cai, Michael Müller, Jörg Bossert, Annett Rechtenbach, and Klaus D. Jandt. Surface structure and composition of flat titanium thin films as a function of film thickness and evaporation rate. *Applied Surface Science*, 250:252–267, 8 2005.

[156] Alexander Axelevitch and Boris Apter. In-situ investigation of optical transmittance in metal thin films. *Thin Solid Films*, 591:261–266, 9 2015.

[157] Guangliang Zhang, Hari Bala, Yueming Cheng, Dong Shi, Xueju Lv, Qingjiang Yu, and Peng Wang. High efficiency and stable dye-sensitized solar cells with an organic chromophore featuring a binary -conjugated spacer. *Chemical Communications*, pages 2198–2200, 2009.

[158] Tomasz Stefaniuk, Piotr Wróbel, Ewa Górecka, and Tomasz Szoplik. Optimum deposition conditions of ultrasmooth silver nanolayers. *Nanoscale Research Letters*, 9:1–9, 3 2014.

[159] Robert M Pasquarelli, David S Ginley, and Ryan O'Hayre. Solution processing of transparent conductors: from flask to film. *Chemical Society Reviews*, 40:5406–5441, 2011.

[160] David R Lide. CRC handbook of chemistry and physics, internet version 2005, 2005.

[161] Gregory J Exarhos and Xiao-Dong Zhou. Discovery-based design of transparent conducting oxide films. *Thin solid films*, 515:7025–7052, 2007.

[162] Tadatsugu Minami. *Transparent Conductive Oxides for Transparent Electrode Applications*, volume 88. Elsevier Inc., 1 edition, 2013.

[163] K L Chopra, S Major, and D K Pandya. Transparent conductors-A status review, 1983.

[164] Hiroshi Kawazoe and Kazushige Ueda. Transparent conducting oxides based on the spinel structure. *Journal of the American Ceramic Society*, 82:3330–3336, 12 1999.

[165] S Shanthi, C Subramanian, and P Ramasamy. Investigations on the optical properties of undoped, fluorine doped and antimony doped tin oxide films. *Crystal Research and Technology: Journal of Experimental and Industrial Crystallography*, 34(8):1037–1046, 1999.

[166] Shihui Yu, Linghong Ding, Chuang Xue, Li Chen, and W. F. Zhang. Transparent conducting Sb-doped SnO_2 thin films grown by pulsed laser deposition. *Journal of Non-Crystalline Solids*, 358:3137–3140, 2012.

[167] Ling Cao, Liping Zhu, Jie Jiang, Ran Zhao, Zhizhen Ye, and Buihui Zhao. Highly transparent and conducting fluorine-doped ZnO thin films prepared by pulsed laser deposition. *Solar Energy Materials and Solar Cells*, 95:894–898, 3 2011.

[168] Khalid Mahmood and Hyung Jin Sung. A dye-sensitized solar cell based on a boron-doped ZnO (BZO) film with double light-scattering-layers structured photoanode. *Journal of Materials Chemistry A*, 2:5408–5417, 2014.

[169] A. R. Babar, P. R. Deshamukh, R. J. Deokate, D. Haranath, C. H. Bhosale, and K. Y. Rajpure. Gallium doping in transparent conductive ZnO thin films prepared by chemical spray pyrolysis. *Journal of Physics D: Applied Physics*, 41, 2008.

[170] Sara Marouf, Abdelkrim Beniaiche, Kasra Kardarian, Manuel J. Mendes, Olalla Sanchez-Sobrado, Hugo Águas, Elvira Fortunato, and Rodrigo Martins. Low-temperature spray-coating of high-performing ZnO:Al films for transparent electronics. *Journal of Analytical and Applied Pyrolysis*, 127:299–308, 9 2017.

[171] Taro Hitosugi, Naoomi Yamada, Shoichiro Nakao, Yasushi Hirose, and Tetsuya Hasegawa. Properties of TiO_2-based transparent conducting oxides. *Physica Status Solidi (A) Applications and Materials Science*, 207:1529–1537, 2010.

[172] A. N. Banerjee and K. K. Chattopadhyay. Recent developments in the emerging field of crystalline p-type transparent conducting oxide thin films. *Progress in Crystal Growth and Characterization of Materials*, 50:52–105, 2005.

[173] Kelvin H.L. Zhang, Kai Xi, Mark G. Blamire, and Russell G. Egdell. P-type transparent conducting oxides. *Journal of Physics Condensed Matter*, 28:383002, 2016.

[174] R. Kykyneshi, B. C. Nielsen, J. Tate, J. Li, and A. W. Sleight. Structural and transport properties of $CuSc_1MgxO_2$ delafossites. *Journal of Applied Physics*, 96:6188–6194, 12 2004.

[175] Hiroshi Kawazoe, Masahiro Yasukawa, Hiroyuki Hyodo, Masaaki Kurita, Hiroshi Yanagi, and Hideo Hosono. P-type electrical conduction in transparent thin films of $CuAlO_2$. *Nature 1997 389:6654*, 389:939–942, 1997.

[176] Hiromichi Ohta, Ken Ichi Kawamura, Masahiro Orita, Masahiro Hirano, Nobuhiko Sarukura, and Hideo Hosono. Current injection emission from a transparent p–n junction composed of p-$SrCu_2O_2$/n-ZnO. *Applied Physics Letters*, 77:475–477, 7 2000.

[177] Michael Hart. *Hubris: The troubling science, economics, and politics of climate change*. Lulu. com, 2015.

[178] Alexandre-Edmond Becquerel. Recherches sur les effets de la radiation chimique de la lumiere solaire au moyen des courants electriques. *CR Acad. Sci*, 9:1, 1839.

[179] Daryl M Chapin, Calvin S Fuller, and Gerald L Pearson. A new silicon p-n junction photocell for converting solar radiation into electrical power. *Journal of Applied Physics*, 25:676–677, 1954.

[180] Biju Mani Rajbongshi and Anil Verma. *Emerging Nanotechnology for Third Generation Photovoltaic Cells BT - Nanotechnology: Applications in Energy, Drug and Food*, pages 99–133. Springer International Publishing, 2019.

[181] W West. First hundred years of spectral sensitization. *Photographic Science and Engineering*, 18:35–48, 1974.

[182] James Moser. Notiz über verstärkung photoelektrischer ströme durch optische sensibilisirung. *Monatshefte für Chemie und verwandte Teile anderer Wissenschaften*, 8:373, 1887.

[183] Susumu Namba and Yasushi Hishiki. Color sensitization of zinc oxide with cyanine dyes1. *The Journal of Physical Chemistry*, 69:774–779, 1965.

[184] H Gerischer, M E Michel-Beyerle, F Rebentrost, and H Tributsch. Sensitization of charge injection into semiconductors with large band gap. *Electrochimica Acta*, 13:1509–1515, 1968.

[185] E Daltrozzo and H Tributsch. On the mechanism of spectral sensitization: Rhodamin b sensitized electron transfer to zinc oxide. 1975.

[186] Mark T Spitler and Melvin Calvin. Electron transfer at sensitized TiO_2 electrodes. *The Journal of Chemical Physics*, 66:4294–4305, 1977.

[187] K Kalyanasundaram, N Vlachopoulos, V Krishnan A Monnier, and M Grátzel. Sensitization of TiO_2 in the visible light region using zinc porphyrins. pages 2342–2347, 1987.

[188] Ladislav Kavan and Michael Grätzel. Nafion modified TiO_2 electrodes: photoresponse and sensitization by Ru (II)-bipyridyl complexes. *Electrochimica acta*, 34:1327–1334, 1989.

[189] Brian O'Regan and Michael Grätzel. A low-cost, high-efficiency solar cell based on dye-sensitized colloidal TiO_2 films. *Nature*, 353:737–740, 10 1991.

[190] Simon Mathew, Aswani Yella, Peng Gao, Robin Humphry-Baker, Basile F.E. Curchod, Negar Ashari-Astani, Ivano Tavernelli, Ursula Rothlisberger, Md Khaja Nazeeruddin, and Michael Grätzel. Dye-sensitized solar cells with 13 *Nature Chemistry*, 6:242–247, 2014.

[191] Jiangxin Wang, Chaoyi Yan, Guofa Cai, Mengqi Cui, Alice Lee-Sie Eh, Pooi See Lee, J X Wang, C Y Yan, G F Cai, M Q Cui, A L-S Eh, and P S Lee. Extremely stretchable electroluminescent devices with ionic conductors. *Advanced Materials*, 28:4490–4496, 6 2016.

[192] Changming Qu, Yun Xu, Yu Xiao, Shaochun Zhang, Hanyun Liu, and Guofeng Song. Multifunctional displays and sensing platforms for the future: A review on flexible alternating current electroluminescence devices. *ACS Applied Electronic Materials*, 3:5188–5210, 12 2021. doi: 10.1021/acsaelm.1c00833.

[193] P. D. Rack, A. Naman, P. H. Holloway, S. S. Sun, and R. T. Tuenge. Materials used in electroluminescent displays. *MRS Bulletin*, 21:49–58, 1996.

[194] G. Blasse and B. C. Grabmaier. A general introduction to luminescent materials. *Luminescent Materials*, pages 1–9, 1994.

[195] Chun Ting Li, Yu Lin Tsai, and Kuo Chuan Ho. Earth abundant silicon composites as the electrocatalytic counter electrodes for dye-sensitized solar cells. *ACS Applied Materials and Interfaces*, 8:7037–7046, 2016.

[196] Can Hui Yang, Baohong Chen, Jinxiong Zhou, Yong Mei Chen, Zhigang Suo, C H Yang, B H Chen, X Zhou, Y M Chen, Z G Suo, and John A Paulson. Electroluminescence of giant stretchability. *Advanced Materials*, 28:4480–4484, 6 2016.

[197] Xiuru Xu, Dan Hu, Lijia Yan, Shaoli Fang, Clifton Shen, Yueh Lin Loo, Yuan Lin, Carter S. Haines, Na Li, Anvar A. Zakhidov, Hong Meng, Ray H. Baughman, and Wei Huang. Polar-electrode-bridged electroluminescent displays: 2d sensors remotely communicating optically. *Advanced Materials*, 29:1703552, 11 2017.

[198] Guojin Liang, Ming Yi, Haibo Hu, Ke Ding, Lei Wang, Haibo Zeng, Jiang Tang, Lei Liao, Cewen Nan, Yunbin He, and Changhui Ye. Coaxial-structured weavable and wearable electroluminescent fibers. *Advanced Electronic Materials*, 3:1700401, 12 2017.

[199] Sanjay Tiwari, Shikha Tiwari, and B. P. Chandra. Characteristics of a.c. electroluminescence in thin film ZnS:Mn display devices. *Journal of Materials Science: Materials in Electronics*, 15:569–574, 9 2004.

[200] Peter Blake, Paul D. Brimicombe, Rahul R. Nair, Tim J. Booth, Da Jiang, Fred Schedin, Leonid A. Ponomarenko, Sergey V. Morozov, Helen F. Gleeson, Ernie W. Hill, Andre K. Geim, and Kostya S. Novoselov. Graphene-based liquid crystal device. *Nano Letters*, 8:1704–1708, 6 2008.

[201] Je Hong Park, Sung Hun Lee, Jong Su Kim, Ae Kyung Kwon, Hong Lee Park, and Sang Do Han. White-electroluminescent device with ZnS:Mn, Cu, Cl phosphor. *Journal of Luminescence*, 126:566–570, 10 2007.

[202] Thomas R. Anderson, Ed Hawkins, and Philip D. Jones. CO_2, the greenhouse effect and global warming: from the pioneering work of arrhenius and callendar to today's earth system models. *Endeavour*, 40:178–187, 9 2016.

[203] Abdeen Mustafa Omer. Energy use and environmental impacts: A general review. *Advances in Energy Research*, 17:1–38, 4 2014.

[204] Xiao-Feng Wang, Yasushi Koyama, Hiroyoshi Nagae, Yumiko Yamano, Masayoshi Ito, and Yuji Wada. Photocurrents of solar cells sensitized by aggregate-forming polyenes: enhancement due to suppression of singlet–triplet annihilation by lowering of dye concentration or light intensity. *Chemical physics letters*, 420:309–315, 2006.

[205] Cong Zhang, Wei Fan, Shujuan Wang, Qi Wang, Yifan Zhang, and Kai Dong. Recent progress of wearable piezoelectric nanogenerators. *ACS Applied Electronic Materials*, 3:2449–2467, 6 2021.

[206] Youfan Hu, Long Lin, Yan Zhang, and Zhong Lin Wang. Replacing a battery by a nanogenerator with 20 V output. *Advanced Materials*, 24:110–114, 1 2012.

[207] Dengwei Hu, Minggang Yao, Yong Fan, Chunrui Ma, Mingjin Fan, and Ming Liu. Strategies to achieve high performance piezoelectric nanogenerators. *Nano Energy*, 55:288–304, 1 2019.

[208] Aifang Yu, Ming Song, Yan Zhang, Jinzong Kou, Junyi Zhai, and Zhong Lin Wang. A self-powered ac magnetic sensor based on piezoelectric nanogenerator. *Nanotechnology*, 25:455503, 10 2014.

[209] Youfan Hu and Zhong Lin Wang. Recent progress in piezoelectric nanogenerators as a sustainable power source in self-powered systems and active sensors. *Nano Energy*, 14:3–14, 5 2015.

[210] Siu-Fung Leung, Kang-Ting Ho, Po-Kai Kung, Vincent K S Hsiao, Husam N Alshareef, Zhong Lin Wang, Jr-Hau He, S f Leung, K t Ho, P k Kung, V K S Hsiao, J h He, H N Alshareef Physical Sciences, and Z L Wang. A self-powered and flexible organometallic halide perovskite photodetector with very high detectivity. *Advanced Materials*, 30:1704611, 2 2018.

[211] Yifan Gao and Zhong Lin Wang. Electrostatic potential in a bent piezoelectric nanowire. the fundamental theory of nanogenerator and nanopiezotronics. *Nano Letters*, 7:2499–2505, 8 2007.

[212] Xudong Wang, Jinhui Song, Jin Liu, and Lin Wang Zhong. Direct-current nanogenerator driven by ultrasonic waves. *Science*, 316:102–105, 4 2007.

[213] Sheng Xu, Yong Qin, Chen Xu, Yaguang Wei, Rusen Yang, and Zhong Lin Wang. Self-powered nanowire devices. *Nature Nanotechnology 2010 5:5*, 5:366–373, 3 2010.

[214] Yang Yang, Haiying Wang, Xiang Li, and Ce Wang. Electrospun mesoporous W6+-doped TiO_2 thin films for efficient visible-light photocatalysis. *Materials Letters*, 63:331–333, 2009.

[215] Xiaocui Li, You Meng, Rong Fan, Sufeng Fan, Chaoqun Dang, Xiaobin Feng, Johnny C. Ho, and Yang Lu. High elasticity of $CsPbBr_3$ perovskite nanowires for flexible electronics. *Nano Research 2021 14:11*, 14:4033–4037, 3 2021.

[216] Weixin Zhou, Jun Chen, Yi Li, Danbei Wang, Jianyu Chen, Xiaomiao Feng, Zhendong Huang, Ruiqing Liu, Xiujing Lin, Hongmei Zhang, Baoxiu Mi, and Yanwen Ma. Copper mesh templated by breath-figure polymer films as flexible transparent electrodes for organic photovoltaic devices. *ACS Applied Materials and Interfaces*, 8:11122–11127, 5 2016.

[217] AD Chintagunta, A Kumar, SJ Kumar, and ML Verma. Metal and metal oxides for energy and electronics. *Cham: Springer*, pages 331–353, 2020.

[218] Wei Li, Chao Ding, Jinze Li, Qingying Ren, Gang Bai, and Jie Xu. Sensing mechanism of Sb, S doped SnO_2 (110) surface for CO. *Applied Surface Science*, 502:144140, 2 2020.

[219] G. Leftheriotis, P. Yianoulis, and D. Patrikios. Deposition and optical properties of optimised ZnS/Ag/ZnS thin films for energy saving applications. *Thin Solid Films*, 306:92–99, 8 1997.

[220] M. P.S. Rana, Fouran Singh, Sandhya Negi, Subodh K. Gautam, R. G. Singh, and R. C. Ramola. Band gap engineering and low temperature transport phenomenon in highly conducting antimony doped tin oxide thin films. *Ceramics International*, 42:5932–5941, 4 2016.

[221] Jian Xu, Shuiping Huang, and Zhanshan Wang. First principle study on the electronic structure of fluorine-doped SnO_2. *Solid State Communications*, 149:527–531, 4 2009.

[222] Soumen Das and V. Jayaraman. SnO_2: A comprehensive review on structures and gas sensors. *Progress in Materials Science*, 66:112–255, 10 2014.

[223] Nilesh Mazumder, Dipayan Sen, Subhajit Saha, Uttam Kumar Ghorai, Nirmalya Sankar Das, and Kalyan Kumar Chattopadhyay. Enhanced ultraviolet emission from Mg doped SnO_2 nanocrystals at room temperature and its modulation upon H_2 annealing. *Journal of Physical Chemistry C*, 117:6454–6461, 3 2013.

[224] A. Ayeshamariam, S. Ramalingam, M. Bououdina, and M. Jayachandran. Preparation and characterizations of SnO_2 nanopowder and spectroscopic (FT-IR, FT-Raman, UV–Visible and NMR) analysis using HF and DFT calculations. *Spectrochimica Acta Part A: Molecular and Biomolecular Spectroscopy*, 118:1135–1143, 1 2014.

[225] Alexandre J.C. Lanfredi, Renan R. Geraldes, Olivia M. Berengue, Edson R. Leite, and Adenilson J. Chiquito. Electron transport properties of undoped SnO_2 monocrystals. *Journal of Applied Physics*, 105:23708, 1 2009.

[226] Yiting Chen, R. Stephen Carmichael, and Tricia Breen Carmichael. patterned, flexible, and stretchable silver nanowire/polymer composite films as transparent conductive electrodes. *ACS Applied Materials and Interfaces*, 11:31210–31219, 8 2019.

[227] Funda Aksoy Akgul, Cebrail Gumus, Ali O. Er, Ashraf H. Farha, Guvenc Akgul, Yuksel Ufuktepe, and Zhi Liu. Structural and electronic properties of SnO_2. *Journal of Alloys and Compounds*, 579:50–56, 2013.

[228] Güven Turgut, Eyüp Fahri Keskenler, Serdar Aydin, Erdal Sönmez, Seydi Doğan, Bahattin Düzgün, and Mehmet Ertuğrul. Effect of Nb doping on structural, electrical and optical properties of spray deposited SnO_2 thin films. *Superlattices and Microstructures*, 56:107–116, 2013.

[229] Steven Chu and Arun Majumdar. Opportunities and challenges for a sustainable energy future. *Nature*, 488:294–303, 2012.

[230] Kasturi Chopra. *Thin film device applications*. Springer Science & Business Media, 2012.

[231] Michael Faraday. Lix. experimental relations of gold (and other metals) to light.—the bakerian lecture. *The London, Edinburgh, and Dublin Philosophical Magazine and Journal of Science*, 14:512–539, 2018.

[232] Elvira Fortunato, David Ginley, Hideo Hosono, and David C. Paine. Transparent conducting oxides for photovoltaics. *MRS Bulletin*, 32:242–247, 2007.

[233] Rakesh A. Afre, Nallin Sharma, Maheshwar Sharon, and Madhuri Sharon. Transparent conducting oxide films for various applications: A review. *Reviews on Advanced Materials Science*, 53:79–89, 2018.

[234] Nurul Nazli Rosli, Mohd Adib Ibrahim, Norasikin Ahmad Ludin, Mohd Asri Mat Teridi, and Kamaruzzaman Sopian. A review of graphene based transparent conducting films for use in solar photovoltaic applications. *Renewable and Sustainable Energy Reviews*, 99:83–99, 2019.

[235] Vyomesh R. Buch, Amit Kumar Chawla, and Sushant K. Rawal. Review on electrochromic property for WO_3 thin films using different deposition techniques. *Materials Today: Proceedings*, 3:1429–1437, 1 2016.

[236] Shriram Ramanathan. Thin film metal-oxides. *Harvard University: Springer New York Dordrecht Heidelberg London, London*, 2010.

[237] Peter M Martin. *Handbook of deposition technologies for films and coatings: science, applications and technology*. William Andrew, 2009.

[238] P. J. Martin. Ion-based methods for optical thin film deposition. *Journal of Materials Science*, 21:1–25, 1986.

[239] F. A. Green and B. N. Chapman. Electron effects in magnetron sputtering. *Journal of Vacuum Science and Technology*, 13:165–168, 1 1976.

[240] G. A. Kimmel and B. H. Cooper. Dynamics of resonant charge transfer in low-energy alkali-metal-ion scattering. *Physical Review B*, 48:12164, 10 1993.

[241] Charles Hard Townes. Theory of cathode sputtering in low voltage gaseous discharges. *Physical Review*, 65:319, 6 1944.

[242] K. H. Kingdon and Irving Langmuir. The removal of thorium from the surface of a thoriated tungsten filament by positive ion bombardment. *Physical Review*, 22:148, 8 1923.

[243] Erich B Henschke and Richard M Noyes. Threshold energies in mechanical collision theories of cathode sputtering. *Journal of Applied Physics*, 33:1773–1778, 5 1962.

[244] Frank Keywell. Measurements and collision—radiation damage theory of high-vacuum sputtering. *Physical Review*, 97:1611, 3 1955.

[245] G. Korotcenkov and B. K. Cho. Spray pyrolysis deposition of undoped SnO_2 and In_2O_3 films and their structural properties. *Progress in Crystal Growth and Characterization of Materials*, 63:1–47, 2017.

[246] JC Viguie and J Spitz. Chemical vapor deposition at low temperatures. *J. electrochem. Soc*, 122(4):585–588, 1975.

[247] Shou Shing Hsieh and Sueng Yang Luo. Droplet impact dynamics and transient heat transfer of a micro spray system for power electronics devices. *International Journal of Heat and Mass Transfer*, 92:190–205, 2016.

[248] Pramod S Patil. Versatility of chemical spray pyrolysis technique. *Materials Chemistry and physics*, 59:185–198, 1999.

[249] D. Paul Joseph, M. Saravanan, B. Muthuraaman, P. Renugambal, S. Sambasivam, S. Philip Raja, P. Maruthamuthu, and C. Venkateswaran. Spray deposition and characterization of nanostructured Li doped NiO thin films for application in dye-sensitized solar cells. *Nanotechnology*, 19:485707, 11 2008.

[250] B D Cullity and S R Stock. Elements of X-ray diffraction. *Upper Saddle River, NJ*, page 388, 2001.

[251] N.S. McIntyre. *Quantitative Surface Analysis of materials*. ASTM Special Technical Publication, 1977.

[252] Cedric J Powell and P E Larson. Quantitative surface analysis by x-ray photoelectron spectroscopy. *Applications of Surface Science*, 1:186–201, 1978.

[253] C W Oatley, D McMullan, and K C A Smith. The development of the scanning electron microscope. *The Beginnings of Electron Microscopy*, pages 443–482, 1985.

[254] Hans Jürgen Butt, Brunero Cappella, and Michael Kappl. Force measurements with the atomic force microscope: Technique, interpretation and applications. *Surface Science Reports*, 59:1–152, 2005.

[255] G Binnig, C.F. Quate, and Ch Gerber. Atomi force microscope. *Physical Review Letters*, 56, 1986.

[256] Robert N Wenzel. Resistance of solid surfaces to wetting by water. *Industrial Engineering Chemistry*, 28:988–994, 1936.

[257] Yiming Wang Chenying Wang Wei Ren Zhuangde Jiang Changsheng Li, Shuming Yang. Measurement and characterization of a nano scale multipe step height sample using stylus profiler. *Applied Surface Science*, 387:732–735, 2016.

[258] Yang Leng. *Related Titles Characterization of Surfaces and Nanostructures Basic Concepts of X-Ray Diffraction Characterization of Solid Materials and Heterogeneous Catalysts Advanced Characterization Techniques for Thin Film Solar Cells Characterization Techniques*. 2013.

[259] D. F. Swinehart. The beer-lambert law. *Journal of Chemical Education*, 39:333, 2009.

[260] J Tauc, Radu Grigorovici, and Anina Vancu. Optical properties and electronic structure of amorphous germanium. *physica status solidi (b)*, 15:627–637, 1966.

[261] G. D. Gilliland. *Photoluminescence spectroscopy of crystalline semiconductors*, volume 18. 1997.

[262] Sidney Perkowitz. *Optical characterization of semiconductors: infrared, Raman, and photoluminescence spectroscopy*, volume 14. Elsevier, 2012.

[263] H. Sefardjella, B. Boudjema, A. Kabir, and G. Schmerber. Structural and photoluminescence properties of SnO_2 obtained by thermal oxidation of evaporated Sn thin films. *Current Applied Physics*, 13:1971–1974, 2013.

[264] Leo J van der Pauw. A method of measuring the resistivity and hall coefficient on lamellae of arbitrary shape. *Philips technical review*, 20:220–224, 1958.

[265] Ch Surya Prakasarao, Pratim Hazarika, Slavia Deeksha DSouza, Jean Maria Fernandes, M. Kovendhan, R. Arockia Kumar, and D. Paul Joseph. Investigation of ultra-thin and flexible Au–Ag–Au transparent conducting electrode. *Current Applied Physics*, 20:1118–1124, 10 2020.

[266] Neetu, Shalini Singh, Pankaj Srivastava, and Lal Bahadur. Hydrothermal synthesized Nd-doped TiO_2 with anatase and brookite phases as highly improved photoanode for dye-sensitized solar cell. *Solar Energy*, 208:173–181, 9 2020.

[267] Azimah Omar and Huda Abdullah. Electron transport analysis in zinc oxide-based dye-sensitized solar cells: A review. *Renewable and Sustainable Energy Reviews*, 31:149–157, 2014.

[268] Azimah Omar, Mohd Syukri Ali, and Nasrudin Abd Rahim. Electron transport properties analysis of titanium dioxide dye-sensitized solar cells (TiO_2-DSSCs) based natural dyes using electrochemical impedance spectroscopy concept: A review. *Solar Energy*, 207:1088–1121, 9 2020.

[269] Mario Pagliaro, Rosaria Ciriminna, and Giovanni Palmisano. Bipv: merging the photovoltaic with the construction industry. *Progress in Photovoltaics: Research and Applications*, 18:61–72, 1 2010.

[270] Jihuai Wu, Zhang Lan, Sanchun Hao, Pingjiang Li, Jianming Lin, Miaoliang Huang, Leqing Fang, and Yunfang Huang. Progress on the electrolytes for dye-sensitized solar cells. *Pure and Applied Chemistry*, 80:2241–2258, 2008.

[271] Tao Dong, João Simões, and Zhaochu Yang. Flexible photodetector based on 2d materials: Processing, architectures, and applications. *Advanced Materials Interfaces*, 7:1901657, 2 2020.

[272] W. K. Choi, T. H. Liew, M. K. Dawood, Henry I. Smith, C. V. Thompson, and M. H. Hong. Synthesis of silicon nanowires and nanofin arrays using interference lithography and catalytic etching. *Nano Letters*, 8:3799–3802, 2008.

[273] Eric Singh, Ki Seok Kim, Geun Young Yeom, and Hari Singh Nalwa. Two-dimensional transition metal dichalcogenide-based counter electrodes for dye-sensitized solar cells. *RSC Advances*, 7:28234–28290, 2017.

[274] Nurettin Sezer and Muammer Koç. A comprehensive review on the state-of-the-art of piezoelectric energy harvesting. *Nano Energy*, 80:105567, 2 2021.

[275] Yanqing Li, Li Wei Tan, Xiao Tao Hao, Kian Soo Ong, Furong Zhu, and Liang Sun Hung. Flexible top-emitting electroluminescent devices on polyethylene terephthalate substrates. *Applied Physics Letters*, 86:153508, 4 2005.

[276] Pengjian Wang, Junfeng Hui, Tingbiao Yuan, Peng Chen, Yue Su, Wenjie Liang, Fulin Chen, Xiaoyan Zheng, Yuxin Zhao, and Shi Hu. Ultrafine nanoparticles of W-doped SnO_2 for durable H_2S sensors with fast response and recovery. *RSC Advances*, 9:11046–11053, 2019.

[277] Junlu Sun, Yu Chang, Lin Dong, Kuikui Zhang, Qilin Hua, Jinhao Zang, Qiushuo Chen, Yuanyuan Shang, Caofeng Pan, and Chongxin Shan. Mxene enhanced self-powered alternating current electroluminescence devices for patterned flexible displays. *Nano Energy*, 86:106077, 8 2021.

[278] Yu Chang, Junlu Sun, Lin Dong, Fuhang Jiao, Shulong Chang, Yong Wang, Juan Liao, Yuanyuan Shang, Weiwei Wu, Yu Qi, and Chong Xin Shan. Self-powered multi-color display based on stretchable self-healing alternating current electroluminescent devices. *Nano Energy*, 95:107061, 5 2022.

[279] Yanshuo Sun, Laipan Zhu, Jin Yang, Jianjun Zhang, Baodong Chen, Zhong Lin Wang, Y Sun, L Zhu, J Yang, J Zhang, B Chen, and Z L Wang. Flexible alternating-current electroluminescence plunging to below 1 Hz frequency by triboelectrification. *Advanced Optical Materials*, 10:2101918, 1 2022.

[280] Mindong Zheng, Jiamiao Ni, Fei Liang, Moo Chin Wang, and Xiujian Zhao. Effect of annealing temperature on the crystalline structure, growth behaviour and properties of SnO_2:Sb thin films prepared by radio frequency (RF)-magnetron sputtering. *Journal of Alloys and Compounds*, 663:371–378, 2016.

[281] Dong Yeol Park, Yo Seb Lee, Joo Hyun Kim, Sang Jin Lee, Seong Keun Cho, and Sung Hoon Choa. Effects of annealing temperature and hard coating layer on mechanical flexibility of indium tin oxide electrode. *Nanoscience and Nanotechnology Letters*, 9:1185–1189, 8 2017.

[282] H. W. Deng, Y. J. Zhao, C. J. Liang, W. S. Jiang, and Y. M. Ning. Effective skin depth for multilayer coated conductor. *Progress In Electromagnetics Research M*, 9:1–8, 2009.

[283] Juan Zhu, Donggeon Han, Xiaodong Wu, Jonathan Ting, Shixuan Du, and Ana C. Arias. Highly flexible transparent micromesh electrodes via blade-coated polymer networks for organic light-emitting diodes. *ACS Applied Materials and Interfaces*, 12:31687–31695, 7 2020.

[284] Chengang Ji, Dong Liu, Cheng Zhang, and L. Jay Guo. Ultrathin-metal-film-based transparent electrodes with relative transmittance surpassing 100 *Nature Communications*, 11, 12 2020.

[285] Lei Shao, Xiaohui Zhao, Shipeng Gu, Yaping Ma, Yang Liu, Xinwu Deng, Hongchuan Jiang, and Wanli Zhang. Pt thin-film resistance temperature detector on flexible hastelloy tapes. *Vacuum*, 184:109966, 2 2021.

[286] S. Iwatsubo. Morphology and characteristics of ultrathin au films with ultraviolet transparency and conductivity deposited by dual ion beam sputtering. *Vacuum*, 74:631–636, 6 2004.

[287] T. Godfroid, R. Gouttebaron, J. P. Dauchot, Ph Leclère, R. Lazzaroni, and M. Hecq. Growth of ultrathin Ti films deposited on SnO_2 by magnetron sputtering. *Thin Solid Films*, 437:57–62, 8 2003.

[288] F C Frank. J. h. van der merwe. *Proc. Roy. Soc. A*, 198:216, 1949.

[289] F C Frank and J H van der Merwe. Ii. misfitting monolayers and oriented overgrowth. *Proc. Roy. Soc. London A*, 198:216–225, 1949.

[290] T. T. Chau, W. J. Bruckard, P. T.L. Koh, and A. V. Nguyen. A review of factors that affect contact angle and implications for flotation practice. *Advances in Colloid and Interface Science*, 150:106–115, 9 2009.

[291] Ch Surya Prakasarao, Slavia Deeksha D'Souza, Pratim Hazarika, S. N. Karthiselva, R. Ramesh Babu, M. Kovendhan, R. Arockia Kumar, and D. Paul Joseph. Fabrication and stability investigation of ultra-thin transparent and flexible Cu-Ag-Au tri-layer film on PET. *AIP Conference Proceedings*, 1942:080010, 4 2018.

[292] Chao Ping Liu, Yishu Foo, M. Kamruzzaman, Chun Yuen Ho, J. A. Zapien, Wei Zhu, Y. J. Li, Wladek Walukiewicz, and Kin Man Yu. Effects of free carriers on the optical properties of doped CdO for full-spectrum photovoltaics. *Physical Review Applied*, 6:064018, 12 2016.

[293] Mark Fox and George F Bertsch. Optical properties of solids. *Citation: American Journal of Physics*, 70:1269, 12 2002.

[294] Hailin Peng, Wenhui Dang, Jie Cao, Yulin Chen, Di Wu, Wenshan Zheng, Hui Li, Zhi-Xun Shen, and Zhongfan Liu. Topological insulator nanostructures for near-infrared transparent flexible electrodes. *Nature chemistry*, 4(4):281–286, 2012.

[295] A. D. Laforge, A. Frenzel, B. C. Pursley, Tao Lin, Xinfei Liu, Jing Shi, and D. N. Basov. Optical characterization of Bi_2Se_3 in a magnetic field: Infrared evidence for magnetoelectric coupling in a topological insulator material. *Physical Review B - Condensed Matter and Materials Physics*, 81:125120, 3 2010.

[296] Yan-Gang Bi, Yue-Feng Liu, Xu-Lin Zhang, Da Yin, Wen-Quan Wang, Jing Feng, Hong-Bo Sun, Y.-G Bi, Y.-F Liu, X.-L Zhang, D Yin, J Feng, B H Sun, and Q W Wang. Ultrathin metal films as the transparent electrode in ITO-free organic optoelectronic devices. *Advanced Optical Materials*, 7:1800778, 3 2019.

[297] R. S. Markiewicz and L. A. Harris. Two-dimensional resistivity of ultrathin metal films. *Physical Review Letters*, 46:1149, 4 1981.

[298] Biswajit Mahapatra and Sanjit Sarkar. Understanding of mobility limiting factors in solution grown al doped zno thin film and its low temperature remedy. *Heliyon*, 8(10):e10961, 2022.

[299] Y. Muraoka, N. Takubo, and Z. Hiroi. Photoinduced conductivity in tin dioxide thin films. *Journal of Applied Physics*, 105:103702, 5 2009.

[300] Wilhelm Melitz, Jian Shen, Andrew C. Kummel, and Sangyeob Lee. Kelvin probe force microscopy and its application. *Surface Science Reports*, 66:1–27, 1 2011.

[301] Gregory N. Derry, Megan E. Kern, and Eli H. Worth. Recommended values of clean metal surface work functions. *Journal of Vacuum Science Technology A: Vacuum, Surfaces, and Films*, 33:060801, 10 2015.

[302] J. Hölzl and F. K. Schulte. Work function of metals. pages 1–150, 1979.

[303] R. Schlaf, H. Murata, and Z. H. Kafafi. Work function measurements on indium tin oxide films. *Journal of Electron Spectroscopy and Related Phenomena*, 120:149–154, 10 2001.

[304] Kiyoshi Sugiyama, Hisao Ishii, Yukio Ouchi, and Kazuhiko Seki. Dependence of indium–tin–oxide work function on surface cleaning method as studied by ultraviolet and X-ray photoemission spectroscopies. *Journal of Applied Physics*, 87:295, 12 1999.

[305] Y. Park, V. Choong, Y. Gao, B. R. Hsieh, and C. W. Tang. Work function of indium tin oxide transparent conductor measured by photoelectron spectroscopy. *Applied Physics Letters*, 68:2699, 6 1998.

[306] Th Kugler, W. R. Salaneck, H. Rost, and A. B. Holmes. Polymer band alignment at the interface with indium tin oxide: consequences for light emitting devices. *Chemical Physics Letters*, 310:391–396, 9 1999.

[307] Z. Suo, E. Y. Ma, H. Gleskova, and S. Wagner. Mechanics of rollable and foldable film-on-foil electronics. *Applied Physics Letters*, 74:1177, 2 1999.

[308] Da Yin, Jing Feng, Nai Rong Jiang, Rui Ma, Yue Feng Liu, and Hong Bo Sun. Two-dimensional stretchable organic light-emitting devices with high efficiency. *ACS Applied Materials and Interfaces*, 8:31166–31171, 11 2016.

[309] Hongkyu Kang, Suhyun Jung, Soyeong Jeong, Geunjin Kim, and Kwanghee Lee. Polymer-metal hybrid transparent electrodes for flexible electronics. *Nature Communications 2015 6:1*, 6:1–7, 3 2015.

[310] Y. Manjula, R. Rakesh Kumar, P. Missak Swarup Raju, G. Anil Kumar, T. Venkatappa Rao, A. Akshaykranth, and P. Supraja. Piezoelectric flexible nanogenerator based on ZnO nanosheet networks for mechanical energy harvesting. *Chemical Physics*, 533:110699, 2020.

[311] Jasleen Kaur and · Harminder Singh. Synthesis and fabrication of zinc oxide nanostrands based piezoelectric nanogenerator. *Journal of Materials Science: Materials in Electronics*, 30:4437–4445, 2019.

[312] Harish Chander, V. Shanker, D. Haranath, Suman Dudeja, and Pooja Sharma. Characterization of zns:cu, br electroluminescent phosphor prepared by new route. *Materials Research Bulletin*, 38:279–288, 1 2003.

[313] Minghui He, Kaili Zhang, Guangxue Chen, Junfei Tian, and Bin Su. Ionic gel paper with long-term bendable electrical robustness for use in flexible electroluminescent devices. *ACS Applied Materials and Interfaces*, 9:16466–16473, 5 2017.

[314] Jue Hou, Minsu Liu, Huacheng Zhang, Yanlin Song, Xuchuan Jiang, Aibing Yu, Lei Jiang, and Bin Su. Healable green hydrogen bonded networks for circuit repair, wearable sensor and flexible electronic devices. *Journal of Materials Chemistry A*, 5:13138–13144, 6 2017.

[315] Ruiping Tong, Guangxue Chen, Junfei Tian, and Minghui He. Highly transparent, weakly hydrophilic and biodegradable cellulose film for flexible electroluminescent devices. *Carbohydrate Polymers*, 227:115366, 1 2020.

[316] Michael Bredol and Hubert Schulze Dieckhoff. Materials for powder-based AC-electroluminescence. *Materials 2010, Vol. 3, Pages 1353-1374*, 3:1353–1374, 2 2010.

[317] Wanasinghe Arachchige Dumith Madushanka Jayathilaka, Amutha Chinnappan, Ju Nie Tey, Jun Wei, and Seeram Ramakrishna. Alternative current electroluminescence and flexible light emitting devices. *Journal of Materials Chemistry C*, 7:5553–5572, 5 2019.

[318] Yanbin Tong, Zijiang Jiang, Cheng Wang, Yi Xin, Zonghao Huang, Sidong Liu, and Chunbo Li. Effect of annealing on the morphology and properties of ZnS:Mn nanoparticles/PVP nanofibers. *Materials Letters*, 62:3385–3387, 7 2008.

[319] K. G. Kostov, A. L.R. Dos Santos, P. A.P. Nascente, M. E. Kayama, and R. P. Mota. Modification of polyethylene terephthalate by atmospheric pressure dielectric barrier discharge (DBD) in view of improving the polymer wetting properties. *Journal of Physics: Conference Series*, 356:012006, 3 2012.

[320] Y. W. Mo, D. E. Savage, B. S. Swartzentruber, and M. G. Lagally. Kinetic pathway in stranski-krastanov growth of Ge on Si(001). *Physical Review Letters*, 65:1020–1023, 1990.

[321] Ching Lien Hsiao, Justinas Palisaitis, Per O.Å. Persson, Muhammad Junaid, Elena Alexandra Serban, Per Sandström, Lars Hultman, and Jens Birch. Nucleation and core-shell formation mechanism of self-induced inxal1xn core-shell nanorods grown on sapphire substrates by magnetron sputter epitaxy. *Vacuum*, 131:39–43, 9 2016.

[322] Amir Masoud Badkoobehhezaveh, Eric Hopmann, and Abdulhakem Y. Elezzabi. Flexible multicolor electroluminescent devices on cellulose nanocrystal platform. *Advanced Engineering Materials*, 22:1901452, 5 2020.

[323] Guoqing Zhao, Soo Min Kim, Sang Geul Lee, Tae Sung Bae, Chae Won Mun, Sunghun Lee, Huashun Yu, Gun Hwan Lee, Hae Seok Lee, Myungkwan Song, and Jungheum Yun. Bendable solar cells from stable, flexible, and transparent conducting electrodes fabricated using a nitrogen-doped ultrathin copper film. *Advanced Functional Materials*, 26:4180–4191, 6 2016.

[324] Dewei Zhao, Cheng Zhang, Hyunsoo Kim, and L. Jay Guo. High-performance Ta_2O_5/Al-doped Ag electrode for resonant light harvesting in efficient organic solar cells. *Advanced Energy Materials*, 5:1500768, 9 2015.

[325] Yan Gang Bi, Fang Shun Yi, Jin Hai Ji, Chi Ma, Wen Quan Wang, Jing Feng, and Hong Bo Sun. Ultrathin au electrodes based on a hybrid nucleation layer for flexible organic light-emitting devices. *IEEE Transactions on Nanotechnology*, 17:1077–1081, 9 2018.

[326] Da Yin, Zhi Yu Chen, Nai Rong Jiang, Yue Feng Liu, Yan Gang Bi, Xu Lin Zhang, Wei Han, Jing Feng, and Hong Bo Sun. Highly transparent and flexible fabric-based organic light emitting devices for unnoticeable wearable displays. *Organic Electronics*, 76:105494, 1 2020.

[327] Xiaoyang Guo, Xingyuan Liu, Fengyuan Lin, Hailing Li, Yi Fan, and Nan Zhang. Highly conductive transparent organic electrodes with multilayer structures for rigid and flexible optoelectronics. *Scientific Reports 2015 5:1*, 5:1–9, 5 2015.

[328] Brian O'Neill. Indium market forces, a commercial perspective. *Conference Record of the IEEE Photovoltaic Specialists Conference*, pages 556–559, 2010.

[329] Martin A. Green. Estimates of Te and In prices from direct mining of known ores. *Progress in Photovoltaics: Research and Applications*, 17:347–359, 8 2009.

[330] Kenneth J. Button, Clifton G. Fonstad, and Wolfgang Dreybrodt. Determination of the electron masses in stannic oxide by submillimeter cyclotron resonance. *Physical Review B*, 4:4539–4542, 1971.

[331] Wenwu Liu, Wei Jiang, Yu cheng Liu, Wenjun Niu, and Maocheng Liu. Platinum-free ternary metallic selenides as nanostructured counter electrode for high-efficiency dye-sensitized solar cell by interface engineering. 2020.

[332] A. N. Banerjee, S. Kundoo, P. Saha, and K. K. Chattopadhyay. Synthesis and characterization of nano-crystalline fluorine-doped tin oxide thin films by sol-gel method. *Journal of Sol-Gel Science and Technology 2003 28:1*, 28:105–110, 8 2003.

[333] A. N. Banerjee, R. Maity, S. Kundoo, and K. K. Chattopadhyay. Poole-frenkel effect in nanocrystalline SnO_2:F thin films prepared by a sol-gel dip-coating technique. *physica status solidi (a)*, 201:983–989, 4 2004.

[334] Morteza Asadzadeh, Fariba Tajabadi, Davoud Dastan, Parvaneh Sangpour, Zhicheng Shi, and Nima Taghavinia. Facile deposition of porous fluorine doped tin oxide by dr. blade method for capacitive applications. *Ceramics International*, 47:5487–5494, 2 2021.

[335] James Proscia and Roy G. Gordon. Properties of fluorine-doped tin oxide films produced by atmospheric pressure chemical vapor deposition from tetramethyltin, bromotrifluoromethane and oxygen. *Thin Solid Films*, 214:175–187, 7 1992.

[336] Sekhar C. Ray, Malay K. Karanjai, and Dhruba Dasgupta. Preparation and study of doped and undoped tin dioxide films by the open air chemical vapour deposition technique. *Thin Solid Films*, 307:221–227, 10 1997.

[337] Seigi Suh, Zuhua Zhang, Wei Kan Chu, and David M. Hoffman. Atmospheric-pressure chemical vapor deposition of fluorine-doped tin oxide thin films. *Thin Solid Films*, 345:240–243, 5 1999.

[338] P. Yang, L. R. Jiang, J. Y. Wu, F. Chen, J. A.Galaviz Perez, Q. Shen, J. M. Schoenung, and L. M. Zhang. Effect of oxygen flow rate on electrical and optical properties of ATO thin films prepared by RF magnetron sputtering. *Key Engineering Materials*, 616:178–182, 2014.

[339] Wan Zurina Samad, Mohd Ambar Yarmo, Muhamad Mat Salleh, and Ashkan Shafiee. Structural, optical and electrical properties of fluorine doped tin oxide thin films deposited using ink jet printing technique. *Sains Malaysiana*, 40:251–257, 2011.

[340] R. Pommier, C. Gril, and J. Marucchi. Sprayed films of indium tin oxide and fluorine-doped tin oxide of large surface area. *Thin Solid Films*, 77:91–98, 3 1981.

[341] H. H. Afify, R. S. Momtaz, W. A. Badawy, and S. A. Nasser. Some physical properties of fluorine-doped SnO_2 films prepared by spray pyrolysis. *Journal of Materials Science: Materials in Electronics 1991 2:1*, 2:40–45, 3 1991.

[342] G. C. Morris and A. E. McElnea. Fluorine doped tin oxide films from spray pyrolysis of stannous fluoride solutions. *Applied Surface Science*, 92:167–170, 2 1996.

[343] D. Zaouk, Y. Zaatar, A. Khoury, C. Llinares, J. P. Charles, and J. Bechara. Electrical and optical properties of pyrolytically electrostatic sprayed fluorine-doped tin–oxide: Dependence on substrate–temperature and substrate–nozzle distance. *Journal of Applied Physics*, 87:7539, 4 2000.

[344] Maxence Urbani, Maria Eleni Ragoussi, Mohammad Khaja Nazeeruddin, and Tomás Torres. Phthalocyanines for dye-sensitized solar cells. *Coordination Chemistry Reviews*, 381:1–64, 2019.

[345] A. V. Moholkar, S. M. Pawar, K. Y. Rajpure, and C. H. Bhosale. Effect of solvent ratio on the properties of highly oriented sprayed fluorine-doped tin oxide thin films. *Materials Letters*, 61:3030–3036, 6 2007.

[346] Artur Rydosz, Katarzyna Dyndał, Wojciech Andrysiewicz, Dominik Grochala, and Konstanty Marszałek. Glad magnetron sputtered ultra-thin copper oxide films for gas-sensing application. *Coatings 2020, Vol. 10, Page 378*, 10:378, 4 2020.

[347] Ali Talib Abood, Obaida Amer Abdul Hussein, Muhammad Hameed Al-Timimi, Mustafa Zaid Abdullah, Hussein Mahdi S. Al Aani, and Widad H. Albanda. Structural and optical properties of nanocrystalline SnO_2 thin films growth by electron beam evaporation. *AIP Conference Proceedings*, 2213:020036, 3 2020.

[348] Nihal A. AbdulWahhab. Optical properties of SnO_2 thin films prepared by pulsed laser deposition technique. *Journal of Optics (India)*, 49:41–47, 3 2020.

[349] R. Ramarajan, M. Kovendhan, K. Thangaraju, D. Paul Joseph, and R. Ramesh Babu. Facile deposition and characterization of large area highly conducting and transparent Sb-doped SnO_2 thin film. *Applied Surface Science*, 487:1385–1393, 2019.

[350] R. Ramarajan, Nandarapu Purushothamreddy, Reshma K. Dileep, M. Kovendhan, Ganapathy Veerappan, K. Thangaraju, and D. Paul Joseph. Large-area spray deposited Ta-doped SnO_2 thin film electrode for DSSC application. *Solar Energy*, 211:547–559, 2020.

[351] R. Ramarajan. Thermal stability study of niobium doped SnO_2 thin film for transparent conducting oxide application. *Superlattices and Microstructures*, 135:106274, 2019.

[352] R. Ramarajan, M. Kovendhan, K. Thangaraju, D. Paul Joseph, R. Ramesh Babu, and Viswanathan Elumalai. Enhanced optical transparency and electrical

conductivity of Ba and Sb co-doped SnO_2 thin films. *Journal of Alloys and Compounds*, 823, 2020.

[353] A Abdel Galil and N L Moussa I S Yahia. Synthesis and optical characterization of nanocrystalline fluorine - doped tin oxide films : conductive window layer for optoelectronic applications. *Applied Physics A*, 127:1–16, 2021.

[354] Zahra Mahmoudiamirabad and Hosein Eshghi. Achievements of high figure of merit and infra-red reflectivity in SnO_2:F thin films using spray pyrolysis technique. *Superlattices and Microstructures*, 152:106855, 4 2021.

[355] Bon Ryul Koo, Dong Hyeun Oh, Doh Hyung Riu, and Hyo Jin Ahn. Improvement of transparent conducting performance on oxygen-activated fluorine-doped tin oxide electrodes formed by horizontal ultrasonic spray pyrolysis deposition. *ACS Applied Materials and Interfaces*, 9:44584–44592, 12 2017.

[356] Shahin Sheikh, Mehrdad Shokooh-Saremi, and Mohammad Mehdi Bagheri-Mohagheghi. Transparent microstrip patch antenna based on fluorine-doped tin oxide deposited by spray pyrolysis technique. *IET Microwaves, Antennas Propagation*, 9:1221–1229, 8 2015.

[357] Chitra Agashe, J. Hüpkes, G. Schöpe, and M. Berginski. Physical properties of highly oriented spray-deposited fluorine-doped tin dioxide films as transparent conductor. *Solar Energy Materials and Solar Cells*, 93:1256–1262, 8 2009.

[358] A. V. Moholkar, S. M. Pawar, K. Y. Rajpure, and C. H. Bhosale. Effect of solvent ratio on the properties of highly oriented sprayed fluorine-doped tin oxide thin films. *Materials Letters*, 61:3030–3036, 6 2007.

[359] A. A. Yadav, E. U. Masumdar, A. V. Moholkar, K. Y. Rajpure, and C. H. Bhosale. Effect of quantity of spraying solution on the properties of spray deposited fluorine doped tin oxide thin films. *Physica B: Condensed Matter*, 404:1874–1877, 6 2009.

[360] D. Prabha, S. Ilangovan, V.S. Nagarethinam, and A.R. Balu. Effect of solvent volume on the physical properties of spray deposited nano needle structured Sn_2S_3 thin films. *http://dx.doi.org/10.1080/14328917.2015.1134854*, 20:307–311, 2016.

[361] G. Muruganantham, K. Ravichandran, K. Saravanakumar, P. Philominathan, and B. Sakthivel. Effect of doping level on physical properties of antimony

doped nanocrystalline tin oxide films fabricated using low cost spray technique. *Surface Engineering*, 27:376–381, 2011.

[362] R. Anne Sarah Christinal, I. Prakash, Sujay Chakravarty, and A. Leo Rajesh. Spray pyrolysed Cu_2ZnSnS_4 thin film photovoltaic cell fabricated using cost effective materials. *Physica B: Condensed Matter*, 637:413911, 7 2022.

[363] Soumen Das, Soumitra Kar, and Subhadra Chaudhuri. Optical properties of SnO_2 nanoparticles and nanorods synthesized by solvothermal process. *Journal of Applied Physics*, 99:114303, 6 2006.

[364] Kenji Murakami, Isao Yagi, and Shoji Kaneko. Oriented growth of tin oxide thin films on glass substrates by spray pyrolysis of organotin compounds. *Journal of the American Ceramic Society*, 79:2557–2562, 10 1996.

[365] Devinda Liyanage, Herath Mudiyanselage, Navaratne Bandara, Viraj Jayaweera, and Kenji Murakami. Ethylene glycol assisted synthesis of fluorine doped tin oxide nanorods using improved spray pyrolysis deposition method. 085501, 2013.

[366] Dominic B. Potter, Ivan P. Parkin, and Claire J. Carmalt. The effect of solvent on Al-doped ZnO thin films deposited via aerosol assisted CVD. *RSC Advances*, 8:33164–33173, 9 2018.

[367] Murat Tomakin. Structural and optical properties of ZnO and Al-doped ZnO microrods obtained by spray pyrolysis method using different solvents. *Superlattices and Microstructures*, 51:372–380, 3 2012.

[368] Jianwen Yang, Ting Meng, Zhao Yang, Can Cui, and Qun Zhang. Investigation of tungsten doped tin oxide thin film transistors. *Journal of Physics D: Applied Physics*, 48:435108, 2015.

[369] J C Viguie and J Spitz. Chemical vapor deposition at low temperatures. *J. Electrochem. Soc*, 122:585–588, 1975.

[370] Vanna Torrisi, Maria Censabella, Giovanni Piccitto, Giuseppe Compagnini, Maria Grazia Grimaldi, and Francesco Ruffino. Characteristics of Pd and Pt nanoparticles produced by nanosecond laser irradiations of thin films deposited on topographically-structured transparent conductive oxides. *Coatings 2019, Vol. 9, Page 68*, 9:68, 1 2019.

[371] Satish Kumar, Ajit K Mahapatro, and Puspashree Mishra. Applied surface science swift heavy silver (Ag+7) ion irradiation induced self assembled nanodots on MBE grown gallium antimonide (GaSb). *Applied Surface Science*, 462:815–821, 2018.

[372] G Muruganantham, K Ravichandran, K Saravanakumar, and K Swaminathan. Effect of solvent volume on the physical properties of sprayed fluorine-doped zinc oxide thin films. 436:429–436, 2012.

[373] Mohd Amirul Syafiq Mohd Yunos, Zainal Abidin Talib, and Wan Mahmood Mat Yunus. Annealing and light effect on structural and electrical properties of thermally evaporated Cu_2SnSe_3 thin films. *Journal of Chemical Engineering and Materials Science*, 2:103–109, 9 2013.

[374] G. Shanmugavel, A.R. Balu, and V.S. Nagarethinam. Preparation of cadmium oxide thin films by spray technique using perfume atomizer and effect of solvent volume on their physical properties. *International Journal of Chemistry and Materials Research*, 2:88–101, 2014.

[375] Bernard J Ryan and Kristin M Poduska. Roughness effects on contact angle measurements roughness effects on contact angle measurements. 1074, 2014.

[376] H. El-Zahed, A. El-Korashy, and M. Abdel Rahem. Effect of heat treatment on some of the optical parameters of $Cu_9Ge_{11}Te_{80}$ films. *Vacuum*, 68:19–27, 10 2002.

[377] J. Tauc and A. Menth. States in the gap. *Journal of Non-Crystalline Solids*, 8-10:569–585, 6 1972.

[378] N F Mott. Electronic process in non-crystalline materials. *Journal of Non-Crystalline Solids*, 1:1, 1968.

[379] L. Z. Liu, X. L. Wu, J. Q. Xu, T. H. Li, J. C. Shen, and Paul K. Chu. Oxygen-vacancy and depth-dependent violet double-peak photoluminescence from ultrathin cuboid SnO_2 nanocrystals. *Applied Physics Letters*, 100:121903, 3 2012.

[380] Tamita Rakshit, Indranil Manna, and Samit K. Ray. Effect of SnO_2 concentration on the tuning of optical and electrical properties of ZnO-SnO_2 composite thin films. *Journal of Applied Physics*, 117:025704, 1 2015.

[381] Rongmei Liu, Wei Du, Qun Chen, Feng Gao, Chengzhen Wei, Jing Sun, and Qingyi Lu. Fabrication of Zn_2SnO_4/SnO_2 hollow spheres and their application in dye-sensitized solar cells. *RSC Advances*, 3:2893–2896, 2013.

[382] A. Boukhachem, O. Kamoun, C. Mrabet, C. Mannai, N. Zouaghi, A. Yumak, K. Boubaker, and M. Amlouk. Structural, optical, vibrational and photoluminescence studies of Sn-doped MoO_3 sprayed thin films. *Materials Research Bulletin*, 72:252–263, 12 2015.

[383] A. Tressaud, F. Moguet, S. Flandrois, M. Chambon, C. Guimon, G. Nanse, E. Papirer, V. Gupta, and O. P. Bahl. On the nature of c-f bonds in various fluorinated carbon materials: XPS and TEM investigations. *Journal of Physics and Chemistry of Solids*, 57:745–751, 6 1996.

[384] I. Palchan, M. Crespin, H. Estrade-Szwarckopf, and B. Rousseau. Graphite fluorides: An XPS study of a new type of C-F bonding. *Chemical Physics Letters*, 157:321–327, 5 1989.

[385] Shanshan Wu, Shuai Yuan, Liyi Shi, Yin Zhao, and Jianhui Fang. Preparation, characterization and electrical properties of fluorine-doped tin dioxide nanocrystals. *Journal of colloid and interface science*, 346:12–16, 6 2010.

[386] A. I. Martínez, L. Huerta, J. M. O-Rueda De León, D. Acosta, O. Malik, and M. Aguilar. Physicochemical characteristics of fluorine doped tin oxide films. *Journal of Physics D: Applied Physics*, 39:5091, 11 2006.

[387] F. Arefi-Khonsari, N. Bauduin, F. Donsanti, and J. Amouroux. Deposition of transparent conductive tin oxide thin films doped with fluorine by PACVD. *Thin Solid Films*, 427:208–214, 3 2003.

[388] Supriyono, Ahmad Zakaria, Yuni Krisyuningsih Krisnandi, and Jarnuzi Gunlazuardi. Co-sensitized TiO_2 photoelectrodes by multiple semiconductors (PbS/Pb0.05Cd0.95S/CdS)to enhance the performance of a solar cell. *Oriental Journal of Chemistry*, 33:2271–2281, 2017.

[389] Suk In Noh, Hyo Jin Ahn, and Doh Hyung Riu. Photovoltaic property dependence of dye-sensitized solar cells on sheet resistance of FTO substrate deposited via spray pyrolysis. *Ceramics International*, 38:3735–3739, 7 2012.

[390] T. C. Yeh, Q. Zhu, D. B. Buchholz, A. B. Martinson, R. P.H. Chang, and T. O. Mason. Amorphous transparent conducting oxides in context: Work function survey, trends, and facile modification. *Applied Surface Science*, 330:405–410, 3 2015.

[391] K. Jagadeesh Kumar, N. Ravi Chandra Raju, and A. Subrahmanyam. Thickness dependent physical and photocatalytic properties of ITO thin films prepared by

reactive DC magnetron sputtering. *Applied Surface Science*, 257:3075–3080, 1 2011.

[392] M. G. Helander, M. T. Greiner, Z. B. Wang, W. M. Tang, and Z. H. Lu. Work function of fluorine doped tin oxide. *Journal of Vacuum Science Technology A: Vacuum, Surfaces, and Films*, 29:011019, 1 2011.

[393] Qiquan Qiao and James T. McLeskey. Water-soluble polythiophenenanocrystalline TiO_2 solar cells. *Applied Physics Letters*, 86:153501, 4 2005.

[394] D. S. Shang, L. Shi, J. R. Sun, B. G. Shen, F. Zhuge, R. W. Li, and Y. G. Zhao. Improvement of reproducible resistance switching in polycrystalline tungsten oxide films by in situ oxygen annealing. *Applied Physics Letters*, 96:072103, 2 2010.

[395] Qiquan Qiao, James Beck, Ryan Lumpkin, Jake Pretko, and James T. Mcleskey. A comparison of fluorine tin oxide and indium tin oxide as the transparent electrode for P3OT/TiO_2 solar cells. *Solar Energy Materials and Solar Cells*, 90:1034–1040, 5 2006.

[396] Miao Wang, Xong Yin, Xu Rui Xiao, XiaoWen Zhou, Zheng Zhong Yang, Xue Ping Li, and Yuan Lin. A new ionic liquid based quasi-solid state electrolyte for dye-sensitized solar cells. *Journal of Photochemistry and Photobiology A: Chemistry*, 194:20–26, 2008.

[397] Annica Andersson, Nicklas Johansson, Per Bröms, Nu Yu, Donald Lupo, and William R Salaneck. Fluorine tin oxide as an alternative to indium tin oxide in polymer LEDs. *Advanced Materials*, 10:859–863, 8 1998. https://doi.org/10.1002/(SICI)1521-4095(199808)10:113.0.CO;2-1.

[398] L. Zhao, C. L. Zhou, H. L. Li, H. W. Diao, and W. J. Wang. Role of the work function of transparent conductive oxide on the performance of amorphous/crystalline silicon heterojunction solar cells studied by computer simulation. *physica status solidi (a)*, 205:1215–1221, 5 2008.

[399] Emanuele Centurioni and Daniele Iencinella. Role of front contact work function on amorphous silicon/crystalline silicon heterojunction solar cell performance. *IEEE Electron Device Letters*, 24:177–179, 3 2003.

[400] Matthias Batzill and Ulrike Diebold. The surface and materials science of tin oxide. *Progress in Surface Science*, 79:47–154, 2005.

[401] S. Rahemi Ardekani, Alireza Sabour Rouh Aghdam, Mojtaba Nazari, Amir Bayat, E. Yazdani, and Esmaiel Saievar-Iranizad. A comprehensive review on ultrasonic spray pyrolysis technique: Mechanism, main parameters and applications in condensed matter. *Journal of Analytical and Applied Pyrolysis*, 141:104631, 2019.

[402] Agus Purwanto, Hendri Widiyandari, and Arif Jumari. Fabrication of high-performance fluorine doped–tin oxide film using flame-assisted spray deposition. *Thin Solid Films*, 520:2092–2095, 1 2012.

[403] V. Gokulakrishnan, S. Parthiban, K. Jeganathan, and K. Ramamurthi. Investigations on the structural, optical and electrical properties of Nb-doped SnO_2 thin films. *Journal of Materials Science*, 46:5553–5558, 2011.

[404] Chitra Agashe and S. S. Major. Effect of heavy doping in SnO_2:F films. *Journal of Materials Science*, 31:2965–2969, 6 1996.

[405] R. D. SHANNON. Revised effective ionic radii and systematic studies of interatomie distances in halides and chaleogenides. *Acta Cryst*, 10:751–767, 1976.

[406] R. Ramarajan, M. Kovendhan, K. Thangaraju, D. Paul Joseph, R. Ramesh Babu, and Viswanathan Elumalai. Enhanced optical transparency and electrical conductivity of Ba and Sb co-doped SnO_2 thin films. *Journal of Alloys and Compounds*, 823:153709, 2020.

[407] Reddivari Muniramaiah, Nandarapu Purushotham Reddy, Rompivalasa Santhosh, Jean Maria Fernandes, Dilli Babu Padmanaban, Gouranga Maharana, M. Kovendhan, Ganapathy Veerappan, Gangalakurti Laxminarayana, Murali Banavoth, and D. Paul Joseph. Solvent effect on the optoelectronic properties of fluorine doped SnO_2 thin films prepared by spray-pyrolysis. *Surfaces and Interfaces*, 33:102174, 10 2022.

[408] A. M. El Sayed, S. Taha, Mohamed Shaban, and G. Said. Tuning the structural, electrical and optical properties of tin oxide thin films via cobalt doping and annealing. *Superlattices and Microstructures*, 95:1–13, 2016.

[409] Agnès Smith, Jean Marc Laurent, David S. Smith, Jean Pierre Bonnet, and Rafael Rodriguez Clemente. Relation between solution chemistry and morphology of SnO_2-based thin films deposited by a pyrosol process. *Thin Solid Films*, 266:20–30, 1995.

[410] G. Gordillo, L. C. Moreno, W. de la Cruz, and P. Teheran. Preparation and characterization of SnO_2 thin films deposited by spray pyrolysis from $SnCl_2$ and $SnCl_4$ precursors. *Thin Solid Films*, 252:61–66, 11 1994.

[411] A. R. Babar, S. S. Shinde, A. V. Moholkar, C. H. Bhosale, J. H. Kim, and K. Y. Rajpure. Sensing properties of sprayed antimony doped tin oxide thin films: Solution molarity. *Journal of Alloys and Compounds*, 509:3108–3115, 2011.

[412] E. Elangovan, S. A. Shivashankar, and K. Ramamurthi. Studies on structural and electrical properties of sprayed SnO_2:Sb films. *Journal of Crystal Growth*, 276:215–221, 2005.

[413] Chitra Agashe, M. G. Takwale, V. G. Bhide, Shailaja Mahamuni, and S. K. Kulkarni. Effect of sn incorporation on the growth mechanism of sprayed SnO_2 films. *Journal of Applied Physics*, 70:7382, 8 1998.

[414] Saji Chacko, Ninan Sajeeth Philip, K. G. Gopchandran, Peter Koshy, and V. K. Vaidyan. Nanostructural and surface morphological evolution of chemically sprayed SnO_2 thin films. *Applied Surface Science*, 254:2179–2186, 1 2008.

[415] Prabitha B. Nair, V. B. Justinvictor, Georgi P. Daniel, K. Joy, V. Ramakrishnan, David Devraj Kumar, and P. V. Thomas. Structural, optical, photoluminescence and photocatalytic investigations on Fe doped TiO_2 thin films. *Thin Solid Films*, 550:121–127, 1 2014.

[416] M. Jothibas, C. Manoharan, S. Johnson Jeyakumar, P. Praveen, I. Kartharinal Punithavathy, and J. Prince Richard. Synthesis and enhanced photocatalytic property of Ni doped ZnS nanoparticles. *Solar Energy*, 159:434–443, 1 2018.

[417] Chafia Khelifi, Abdallah Attaf, Hanane saidi, Anouar Yahia, and Mohamed Dahnoun. Investigation of F doped SnO_2 thin films properties deposited via ultrasonic spray technique for several applications. *Surfaces and Interfaces*, 15:244–249, 6 2019.

[418] Laureen Ida Monzon Ballesteros, Christopher Jude Vergara, and Armando Somintac. Fluorine-doped SnO_2 thin film as chemiresistive gas sensor for room temperature monitoring of fish freshness. *PISIKA - Journal of the Physics Society of the Philippines*, 1:10–10, 12 2018.

[419] Getnet Kacha Deyu, David Muñoz-Rojas, Laetitia Rapenne, Jean Luc Deschanvres, Andreas Klein, Carmen Jiménez, and Daniel Bellet. SnO_2 films deposited

by ultrasonic spray pyrolysis: Influence of Al incorporation on the properties. *Molecules (Basel, Switzerland)*, 24:1–16, 2019.

[420] R. Ramarajan, M. Kovendhan, K. Thangaraju, D. Paul Joseph, and R. Ramesh Babu. Facile deposition and characterization of large area highly conducting and transparent Sb-doped SnO_2 thin film. *Applied Surface Science*, 487:1385–1393, 2019.

[421] B Akbari, M Pirhadi Tavandashti, and M Zandrahimi. Particle size characterization of nanoparticles – a practicalapproach. *Iranian Journal of Materials Science Engineering*, 8:48, 2011.

[422] Kue Ho Kim, Bon Ryul Koo, and Hyo Jin Ahn. Sheet resistance dependence of fluorine-doped tin oxide films for high-performance electrochromic devices. *Ceramics International*, 44:9408–9413, 6 2018.

[423] E. Shanthi, A. Banerjee, V. Dutta, and K. L. Chopra. Electrical and optical properties of tin oxide films doped with f and (Sb+F). *Journal of Applied Physics*, 53:1615–1621, 1982.

[424] I. M. Costa, T. R. Cunha, L. Cichetto, M. A. Zaghete, and A. J. Chiquito. Investigation on the optical and electrical properties of undoped and Sb-doped SnO_2 nanowires obtained by the VLS method. *Physica E: Low-dimensional Systems and Nanostructures*, 134:114856, 10 2021.

[425] Yasemin Pepe, Ahmet Karatay, Yusuf Osman Donar, Selva Bilge, Elif Akhuseyin Yildiz, Mustafa Yuksek, Ali Sınağ, and Ayhan Elmali. Effect of Cr/Sb doping and annealing on nonlinear absorption coefficients of SnO_2 /PMMA nanocomposite films. *Materials Chemistry and Physics*, 255:123596, 11 2020.

[426] A. R. Babar, S. S. Shinde, A. V. Moholkar, C. H. Bhosale, J. H. Kim, and K. Y. Rajpure. Structural and optoelectronic properties of antimony incorporated tin oxide thin films. *Journal of Alloys and Compounds*, 505:416–422, 2010.

[427] Alexander Smakula. Über erregung und entfärbung lichtelektrisch leitender alkalihalogenide. *Zeitschrift für Physik*, 59:603–614, 9 1930.

[428] Reddivari Muniramaiah, Jean Maria Fernandes, M. Manivel Raja, Dilli Babu Padmanaban, P. Supraja, M. Rakshita, Nandarapu Purushotham Reddy, Gouranga Maharana, M. Kovendhan, Ganapathy Veerappan, Gangalakurti

Laxminarayana, R. Rakesh Kumar, D. Haranath, and D. Paul Joseph. Mechanically stable ultrathin flexible metallic au/pt/au tri-layer as an alternative transparent conducting electrode for optoelectronic device applications. *Vacuum*, 206:111487, 12 2022.

[429] Dasari Sunil Gavaskar, P. Nagaraju, and M. V.Ramana Reddy. Investigations on RuO_2–In_2O_3 nanostructured porous composite thin films for benzene detection. *Microporous and Mesoporous Materials*, 345:112247, 11 2022.

[430] Sunil Gavaskar Dasari, Pothukanuri Nagaraju, Vijayakumar Yelsani, and M. V. Ramana Reddy. Mesoporous sieve structured ITO-based thin films for enhanced formaldehyde detection. *Journal of Materials Science: Materials in Electronics*, 33:23447–23467, 10 2022.

[431] D. Paul Joseph, R. Radha, Jean Maria Fernandes, Reddivari Muniramaiah, Nandarapu Purushothamreddy, M. Kovendhan, and C. Venkateswaran. Investigation of the transparent conducting properties of spray-pyrolyzed Li and F co-doped SnO_2 thin film electrodes. *Journal of Materials Science: Materials in Electronics*, 33:8435–8445, 4 2022.

[432] S. Sujatha Lekshmy, Georgi P. Daniel, and K. Joy. Microstructure and physical properties of sol gel derived SnO_2:Sb thin films for optoelectronic applications. *Applied Surface Science*, 274:95–100, 6 2013.

[433] Yong Jun Seo, Geun Woo Kim, Chang Hoon Sung, M. S. Anwar, Chan Gyu Lee, and Bon Heun Koo. Characterization of transparent and conductive electrodes of Nb-doped SnO_2 thin film by pulsed laser deposition. *Current Applied Physics*, 11:S310–S313, 5 2011.

[434] Tai Hua Xie and Jun Lin. Origin of photocatalytic deactivation of TiO_2 film coated on ceramic substrate. *Journal of Physical Chemistry C*, 111:9968–9974, 7 2007.

[435] Yanmin Wang. Recent research progress on polymer electrolytes for dye-sensitized solar cells. *Solar Energy Materials and Solar Cells*, 93:1167–1175, 2009.

[436] Tim Leshuk, Roozbeh Parviz, Perry Everett, Harish Krishnakumar, Robert A. Varin, and Frank Gu. Photocatalytic activity of hydrogenated TiO_2. *ACS Applied Materials and Interfaces*, 5:1892–1895, 3 2013.

[437] Ming Kong, Yuanzhi Li, Xiong Chen, Tingting Tian, Pengfei Fang, Feng Zheng, and Xiujian Zhao. Tuning the relative concentration ratio of bulk defects to surface defects in TiO_2 nanocrystals leads to high photocatalytic efficiency. *Journal of the American Chemical Society*, 133:16414–16417, 10 2011.

[438] Malin B. Johansson, Andreas Mattsson, Sten Eric Lindquist, Gunnar A. Niklasson, and Lars Österlund. The importance of oxygen vacancies in nanocrystalline WO_3 thin films prepared by dc magnetron sputtering for achieving high photoelectrochemical efficiency. *Journal of Physical Chemistry C*, 121:7412–7420, 4 2017.

[439] Sumaira Mehraj, M. Shahnawaze Ansari, and Alimuddin. Annealed SnO_2 thin films: Structural, electrical and their magnetic properties. *Thin Solid Films*, 589:57–65, 8 2015.

[440] M. Ali Yldrm, Yunus Akaltun, and Aytun Ate. Characteristics of SnO_2 thin films prepared by SILAR. *Solid State Sciences*, 14:1282–1288, 9 2012.

[441] Jin Jeong, Seong Pyung Choi, Cha Ik Chang, Dong Chan Shin, Jin Sung Park, B. T. Lee, Yeong Jun Park, and Ho Jun Song. Photoluminescence properties of SnO_2 thin films grown by thermal CVD. *Solid State Communications*, 127:595–597, 9 2003.

[442] Boucherka Teldja, Brihi Noureddine, Berbadj Azzeddine, and Touati Meriem. Effect of indium doping on the uv photoluminescence emission, structural, electrical and optical properties of spin-coating deposited SnO_2 thin films. *Optik*, 209:164586, 5 2020.

[443] Kangrong Lai, Yi Sun, Huimin Chen, Lili Zhi, and Wei Wei. Effect of oxygen vacancy and Al-doping on the electronic and optical properties in SnO_2. *Physica B: Condensed Matter*, 428:48–52, 11 2013.

[444] Xiaoyang Pan, Min Quan Yang, Xianzhi Fu, Nan Zhang, and Yi Jun Xu. Defective TiO_2 with oxygen vacancies: synthesis, properties and photocatalytic applications. *Nanoscale*, 5:3601–3614, 4 2013.

[445] S. Sujatha Lekshmy, Georgi P. Daniel, and K. Joy. Microstructure and physical properties of sol gel derived SnO_2:Sb thin films for optoelectronic applications. *Applied Surface Science*, 274:95–100, 2013.

[446] Soo Won Heo, Yoon Duk Ko, Young Sung Kim, and Doo Kyung Moon. Enhanced performance in polymer light emitting diodes using an indium–zinc–tin

oxide transparent anode by the controlling of oxygen partial pressure at room temperature. *Journal of Materials Chemistry C*, 1:7009–7019, 10 2013.

[447] Kyuha Lee, A young Kim, Ji Hun, Hun gi Jung, Wonchang Choi, Hwa Young, and Joong Kee. Applied surface science effect of micro-patterned fluorine-doped tin oxide films on electrochromic properties of prussian blue films. *Applied Surface Science*, 313:864–869, 2014.

[448] Martin Eschle, Ellen Moons, and Michael Grätzel. Construction of the energy diagram of an organic semiconductor film on SnO_2:F by surface photovoltage spectroscopy. *Optical Materials*, 9:138–144, 1 1998.

[449] Zahra Karami Horastani, Sayed Masoud Sayedi, Mohammad Hossein Sheikhi, and Esmaeil Rahimi. Effect of silver additive on electrical conductivity and methane sensitivity of SnO_2. *Materials Science in Semiconductor Processing*, 35:38–44, 7 2015.

[450] D. R. Deepu, C. Sudha Kartha, and K. P. Vijayakumar. How spray rate influences the formation and properties of transparent conducting SnO_2 thin films. *Journal of Analytical and Applied Pyrolysis*, 121:24–28, 9 2016.

[451] Jack E.N. Swallow, Benjamin A.D. Williamson, Thomas J. Whittles, Max Birkett, Thomas J. Featherstone, Nianhua Peng, Alex Abbott, Mark Farnworth, Kieran J. Cheetham, Paul Warren, David O. Scanlon, Vin R. Dhanak, and Tim D. Veal. Self-compensation in transparent conducting F-doped SnO_2. *Advanced Functional Materials*, 28:1701900, 1 2018.

[452] Silvia Leticia Fernandes, Luiz Gustavo Simão Albano, Lucas Jorge Affonço, José Humberto Dias da Silva, Elson Longo, and Carlos Frederico de Oliveira Graeff. Exploring the properties of niobium oxide films for electron transport layers in perovskite solar cells. *Frontiers in Chemistry*, 7:50, 2019.

[453] E. Elangovan and K. Ramamurthi. Studies on micro-structural and electrical properties of spray-deposited fluorine-doped tin oxide thin films from low-cost precursor. *Thin Solid Films*, 476:231–236, 4 2005.

[454] G. Rey, C. Ternon, M. Modreanu, X. Mescot, V. Consonni, and D. Bellet. Electron scattering mechanisms in fluorine-doped SnO_2 thin films. *Journal of Applied Physics*, 114:183713, 11 2013.

[455] Kyung Hee Park and Marshal Dhayal. High efficiency solar cell based on dye sensitized plasma treated nano-structured TiO_2 films. *Electrochemistry Communications*, 11:75–79, 2009.

[456] Michael Grätzel. Dye-sensitized solar cells. *Journal of Photochemistry and Photobiology C: Photochemistry Reviews*, 4:145–153, 10 2003.

[457] Jiayu Wang, Kuan Liu, Lanchao Ma, and Xiaowei Zhan. Triarylamine: Versatile platform for organic, dye-sensitized, and perovskite solar cells. *Chemical Reviews*, 116(23):14675–14725, 2016. PMID: 27960267.

[458] B J Ingram, G B Gonzalez, D R Kammler, M I Bertoni, and T O Mason. Chemical and structural factors governing transparent conductivity in oxides. pages 167–175, 2004.

[459] Pedro Barquinha, Rodrigo Martins, Luis Pereira, and Elvira Fortunato. *Transparent oxide electronics: from materials to devices*. John Wiley Sons, 2012.

[460] Güven Turgut and Erdal Sönmez. Synthesis and characterization of Mo doped SnO2 thin films with spray pyrolysis. *Superlattices and Microstructures*, 69:175–186, 2014.

[461] Ana Espinosa, Nadiezhda Sánchez, Jorge Sánchez-Marcos, Alicia De Andrés, and M. Carmen Muñoz. Origin of the magnetism in undoped and Mn-doped SnO_2 thin films: Sn vs oxygen vacancies. *Journal of Physical Chemistry C*, 115:24054–24060, 2011.

[462] Shoichiro Nakao, Naoomi Yamada, Yasushi Hirose, and Tetsuya Hasegawa. Enhanced carrier generation in Nb-doped SnO_2 thin films grown on strain-inducing substrates. *Applied Physics Express*, 5:3–6, 2012.

[463] Yu Muto, Nobuto Oka, Naoki Tsukamoto, Yoshinori Iwabuchi, Hidefumi Kotsubo, and Yuzo Shigesato. High-rate deposition of Sb-doped SnO_2 films by reactive sputtering using the impedance control method. *Thin Solid Films*, 520:1178–1181, 2011.

[464] Shoichiro Nakao, Naoomi Yamada, Taro Hitosugi, Yasushi Hirose, Toshihiro Shimada, and Tetsuya Hasegawa. Fabrication of transparent conductive W-doped SnO_2 thin films on glass substrates using anatase TiO_2 seed layers. *Physica Status Solidi (C) Current Topics in Solid State Physics*, 2011.

[465] Gui Wang, Likun Wang, Yan Zhu, Yingeng Wang, Yu Su, Wenhao Cai, Jingkai Yang, and Hongli Zhao. Insight into electronic structure and optical properties of Nb and F co-doped SnO_2 with hybrid functional theoretical method. *Ceramics International*, 46:10341–10347, 2020.

[466] Likun Wang, Jianyuan Yu, Xiaoyou Niu, Li Wang, Chen Fu, Rumeng Qiu, and Weijing Yan. Effect of F and Nb co-doping on structural , electrical and optical properties of spray deposited tin oxide thin fi lms. *Thin Solid Films*, 649:147–153, 2018.

[467] Reddivari Muniramaiah, Nandarapu Purushotham Reddy, Rompivalasa Santhosh, Gouranga Maharana, Jean Maria Fernandes, Dilli Babu Padmanaban, M. Kovendhan, Ganapathy Veerappan, Gangalakurti Laxminarayana, Murali Banavoth, and D. Paul Joseph. Anionic fluorine and cationic niobium co-doped tin oxide thin films as transparent conducting electrodes for optoelectronic applications. *physica status solidi (a)*, 5 2023.

[468] M. Esro, S. Georgakopoulos, H. Lu, G. Vourlias, A. Krier, W. I. Milne, W. P. Gillin, and G. Adamopoulos. Solution processed SnO_2:Sb transparent conductive oxide as an alternative to indium tin oxide for applications in organic light emitting diodes. *Journal of Materials Chemistry C*, 4:3563–3570, 2016.

[469] H. Kaneko and K. Miyake. Physical properties of antimony-doped tin oxide thick films. *Journal of Applied Physics*, 53:3629–3633, 1982.

[470] V. Gokulakrishnan, S. Parthiban, K. Jeganathan, and K. Ramamurthi. Investigations on the structural, optical and electrical properties of Nb-doped SnO_2 thin films. *Journal of Materials Science*, 46:5553–5558, 2011.

[471] A. Heiras-Trevizo, P. Amézaga-Madrid, L. Corral-Bustamante, W. Antúnez-Flores, P. Pizá Ruiz, and M. Miki-Yoshida. Structural, morphological, optical and electrical properties of Sb-doped SnO_2 thin films obtained by aerosol assisted chemical vapor deposition. *Thin Solid Films*, 638:22–27, 2017.

[472] N Kikuchi, E Kusano, E Kishio, and A Kinbara. Electrical and mechanical properties of SnO_2:Nb films for touch screens. *Vacuum*, 66:365–371, 2002.

[473] J. Montero, J. Herrero, and C. Guillén. Preparation of reactively sputtered Sb-doped SnO_2 thin films: Structural, electrical and optical properties. *Solar Energy Materials and Solar Cells*, 94:612–616, 2010.

[474] Tetsuo Tsuchiya, F. Kato, T. Nakajima, K. Igarashi, and T. Kumagai. Direct conversion of a metal organic compound to epitaxial Sb-doped SnO_2 film on a (0 0 1) TiO_2 substrate using a Kr-F laser, and its resulting electrical properties. *Applied Surface Science*, 255:9808–9812, 2009.

[475] Ai Yoshie Suzuki, Kenji Nose, Ai Ueno, Masao Kamiko, and Yoshitaka Mitsuda. High transparency and electrical conductivity of SnO_2:Nb thin films formed through (001)-oriented SnO:Nb on glass substrate. *Applied Physics Express*, 5:5–8, 2012.

[476] Keun Soo Kim, Seog Young Yoon, Won Jae Lee, and Kwang Ho Kim. Surface morphologies and electrical properties of antimony-doped tin oxide films deposited by plasma-enhanced chemical vapor deposition. *Surface and Coatings Technology*, 138:229–236, 2001.

[477] M. E. White, O. Bierwagen, M. Y. Tsai, and J. S. Speck. Electron transport properties of antimony doped SnO_2 single crystalline thin films grown by plasma-assisted molecular beam epitaxy. *Journal of Applied Physics*, 106, 2009.

[478] Sapna D. Ponja, Benjamin A.D. Williamson, Sanjayan Sathasivam, David O. Scanlon, Ivan P. Parkin, and Claire J. Carmalt. Enhanced electrical properties of antimony doped tin oxide thin films deposited: Via aerosol assisted chemical vapour deposition. *Journal of Materials Chemistry C*, 6:7257–7266, 2018.

[479] Yoshimasa A Ono. Electroluminescent displays. 5 1995.

[480] Gaytri Sharma, Sang Do Han, Jung Duk Kim, Satyender P. Khatkar, and Young Woo Rhee. Electroluminescent efficiency of alternating current thick film devices using ZnS:Cu,Cl phosphor. *Materials Science and Engineering: B*, 131:271–276, 7 2006.

[481] P. Blaha, K. Schwarz, G. Madsen, D. Kvasnicka, J. Luitz, Robert Laskowsk, F. Tran, and L. Marks. Wien2k: An augmented plane wave plus local orbitals program for calculating crystal properties. *undefined*, 2019.

[482] John P. Perdew, Kieron Burke, and Matthias Ernzerhof. Generalized gradient approximation made simple. *Physical Review Letters*, 78:1396, 2 1997.

[483] A. Svane and E. Antoncik. Electronic structure of rutile SnO_2, GeO_2 and TeO_2. *Journal of Physics and Chemistry of Solids*, 48:171–180, 1 1987.

[484] Yongle Hu, Lin Li, Chunhui Xu, and Ping Yang. Study of high metal doped SnO_2 for photovoltaic devices. *Materials Today Communications*, 27, 6 2021.

[485] R. O. Jones and O. Gunnarsson. The density functional formalism, its applications and prospects. *Reviews of Modern Physics*, 61:689, 7 1989.

[486] C. Z. Chen, N. Y. Wen, H. J. Chen, Y. Li, and C. B. Cai. Enhanced conductivity and high thermal stability of W-doped SnO_2 based on first-principle calculations. *Brazilian Journal of Physics*, 47:26–33, 2017.

[487] D Jayathilake and T Nirmal Peiris. Overview on transparent conducting oxides and state of the art of low-cost doped ZnO systems. *SF J Material Chem Eng1 (1)*, 1004, 2018.

[488] G. K. Williamson and W. H. Hall. X-ray line broadening from filed aluminium and wolfram. *Acta Metallurgica*, 1:22–31, 1 1953.

[489] C. Marcel, N. Naghavi, G. Couturier, J. Salardenne, and J. M. Tarascon. Scattering mechanisms and electronic behavior in transparent conducting $Zn_xIn_2O_{x+3}$ indium–zinc oxide thin films. *Journal of Applied Physics*, 91:4291, 3 2002.

[490] T. S. Moss. The interpretation of the properties of indium antimonide. *Proceedings of the Physical Society. Section B*, 67:775, 10 1954.

[491] Elias Burstein. Anomalous optical absorption limit in insb. *Physical Review*, 93:632, 2 1954.

[492] Nandarapu Purushotham Reddy, Reddivari Muniramaiah, Rompivalasa Santhosh, Jean Maria Fernandes, Dilli Babu Padmanaban, Gouranga Maharana, M. Kovendhan, D. Paul Joseph, and Banavoth Murali. Cost-effective Sb-doped SnO_2 films as stable and efficient alternative transparent conducting electrodes for dye-sensitized solar cells. *Journal of Materials Chemistry C*, 10:7997–8008, 5 2022.

[493] Getnet Kacha Deyu, David Muñoz-Rojas, Laetitia Rapenne, Jean Luc Deschanvres, Andreas Klein, Carmen Jiménez, and Daniel Bellet. SnO_2 films deposited by ultrasonic spray pyrolysis: Influence of Al incorporation on the properties. *Molecules 2019, Vol. 24, Page 2797*, 24:2797, 7 2019.

[494] Sk F. Ahmed, S. Khan, P. K. Ghosh, M. K. Mitra, and K. K. Chattopadhyay. Effect of Al doping on the conductivity type inversion and electro-optical prop-

erties of SnO_2 thin films synthesized by sol-gel technique. *Journal of Sol-Gel Science and Technology*, 39:241–247, 9 2006.

[495] S. K. Sinha, S. K. Ray, and I. Manna. Effect of Al doping on structural, optical and electrical properties of SnO2 thin films synthesized by pulsed laser deposition. *http://dx.doi.org/10.1080/14786435.2014.962641*, 94:3507–3521, 11 2014.

[496] Chafia Khelifi, Abdallah Attaf, Hanane saidi, Anouar Yahia, and Mohamed Dahnoun. Investigation of F doped SnO_2 thin films properties deposited via ultrasonic spray technique for several applications. *Surfaces and Interfaces*, 15:244–249, 2019.

[497] Manjeet Kumar, Bikmramjeet Singh, Pankaj Yadav, Vishwa Bhatt, Manoj Kumar, Kulwinder Singh, A. C. Abhyankar, Akshay Kumar, and Ju Hyung Yun. Effect of structural defects, surface roughness on sensing properties of Al doped ZnO thin films deposited by chemical spray pyrolysis technique. *Ceramics International*, 43:3562–3568, 2017.

[498] Jaswinder Kaur, Somnath C. Roy, and M. C. Bhatnagar. Highly sensitive SnO_2 thin film NO_2 gas sensor operating at low temperature. *Sensors and Actuators, B: Chemical*, 123:1090–1095, 2007.

[499] Shivaraj B. W., H. N. Narasimha Murthy, M. Krishna, and S. C. Sharma. Investigation of influence of spin coating parameters on the morphology of ZnO thin films by taguchi method. *International Journal of Thin Films Science and Technology*, 2:143–154, 2013.

[500] S. Jayapandi, S. Premkumar, V. Ramakrishnan, D. Lakshmi, S. Shanavas, R. Acevedo, and K. Anitha. Enhanced visible light photocatalytic performance of SnO_2 nanoparticle co-doped with (Co, Nb) for organic dye degradation. *Journal of Materials Science: Materials in Electronics*, 31:10689–10701, 7 2020.

[501] E. Kh Shokr, M. M. Wakkad, H. A. Abd El-Ghanny, and H. M. Ali. Sb-doping effects on optical and electrical parameters of SnO_2 films. *Journal of Physics and Chemistry of Solids*, 61:75–85, 1 2000.

[502] Yang Yi Lin, Hsin Yi Lee, Ching Shun Ku, Li Wei Chou, and Albert T. Wu. Bandgap narrowing in high dopant tin oxide degenerate thin film produced by atmosphere pressure chemical vapor deposition. *Applied Physics Letters*, 102, 2013.

[503] A. Oprea, E. Moretton, N. Bârsan, W. J. Becker, J. Wöllenstein, and U. Weimar. Conduction model of SnO_2 thin films based on conductance and hall effect measurements. *Journal of Applied Physics*, 100, 2006.

[504] H. Bisht, H. T. Eun, A. Mehrtens, and M. A. Aegerter. Comparison of spray pyrolyzed FTO, ATO and ITO coatings for flat and bent glass substrates. *Thin Solid Films*, 351:109–114, 1999.

[505] Seung Yup Lee and Byung Ok Park. Structural, electrical and optical characteristics of SnO_2:Sb thin films by ultrasonic spray pyrolysis. *Thin Solid Films*, 510:154–158, 2006.

[506] D H Zhang and H L Ma. Scattering mechanisms of charge carriers in transparent conducting oxide films. *App. Phys. A: Mater. Sci. Proc.*, 62:487–492, 1996.

[507] Sarah R. Cowan, Philip Schulz, Anthony J. Giordano, Andres Garcia, Bradley A. Macleod, Seth R. Marder, Antoine Kahn, David S. Ginley, Erin L. Ratcliff, and Dana C. Olson. Chemically controlled reversible and irreversible extraction barriers via stable interface modification of zinc oxide electron collection layer in polycarbazole-based organic solar cells. *Advanced Functional Materials*, 24:4671–4680, 8 2014.

[508] Erin L. Ratcliff, Andres Garcia, Sergio A. Paniagua, Sarah R. Cowan, Anthony J. Giordano, David S. Ginley, Seth R. Marder, Joseph J. Berry, and Dana C. Olson. Investigating the influence of interfacial contact properties on open circuit voltages in organic photovoltaic performance: Work function versus selectivity. *Advanced Energy Materials*, 3:647–656, 5 2013.

[509] Seong Sik Shin, Dong Wook Kim, Daesub Hwang, Jae Ho Suk, Lee Seul Oh, Byung Suh Han, Dong Hoe Kim, Ju Seong Kim, Dongho Kim, and Jin Young Kim. Controlled interfacial electron dynamics in highly efficient Zn_2SnO_4-based dye-sensitized solar cells. *ChemSusChem*, 7:501–509, 2014.

[510] Unsal Koldemir, Jennifer L. Braid, Amanda Morgenstern, Mark Eberhart, Reuben T. Collins, Dana C. Olson, and Alan Sellinger. Molecular design for tuning work functions of transparent conducting electrodes. *Journal of Physical Chemistry Letters*, 6:2269–2276, 6 2015.

[511] Alexey N. Krasnov. Electroluminescent displays: history and lessons learned. *Displays*, 24:73–79, 8 2003.

[512] J.J. Shea. Handbook of optical materials. *IEEE Electrical Insulation Magazine*, 20:46–46, 10 2004.

[513] S. Pakeva and R. Dafinova. The electroluminescence of ZnS: Pb, Cu, Br phosphors. *physica status solidi (a)*, 106:K97–K100, 3 1988.

[514] Philippe F. Smet, Iwan Moreels, Zeger Hens, and Dirk Poelman. Luminescence in sulfides: A rich history and a bright future. *Materials 2010, Vol. 3, Pages 2834-2883*, 3:2834–2883, 4 2010.

[515] Bipin Kumar Gupta, Satbir Singh, Garima Kedawat, Kanika, Pawan Kumar, Amit Kumar Gangwar, Tharangattu N. Narayanan, Angel A. Marti, Robert Vajtai, and P. M. Ajayan. A novel electroluminescent device based on a reduced graphene oxide wrapped phosphor (ZnS:Cu,Al) and hexagonal-boron nitride for high-performance luminescence. *Nanoscale*, 9:5002–5008, 4 2017.

[516] Ch Satya Kamal, R. K. Mishra, Dinesh K. Patel, K. Ramachandra Rao, V. Sudarsan, and R. K. Vatsa. Effect of structure, size and copper doping on the luminescence properties of ZnS. *Materials Research Bulletin*, 81:127–133, 9 2016.